

TRANSITORY CONTROL OF SEPARATED SHEAR LAYER
USING IMPULSIVE JET ACTUATION

A Dissertation
Presented to
The Academic Faculty

by

George T. K. Woo

In Partial Fulfillment
of the Requirements for the Degree
Doctor of Philosophy in the
School of Mechanical Engineering

Georgia Institute of Technology
December 2014

Copyright © 2014 by George T. K. Woo

TRANSITORY CONTROL OF SEPARATED SHEAR LAYER
USING IMPULSIVE JET ACTUATION

Approved by:

Professor Ari Glezer, Committee Chair
School of Mechanical Engineering
Georgia Institute of Technology

Professor Marc K. Smith
School of Mechanical Engineering
Georgia Institute of Technology

Professor Minami Yoda
School of Mechanical Engineering
Georgia Institute of Technology

Professor Marilyn Smith
School of Aerospace Engineering
Georgia Institute of Technology

Professor Mark Costello
School of Aerospace Engineering
Georgia Institute of Technology

Date Approved: October 30, 2014

Dedicated to my parents,
Jack Woo & Cuirong Huang.

ACKNOWLEDGEMENTS

I am hugely indebted to many people for their help and support in my graduate school journey.

First of all, I would like to extend my greatest gratitude to my thesis and research adviser, Professor Ari Glezer, for his guidance and enduring support. I have always enjoyed the pursuit of excellence and in the sciences, and Professor Glezer helped me strive for even better. He constantly challenged me to be creative, rigorous and hands-on with all aspects of my research, and provided me with invaluable advice and opportunities, and with many unmatched resources to accomplish my goals. Professor Glezer has been exceptionally thorough and exceedingly challenged me during the process of writing this dissertation. I would also like to thank him for his patience, counsel, and generosity in having me as his student and for the many learning opportunities at conferences in Europe and Asia, and in the U.S. It has been a pleasure working with you. I was also fortunate to get to know Professor Glezer and his family on a personal level. Professor Glezer and his wife, Maggie, were always willing to help with my many personal endeavors and were amazing hosts for the annual Winter Solstice dinner. I have many fond memories of Professor Glezer outside of the lab. One that vividly comes to mind is our conference trip to Seoul where we ventured through the city in search for vegetarian foods.

I am also very grateful for the time invested by the other committee members throughout the course of my Ph.D. studies and during the many revisions of my dissertation. I truly appreciate the technical comments and insights provided by the committee, and their patience in helping me develop a thorough and quality dissertation. I

would like to thank Professors Marilyn Smith and Mark Costello for providing me with their expansive knowledge on rotorcraft aerodynamics. Professor Smith has helped tremendously in guiding me to refine this thesis to better serve the wider interests of researchers in the rotorcraft community and Professor Costello has provided invaluable feedback on the applications of my research. I also would like to acknowledge the expertise of Professors Minami Yoda and Marc Smith, and their thoughtful comments relating to the subject of fluid mechanics in my thesis. I truly appreciate the inputs by Professor Yoda to help elevate the experimental integrity of my research and the questions by Professor Smith on the underlying physics in my dissertation. The rigor demonstrated by my committee members is second to none.

I am deeply grateful for the friendship, camaraderie and technical help from the past and present members of Professor Glezer's Fluid Mechanics Research Lab. I have thoroughly enjoyed the privileges of growing personally and professionally in the company of a diverse and very pleasant group of people. I am thankful for former labmates Dr. Donavon Gerty, Philip Abramson, Brett Warta and Hanif Hunter for helping me settle into the new environment, and for Ashok Rajendar and Abe Gissen for the much-needed support when we began our FMRL journey together. I would like to acknowledge the steadfast friendship and help with my research from my fellow labmates whom I have spent countless hours with at Georgia Tech for the majority of the past seven years. Special gratitude goes to Dr. Daniel Brzozowski, Abe Gissen, John Kearney, Mark Simpson, Thomas Boziuk, Thomas Lambert, Dr. Pablo Hidalgo, and Taylor Jones for their help in overcoming many of my hurdles in the lab. I was also fortunate to have the opportunity to work with and learn from Zicheng Gong, Sourabh

Jha and Yuehan Tan, the younger talents of FMRL. I am grateful for my FMRL colleagues and their significant others for the many daily and special meals we enjoyed together (e.g., Thanksgiving, Independence Day, Outback, and Super Bowl). In particular, I am grateful for the many great (and mediocre) movies and adventures (e.g., weddings, conferences, road trips, trivia nights, golf, visits to the barn, swimming, fishing and six flags), and the unimaginable patience when it came to sharing lab equipment and storage space on the farm-server. I also would like to thank Dr. Chris Rinehart and Michael DeSalvo, tenured FMRL members, for their help. I wish all present FMRL members happiness and all the success in their pursuit of academic knowledge. I thoroughly enjoyed everyone's company and look forward to another opportunity to view sporting events such as the World Cup and the Olympics, and cheering for the U.S. More importantly, I would like to thank everyone at FMRL, especially John Kearney, Mark Simpson and Abe Gissen for their personal advice and support.

My tenure in FMRL would not be successful without the mentoring, technical assistance and friendship of Dr. Daniel Brzozowski, starting from my first visit to Georgia Tech in 2007 to providing me with accommodation for the first summer after I joined the FMRL to his limitless experience with acquiring and processing PIV to the recent career advice as I began my job search. I am deeply grateful for all the personal support from Dr. Daniel Brzozowski during his doctoral tenure at FMRL, and also for his data processing codes.

I would like to thank the research engineers (Drs. Thomas Crittenden, Bojan Vukasinovic, Slava Yorish and Pablo Hidalgo, and Jelena Vukasinovic and John Culp), postdoctoral researcher (Dr. Boris Zakharin), and administrators (Judy Diamond and

Dana Foster) at FMRL for their help over the years. I would also like to acknowledge the technical assistance from Dr. Crittenden on the COMPACT that has been the core of my research, the design and machining of complex parts and instrumentations from Dr. Slava Yorish and John Culp, and the mentoring from Dr. Bojan Vukasinovic (and his Serbian humor). I am also grateful for the tremendous dedication John Culp has in developing the state-of-the-art technologies for the wind tunnel, traverse, PIV and farm-server facilities that I have been 100% dependent on for my research, and for his help in recovering my data following several power failures. I wish all FMRL members and their families that I have met over the years every success in their endeavors.

I would also like to thank Stanford Professors John Eaton and Godfrey Mungal for being great mentors and for the research opportunities during my Masters degree that provided me with invaluable skills for my doctoral research. I am also grateful for the wonderful undergraduate and high school education experiences in New Zealand, and in the Solomon Islands that have contributed to my knowledge and passion prior to arriving in the U.S.

I would also like to gratefully acknowledge the financial support received from NASA's Subsonic Rotary Wing and the AFOSR under award NNX07AD08A and grant FA9550-11-1-0077, respectively.

Finally, I would like to express my deepest gratitude to both the Woo and Chan families for their unconditional support. This dissertation is dedicated to my parents, Jack and Cuirong, whom are instrumental in all of my academic achievements. Their love, work ethics and sacrifices have inspired me and without their encouragement, none of this would be possible. My parents' determination has given me many once-in-a-lifetime

opportunities. I am also grateful of my siblings, Stephen, David and Mary, for being great role models during my childhood and for all the help they have given me with my studies. I could not have asked for a more loving and supportive family for the past 30 years. Despite the 15000 km separation, my years in the U.S. are filled with fond memories of my family. I want to also thank my girlfriend, Jennifer Chan, her parents Dr. Chiu and Anita, and sister, Katie who have cared and supported me throughout the past seven years. They have made my studies so much more fun with their humor, kindness and amazing cooking, and our lovely overseas holiday trips together, and have always encouraged me in my studies and were there to offer valued advice and support. My girlfriend is always a joy to be with, and has been a champion for my research. She is always here for me whenever I need help, and is a constant reminder of the important things outside of work. Jennifer is an inspiration for me with her endless encouragement, compassion, and patience. I am truly fortunate to have found someone who understands me, and shares my passion for learning and intellectual curiosity, and determination for excellence. I thank her for having changed my life in many pleasant ways, and for making me smile.

TABLE OF CONTENTS

ACKNOWLEDGEMENTS.....	iii
LIST OF TABLES.....	xi
LIST OF FIGURES.....	xii
NOMENCLATURE.....	xxii
SUMMARY.....	xxiv
I. MOTIVATION AND LITERATURE REVIEW.....	1
1.1. Overview of Thesis Research.....	1
1.2. Aerodynamic Flow Control of Separation over Airfoils.....	3
1.2.1. Some Aspects of the Physics of Separation Flow Control.....	3
1.2.2. Active Fluidic-Based Technologies.....	6
1.2.3. Control of Time-Dependent Separation.....	9
1.2.4. A Note on Finite-Span Actuation.....	11
1.3. Thesis Objectives.....	12
II. EXPERIMENTAL SETUP AND PROCEDURE.....	15
2.1. Wind Tunnel Setup.....	15
2.1.1. The Airfoil Model.....	16
2.1.2. Fences.....	19
2.2. Traverse Mechanism.....	21
2.2.1. Pitch Axis.....	22
2.2.2. Load Cells.....	24
2.3. Flow Measurements using Particle Image Velocimetry (PIV).....	25
2.3.1. The PIV System.....	25
2.3.2. PIV Image Acquisition Procedure.....	28
2.3.3. PIV Image Processing.....	30
2.3.4. Vector Computation and Derived Quantities.....	32
2.4. Aerodynamic Loads.....	39
2.5. Pressure Measurements.....	41
2.6. Surface Oil Visualization.....	43

III.	COMBUSTION POWERED ACTUATORS	56
3.1.	Basic Concept.....	56
3.2.	Structure of The Actuator Array	58
3.3.	Bench Top Characterization of the Actuator Array	60
IV.	TRANSITORY PULSED ATTACHMENT	74
4.1.	Transitory Effects of Single Pulse Actuation.....	74
4.1.1.	The Base Flow	74
4.1.2.	Global Characteristics of the Actuated Flow.....	77
4.1.3.	Near Wake Measurements	81
4.2.	The Interaction of a Momentary Pulsed Jet with the Cross Flow	88
4.2.1.	Severing of the Shear Layer and Formation of Vortical Structures	88
4.2.2.	Attachment Mechanisms	97
V.	SUCCESSIVE ACTUATION.....	119
5.1.	Aerodynamic Performance Enhancement using Successive Actuation Pulses	119
5.1.1.	Transitory Flow Attachment and Circulation Build-Up.....	119
5.1.2.	Burst-Modulated Pulses.....	125
5.2.	Interactions of Repetitive Pulsed Actuation with the Cross Flow	126
5.2.1.	Formation of Vortical Structures using Successive Pulses at $T_{rep} = T_{conv}$	127
5.2.2.	Effects of Decreasing T_{rep}	132
VI.	FINITE-SPAN UNBOUNDED TRANSITORY ACTUATION IN A NOMINALLY 2-D SEPARATED FLOW	152
6.1.	Unbounded Attachment	152
6.1.1.	Characterization of the Separated Flow.....	152
6.1.2.	Single Pulse, Spatially-Compact Actuation.....	155
6.2.	The Interface between the Actuated and Unactuated Flow Domains .	161
6.2.1.	Global Flow Structures	161
6.2.2.	The Effect of the Severed CW Vortex on Attachment	166
6.2.3.	Spanwise Spreading of Attachment.....	170

VII.	UNBOUNDED ACTUATION IN A NOMINALLY 3-D SEPARATED FLOW	190
	190
7.1.	The Base Flow Field	190
7.2.	Pulsed Transients in 3-D Separation on a Static Airfoil	193
7.2.1.	Actuation Effects	194
7.2.2.	3-D Velocity and Vorticity Field.....	197
7.3.	Controlled, Transitory 3-D Attachment on a Dynamically-Pitching Airfoil.....	201
7.3.1.	Timed-Interactions of a Single Actuation Pulse with Time- Periodic Separation.....	202
7.3.2.	Multiple Pulses and Staged-Actuation.....	209
VIII.	CONCLUSIONS	245
8.1.	Overview	245
8.2.	Bounded, 2-D Actuation	247
8.3.	Unbounded Actuation	250
8.4.	Contributions of the Present Work.....	254
8.5.	Recommendations for Future Work.....	255
A.	PARTICLE IMAGE VELOCIMETRY DATA	257
B.	PRESSURE PORT DATA.....	261
	REFERENCES	262
	VITA.....	278

LIST OF TABLES

Table 5.1:	Timing of PIV images in Figure 5.6 following the 1 st (a), 5 th (b), 10 th (c), 15 th (d), and 25 th (e) pulses separated by $T_{\text{rep}} = T_{\text{conv}}$	145
Table A.1:	Static Airfoil PIV Data.....	258
Table A.1:	(Continued).	259
Table A.2:	Dynamic Pitching Airfoil PIV Data.....	260
Table B.1:	Pressure Port Locations on Airfoil at $\alpha = 0^\circ$	261

LIST OF FIGURES

Figure 2.1:	CAD model of the wind tunnel facility showing the flow contraction and test section with an airfoil model mounted to the 2-DOF traverse mechanism. Other upstream and downstream sections of the tunnel facility are not included.	45
Figure 2.2:	NACA4415 airfoil model: (a) Cross sectional view showing location of actuator jets at $x_a/c = 0.15$, and (b) Top view showing the spanwise actuator array (having span S_{act}), and the streamwise fences separating the actuated (“A”) and unactuated (“B”) flow domains.	45
Figure 2.3:	CAD model of airfoil model: a) Assembled with fences, mounting shaft and the dummy sections, and (b) Close up view of the actuator array and internal structure of the mounting shaft.	46
Figure 2.4:	Schematic of the seven rectangular jet orifices in the actuator module shown in Figures 2.2 and 2.3. The orifices are aligned to the span of the airfoil.	47
Figure 2.5:	Scaled outline of the streamwise fences (a – d) relative to the airfoil.	47
Figure 2.6:	CAD model of the traverse mechanism: a) The front and back carriages with laboratory coordinates shown and b) The load cell mounted to the gimbal.	48
Figure 2.7:	Timing of model pitch motion $\alpha(t) = \alpha_0 + \alpha_p \sin(\Omega t)$ and actuation.	49
Figure 2.8:	CAD model of PIV windows installed on the wind tunnel ceiling of the test section: (a) Viewed from above the tunnel and (b) Viewed from inside the test section showing the windows flush to the ceiling.	50
Figure 2.9:	CAD model of dual-level calibration plate used for PIV showing the machined pattern of round dots.	51
Figure 2.10:	Schematic of overlapping PIV windows used. The different colors represent domains investigated in the different sections of the dissertation.	51
Figure 2.11:	Setup of stereo-PIV showing (a) measurement coordinates and flow domain within laser sheet in green and, and (b) the relative angle of the measurement plane to the wind tunnel coordinates.	52
Figure 2.12:	Sample images acquired using PIV camera above the airfoil illuminated using Nd:YLF laser: (a) Raw instantaneous phase-locked image of flow seeded with fog particles and (b) “Background” image averaged over 50 instantaneous realizations without fog particles.	53
Figure 2.13:	Pre-processed PIV images corresponding to Figure 2.11a. Background image in Figure 2.11b is subtracted (a) and with fixed	

	mask applied (b). Minimum intensities from the sequence of 200 realizations are subtracted (c) and with fixed mask applied (d).	54
Figure 2.14:	The measured lift and pitching moment coefficients acting at the pitch axis away from the reference quarter-chord location.	55
Figure 3.1:	Basic concept of combustion-powered (COMPACT) actuator.	66
Figure 3.2:	Actuation timing of a burst of N pulses separated by T_{rep} , followed by a second burst delayed by T_{delay}	66
Figure 3.3:	(a) CAD model of actuator module showing internal structure of the seven $O(1 \text{ cm}^3)$ combustion chambers, spark plugs and needle valves, and the manifold for the reactants, and (b) Cross-section view inside a chamber and its orifice showing reactant flow paths, and other manifold components. The airfoil coordinates are included.....	67
Figure 3.4:	Photos of (a) Rimfire V1 Viper spark plug, and (b) Combustion chamber equipped with 0.1 mm thick brass shim insert with 7 laser cut holes. Two 6.35 mm thick 316SS fluidic valves wire-EDM from porous media grades; 2 (c) and 10 (d).	68
Figure 3.5:	Particulate deposited on porous media following continual use in combustion chamber (a – c). These fluidic valves are identical in size with valves in Figure 3.4c & d.....	68
Figure 3.6:	Phase-locked schlieren images of the pulsed jet emanating from the center actuator of the array following actuation (at $t = 0$): 0.49 (a), 0.61 (b), 0.73 (c), 0.80 (d), 0.85 (e), 0.98 (f), 1.22 (g), 1.46 (h), 1.71 (i), and 2.15 (j) ms. These phases correspond to the marked timings on the chamber pressure time traces in Figure 3.7.....	69
Figure 3.7:	Phase-averaged, pressure-time history of the center combustor following the single pulsed jet triggered at $t = 0$ (→). The pulse is repeated with $T_{\text{rep}} = 200$ (←), 100 (→), 50 (←) and 33.3 (→) ms. The corresponding timings of the jet in Figures 3.6 are labeled (a) - (j) and marked (●).	69
Figure 3.8:	Phase-averaged pressure traces (–) and corresponding ± 1 standard deviation band (shaded) of center chamber in the array for repeated actuation: $T_{\text{rep}} = 1000$ (a), 200 (b), and 100 (c) ms. The combustion is stoichiometric with 0.36 LPM of reactants.....	70
Figure 3.9:	Phase-averaged pressure traces (–) and corresponding ± 1 standard deviation band (shaded) inside the 1st (a), 3rd (b), 5th (c), and 7th (d) actuators in the array for repeated actuation ($T_{\text{rep}} = 200$ ms), and the corresponding mean (–) and standard deviation across all seven actuators (e). The combustion equivalence ratio is 0.6 with 3.5 LPM of reactants.....	71
Figure 3.10:	Phase-averaged pressure traces (–) and the corresponding ± 1 standard deviation band (shaded) inside center actuator for $T_{\text{rep}} = 10$ (a), 6.67	




	(b) and 5 (c) ms. The equivalence ratio is 0.6 with 10 LPM of reactants.	72
Figure 3.11:	Examples of the instantaneous pressure start-up transients inside the center actuator following trigger at $t = 0$ and the pulses are repeated with $T_{\text{rep}} = 10$ (a), and 6.67 (b) ms under identical conditions in Figure 3.10.....	73
Figure 4.1:	(a) Base flow lift coefficient, C_L , computed from mid-span pressure distribution C_p for $0 \leq \alpha \leq 24^\circ$ for current NACA 4415 airfoil configuration ($S_{\text{fence}} = 0.35c$) at $Re_c = 5.7 \times 10^5$, and (b) Distributions of C_p for $\alpha = 14$ (●), 16.5 (●) and 19° (●) (the green arrow shows the streamwise location of the actuator orifice).....	104
Figure 4.2:	Surface oil visualizations obtained at 5 (a) and 15 (b) minutes following air flow show progression of nominally 2-D separation line on the airfoil spanwise-confined by fences at S_{fence} apart on the left and right sides of each image. The arrows mark local flow features and the actuators are also marked (-).	105
Figure 4.3:	Time sequence of phase-averaged vorticity concentrations following single-pulse actuation at $t = 0$; $t/T_{\text{conv}} = 0$ (a), 0.16 (b), 0.32 (c), 0.48 (d), 0.64 (e), 0.8 (f), 0.96 (g), 1.12 (h), 1.28 (i), 1.44 (j), 1.6 (k), 1.76 (l), 1.92 (m), 3.2 (n) and 4.8 (o). Location of the jet orifice is marked by black triangle in (a).	106
Figure 4.4:	Phase-averaged changes in surface pressure measured by distributed sensors on airfoil (a) following single actuation pulse: b) $0 \leq t/T_{\text{conv}} \leq 40$, and c) and $0 \leq t/T_{\text{conv}} \leq 4$. Time traces shown at $x/c = 0$ (—), 0.25 (—), 0.45 (—) and 0.68 (—) on the pressure side, and 0.5 (—) the on suction side. The location of actuator array is marked by triangle in (a).	107
Figure 4.5:	Flow field in the near wake (velocity vectors and vorticity concentrations) following single-pulse actuation at $t = 0$; $t/T_{\text{conv}} = 0$ (a), 0.32 (b), 0.48 (c), 0.8 (d), 0.96 (e), 1.12 (f), 1.28 (g), 1.44 (h), 1.6 (i), 1.76 (j), 2.08 (k), 2.72 (l), 4.64 (m), 6.24 (n) and 11.04 (o).....	108
Figure 4.6:	Cross stream distributions on the near wake of the streamwise, u (a), and cross stream, v (b) velocity components and of the spanwise vorticity, ω (c) measured at $0.25c$ downstream from trailing edge following single-pulse actuation at $t/T_{\text{conv}} = 0$ (—), 0.48 (—), 0.96 (—), 1.6 (—), and 2.72 (—).	109
Figure 4.7:	Time evolution of phase-averaged cross stream distribution of vorticity flux, $\omega_z u$, at $x/c = 0.25$ downstream of the trailing edge overlaid $y_{\text{wake}}(t; x/c)$, (- -) following single-pulse actuation; CW ($y > y_{\text{wake}}$) and CCW ($y < y_{\text{wake}}$). Red and blue ovals mark the shedding of the CCW and CW vortices, respectively, as shown in Figure 4.5. The time axis colors represent the CW vortex shedding  , attachment  , and relaxation 	109



Figure 4.8:	(a) Variation in the normalized vorticity flux $(d\Gamma/dt)^*$ in the near wake ($x/c = 1.25$, following an actuation pulse $[(d\Gamma/dt) = -(cU_\infty)^{-1} \int_{y_0}^{y_1} u \cdot \omega_z dy]$: top (●, CW) and bottom (●, CCW) surfaces, and their sum (●), and (b) The corresponding incremental changes in circulation. The schematic on the left illustrates the cross stream vorticity distribution. . 110
Figure 4.9:	Time traces of the incremental changes (relative to the unforced flow) in streamwise (●) and cross stream (●) momentum fluxes across the wake. 111
Figure 4.10:	Raster plots of phase-averaged spanwise vorticity concentrations superimposed with streamlines following single-pulse actuation at $t/T_{conv} = 0$ (a), and 0.2 (b). The dividing streamline connects the stagnation point “S0”. Actuator location is marked with black triangle. 112
Figure 4.11:	Raster plots of phase-averaged spanwise vorticity following a single-pulse actuation at $t/T_{conv} = 0.2$ superimposed with (a) velocity vectors and (b) velocity vectors relative to base flow. Corresponding contour of the changes in the streamwise, Δu (c) and cross stream velocity, Δv (d) relative to base flow. 113
Figure 4.12:	Raster plots of phase-averaged spanwise vorticity superimposed with velocity vectors following a single-pulse actuation at $t/T_{conv} = 0.24$ (a), 0.28 (b), 0.32 (c), 0.36 (d), 0.4 (e), 0.52 (f), 0.8 (g) and 1.16 (h). The “severed” region of low vorticity concentration is marked by †. 114
Figure 4.13:	$x-t$ contour plot of phase-averaged vorticity flux F_ω showing flow structure celerity over airfoil (-) and marked (--) corresponding to the time traces of vorticity flux relative to base flow, ΔF_ω^* , following single actuation pulse. at $x/c = 0.24$ (i), 0.28 (ii), 0.38 (iii) and 0.48 (iv), and at $t/T_{conv} = 0.28$ (v), 0.40 (vi), 0.52 (vii) and 0.84 (viii). 115
Figure 4.14:	Phase-averaged raster plots of $d\omega/dt$ at $t/T_{conv} = 0.24$ (a), 0.28 (b), 0.32 (c) and 0.76 (d) with iso-contours of $\omega = 400$ (---) and -800 s^{-1} (---), and regions marked “A” – “E”..... 116
Figure 4.15:	Raster plots of phase-averaged of spanwise vorticity superimposed with streamlines following actuation at $t/T_{conv} = 0.24$ (a), 0.28 (b), 0.32 (c), 0.36 (d), 0.52 (e), and 0.76 (f). Approximate locations of stagnation points are marked “S0” and “S1”. 117
Figure 4.16:	Phase-averaged raster plots of the pressure gradients, dC_p/dx (a, c) and dC_p/dy (b, d) following actuation at $t/T_{conv} = 0.52$ (a, b), and 0.76 (c, d) corresponding to the flow in Figures 4.15e and f, respectively..... 118
Figure 5.1:	Lift increment induced by time-periodic pulse actuation with increased repetition rate St_{act} 140

Figure 5.2:	Time traces of the incremental change in circulation around a static airfoil following repetitive actuation with $N = 1$ (●), 5 (●), 10 (●), and 25 (●) pulses ($T_{\text{rep}} = T_{\text{conv}}$).	140
Figure 5.3:	Phase-averaged vorticity over the airfoil following the 1 st (b-f), 2 nd (g-k), 3 rd (l-p), 4 th (q-u) and 5 th (v-z) successive pulses separated ($T_{\text{rep}} = T_{\text{conv}}$). The base flow is shown in (a).	141
Figure 5.4:	Instantaneous pressure distributions around the airfoil at $x/c = 0$ (b), 0.24 (c), 0.45 (c), 0.68 (d) on suction side and 0.5 (f) on pressure side for $N = 1$ (←), 5 (←), 10 (←) and 25 (←) pulses at $St_{\text{act}} = 1$. The pressure sensor locations (b - f) are marked in (a).	142
Figure 5.5:	(a) Temporal variation of the normalized vorticity flux for two consecutive repeating actuation bursts ($N = 5$) with $T_{\text{delay}} = 4T_{\text{conv}}$: Suction surface (negative) flux (▼), pressure surface (positive) flux (▲), and the net flux (◆). (b) The corresponding incremental changes in circulation (●). Circulation for a single burst ($N = 5$) are shown for reference in gray (●).	143
Figure 5.6:	Phase-averaged vorticity in the vicinity of the actuator orifice showing the interactions between the actuation jet and the cross flow following the 1 st (a), 5 th (b), 10 th (c), 15 th (d), and 25 th (e) pulses separated by $T_{\text{rep}} = T_{\text{conv}}$. The PIV timing is shown in Table 5.1. Streamlines are included and streamwise location of actuators is marked by triangle.	144
Figure 5.7:	$x-t$ raster plots of phase-averaged vorticity flux for 10 successive actuation pulses ($T_{\text{rep}} = T_{\text{conv}}$) showing the differences in propagation speeds of the induced vorticity concentrations. Vorticity flux levels are the same as in Figure 5. Arrows indicate location of the actuators. .	145
Figure 5.8:	Phase-averaged circulation increments induced by repetitive burst actuation $N = 50$ and $T_{\text{rep}} = 0.4T_{\text{conv}}$ (blue) and $N = 25$, $T_{\text{rep}} = T_{\text{conv}}$ (gray). Actuation timing is shown below the traces.	146
Figure 5.9.	Phase-averaged vorticity in the vicinity of the actuator orifice showing the interactions between the actuation jet and the cross flow following the 1 st pulse separated by $T_{\text{rep}} = 0.4T_{\text{conv}}$ (a-e, k-o and u-w) and $T_{\text{rep}} = T_{\text{conv}}$ (f-j, o-t and x-z).....	147
Figure 5.10:	Phase-averaged vorticity in the vicinity of the actuator orifice showing the interactions between the actuation jet and the cross flow separated for $T_{\text{rep}} = 0.4T_{\text{conv}}$	148
Figure 5.11:	Phase-averaged vorticity superimposed with streamlines showing the successive actuation effects at $t/T_{\text{conv}} = 0.6$ (i), 0.64 (ii), 0.68 (iii), 0.72 (iv), 0.76 (v), and 0.8 (vi) for $St_{\text{act}} = 1$ (a), 2.5 (b) and 3.5 (c). During these times, the effects are following the 1 st (a) and 2 nd (b and c) pulses.....	149

Figure 5.12:	Phase-averaged vorticity superimposed with streamlines showing the successive actuation effects following the 3 rd pulse for $St_{act} = 1$ at $t/T_{conv} = 2.24, 2.28$ and 2.32 (a-i to a-iii), $St_{act} = 2.5$ at $t/T_{conv} = 1, 1.04$ and 1.08 (b-i to b-iii), and $St_{act} = 3.5$ at $t/T_{conv} = 0.84, 0.88$ and 0.92 (c-i to c-iii).	150
Figure 5.13:	$x-t$ raster plots of phase-averaged vorticity flux for 10 successive actuation pulses at $T_{rep} = 0.4T_{conv}$ (a) and $T_{rep} = 0.285T_{conv}$ (b), showing the differences in propagation speeds of the induced vorticity concentrations and the interactions between the vorticity concentrations within the measurement domain. Enclosed dashed region indicates the interaction between the first and second pulses. Arrows indicate streamwise location of the actuator array.....	151
Figure 6.1:	Cross stream distributions of streamwise velocity, u , in the base flow over the airfoil ($S_{fence}/c = 1.07$) at $x/c = 0.64$ (a) and 0.94 (b), and in the near wake at $x/c = 1.23$ (c) in the spanwise planes $z/c = 0$ (—), 0.088 (—), 0.175 (—), 0.219 (—) and 0.284 (—). The corresponding iso-surface contours of the spanwise vorticity over the airfoil without showing the fences (d).	177
Figure 6.2:	Phase-averaged vorticity and velocity maps in the cross stream planes $z/c = 0$ (a & b) and 0.22 (c) in the near wake at $\alpha = 19^\circ$ following single pulse actuation for the bounded (2-D, a-i to a-vii) and the unbounded (3-D, rows b and c) configurations: $t/T_{conv} = 0$ (i), 1.28 (ii), 1.6 (iii), 2.08 (iv), 2.24 (v), 2.56 (vi) and 4.64 (vii). The spanwise extent of the pulsed jet actuation (blue arrows) and the PIV plane (—) are shown schematically on the left side of each sequence.	178
Figure 6.3:	Time evolution of phase-averaged cross stream distribution of vorticity flux, $\omega_z u$, at $x/c = 0.25$ downstream of the trailing edge following single-pulse finite span actuation at spanwise planes; $z/c = 0$ (a), 0.22 (b) and 0.33 (c). Black and red ovals in (a) mark the low-vorticity region between shed CW vortex and attaching boundary layer, and modification to the CCW and CW layers, respectively, as shown in Figure 6.2.....	179
Figure 6.4:	Phase-averaged incremental change in circulation following a single actuation pulse for 2-D (● at $z = 0$) and 3-D finite span (●, ● and ● at $z = 0, 0.22c$ and $0.33c$, respectively) actuation configurations.	180
Figure 6.5:	Phase-averaged vorticity and streamlines following single spanwise-unbounded ($S_{act} \approx 0.13c$ and $S_{fence} \approx c$) pulsed actuation in the cross stream planes shown as columns: $z/S_{act} = 0$ (a), 0.42 (b), 1.25 (c), 1.67 (d), and 2.24 (e). The measurement times are constant in each row; $t/T_{conv} = 0$ (i), 1.12 (ii), 1.52 (iii), and 2.32 (iv)	181
Figure 6.5:	(Continued)	182
Figure 6.6:	Distributions of phase-averaged spanwise vorticity in multiple cross stream planes spaced 5 mm apart ($0 \leq z/c \leq 0.265$) mirrored about	

- $z = 0$ and viewed downstream from the leading edge at $t/T_{\text{conv}} = 0$ (a), 0.72 (b), 0.8 (c), 0.88 (d), 0.96 (e), 1.04 (f), 1.12 (g), 1.2 (h) and 1.28 (i). The three actuator array is marked at the upstream edge. The arrow in (b) marks the outermost severing of the shear layer at that instance. 183
- Figure 6.7: Distribution of phase-averaged spanwise vorticity, ω_z , across the span at $x/c = 0.76$ mirrored about $z = 0$ at $t/T_{\text{conv}} = 0$ (a), 0.72 (b), 0.88 (c), 0.96 (d), 1.04 (e), 1.12 (f), 1.2 (g), 1.28 (h), 1.36 (i), 1.44 (j), 1.52 (k), 1.68 (l), 1.92 (m), 2.32 (n) and 3.12 (o). The airfoil surface is shown as dashed line. 184
- Figure 6.8: Distribution of phase-averaged spanwise vorticity, ω_z , across the span at $x/c = 0.85$ (a-e) and 0.95 (f-j) for the flow in Figure 6.5 mirrored about $z = 0$ at $t/T_{\text{conv}} = 1.52$ (a, f), 1.68 (b, g), 1.92 (c, h), 2.32 (d, i), and 3.12 (e, j). The airfoil surface is shown as dashed line. 185
- Figure 6.9: Distribution of the phase-averaged cross stream velocity, v , across the span at $x/c = 0.76$ for the flow in Figure 6.8 mirrored about $z = 0$ at the same timing t/T_{conv} as in Figure 6.7. 186
- Figure 6.10: Phase-averaged contours of streamwise flux of vorticity, $\int \omega u \, dy$, computed at each location x from the PIV planes for $t/T_{\text{conv}} = 0.64$ (a), 0.72 (b), 0.8 (c), 0.88 (d), 0.96 (e), 1.04 (f), 1.12 (g), 1.2 (h), 1.28 (i), 1.36 (j), 1.44 (k), 1.52 (l), 1.6 (m), 1.68 (n), 1.76 (o) and 1.84 (p). The spanwise actuator array is shown for reference at the bottom of each plot. The labeled contours represent increased (“I” and “III”) and decreased (“II”) CW vorticity flux. The circles represent the spanwise edges of “I” (○) and “II” (●) at the previous instance. The data are mirrored about $z = 0$ 187
- Figure 6.11: Raster plots of spanwise vorticity in three y - z planes overlaid on the airfoil illustrating averaging of $\omega(y, z; t)$ within the domain $0.05 \leq y/c \leq 0.1$ above the surface that is represented by the dashed lines located at $y = \Delta y$ at each x . The location $z = z_o$ along the dash lines for which $\omega(\Delta y, z) = \omega_b = -300 \, \text{s}^{-1}$ is marked by (●). The data are mirrored about $z = 0$ 188
- Figure 6.12: (a) Phase-averaged contours in the x - z plane for $1.12 \leq t/T_{\text{conv}} \leq 2.32$ where each contour represents the loci of $z_o(x)$ within $0.05 \leq y/c \leq 0.1$ above the surface for which $\omega = \omega_b = -300 \, \text{s}^{-1}$ (cf., Figure 6.11). These loci represent the spanwise and streamwise development of the effects of the actuation on the boundary layer above the airfoil’s surface. The spanwise edge of each contour is marked by (●). (b) The spreading rate of the interface between the attached and outer flow is estimated by the celerity of the edges of the contour lines in (a) in the streamwise (○, Δx) and spanwise (●, Δz) directions, and are compared with the streamwise growth rate of the loci on the centerline (○, Δx). The data are mirrored about $z = 0$ 189

Figure 7.1:	Surface oil visualization of base flow over airfoil at 1 (a), 7 (b), 36 (c) and 105 (d) minutes. Arrows mark free stream flow direction (a), separation line (b), spanwise flow (c), and counter-rotating swirl (d). Green lines (d) show measurement locations of planar-PIV at $z/c = 0$ (i), 0.16 (ii), 0.27 (iii) and 0.39 (iv), and stereo-PIV at $x/c = 0.78$ (v). Location of actuators is marked (- -).....	222
Figure 7.2:	Base flow velocity profiles of u (a) and w (b) obtained from stereo-PIV at $x/c = 0.78$ and above airfoil surface; $\Delta y/c = 0.074$ (●), 0.17 (●) and 0.233 (●). Symmetry plane is at mid-span ($z = 0$).....	223
Figure 7.3:	Cross stream distribution of streamwise velocity, u , in the base flow over the airfoil at $x/c = 0.46$ (a), 0.71 (b), 0.96 (c) and in the near wake at $x/c = 1.22$ (d) in the spanwise planes: $z/c = 0$ (⇐), 0.16 (⇐), 0.27 (⇐) and 0.39 (⇐).....	224
Figure 7.4:	Contours of spanwise vorticity obtained in the four spanwise planes in Figure 7.3 ($z/c = 0, 0.16, 0.27$ and 0.39) and mirrored about $z = 0$ showing flow relative to actuators (a) and spanwise variations across the wake (b). The PIV planes (as edges) and actuators (as rectangular blocks) are outlined, and the streamwise fences are not included.	225
Figure 7.5:	Phase-averaged PIV measurements of spanwise vorticity following single pulse actuation for the planes located at $z/c = 0$ (column a), 0.17 (b), 0.27 (c), and 0.39 (d) at $t/T_{\text{conv}} = 0$ (row i), 0.4 (ii), 0.64 (iii), 0.88 (iv), 1.12 (v), 1.52 (vi), 1.76 (vii), and 2.64 (viii).....	226
Figure 7.5:	(Continued).....	227
Figure 7.6:	Phase-averaged spanwise vorticity following single pulse actuation for the PIV planes located at $z/c = 0, 0.17, 0.27,$ and 0.39 , which are also mirrored about $z = 0$: $t/T_{\text{conv}} = 0.1$ (a), 0.56 (b), 0.72 (c), 1.2 (d) and 2.08 (e). The outline of measurement frames is included.	228
Figure 7.7:	Phase-averaged raster plot of $\hat{\omega}_x$ obtained from stereoscopic PIV measurements at $0.2c$ from the trailing edge following single pulsed actuation $t/T_{\text{conv}} = 0$ (a), 0.88 (b), 1.04 (c), 1.12 (d), 1.2 (e), 1.28 (f), 1.36 (g), 1.44 (h), 1.52 (i), 1.6 (j), 1.68 (k), 1.76 (l), 1.84 (m), 1.92 (n), 2.0 (o), 2.08 (p), 2.96 (q), 5.12 (r), 5.92 (s) and 6.56 (t). The data are mirrored about $z = 0$	229
Figure 7.8:	Phase-averaged raster plot of streamwise velocity, \hat{u} , obtained from stereoscopic PIV measurements at $x/c = 0.78$ angled 30° to the vertical following single pulsed actuation; $t/T_{\text{conv}} = 0$ (a), 0.8 (b), 0.88 (c), 1.28 (d), 1.44 (e), 1.6 (f), 1.92 (g) and 2.96 (h). The data are mirrored about $z = 0$	230
Figure 7.9:	Phase-averaged raster plot of cross stream velocity, \hat{v} , obtained from stereoscopic PIV measurements at $x/c = 0.78$ angled 30° to the vertical following single pulsed actuation; $t/T_{\text{conv}} = 0$ (a), 0.8 (b), 0.88	

	(c), 1.28 (d), 1.44 (e), 1.6 (f), 1.92 (g) and 2.96 (h). The data are mirrored about $z = 0$	230
Figure 7.10:	Iso-surfaces of the phase-averaged spanwise vorticity viewed from above the airfoil for the unbounded actuation in the 2-D (row “a”), and 3-D (row “b”) base flows following actuation ($t = 0$) at $t/T_{\text{conv}} = 0.56$ (i), 0.64 (ii), 0.72 (iii), 0.8 (iv), 0.88 (v), 0.96 (vi), 1.04 (vii), 1.12 (viii) and 1.2 (ix). The data are mirrored about $z = 0$	231
Figure 7.10:	(Continued)	232
Figure 7.11:	Iso-surfaces of the phase-averaged spanwise vorticity for the unbounded actuation in the 2-D (row “a”) and 3-D (row “b”) base flows following actuation ($t = 0$) at $t/T_{\text{conv}} = 0.56$ (i), 0.64 (ii), 0.72 (iii), 0.8 (iv), 0.88 (v), 0.96 (vi), 1.04 (vii), 1.12 (viii), 1.2 (ix) and 2.4 (x). The data are mirrored about $z = 0$	233
Figure 7.11:	(Continued)	234
Figure 7.12:	Variation of C_L , (a-h) and $C_{M,c/4}$, (i-p) with α during the pitch cycle ($k = 0.115$). Single-pulse actuation marked with \bullet is applied at $T_{\text{start}}/T_P = 0$ (a,i), 0.096 (b,j), 0.128 (c,k), 0.16 (d,l), 0.192 (e,m), 0.24 (f,n), 0.32 (g,o) and 0.48 (h,p). The corresponding traces for the base flow are shown in dashed curves and the directions of the phase plots are indicated by an arrow (a, i).	235
Figure 7.13:	Variations in hysteresis of (a, c) and cycle-averaged (b, d) unsteady C_L (a-b) and C_M (c-d) lift (a and b) for single-pulse actuation applied during the pitchy cycle with different T_{start} (\bullet). The background colors represent the up-  , and downstrokes  . The corresponding actuation cases in Figure 7.12 are included (\bullet).	236
Figure 7.14:	Variations with time of the phase-averaged circulation increments for the base flow (a) and following single pulse actuation at $T_{\text{start}} = 150$ ms (b) at $z/S_{\text{act}} = 0$ (\bullet), 0.47 (\bullet), 0.78 (\bullet) and 1.11 (\bullet).	237
Figure 7.15:	Variations of phase-averaged circulation increments with α following single pulse actuation at $T_{\text{start}} = 150$ ms at $z/S_{\text{act}} = 0$ (\bullet), 0.47 (\bullet), 0.78 (\bullet) and 1.11 (\bullet).	238
Figure 7.16:	Variations in lift C_L (a), and pitching moment $C_{M,c/4}$ (b) of $N = 5, 10, 15$ and 20 actuation pulses evenly-distributed in time during the pitching cycle the pitching cycle. The base flow curves are shown in gray.	239
Figure 7.17:	Variations in lift C_L (a), and pitching moment $C_{M,c/4}$ (b) of $N = 8$ and 20 actuation pulses evenly-distributed in time during the pitching cycle, and the 8-pulse “rapid” actuation sequence. The baseline curves are shown in gray.....	239
Figure 7.18:	Phase-averaged vorticity maps and velocity distributions above the airfoil and in the near wake during the pitching cycle; baseline (column a) and pulsed actuation (columns b-d). In columns (a) and	

(b): $\alpha = 15.0^\circ$ ($t/T_p = 0.038$), (i), 17.2° ($t/T_p = 0.150$), (ii), 18° , ($t/T_p = 0.261$), (iii), 15.7° ($t/T_p = 0.429$), (iv) and 11.2° ($t/T_p = 0.621$) (v). The images in columns c and d are taken at fixed delays relative to column b of $\Delta t/T_p = 0.016$ and 0.032 , respectively..... 240

Figure 7.19: $x-t$ raster plot of phase-averaged vorticity flux for 8-pulse actuation showing propagation velocities of the induced CW vorticity concentrations. 241

Figure 7.20: Phase-averaged vorticity and velocity maps in the near wake during the pitching cycle of the airfoil in the absence (a-e) and presence (f-j) of actuation. The timing of the images in each row is measured relative to t_0 when the airfoil is pitching up through $\alpha_0 = 14^\circ$. (a,f) $t/T_{conv} = 0$ (14° upstroke), (b,g) 2.8 (16.5° upstroke), (c,h) 9.4 (16.8° downstroke), (d,i) 14 (12.5° downstroke), and (e,j) 19 (10.1° upstroke). Pulsed actuation is applied using $N = 8$ pulses equally spaced in time ($T_{rep} = 35$ msec), triggered at the start of the pitching cycle (i.e. $T_{start} = 0$). 242

Figure 7.21: Raster plots of the phase-averaged cross stream distribution of vorticity flux (CW and CCW) during the pitching cycle of the airfoil measured at $0.25c$ downstream of the trailing edge in the absence (a) and presence (b) of actuation. Included are the corresponding line traces of the time-rate change of circulation: $(d\Gamma/dt)_{CW}$ and $(d\Gamma/dt)_{CCW}$. Also included for reference are the five instances during the cycle (i through v) that are marked in Figures 7.18 and 7.19. 243

Figure 7.22: Phase-averaged line traces of $(d\Gamma/dt)_{CW}$, $(d\Gamma/dt)_{CCW}$ and their sum $d\Gamma/dt$ in the presence of actuation. The corresponding time traces for the baseline flow are shown for reference (gray)..... 244

Figure 7.23: (a) Phase-averaged circulation increment for the pitch cycle in the absence (\bullet) and presence (\bullet) of pulsed actuation ($N = 8$, $T_{pulse} = 1.4T_{conv}$, \bullet), and (b) Phase-averaged net change in global circulation due to the actuation relative to the base flow (\bullet). 244

NOMENCLATURE

Roman

c	airfoil model chord length, [m]
C_L, C_M	lift and pitching moment coefficients
C_p	pressure coefficient ($\Delta p / (0.5 \rho U_\infty^2)$)
k	airfoil pitch reduced frequency ($\Omega c / 2U_\infty$)
N	number of pulses in burst actuation
Re_c	Reynolds number based on airfoil chord
S	airfoil model span [m]
S_{act}	span of airfoil actuator module [m]
S_{fence}	spanwise distance between parallel streamwise partitions [m]
t	time [ms]
T_{burst}	burst duration of pulsed jets [ms]
T_{conv}	flow convective time [ms]
T_{delay}	time between a burst of pulses [ms]
T_{rep}	time between successive pulse jets [ms]
T_{start}	actuation time relative to $\alpha = \alpha_o$ [ms]
St_{act}	actuation Strouhal number (T_{conv} / T_{rep})
U_∞	wind tunnel free-stream velocity [$m \cdot s^{-1}$]
u, v, w	flow velocities [$m \cdot s^{-1}$]
x_{act}	streamwise location of actuator [m]
x, y, z	wind tunnel coordinates [m]

Greek

α_0, α	airfoil pitch angle [°]
α_p	airfoil pitch angle amplitude [°]
Γ_0, Γ	sectional circulation [$\text{m}^2 \cdot \text{s}^{-1}$]
Ω	airfoil pitch frequency [$\text{rad} \cdot \text{s}^{-1}$]
ω_x, ω_z	streamwise and spanwise vorticity [s^{-1}]

Acronym

AFOSR	Air Force Office of Scientific Research
COMPACT	COMbustion Powered ACTuation
CCD/CMOS	Charge-Coupled Device/Complementary Metal-Oxide Semiconductor
CW, CCW	clockwise, counter-clockwise
DOF	Degree-of-Freedom
EDM	Electrical Discharge Machining
NASA	National Aeronautics and Space Administration
PIV	Particle Image Velocimetry
SLA	Stereo-Lithography

SUMMARY

The dynamics of controlled transitory 2- and 3-D attachment of the separated flow over a 2-D airfoil model are investigated in wind tunnel experiments. Pulsed actuation is effected on time scales that are an order of magnitude shorter than the characteristic convective time scale of the base flow by momentary jets that are generated by a spanwise array of combustion-based actuators. The effects of the transitory actuation on the aerodynamic characteristics of the airfoil are assessed using measurements of the global lift force and pitching moment and of streamwise distributions of surface pressure, and planar and stereoscopic particle image velocimetry (PIV) acquired phase-locked to the actuation waveform.

A single spanwise-bounded actuation pulse leads to 2-D severing of the separated vorticity layer and the subsequent shedding of a large-scale stall vortex that are followed by momentary attachment of the upstream boundary layer and ultimately re-separation that are accompanied by a strong transitory change in the airfoil's circulation. It is shown that the primary mechanism for the attachment is alteration of the adverse pressure gradient of the separated base flow by local blockage of the momentary jet and the formation of the large-scale stall vortex. The disparity between the characteristic time scales of flow attachment and subsequent separation [$O(T_{\text{conv}})$ and $O(10T_{\text{conv}})$, respectively] is exploited for temporal and spatial extensions of the attachment and enhancement of the global aerodynamic performance using strings of successive actuation pulses.

Pulsed actuation effected by an unbounded actuator array leads to spanwise spreading of the induced transitory 3-D flow attachment well beyond the spanwise edges of the

actuators. It is shown that 3-D pulsed actuation enhances the accumulation of vorticity over the airfoil and improves its aerodynamic performance compared to 2-D, spanwise-bounded actuation. When the airfoil is undergoing time-periodic pitch oscillations beyond its static stall margin, a sequence of staged 3-D actuation pulses coupled to the airfoil's motion can lead to reduced lift hysteresis and increased pitch stability (lower “negative damping”) that are typically associated with the presence of dynamic stall.

CHAPTER I

MOTIVATION AND LITERATURE REVIEW

1.1. Overview of Thesis Research

Flow separation over aerodynamic surfaces (e.g., airfoils or flaps at high angles of incidence) occurs when the pressure gradient imposed on the surface boundary layer becomes sufficiently adverse. The thickness of the viscous layer increases as momentum is reduced by the wall shear and pressure gradient, and at some point the layer separates from the bounding surface. The separation is accompanied by profound changes in the flow structure and pressure distribution over the surface and consequently in significant loss of aerodynamic performance (e.g., reduction in lift and increase in drag) that for aeronautic applications can lead to need for higher engine power, and to flight instabilities and severe structural effects.

Understanding the fluid mechanics of flow separation (e.g., Chang, 1970; and Schlichting and Klaus, 2000) would allow engineers to estimate operating conditions under which separation occurs and to safely avoid these off-design and potentially hazardous conditions. The ability to manipulate a flow field to improve efficiency or performance beyond current limitations can lead to improved maneuverability, increased range and payload, and reduce adverse environmental impact. The detrimental effects associated with flow separation that are often coupled to moving aerodynamic structures have spurred much interest in its mitigation and control using both passive (e.g., Volino, 2003; Godard and Stanislas, 2006a, 2006b; and Godard et al., 2006) and active (e.g., Donovan et al., 1998; Brunn et al., 2007; and Gorton et al., 2004) approaches.

The goal of the research reported in the present dissertation is to conduct experimental investigations of the fundamental two- and three-dimensional flow mechanisms by which anharmonic transitory pulsed actuation can manipulate and control stalled flow over airfoils. The research was divided into two primary phases (supported by NASA and AFOSR) that included a series of wind tunnel experiments using a 2-D wing model.

The first phase (supported by NASA's Subsonic Rotating Wing Program) was motivated by potential application of transitory separation control to the mitigation of the adverse effects of the rotating blade stall (RBS) on the retreating blades of rotorcraft in forward flight. The two primary goals of this phase of the work were to demonstrate the control effectiveness of brief momentum pulses having a characteristic time scale that is an order of magnitude shorter than the characteristic time scale of the global, nominally two-dimensional base flow, and to investigate the 2-D flow mechanisms and time scales of the ensuing flow attachment and separation. Actuation was effected by momentary jets driven by rapid chemical actuation. As part of this NASA Program, these experiments were complemented by laboratory investigations of the actuation technology (Rajendar et al., 2008, 2010), and numerical simulations (Srinivasan et al., 2008).

The second phase of the present investigations was supported by AFOSR's Flow Interactions and Control Program. Building on the findings of the first phase this research was motivated by the need to develop advanced approaches for unsteady aerodynamic flow control (e.g., for unmanned aerial vehicle (UAV) flight platforms). The second phase extended the earlier findings of nominally 2-D pulse actuation in a 2-D base flow to 3-D actuation in both 2-D and 3-D stalled flows. The primary objective of

this phase of the research was to investigate the spatial and temporal scales of the effects of the actuation and the coupling between the production, accumulation, and shedding of vorticity concentrations on a static and a pitching lifting surface. This program included collaboration with numerical efforts by Haering and Moser (2013) using detached large eddy simulation.

1.2. Aerodynamic Flow Control of Separation over Airfoils

Aerodynamic flow control is concerned with direct manipulation of wall-bounded and free shear flows over a variety of aerodynamic surfaces to achieve specific objectives in a broad range of interdisciplinary applications. Examples include aeroacoustics (Chatellier et al., 2006; and Panickar and Raman, 2009), aeroelasticity (O'Donnell et al., 2007), and turbomachinery (Bloxham and Bons, 2010, 2014). These applications often involve the detrimental effects of flow separation that has motivated many innovative flow control approaches to improve existing capabilities and to develop new solutions.

1.2.1. Some Aspects of the Physics of Separation Flow Control

An early approach to control boundary layer separation involved the direct application of suction to remove low-energy flow near the surface and/or blowing to add momentum to the near-wall fluid. As described by Cattafesta and Sheplak (2011), one of the earliest forms of boundary layer flow control was the foundational work of Prandtl who in 1904 used steady suction through a slot on the surface of a cylinder to demonstrate the prevention of separation. According to Gad-el-Hak (2007), the effects of steady suction on boundary layer flows were further investigated in the late 1930s and early 1940s when European researchers (e.g., Schrenk in 1935 and Pfenninger in 1946) successfully improved lift and decreased drag on thick airfoils by delaying boundary layer transition.

The use of continuous blowing (jet) through slots for boundary layer and separation control was demonstrated somewhat later than suction (e.g., Bradley and Wray, 1974). Hazen (1968) showed that both suction and blowing effects on the boundary layer effected through leading edge slots reduced the separated flow over a thick airfoil, albeit suction performed better and completely prevented the separation. Many of the early flow control investigations also examined the effects of different blowing configurations in several applications that included blowing on swept wings (Ayers and Wilde, 1956; and Kukainis, 1969), tangential blowing on airfoils (Wood and Roberts, 1986, 1988), trailing edge blowing (McLachlan, 1989) and on flaps (Hazen, 1968), and have been instrumental in the subsequent development of modern flow control techniques. It has been argued that although passive (continuous) suction is generally more effective and energy efficient than passive blowing for flow control, the practical implementation of suction would require substantial heavy hardware (Gad-el-Hak, 1998, 2007) therefore suction is less ideal for aviation applications. However, the interest for implementing suction as a potential viable boundary layer control technology led to a flight test by NASA on the modified fighter F-16XL, demonstrating that laminar flow on the aircraft wing can be obtained using suction at Mach 2.0 (Marshall, 1999).

In more recent investigations, the introduction of unsteadiness to the jet flow can achieve comparable gains as with steady blowing although requiring a lower jet momentum by one to two orders of magnitude. For example, it was experimentally demonstrated (Seifert et al., 1993, 1996) that oscillatory blowing can delay airfoil stall much more efficiently than steady blowing. Modern fluidic actuators typically utilize the time-periodic injection of jets into the cross flow over aerodynamic surfaces and can be

instrumented flush to a solid surface to act directly on the boundary layer. The details of the mechanism effected by continuous and time-periodic injection of fluid into the boundary layer flow differ in that the former approach generally modifies the mean flow structure while the latter *actively* leverages flow instabilities in the shear layer through periodic interactions with the flow, and can redirect flow and form secondary flow structures similar to the effects induced by mechanical devices (e.g., vortex generators).

Some of the more traditional aerodynamic active flow control techniques using fluidic devices for suppressing flow separation have relied on the flow receptivity to actuation (manipulation of the flow) within a narrow-band of frequencies close to the unstable frequencies of the near wake. In these techniques, the actuation period scales with the advection time over the length of the separated flow domain and corresponds to an actuation Strouhal number of $St_{act} \sim O(1)$. A different approach to reduce flow separation uses high-frequency actuation [$St_{act} \sim O(10)$], which is decoupled from the global flow (wake) instabilities by modifying the apparent aerodynamic shape of the surface and thereby the streamwise pressure gradient upstream of separation to affect quasi-steady or transitory aerodynamic forces. These approaches are typically applied at relatively low flow speeds due to limitations of the actuation impulse.

There has been extensive research on the control of separated flows over lifting surfaces such as airfoils where lift enhancement is typically achieved using active time-harmonic actuation [$St_{act} \sim O(1)$] by Coanda-like deflection of the steady separated shear layer towards the surface (e.g., Ahuja and Burrin, 1984; Neuburger and Wygnanski, 1988; Seifert et al., 1996; Tuck and Soria, 2004; and Sosa et al., 2006). Using high-frequency actuation [$St_{act} \sim O(10)$], flow manipulation is effected by forming a controlled

interaction domain of trapped vorticity between a surface-mounted fluidic actuator and the cross flow above the surface (e.g., Honohan et al., 2000). Amitay and Glezer (2002, 2006) investigated flow transients associated with the onset and termination of actuation that leads to flow attachment over a stalled airfoil, and noted the similarity to the transients that accompany separation and attachment during dynamic stall and also demonstrated that the separated flow is extremely susceptible to transitory actuation. The utility of brief [$O(1 \text{ ms})$], anharmonic high-impulse pulsed jets for effective separation control of the flow over a stalled airfoil was demonstrated by Crittenden et al. (2001), Funk et al. (2002), and Brzozowski and Glezer (2006) where it was shown that when the actuation input was applied with time scales that are significantly shorter than the characteristic advection time over the separated flow domain, the resulting aerodynamic forces are much higher than the forces realized by conventional, continuous time-harmonic actuation.

While earlier investigations demonstrated the utility of separation control by different actuation technologies, detailed understanding of the flow physics for pulsed actuation has been sparse. The primary goal of this dissertation, as discussed in §I.3, is to study the transitory attachment mechanism and expand understanding of the canonical behavior of the unsteady interactions between the pulsed actuation jet and the separating flow.

1.2.2. Active Fluidic-Based Technologies

Actuation technologies developed for aerodynamic flow control are typically categorized as passive, active, or a hybrid combination of the two. Considerable flow control research has been devoted to investigations of passive actuation (e.g., vortex generators, grooves or riblets, Large-Eddy Break-Up devices (LEBUs), etc) since the 1940s (e.g.,

Taylor, 1947; Lin, 1999; and Smith and Gordeyev, 2013) and was reviewed in some detail by Hefner and Bushnell (1990) and Gad-el-Hak et al. (1998). This section focuses on active flow control approaches, which utilize actuators with adjustable operational range and require external power for operation.

Active devices can effect flow control by several means: mechanical (e.g. moving flaps and surfaces), fluidic-based (e.g. unsteady jets), acoustic (e.g., ultrasound resonance tubes), thermal (e.g., plasma actuators), or body forces (non-thermal plasma actuators). Fluidic-based actuation techniques operate by injection of momentum into the cross flow, and thereby can enable actuation away from the flow boundary. The actuation technology reviewed here is limited to fluidic actuation.

A widely-used active jet actuation technology employs electrically powered zero-net-mass-flux actuation jets that are synthesized by time-periodic ingestion and expulsion of the ambient fluid to engender the control jet. The jets are produced through an orifice in a cavity whose volume is changing time-periodically by oscillatory motion of a diaphragm that is typically driven by a piezoelectric driver (e.g. Smith and Glezer, 1998; and Glezer et al., 1999). The jet velocity and therefore momentum follow a similar periodic variation in strength. The utility of these actuators for flow control of separation or stall has been demonstrated in numerous laboratory investigations on bluff bodies (Honohan, 2003) and airfoils (Brzozowski, 2011).

Time-dependent (or time-periodic) pulsed jets are based on intermittent injection of air from a high-pressure air supply through the flow boundary and into the cross flow. Some designs utilize a fast-acting solenoid valve (e.g. Williams et al., 2009) to activate the pulsed jet intermittently. In another design with no moving parts, the external air

enters a fluidic nozzle or oscillator where the internal feedback passages result in a pulsed jet that characteristically oscillates between the two sides of the exit nozzle (Raghu, 2001), and the frequency of oscillation is dependent on the pressure of the external air source. These actuator technologies have the advantage that the jet speed is only limited by the plenum pressure and the pressure drop through the actuator, and therefore they are suitable for use in high-speed flow control applications. However, these devices require substantial supply of air that may limit their use for flow control applications on aircraft.

Although synthetic jet actuators possess a number of attractive attributes, their adaptation for full-scale platform has been delayed by the limited actuation power of current piezoelectric drivers. It was suggested by Gilarranz et al. (2005) that synthetic jet actuators driven mechanically using a piston are capable of producing much higher velocities thus are thought to be more suitable for flow control applications with high flow speeds. However, the additional moving parts and the weight of these piston-driven actuators prohibit adaptation to full-scale applications. Other types of synthetic jet actuators can be engendered by plasma or spark discharge (e.g. Maslov et al., 2008; Caruana, 2010; and Caruana et al., 2013), through heating of air in a cavity using a high-energy electric discharge that leads to a rapid increase in cavity pressure and the formation of a very brief high-speed pulsed jet without any moving parts.

Another variant of the pulsed jet technology is the combustion-driven actuator (Crittenden, 2003) where a high-velocity (impulsive) jet is formed by a combustion process that requires only a moderate inflow of reactants. This technology uses no moving parts, and the chemical reaction acts as a pressure amplifier that produces a brief [O(2 ms)] supersonic pulsed jet. Although the combustion-driven and the valve-driven

pulsed jets are conceptually similar, the characteristic time-scale of the valve-driven jet is considerably longer [$O(20 \text{ ms})$]. The research conducted throughout this dissertation utilizes combustion powered actuation (§III) to produce pronounced, transient perturbations in a shear flow for separation control.

1.2.3. Control of Time-Dependent Separation

In addition to the quasi-steady separation on a static airfoil, the lifting surface can experience unsteady separation (or dynamic stall) and consequently highly-unsteady aerodynamic loads due to velocity variations or during maneuvers that involve time-dependent pitch (e.g., Rival and Tropea, 2010; and Mulleners and Raffel, 2012) and plunge (e.g., Visbal, 2011). The occurrence of dynamic stall when the airfoil's angle of attack is rapidly increased beyond the static stall angles during pitch can lead to strong unstable structural torsion and vibrations, and has been the subject of numerous investigations (e.g., Carta, 1967; McCroskey, 1982; Carr, 1988; Richter et al., 2011; Mueller et al., 2014; and Gardner et al., 2013, 2014). Dynamic stall shares many similarities with the hazardous (and more complex including 3-D and compressibility effects) retreating blade stall on rotorcrafts that can lead to large sudden aerodynamic loads and even to catastrophic structural failure of the blades. These flow effects are beyond the scope of the present thesis.

The detrimental transitory aerodynamic loads and sometimes catastrophic effects of dynamic stall have spurred much interest in its mitigation and control. A number of experimental and numerical investigations have focused on flow control for the mitigation of unsteady separation over airfoils undergoing time-periodic pitch motion using passive and active control approaches. Some traditional passive control approaches

such as the use of vortex generators and flaps (static and moving), and steady blowing and suction were demonstrated with varying degrees of success in suppressing dynamical stall for Mach number flows up to 0.45. Yu et al. (1995) investigated the effects of blowing on the suction surface of an oscillating airfoil on dynamic stall experimentally and numerically and demonstrated significant suppression. Weaver et al. (1998, 2004), Singh et al. (2005), Pape et al. (2012), and Heine et al. (2013) studied the control effectiveness of steady blowing and air-jet vortex generators, respectively, for dynamic stall induced by sinusoidal pitching, while Lee and Gerontakos (2006) used both upward and downward trailing-edge flapping for control. Martin et al. (2008) investigated the combination of a leading-edge glove and vortex generators on an oscillating airfoil in controlling compressible dynamic stall at $M = 0.3$ to 0.4, and demonstrated that severe dynamic stall pitching moments can be alleviated.

For active control approaches, periodic excitation of the separated shear layer using synthetic jets were by far the most studied. Wu et al. (1998), Wake and Lurie (2001), Duraisamy and Baeder (2002), Florea and Wake (2003), and Zanotti et al. (2014) adopted computational methods to evaluate parameters of dynamic stall control using directed synthetic jets and showed qualitative agreement that post-stall lift coefficients can improve by up to 30% with control. Lorber et al. (2000, 2002), Greenblatt and Wagnanski (2001), and Yen and Ahmed (2012) experimentally conducted parametric studies on the control of dynamic stall on oscillating airfoils by time-periodic jet actuation via electromechanical directed synthetic jet actuators and oscillatory blowing, respectively. These investigations indicated that periodic excitation increases the steady and unsteady stall angles, increase the post-stall lift, as well as reduce the unfavorable

unsteady nose-down pitching moment during dynamic stall. More recently, the use of other actuation technologies to alleviate dynamic stall by preventing the formation of the dynamic stall vortex are demonstrated experimentally. Post and Corke (2004, 2006) demonstrated using steady and unsteady plasma actuation to suppress dynamic stall on a pitching airfoil to improve the instability of the airfoil with minimal actuation while Greenblatt et al. (2014) investigated the use of plasma actuation on mitigating the unsteady separation on a vertical-axis turbine.

The present dissertation research focuses on the canonical flow control mechanism of pulsed actuation on the steady and unsteady separation over a 2-D airfoil (effects of 3-D tip flow, compressibility, rotation, and aeroelasticity are beyond the scope of the present research). A significant part of the present studies is the extension of the transitory attachment mechanism to time-dependent separation using coupled interactions of the actuation jets to the flow over a pitching airfoil.

1.2.4. A Note on Finite-Span Actuation

It might be argued that the use of actuators along the entire span of the flow in full-scale applications of flow control may be prohibitive due to cost and weight (e.g., Brzozowski, 2011 and DeSalvo et al., 2012). Furthermore, the flows over an aerodynamic platform are likely to exhibit 3-D characteristic behaviors even for 2-D airfoils with a constant cross section (e.g., wing-tip effects of a finite-span wing), that are manifested by spanwise flow non-uniformities with localized separation across the airfoil span. Of particular relevance to the present investigations are also the large, natural flow structures over an airfoil as induced by the separation at increasing pitch angles. In fact, Winkelmann and Barlow (1980), and Zanin et al. (2008) showed using oil visualization

for different span-to-chord aspect ratio airfoils that the separated flow over airfoils are comprised of localized, spanwise non-uniform stall cells or separation bubbles. For flow control applications over an airfoil having domains of separated and attached flows, finite span actuation can be implemented at specific locations where the local (separated) flow is more susceptible to actuation, thereby minimizing unnecessary actuation efforts elsewhere.

It is also important to note that when these 2-D surfaces undergo time-dependent motions (e.g., pitching and plunging airfoils), the unsteady flow can also amplify the 3-D flow structures as shown by Yilmaz et al. (2010), and Ozen and Rockwell (2012). These flow non-uniformities are commonly observed in rotational systems (e.g., in gas compressors resulting in blade-tip losses in the engine and on rotorcraft blades) and may benefit from finite span actuation. Although there are numerous experimental investigations of discrete (unsteady) jets in a cross flow, most focused on the flow dynamics over a flat plate and in the symmetry plane of the orifice, and there is relatively little work on finite span flow control in three-dimensional flows. In a recent work, Zhang and Zhong (2010) demonstrated a delay in flow separation over a ramp using an array of three circular synthetic jets while Vasile and Amitay (2013) demonstrated using a discrete synthetic jet actuator the formation of secondary flow structures from the 3-D local interactions of a finite span actuation on a swept airfoil with limited separation.

1.3. Thesis Objectives

Earlier investigations of separation control over lifting surfaces have focused primarily on both high- and low-frequency time-periodic actuation. Although these approaches have demonstrated significant improvements in aerodynamic performance, they are based

on a quasi-steady approach that requires continuous actuation and may not be as effective when the base flow is unsteady. In contrast, anharmonic (pulsed) actuation exploits transitory high amplitude response within the flow with characteristic fast onset and slow relaxation times which may require lower actuation power and lends itself to real time control in high speed flow applications.

Earlier work on transitory flow control has not focused on the 2- and 3-D fundamental mechanisms of the flow interactions. Therefore, the primary goal of this thesis is an experimental investigation of the role of 2- and 3-D flow mechanisms engendered by pulsed actuation in the manipulation of a separated shear layer over a static and a dynamically pitching stalled airfoil. Although the present investigations focus on the control of separated flows over a basic airfoil in a small range of flow conditions, this work may lead to future investigations at elevated Mach and Reynolds numbers with radial flow effects and with increased unsteady effects that can demonstrate the utility of this novel flow control technology for future commercial and military applications on fixed and rotary wing aircrafts. The thesis aims to address the following:

- How a single brief pulsed jet effects flow perturbations in the separated shear layer to facilitate transitory flow attachment, and how the attachment can be extended by successive pulses.
- What changes in the flow dynamics when the actuation is limited in span or unbounded and the quasi-steady base flow exhibits either 2- or 3-D separation.
- How the control authority of a single pulsed jet changes when the actuation is coupled to the pitching motion of the airfoil.

To answer these questions, this thesis seeks to advance understanding of separation control using pulsed actuation by investigations of:

- Attachment mechanism of actuation over a static airfoil and the 2-D transient interactions between the single, transitory jet and the separated cross flow.
- Flow interactions of successive actuation pulses and the role of actuation time scales in circulation build-up and in attachment.
- Evolution and spreading of 3-D flow interactions induced by actuation over a fraction of the airfoil's span and comparison with their 2-D counterpart.
- Coupling of actuation timing to airfoil pitching motion and effects on mitigation of dynamic stall.

The experimental setup and measurement techniques are described in §II, and the pulsed jet actuation technology employed in these investigations are discussed in §III. The bounded, 2-D experimental results commence in §IV with the study of the effects from a single pulsed actuation on the statically stalled airfoil followed by the effects of successive actuation in §V. The unbounded, 3-D actuation effects of the pulsed jets on nominally 2-D separation are described in §VI. These investigations are extended to 3-D separation over a static and pitching airfoil in §VII. The main findings of are summarized in §VIII along with recommendations for future work.

CHAPTER II

EXPERIMENTAL SETUP AND PROCEDURE

2.1. Wind Tunnel Setup

The present investigations were conducted in an open-return low-speed wind tunnel facility that has a nominally square test section measuring 0.91 m on each side and is 3 m long with transparent acrylic walls (38.1 mm thick). The tunnel flow is driven by a 1.1 kW (150 hp) blower through a 1:3.8 partitioned diffuser and is conditioned through a series of honeycombs and fine mesh screens located upstream of a 9:1 contraction section upstream of the test section. The quasi-steady tunnel free stream is set by interfacing the blower controller to the laboratory computer using LabView where the command voltage is based on a calibration curve of the blower rpm and test section speed. In addition, a pitot-static probe mounted in the contraction section monitors the dynamic pressure of the flow that is measured using a 0-1 torr MKS Baratron manometer with a resolution of 0.01% of the full scale and $\pm 0.15\%$ reading accuracy.

The CAD model in Figure 2.1 shows details of the tunnel contraction and the test section. All the side walls can open up to allow access to the test section and are nominally sealed when closed. The upper (ceiling) and lower (floor) walls of the test section are adjustable and are equipped with surface pressure ports that are equally spaced at approximately 200 mm apart on the centerline to measure the time-averaged streamwise pressure distribution in the presence of a model inside the tunnel to monitor tunnel wall effects. The movable walls enable static adjustments of the streamwise pressure distribution to correct for some (static) model blockage (blockage effects of the

dynamically pitching airfoil are not corrected). For the steady flow experiments, the blockage effects on the free stream dynamic pressure were also monitored at the contraction section and corrected by adjusting the blower rpm. The tunnel can operate continuously at a maximum (empty) test section speed of $40 \pm 1 \text{ ms}^{-1}$, with free stream turbulence level less than 0.25% (Amitay and Glezer, 2002).

The air temperature in the test section is regulated by the laboratory air conditioning system and is monitored during most experiments, typically stabilizes around $20 \text{ }^{\circ}\text{C}$ within 15 minutes following start-up. On the front and back acrylic side walls of the test section, there is a 50 mm wide through slot that extends vertically ($\sim 0.6 \text{ m}$) to allow for the plunge motion of an airfoil. In the present experiments, these slots are closed with aluminum insets and sealed with tape to maintain uniform and parallel flow in the test section.

2.1.1. The Airfoil Model

The 2-D airfoil model is based on a NACA 4415 profile (Abbott and von Doenhoff, 1959) having a fixed cross section with chord $c = 457 \text{ mm}$ and nominal span $S \approx 0.8 \text{ m}$ (Figure 2.2a). This wing section has a maximum camber of 4% located 40% from the leading edge with a maximum thickness of 15% of the chord. Moderately thick airfoils such as the present model have gradual trailing edge stall where turbulent separation moves upstream from the trailing edge with increasing angle of attack, and are therefore ideal for investigation of separation control approaches. The NACA 4415 is used as a prototypical platform for investigations of the flow mechanisms of pulsed actuation for transitory separation control. Because of the generic characteristics of the airfoil, it is expected that the findings of the present investigations can be easily applied to other

aerodynamic surfaces. In fact, the results of the present investigations have already been extended and successfully demonstrated for transitory attachment of separated flow over a VR-12 airfoil at an elevated Reynolds number (Matalanis et al., 2014) and over a 3-D ramp section on a rotorcraft fuselage model (Woo et al., 2011).

A schematic of the assembled airfoil model is shown in Figure 2.2b where two identical streamwise flow partitions (or fences) are installed symmetrically about the centerplane ($z = 0$) between spanwise segments of the modular model, S_{fence} apart. The locations of these partitions are adjustable and define the spanwise extent of the center segment “A”, which is surrounded by the two outboard segments “B”. An array of seven combustion actuators having a maximum spanwise extent $S_{\text{act}} \approx 0.21S$ is housed within the center airfoil segment (Figure 2.2b) and is aligned with the airfoil span. The flow over the center airfoil segment “A” is tripped using a small-diameter ($6 \times 10^{-4}c$) wire placed spanwise at $x \approx 0.05c$. The fences help isolate this flow from the adjacent outboard segments “B” that are unactuated. In §IV – VII, the flow configuration is either “bounded” or “unbounded” when the fences are directly adjacent the spanwise edges of the actuator array (i.e., $S_{\text{fence}} = S_{\text{act}}$) or further away such that the spanwise extent of the actuation is limited (i.e., $S_{\text{fence}} > S_{\text{act}}$), respectively.

Each of the airfoil segments (“A” and “B”) are constructed using multiple wire-EDM (electric discharge machining) aluminum spanwise sections that are precisely aligned using $\varnothing 12.7$ mm stainless steel spars inside the airfoil, and are assembled together using fasteners. The airfoil surfaces for any two adjacent sections where they interface are sealed using 0.08 mm thick and 25.4 mm wide aluminum tape. Figure 2.3a shows the assembled CAD model including the fences, and a 2.08 m long three-piece mounting

shaft that is connected through and attached inside the model. The mounting shaft consists of a center, solid aluminum square bar (31.75 mm sides) and two end, hollow steel shafts (41.3 mm O.D. and 31.75 mm I.D.) that are connected together with couplings (Figure 2.3a). The axis of the mounting shaft (i.e., the pitching axis of the airfoil) is located $0.35c$ from the leading edge and $0.03c$ above the chord line. The aluminum square bar fits inside the airfoil sections with sliding clearance and is attached to the airfoil with fasteners for rigidity and to transmit the aerodynamic loads from the airfoil surface to the shaft. The internal structures of the sub-assemblies are shown in Figure 2.3b. Although the aluminum sections add weight to the whole assembly, they provide a rigid structure with non-deformable surfaces that is particularly suitable for the significant changes in aerodynamic loads during separation control. The ends of the shaft in the assembled model protrude through the side walls and are mounted on a two degrees-of-freedom traverse described in §2.2. In the present experiments, the free stream tunnel velocity is set at $U_\infty = 20$ m/s ($Re_c \approx 570,000$ based on the chord length of the airfoil) such that the corresponding convective time scale of the flow over the airfoil is $T_{\text{conv}} \approx 25$ ms.

The airfoil is instrumented with a spanwise array of seven combustion powered pulsed jet actuators (COMPACT) that are discussed in detail in §III. The actuation jets emanate nearly normal to the chord line of the airfoil through an array of equally-spaced and internally-contoured rectangular orifices (21.6 mm center to center with a 2.6 mm gap) that are machined into a cover plate. This cover plate is flush-mounted on the suction surface of the airfoil such that the orifices are located along $x_{\text{act}}/c \approx 0.15$ (Figures 2.2a and 2.3). Each orifice measures 19 mm and 0.18 – 0.2 mm in the spanwise and streamwise directions, respectively (Figure 2.4).

2.1.2 Fences

In the current investigations, the airfoil model does not extend completely across the wind tunnel walls to allow the dynamic motion of the airfoil. The assembled model for the wind tunnel experiments has streamwise fences or flow partitions installed to mitigate edge effects including tip vortices and interference effects from the influence of the tunnel side-wall boundary layers. More importantly, the fences were used to condition the flows, as suggested by Davis and Satyanarayana (1978), over the center segment of the airfoil that includes preventing flow across the span from adjacent segments similar to fences used on swept airfoils (e.g., Harper and Maki, 1964). The two fences located symmetrically about the mid-span (center plane) $z = 0$ are used in the present experiments to allow the flow over the center segment “A” to develop in response to the actuation with minimal effects from the outboard segments. To avoid the fences acting as a passive control device by generating streamwise vortices (Govardha et al., 2006), the fences protrude from the airfoil surface to beyond the thickness of the boundary layer, extending above and below the surfaces of the airfoil and beyond its trailing edge, and are commensurate in size with the characteristic cross stream scale of the separated flow domain.

In the present experiments, every effort was made to reduce adverse effects of the fences on the flow. Several flow partitions having different shapes, thicknesses, materials and planform dimensions were considered (Figure 2.5) and qualitative flow effects were identified using tufts and oil visualization on the fences and the airfoil. Compared to the absent of the fences, the most notable alterations to the flow were observed over the airfoil when the fences were placed at the ends of the airfoil near the wind tunnel walls to prevent tip effects. Although these results were not documented and there were

negligible flow effects with minor alterations to the fences (e.g., using beveled edges), three main observations were made that corroborate with conclusions drawn by Giguere and Selig (1997):

- i.* Spanwise cross flow or “flow spillage” (Giguere and Selig, 1997) between the fences and the test section walls owing to the presence of the airfoil model and its wake that depends on the wake and separation size are largely prevented by using a sufficiently large fence (options “a” – “d” in Figure 2.5) and installing a dummy airfoil section between the fence and the wall (Figure 2.3a).
- ii.* The narrow spacing between the fence and the tunnel wall alters the flow on the fence and the dummy airfoil section owing to blockage effects caused by the growing boundary layers downstream from the fence's leading edge. As a result of the blockage, it appears that flow close to the tunnel walls is entrained toward the fences near the leading edge. In the present experiments, a distance of about 38 mm is maintained between the fences and tunnel walls to minimize such flow entrainment
- iii.* Some blockage effects caused by the fences were observed using tufts placed near their leading edges. These effects are minimized using thin (0.007 - 0.01 c) aluminum plates (or transparent 0.01 c thick polycarbonate fences (“d” in Figure 2.5) were used for PIV measurements).

In the present experiments, the span of the center segment of the airfoil is set by a pair of partitions (fences) that can be placed symmetrically about $z = 0$ at discrete spanwise locations between the airfoil's aluminum sections (Figure 2.3) at increments of $\Delta z = 0.15c$ yielding center segments measuring $0.21S \leq S_{\text{fence}} \leq S$. Three primary positions were

used: $S_{\text{fence}} = S_{\text{act}} = 0.21S$ (§IV and V), $S_{\text{fence}} = 0.35S > S_{\text{act}}$ (§VI) and $S_{\text{fence}} = S > S_{\text{act}}$ (§VII).

2.2. Traverse Mechanism

As part of the wind tunnel facility, a 2-DOF traverse mechanism was designed and constructed in an I-beam frame around the test section of the wind tunnel for investigations of trailing edge flow control by Brzozowski (2011). The traverse enables pitch and plunge motions for airfoil models through servo motors mounted on the I-beam frame that are connected to a Quanser Q8-04 I/O board and are programmed in Simulink using a dedicated feedback (PID) controller (Kutay et al., 2007). While in the previous investigations high-frequency pitch and plunge maneuvers were limited to angles of attack that are well below stall, in the present dissertation, the traverse was used in pitch only for investigations of separation control over a static and pitching airfoil without plunge motion. The traverse system is constructed as two (front and back) independent units on the I-beam structure at the front and back sides of the wind tunnel test section, and is equipped with several sensors (e.g., load cells and angular accelerometer) including a quadrature encoder that are connected to the Quanser I/O board. All sensor outputs are amplified and digitized in two (front and back) dedicated electronic box shielded to attenuate electrical noise before they are transmitted to the controller via Ethernet. The data acquisition and PID controller were executed at a sample rate of 1 kHz on a QNX real time operating system using Simulink software, with an uncertainty of ± 0.5 ms for the measurement time interval.

2.2.1. Pitch Axis

As shown in Figure 2.3, the airfoil assembly was attached to the pitching traverse mechanism at each end of the shaft for each of the tunnel entries. In the present investigations, the airfoil pitch axis was fixed vertically at $0.8c$ above the tunnel floor using an electromagnetic brake on the plunge axis. The general location of the traverse relative to the test section of the wind tunnel and the airfoil is shown in Figure 2.1. A close up view of the traverse (excluding the contraction) in Figure 2.6a shows the airfoil shaft connected to an AC brushless servo motor (Baldor BSM80C-250AA, peak torque 42.6 N-m and stall torque 14.2 N-m) on one (back) side of the I-beam frame while the opposite (free) end was connected to an air bearing for nearly frictionless rotational and axial motions.

A resolver that is integrated into the pitch motor measures pitch rotation and the absolute position reference. This is complemented with a high-resolution, incremental optical rotary encoder mounted to the shaft of the motor (Figure 2.6a) that only measures relative angles. The pitch axis was first instrumented with an Emoteq CP3700 hollow-shaft encoder that had a resolution of 9000 counts per revolution and a typical accuracy of ± 24 arcseconds. An Emoteq CP-1250 25-multiplier interpolator was also used with the quadrature multiplication in conjunction with the encoder to increase its resolution to 900,000 counts per revolution. This encoder-cum-interpolator was replaced with a 5000 line count Heidenhain ERN 180 encoder that is used with a 400-fold interpolator, increasing the resolution to 2 million counts per revolution and an improved accuracy of ± 12 arcseconds. The maximum uncertainty in the measured angle for the dynamic experiments was estimated to be $\pm 0.2^\circ$. Although the angular acceleration of the model

can be obtained by computing the second time-derivative of the encoder angular output, it is independently measured using a Columbia Research Labs SR 220RNP angular accelerometer mounted to the end of the rotating shaft, immediately adjacent to the air bearing (Figure 2.6b). The accelerometer is configured to measure $\pm 50 \text{ rad/s}^2$ and has a resolution of 0.01% of the full range.

It should be noted that the pitch motor and the air bearing are connected to the traverse using a gimbal for easier attachment of airfoil models, but this is disadvantageous from the standpoint of structural rigidity. The mounting mechanism increases the deflection of the airfoil across the test section, lowers the assembly's natural vibration frequency, and limits the traverse bandwidth. These structural vibrations were also accentuated in the presence of aerodynamic loads associated with flow separation and attachment that can lead to torsion in the I-beam frame. Some of these vibration effects are compensated for by using a dynamic model generated in an offline calibration that was developed by Brzozowski (2011).

In the static experiments, the static angle of attack can be varied within $-24^\circ \leq \alpha \leq 24^\circ$. In the dynamic pitch investigations, the model was pitching time-periodically about the axis of the shaft with a prescribed angular frequency Ω at an angle of attack $\alpha(t) = \alpha_0 + \alpha_p \cdot \sin(\Omega t)$ where α_0 is the time-averaged angle of attack, α_p is the oscillation amplitude, and $k = \Omega c / 2U_\infty$ is the reduced frequency. Due to the structural vibrations for the current airfoil model, the time-dependent maneuvers were limited to a maximum frequency of 2 Hz. Figure 2.7 shows a schematic representation of the oscillatory motion and the general actuation timing used for the control experiments on both the static and dynamic airfoils. The torque applied to the traverse by the pitch servo

is proportionate to the command voltage to the servo amplifier, and is computed using a dynamic model generated in an offline calibration (Brzozowski, 2011) that is incorporated within the PID controller. Based on this calibration, the residual error in the aerodynamic moment is limited to ± 1.1 Nm.

2.2.2. Load Cells

In addition to the sensors instrumented on the pitch axis of the traverse, time-resolved vertical force on the airfoil model is measured using Transducer Techniques S-Beam load cells that are attached to the traverse and are mounted on each side of the frame (Figure 2.6b). Each load cell has a capacity of 45 kg with a combined error of 0.08% of the full range, and is attached to a rigid 12.7 mm diameter aluminum rod that is connected to the gimbal. The mounting rods for the load cells are aligned vertically ($\pm 0.1^\circ$) to minimize erroneous measurements of the lift force on the model. The load cells were also statically calibrated in the absence of air flow against a set of known weights (up to 2 kg) for most of the tunnel entries. The uncertainty in the lift force measurement including bias and precision errors based on the repeatability of the calibration data corroborated with the manufacturer specifications. An electronic enclosure box equipped with signal conditioning hardware for the sensors and load cells is mounted on each side of the traverse frame (Figure 2.6). The load cell on the back of the traverse is the most susceptible to electrical noise due to its close proximity with the servo motor and the high-voltage electrical lines and required direct isolation. The error attributed to noise for each load cell is about ± 0.05 N.

2.3. Flow Measurements using Particle Image Velocimetry (PIV)

2.3.1. The PIV System

A high-speed, PIV system comprised of the LaVision DaVis 7.2 FlowMaster software and High Speed Controller (HSC) were used in the wind tunnel experiments to characterize the flow over the airfoil. For the present investigations, time-averaged and phase-averaged PIV data of the flow were obtained and processed. It is important to note that the post-processing approach following the cross-correlation computation that was used in the present investigations was originally developed by Honahon (2003) based on the dynamic mean value operator technique outlined by Raffel et al. (1998) and later improved by Brzozowski (2011).

The flow was seeded with small (0.25 - 60 μm diameter) fog particles generated using a commercial (ROSCO Model 1700) fog machine by thermally vaporizing an aqueous glycol solution fluid (mixture of de-ionized water and glycol). The fog particles were first mixed outside of the wind tunnel in a settling chamber and then injected using a heavy-duty vacuum cleaner fan into a thin plenum that is mounted inside the wind tunnel at the largest cross-section of the contraction (Figure 2.1). The plenum has a symmetric airfoil cross-sectional profile and extends across the contraction. The fog particles were redistributed inside the airfoil-shaped plenum and injected along the span through a (~8 mm wide) continuous open slot at the trailing edge to mix with the surrounding air as they accelerated through the contraction. The fog sheet formed in the test section was nominally 20 - 30 mm thick. The fog airfoil is nominally placed vertical at the mid-span ($z = 0$) and can be moved in discrete steps of 76.2 mm along the span of the contraction to vary the spanwise position of the fog sheet within the test section.

The fog sheet is illuminated within the test section using a dual cavity, diode-pumped Quantronix Darwin-Duo-80-M Nd:YLF (neodymium-doped yttrium lithium fluoride) laser. The two independent 527 nm wavelength oscillators in the laser allow for very stable timing between pulses with a timing jitter of < 2 ns, and are capable of repetition rates of 0.1 – 10 kHz. The laser pulses are nominally 120 ns in width and of 25 mJ each at 1 kHz with 0.5 - 1 % rms in energy stability.

The laser and optics (standard combination of mirrors, and spherical and cylindrical lens to create a thin sheet of laser light as described by Raffel et al. (1998)) are mounted above the wind tunnel on optical rails with vibration dampers and fine positioning adjustments (Figure 2.1). The laser beam is directed using the steering mirrors and conditioned with the lenses prior to entering the wind tunnel test section through 6.35 mm thick borosilicate (BK7) glass windows integrated into the wind tunnel upper test section wall that provide laser access of approximately 870 x 560 mm in the streamwise and spanwise directions, respectively (Figure 2.8). The glass windows are flush mounted in the tunnel test section ceiling. These windows were designed specifically by the author for the present investigations and extended the PIV measurement domain significantly to allow for characterizing the flow across the airfoil span and the use of stereoscopic PIV. The optical access for cameras is through the 25.4 mm thick transparent acrylic side walls. The laser sheet is nominally 2 – 3 mm thick, parallel to the side walls of the wind tunnel test section and covers an imaging area that can be varied (about 250 – 400 mm in the streamwise and cross stream directions). The spanwise location of the laser sheet (i.e., relative to $z = 0$) is adjustable on the optical rails to match the fog sheet in the test section.

To reduce experiment time, pairs of PIV images were acquired using a combination of two Phantom v12.1 and one Photron FASTCAM 1024PCI cameras with 1280 x 800 (12-bit) and 1024 x 1024 (10-bit) pixel CMOS sensors of 20 and 17 $\mu\text{m}/\text{pixel}$ spacing, respectively, that are synchronized to each other. The Phantom and Photron cameras can record full-resolution, double-frame images at up to 1000 and 500 frames per second (fps), respectively. Although, these cameras are capable of recording over 50,000 fps at reduced resolution, the maximum acquisition rate of double-frame PIV images in the present investigations is 1000 fps. The cameras are each equipped with a Nikon SLR photography lens (50 or 60 mm focal lengths) without extension tubes and are mounted on heavy duty MOOG tripods outside the wind tunnel. The synchronization of all the cameras and the timing of the laser pulses relative to each other (with resolution of 25 ns), and to the camera exposure time (about half the time between laser repetition pulses) are controlled by the HSC through the DaVis software. Master PIV timing of the experiments also accepts an external trigger signal, enabling the acquisition of phase-locked or conditionally sampled data.

For most of the planar PIV measurements where only the two in-plane velocity components and the out-of plane vorticity component were measured and computed, the laser and fog sheets were nominally parallel to the free stream flow and the camera imagers were near parallel to the laser sheet (i.e., lens and image planes). In some cases, standard DaVis Schiempflug lens adapters were used when the cameras were oriented at an angle to the laser sheet, and the captured images were rewarped using the calibration. For the stereoscopic PIV measurements, the fog seeding airfoil in the tunnel's plenum was re-configured to allow seeding of the flow with fog particles in the horizontal plane,

and the mounting of the laser optics were redesigned to enable rotation of the laser sheet across the span of the test section.

2.3.2. PIV Image Acquisition Procedure

The cameras were first calibrated in DaVis 7.2 against a dual-level target plate (204 x 204 mm) consisting of a precision-machined pattern of 3.2 mm diameter dots spaced at 15 mm apart with a tolerance of ± 0.02 mm (Figure 2.9). The optimal camera f-stop settings are chosen for the calibration based on test cases with the seeded flow prior to conducting the actual experiments. The calibration target is aligned with the laser sheet inside the test section and is imaged with the cameras. During calibration, the image correction parameters are saved and used for the subsequent PIV processing. The DaVis software computes a two-dimensional mapping function from the image coordinates to the corresponding laboratory coordinates. Following calibration, the camera positions, orientations and settings are unchanged for the entire data acquisition. At full resolution, each image pair is about 2 – 2.5 MB. The images are stored on the camera built-in memory prior to downloading to the local PIV computer. In the present experiments, the file transfer from the cameras take a significantly longer time (up to 1.5 image pairs per second) than the duration of the data acquisition.

For the phase-averaged data presented in this thesis, the cameras were synchronized to the actuation waveform with the airfoil motion, and the PIV images were acquired phase-locked to the trigger waveforms. This was repeated to capture instantaneous realizations of the similar events to generate a population of data sets at each phase. Each sequence of PIV images obtained phase-locked to the actuation consisted of multiple concatenated phases (up to 625 in some cases), and were first arranged into data set bins

corresponding to each phase. These bins were then populated together with corresponding images from each run. Unless otherwise noted, the time-averaged and phase-averaged velocity fields were each computed from 500 and 200 instantaneous realizations, respectively. A set of instantaneous double-frame images of the illuminated flow without fog particles were obtained with each data set for image processing to remove spurious reflections. The phase-locked PIV images were triggered at a sequence of predetermined time delays relative to the actuation waveform.

The measurement domains for the PIV data were acquired in multiple cross stream (x - y) planes that include the flow over the airfoil (including in the vicinity of the actuators) and in the near wake that are synchronized to the actuation waveform, and are typically comprised of overlapping fields of view that are used to create composite PIV images. Figure 2.10 shows examples of the different overlapping PIV windows that are used in the present investigations. Phase locked stereoscopic PIV measurements (three velocity components) are also obtained across the airfoil span (§VII). The measurement plane for the stereo-PIV is shown in Figure 2.11a where the spatial domain within the laser sheet is shaded in green and the coordinates in which the data are obtained are superimposed over the airfoil surface. Note that in connection to Figures 7.7 – 7.9, the airfoil surface is at $\hat{y} = 0$ and the plane-normal vorticity is computed in the out-of-plane \hat{x} component of the stereo-PIV data. To minimize surface light reflections, this PIV plane is near normal to the airfoil surface at $x/c \approx 0.78$ such that it is oriented about 30° from the vertical (x - y) plane as shown in Figure 2.11b.

It should be noted that the PIV data set for each experimental configuration is obtained in a single tunnel entry (e.g., the 24 planes of PIV data of three overlapping

windows in §VI were obtained over a period of about 6 days without changing the wind tunnel setup). Repeatability of the experiments is maintained by recording detailed notes of the camera positions and orientations, in addition to using reference images of the field of view from each camera. For each tunnel entry, the experiment is matched to earlier entries (for example, the distances of the airfoil from the tunnel side walls and ceiling is within 1-2 mm for all the entries). In general, experimental conditions are matched by comparing pressure distributions over the airfoil, load cell data, and PIV data with earlier results. During the measurements, spurious laser light reflections from the background objects (e.g., the wind tunnel walls and the partition fences) are minimized by surface treatment with black paint and tape. In addition, the majority of the airfoil surface is black-anodized and other regions are supplemented with a thin coat of black ink to minimize concentrated laser light reflections. Other precautions include designing the camera placement to avoid reflections of laser light, and steering of the laser sheet to take advantage of the airfoil surface curvature, as demonstrated above for the stereo-PIV set up in Figure 2.11b.

2.3.3. PIV Image Processing

The DaVis software package includes a number of image processing tools (e.g., add, subtract, multiply or divide values from or to an image, and time-series operations such as averaging). Some minor image pre-processing steps were often required for the PIV data prior to the vector computation. For each raw, double-frame PIV image of the flow seeded with fog particles (e.g., Figure 2.12a), the corresponding time- or phase-averaged, illuminated background image in the absence of fog (e.g., Figure 2.12b) was first subtracted from it, resulting in a new image (e.g., Figure 2.13a). This step removes background light reflections and often increases the signal-to-noise ratio by enhancing

the contrast of the fog particles in the flow, and is extremely beneficial when the background objects are close to the subject plane. Another similar pre-processing approach first requires averaging or finding the minimum intensity at each pixel from the set of images that correspond to a common phase. The averaged or the minimum-intensity image pair is then subtracted from the original set to remove background noise.

As shown in Figure 2.13c, this procedure is particularly important in improving the quality of the instantaneous PIV images near the surface of the airfoil, allowing the subsequent PIV processing to produce valid velocity vectors that are sufficiently populated at a reasonable spatial resolution within the boundary layer for computing the corresponding vorticity concentrations. However, in the present experimental conditions, there is typically one row of grid points near the solid surface where the velocity vectors are not resolved where in connection to the specific spatial resolutions discussed in the next subsection, this row of absent velocity vectors correspond to within 1.9 to 3.5 mm from the airfoil surface for the range of resolutions.

In addition to the image processing to reduce surface reflections, a “fixed” silhouette mask is drawn manually and applied using the DaVis software to regions within an image for all the camera views. These masks are typically applied to all the instantaneous realizations within a data set in flow regions where there is consistently insufficient laser illumination and also parts of the airfoil in the field of view where fog particles are absent, and are therefore independent of the flow. This procedure of removing “fixed” regions identically in each data set prevents computation of vectors in these masked regions and thus bypasses contamination of valid data in adjacent flow regions without altering the spatial size of the image. As an example, Figures 2.13b and d show images

following the application of a fixed mask on the corresponding instantaneous images in Figures 2.13a and c, respectively. For the dynamic investigations where the airfoil is moving, a new fixed mask is drawn to the outline of the airfoil for each phase and in the present experiments can include up to 625 masks for each field of view. Similarly, an “algorithmic” mask can be computed and applied to regions in an instantaneous image where the local seeding density of the fog particles is inadequate. The location and size of these masked regions computed by the DaVis software can change between instantaneous realizations owing to the temporal and spatial variations in the fog seeding distribution in each data set.

2.3.4. Vector Computation and Derived Quantities

Following the image processing is the vector processing in the DaVis software using the direct cross-correlation analysis of the double frames. This technique and the mathematical analysis are explained in great detail by Raffel et al. (1998), and Adrian and Adrian and Westerweel (2011). Some of the major steps used in the present data processing are outlined in this section.

In both the baseline and actuated flow fields over the airfoil, there are different relevant characteristic scales that are nominally increasing in size downstream from the leading edge and in the near wake owing to separation and to flow control. In this thesis, the investigations are limited to the flow effects following actuation of some of the larger characteristic structures within the regions of interest over the airfoil (the small-scale flow structures and fluctuations are beyond the present scope). A complete list of experiment conditions for the PIV data is contained in Tables A.1 and A.2 in the Appendix, which shows that the present measurements were obtained with nominal image magnifications of 186 - 310 $\mu\text{m}/\text{pixel}$. The velocity vectors were computed using

multi-pass processing starting with a 64 x 64 pixel interrogation window (or “spot size”) with 50% overlap and improved using a finer 32 x 32 (and only one case in §IV uses 16 x 16) pixel domain.

The velocity fields obtained in the near wake and over the airfoil using multiple PIV domains were processed at the final 32 x 32 interrogation window size with a spatial resolution (or spacing between velocity vectors, Δx and Δy) of about 3.5 - 3.9 mm. This range of resolutions is due to minor variations in the PIV set up between the different wind tunnel entries. There is a wide range of flow gradients within the PIV domains in both the near wake and over the airfoil. As shown in §IV, the cross stream thickness of the baseline CCW and CW shear layers where $|\omega| > 0.1U_\infty/c$ increases from 32 – 60 mm at $x/c = 0.3$ to 130 - 180 mm at $x/c = 1.3$. Therefore, the instantaneous velocities across these shear layers are reasonably resolved with at least 10 vectors. On the other hand, for the PIV data set in §IV obtained near the actuators in the vicinity of the orifice where the baseline and actuated flow structures are smaller compared to further downstream, the velocity vectors were processed using the reduced interrogation window size of 16 x 16 pixel with a 50% overlap, obtaining a velocity field of 164 x 158 vectors which corresponds to a spatial resolution of about ($\Delta x = \Delta y$) 1.9 mm. As measured using PIV (§IV and V) the boundary layer thickness is about 10 - 15 mm near the actuator orifice at $x/c = 0.15$ and increases to about 35 mm at the separation point ($x/c \approx 0.3$). This indicates that a minimum of 6 velocity vectors are computed across the cross stream extent of the boundary layer at the actuators. Note that the cross stream extent of the vortical structures induced by the actuation is commensurate with the boundary layer thickness at the separation point. The appropriate mapping stored during the calibration process is

applied to the PIV images during the vector field computation. The stereoscopic PIV processing follows a similar procedure in DaVis, except that the cross-correlation computation uses the two cameras to resolve the third (out-of-plane) velocity component.

The cross-correlations computed in DaVis can sometimes produce extraneous velocity vectors in each instantaneous flow field, which quite often are easily discernable and can be rejected. The process of removing these invalid vectors is incorporated into the vector processing in DaVis where a filter is applied to the vector field based on a specified fractional threshold of the deviation from the median value at each data point. This validation process and the algorithmic mask or silhouette used result in grid points in the instantaneous flow with zero velocity vectors. For the data presented in this thesis, these missing-vector regions in the instantaneous vector fields are not filled in with interpolated vectors or spatially smoothed in DaVis.

Following the vector computation from DaVis, each set of instantaneous vector fields (u , v and w) can be time- and/or phase-averaged and are used to estimate other statistical and derived flow quantities. The averaging (arithmetic mean) is treated identically in both cases where the sample mean is computed from a set of vector fields that consists of N instantaneous realizations in a continuous time-sequence or in phase-locked bins (and repeated for all the bins). For grid locations (i, j) where there are missing a small number instantaneous vectors due to the low-density particle seeding and/or rejected vectors, the averaging uses a sample size smaller than the entire sample size ($N_{i,j} < N$). The usual notation for the time- (e.g., \bar{u} , \bar{v} , \bar{w} and $\bar{\omega}_z$) and phase-averaged (e.g., $\langle u \rangle$, $\langle v \rangle$, $\langle w \rangle$ and $\langle \omega_z \rangle$) quantities are dropped in the thesis where only averaged (and mostly phase-averaged) quantities are shown.

In addition to the uncertainty in the vector computation, the precision of the PIV equipment or experimental setup (e.g., calibration, particle position and displacement, and camera and laser timings) are sources of error in the velocity measurements. A full treatment of these standard sources of error for the present commercial PIV equipment are not given here, however the ensemble-averaged (time or phase) PIV data are briefly discussed by examining the inherent turbulent flow fluctuations that represents the variability associated with the flow field owing to the unsteady nature of the separation and irregular shedding of vortices. Note that these fluctuations vary spatially in the flow field and temporally relative to the onset of actuation, and are most pronounced within the PIV domain in the vicinity of the actuator orifice. These velocity fluctuations in the flow are characterized in the absence and presence of pulsed actuation using PIV data within the domain $[0.1 < x/c < 0.55, -0.06 < y/c < 0.2, \text{ cf., §IV}]$ in which the base flow is nominally attached through $x/c \approx 0.3$ (up to the separated flow domain). The instantaneous PIV realizations were captured phase-locked to the actuation waveform, processed using a 16×16 pixel interrogation domain, and phase-averaged (over 400 realizations). Velocity fluctuations both within and above the surface boundary layer are clearly intensified by presence of the massively stalled turbulent flow over the airfoil and by the frequent shedding of large-scale vorticity concentrations. These turbulence-induced fluctuations are therefore inherently greater than the turbulence intensity of the empty wind tunnel (0.25%) that were measured using hot wire anemometry (*cf.*, §II.1). Of course, these PIV measurements are also affected by variations in seeding density, etc., although these effects are typically small compared to the induced turbulent fluctuations. The rms turbulence-induced fluctuations of the u and v velocity components

in the base flow measured above the attached boundary layer ($0.02 - 0.05c$) and upstream of the actuators ($0.04 \leq x/c \leq 0.07$) are smaller than 1.5 and 0.9 ms^{-1} , respectively (or 5.3% and 3.1% , relative to the local average velocity). As expected, the measurements show that the turbulence-induced velocity fluctuations in the cross flow over the airfoil decrease with increasing distance from the airfoil. For example, farthest from the airfoil within the above PIV domain (at $0.1 < x/c < 0.2$ and $0.12 < y/c < 0.22$) the average rms fluctuations of both u and v decrease to about 0.8 ms^{-1} (or less than $0.04U_\infty$). For comparison, typical rms turbulent fluctuations of u and v within the separated shear layer are much higher, about 7.4 and 4.5 ms^{-1} . Following the onset of the transitory actuation jet, the turbulent variations in the velocity field induced by the penetration of the jet into the cross flow are even larger. The maximum rms fluctuations in u and v near the orifice are 11 and 7 ms^{-1} , respectively, (these fluctuations may be slightly inflated by lower seeding density in the mixed jet fluid), and are smaller than 7.3 ms^{-1} and 5.0 ms^{-1} in the induced CW and CCW vortices, respectively.

The vorticity distributions in the present thesis are computed from the phase averaged velocity field. Clearly, *the phase-averaged velocity field in a forced turbulent shear flow represents the most probable velocity distribution*. These distributions are also characterized by the magnitude of its turbulent rms velocity fluctuations which quantify the characteristic variations relative to the instantaneous realizations. In this sense, the phase averaged vorticity concentrations also represent the most probable distributions and although they resemble the instantaneous (turbulent) realizations they are by no means identical to any of them. This concept is similar to the most probable representation of other coherent structures in turbulent shear flows such as a turbulent spot in a transitional

boundary layer (e.g., Wygnanski, Sokolov and Friedman, 1976; and Cantwell, Coles and Dimotakis, 1978).

The averaged velocities are then used to estimate the vorticity for the samples at each grid point. The processing code developed by Honohan (2003) was used for all the PIV data in this dissertation where the corresponding time- or phase-averaged out-of-plane

vorticity is computed from $\omega_z = \frac{\partial v}{\partial x} - \frac{\partial u}{\partial y}$ (2-D PIV) by estimating the velocity gradients

using a finite difference Richardson Extrapolation within the original Cartesian coordinate system of each view. Similarly, the plane-normal vorticity component

$\hat{\omega}_x = \frac{\partial \hat{w}}{\partial \hat{y}} - \frac{\partial \hat{v}}{\partial \hat{z}}$ is computed from the stereoscopic PIV data. The CW and CCW

concentrations are taken to be negative and positive, respectively. When there are multiple overlapping measurement domains, the final “stitched” grid occupies the total spatial extent of all the individual views. The velocity and vorticity distributions are interpolated onto the composite grid. Phase-averaged pressure gradients can be computed from the Navier-Stokes equations using phase-averaged velocity field at each grid point as described by Honohan (2003).

It is emphasized that phase-averaged vorticity distributions in the present thesis are computed from the phase averaged velocity field. This is common practice in PIV measurements of turbulent shear flows since the instantaneous realizations are typically not sufficiently continuous for differentiations and therefore prone to numerical errors that may overestimate vorticity magnitudes (e.g., Luff et al., 1999). Clearly, the phase-averaged velocity field in a forced turbulent shear flow represents the *most probable* velocity field, and is also characterized by the magnitude of its turbulent rms velocity

fluctuations. In this sense, the phase averaged vorticity concentrations also represent the most probable vorticity distribution and although they resemble the instantaneous (turbulent) realizations they are by no means identical to any of them (similar to a turbulent spot in a transitional boundary layer, or a turbulent puff in transitional pipe flow). Since the instantaneous vorticity distributions are not computed from the instantaneous velocity data, *upper bounds* of the rms turbulent vorticity fluctuations are estimated using the velocity rms fluctuations (as described above). *The average vorticity bounds* within the center of the CW and CCW vortices are about 4% and 18%, respectively. However, as expected, the estimated variations in the computed CW vorticity within the separated shear layer are higher, increasing from 15% at the center to as high as 57% at the outer edges (similar to turbulent intermittency at the cross stream edges of a plane shear layer) where the phase- (or time-) averaged vorticity vanishes.

The phase-averaged velocity fields obtained from the PIV measurements were also used to establish streamline patterns in the center plane ($z = 0$) where it may be assumed that the spanwise velocity component is vanishingly small. An example of the computed streamlines is shown in Figure 4.10. The streamline passing through a spatial location ($x_{s,o}$ and $y_{s,o}$) in the velocity field for each phase-averaged instance is constructed by computing the forward and backward-marching pathlines that originate from ($x_{s,o}$ and $y_{s,o}$) using mid-point integration of the velocity field over a small time-step (Δt_s). The x and y coordinates (x_s and y_s) of each pathline form a streamline (or streamtrace) such that it is constructed everywhere parallel to the velocity field. The time-step (Δt_s) used in the integration to compute each location of the path ($x_s(i, j)$ and $y_s(i, j)$) is variable and is arbitrarily selected to be the minimum of the time required to travel a distance equal to

1/100 of the spacing between the original grid points at the u and v velocities of the previous location $(x_s(i-1, j-1), y_s(i-1, j-1))$, i.e., $(\Delta t_s = \min\{\Delta x/[100u(x_s(i-1, j-1), y_s(i-1, j-1))], \Delta y/[100v(x_s(i-1, j-1), y_s(i-1, j-1))]\}$. Note that a finer time step would result in an increased computation time. The velocity components (u_s and v_s) at the sub-grid points that correspond to the pathline x_s and y_s are estimated using bi-linear interpolation.

Another possible method for computing the streamlines that involves the use of stream functions (e.g., Honohan, 2001) was not used in this dissertation. For the flows in the present investigations that are unsteady, these streamlines computed using this tracking method are “instantaneous” streamlines or “solution trajectories” as referred by Perry and Chong (1987) whom also used a similar approach in their streamline computations. The streamline tracking method used in the present investigations and that used by other researchers for both steady (e.g., Baker, 1978, 1979; Kelso et al., 1996; and Hasselbank and Mungal, 2001) and unsteady flows (e.g., Seal et al., 1995, 1997; and Ozen and Rockwell, 2012) were applied to the symmetry plane where the results presented by these authors share common topological features (e.g., the spiral streamlines that converge and lead to accumulation points) in the flow patterns with the results presented in this dissertation. These convergence points are typically located in flow regions with small velocity magnitude that are difficult to resolve. Stagnation points in the flow near the airfoil surface were as also found from the PIV vector field by locating positions within the flow where the velocity vanishes ($u = v = 0$).

2.4. Aerodynamic Loads

Time-resolved lift and pitching moment were measured phase-locked to the motion command waveform when the airfoil was undergoing time-periodic pitch (§VII). The lift

was assessed from measurements of the two load cells shown in Figure 2.6 where each measures a fraction of the total force on the traverse, including the weight of the airfoil model. The center of mass of the airfoil is located away from its pitching axis toward the trailing edge, and this eccentricity in the mass, albeit small, contributes to a vertical force when the model is oscillating in pitch. The unbalanced force clearly depends on the pitching frequency and amplitude, and varies in time at the frequency of the motion. To remove this force from the measurements, in the dynamic experiments the time-dependent force was acquired in the absence and presence of air flow in the test section. The measurements in the absence of air flow were subsequently subtracted from the measurements obtained with air flow. This procedure also removes the weight of the airfoil model and the balance of the vertical force is ideally the aerodynamic lift. However, the bending and vibrations of the airfoil model induced by flow separation also contribute to linear accelerations that were included in the measured values by the load cells. Following the approach developed by Brzozowski (2011) to remove the vibration-induced forces, a set of six $\pm 5g$ Measurement Systems model 4000 linear accelerometers (single-axis with frequency response up to 300 Hz) with $\pm 1.5\%$ uncertainty are mounted on the shaft to measure the accelerations at discrete locations along the span of the model. The accelerations multiplied by the weighted mass were also subtracted from the total force, providing an estimate for the time-dependent aerodynamic lift force, $L(t)$ (positive L and C_L represents an aerodynamic lift acting in the positive y direction).

Similarly, the torque that was measured from the command voltage on the pitch motor included the contribution from the angular acceleration of the airfoil's moment of inertia about the pitch axis. This inertia effect was removed from the balance of moments

by subtracting the torque in the absence of air flow from the measurements obtained with air flow, providing an estimate of the time-dependent aerodynamic moment, $M(t)$, on the airfoil that acts about the pitch axis, and the corresponding pitching coefficient, $C_M(t) = M(t)/(0.5\rho U_\infty^2 S c^2)$. A positive M (and C_M) represents an aerodynamic pitching moment acting in the clockwise or pitch-up direction. An estimate of the pitching moment coefficient about the quarter-chord of the airfoil is given by $C_{M,c/4} \approx C_M - (x_c - 0.25c)C_L \cos \alpha$ where $x_c - 0.25c \approx 0.1c$ is the distance from the pitch axis to the quarter chord as shown in Figure 2.14. This estimate does not account for contributions from drag, which was not measured in the present investigations. Unless otherwise stated, the phase-locked unsteady lift and pitching moment during the airfoil pitching cycle are averaged over 100 oscillation cycles. The total measurement uncertainty in the lift and pitching moment coefficients in the presence of air flow for the pitching frequency and amplitude in §VII were estimated to be no more than ± 0.06 and ± 0.01 , respectively. The phase-averaged notation, $\langle \rangle$, for the two aerodynamic coefficients (C_L and C_M) are also dropped for the discussion of the results in this dissertation.

2.5. Pressure Measurements

The airfoil is also instrumented with 75 static pressure ports (diameter $3.5 \times 10^{-3}c$) located circumferentially at mid-span, with closely-spaced ports near the leading edge. The ports are each connected to a PSI 48-port connector outside the wind tunnel using 1.59 mm inner diameter urethane tubing (~ 2 m long). These connectors are attached to their corresponding halves that are connected to a high-speed PSI pressure measurement system for acquisition of the time-averaged pressure distribution around the airfoil (the uncertainty of the time-averaged pressure measurements is estimated to be less than 1%

(Brzozowski, 2011). This system measures differential pressure and is calibrated against the ambient pressure in the laboratory. The PSI measurement system is hardware triggered to sample each transducer channel at 100Hz and averages over 256 instantaneous data points for each channel prior to sending the calibrated pressure measurements from all its channels to the user. This procedure was repeated over 100 cycles using LabView where the “instantaneous” averaged pressure values were averaged over the 100 samples for each pressure port on the airfoil surface. These pressure measurements are used to compute static centerline lift on the airfoil model by numerically integrating the distributions (using the trapezoid method) as described in §IV. The pressure port locations (with closely-spaced ports near the leading edge) are included in Table B.1 in the Appendix. Occasionally, a small number (up to five) of pressure port taps on the airfoil surface can be temporarily blocked during an experiment. Although these blocked ports can be omitted or “flagged” using the LabView software, in the present experiments they were fixed before the measurements of all pressure ports were sampled.

Although the pressure scanning system can sample at 100 Hz, the overall frequency response of the entire pressure measurement system including the tubing is estimated to be about 10 - 15 Hz and cannot resolve rapid pressure changes expected during the attachment induced by the pulsed actuation. This limitation in the frequency response of the pressure sampling is estimated by approximating the transducer as a Helmholtz resonator and that the tubing walls are fixed, and is discussed further in §IV. Therefore, in addition to the static pressure ports connected by the long tubing, Honeywell piezoresistive 4-in H₂O analog differential pressure sensors (typical response time 100

μs) were instrumented inside the airfoil directly next to the surface and connected to 1.59 mm inner diameter stainless steel tubing that are less than 10 mm in length. These on-board pressure sensors were used to measure transient changes in pressure at several discrete locations over the airfoil. The factory specified sensitivity curves for these pressure sensors were compared by bench-top calibrations using a water manometer and the steady-state errors are estimated to be less than 1%. The instantaneous time-dependent pressure measurements were acquired in LabView, phase-locked to the motion of the oscillating airfoil over 100 cycles. Although the pressure transducers are temperature compensated for 0 to 70 °C, there is some drift in the signals (less than ± 5 Pa as measured during the bench-top calibrations with the water manometer). To minimize this transducer zero drift, the sensors and electronics were powered on for a minimum of 30 minutes prior to sampling the signals and the lab temperature was regulated. The pressure measurements were reproduced to within an rms error of approximately 50 Pa.

2.6. Surface Oil Visualization

For the flow visualization experiments, a mixture of equal parts 91% propyl alcohol and Aeroshell aviation mineral oil was mixed with Tracerline oil additive fluorescent dye. The oil applied to the airfoil is illuminated using standard (15 W) UV fluorescent light fixtures that are placed above the wind tunnel. The suction surface of the airfoil is lined with a thin (< 0.1 mm) self-adhesive, residue-free vinyl sheet across the airfoil span to form a contiguous smooth surface that prevents oil accumulation between the airfoil sections without affecting the base flow. The contrast of the fluorescent oil was enhanced by selecting an off-white sheet color. A thin, uniform coat of oil, was applied

in the absence of air flow, by brush on the vinyl-covered airfoil to minimize the effects of the oil on the flow. After the tunnel is turned on, the oil continuously forms the flow pattern on the surface and was photographed at regular time intervals using a standard digital camera mounted above the wind tunnel. This process was repeated for each run (often with a fresh coat of oil and a new vinyl sheet) to investigate flow patterns for the different airfoil configurations.

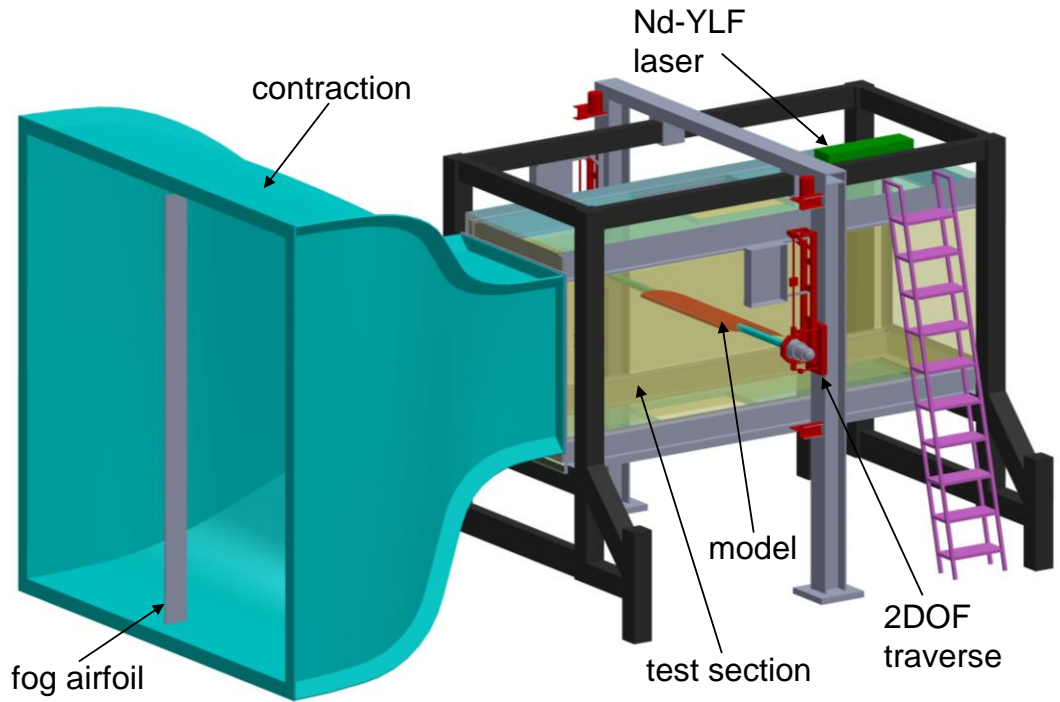


Figure 2.1: CAD model of the wind tunnel facility showing the flow contraction and test section with an airfoil model mounted to the 2-DOF traverse mechanism. Other upstream and downstream sections of the tunnel facility are not included.

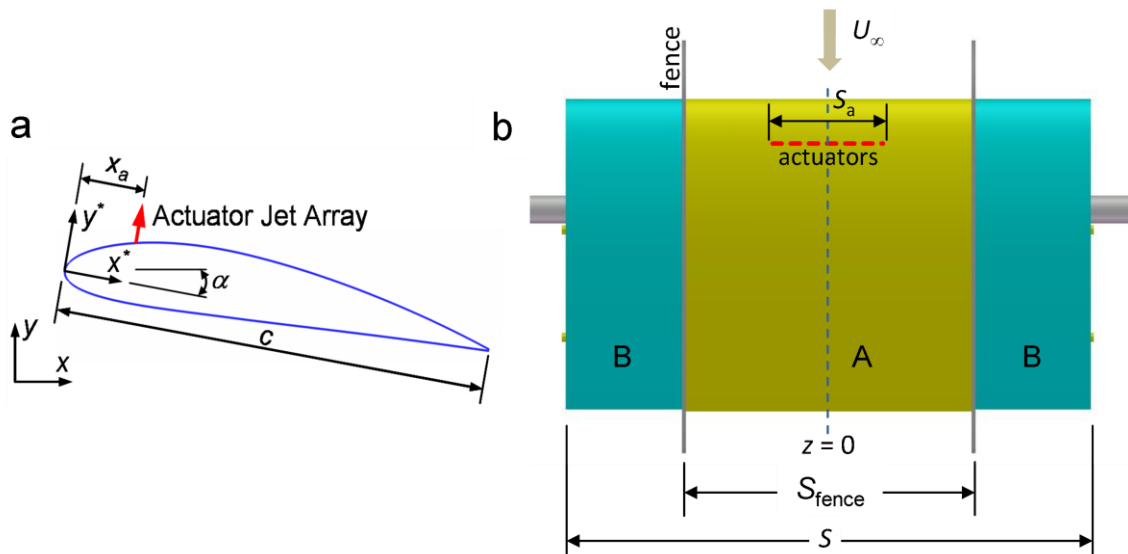


Figure 2.2: NACA4415 airfoil model: (a) Cross sectional view showing location of actuator jets at $x_a/c = 0.15$, and (b) Top view showing the spanwise actuator array (having span S_{act}), and the streamwise fences separating the actuated (“A”) and unactuated (“B”) flow domains.

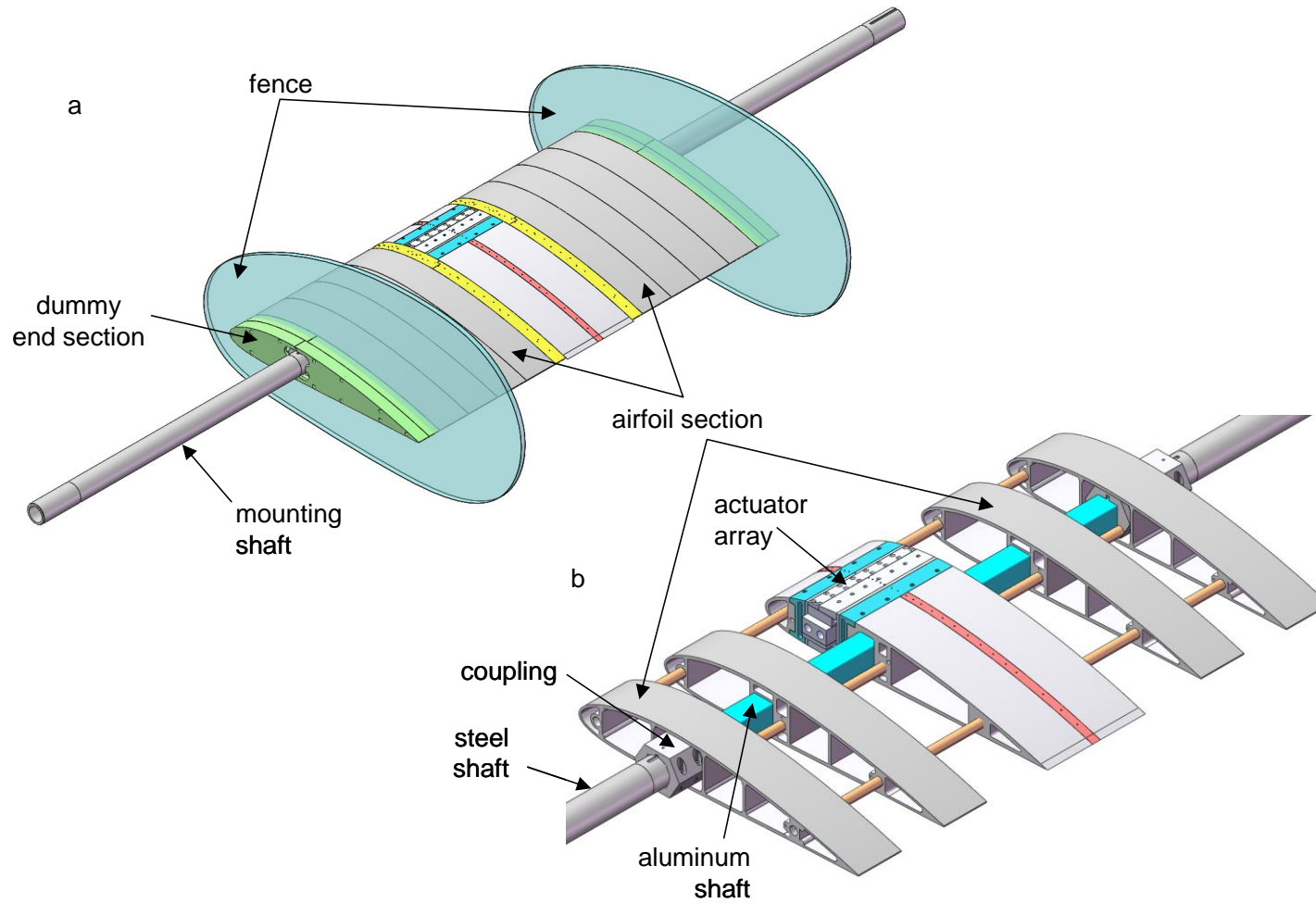


Figure 2.3: CAD model of airfoil model: a) Assembled with fences, mounting shaft and the dummy sections, and (b) Close up view of the actuator array and internal structure of the mounting shaft.

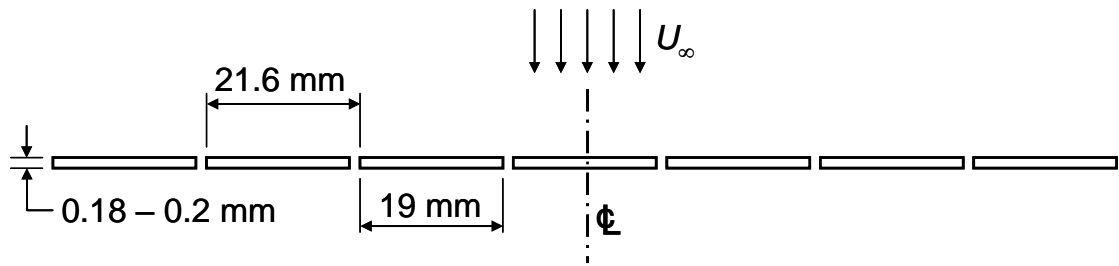


Figure 2.4: Schematic of the seven rectangular jet orifices in the actuator module shown in Figures 2.2 and 2.3. The orifices are aligned to the span of the airfoil.

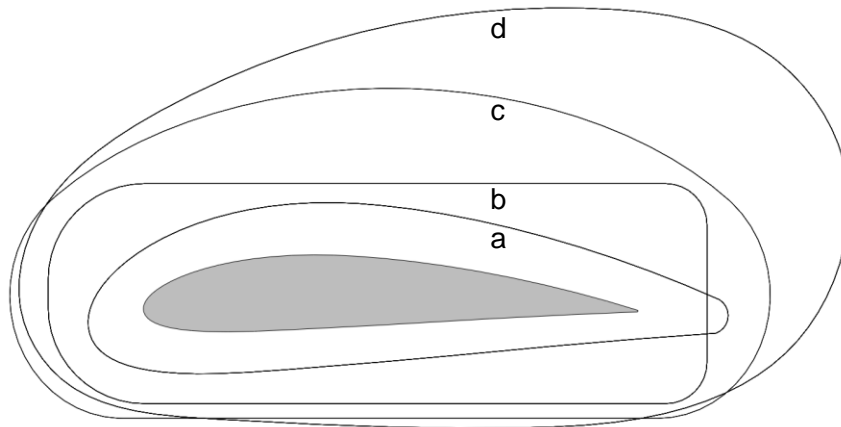


Figure 2.5: Scaled outline of the streamwise fences (a – d) relative to the airfoil.

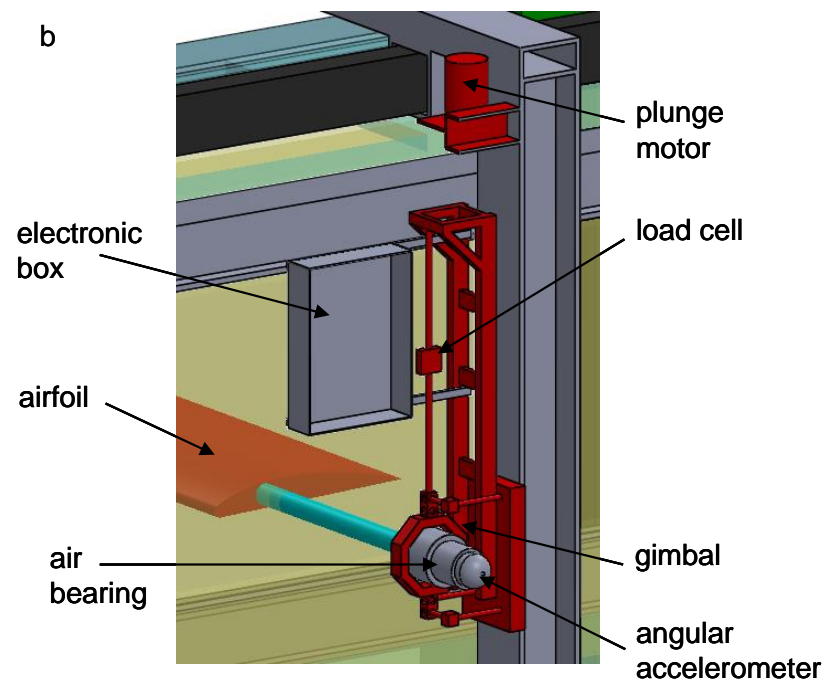
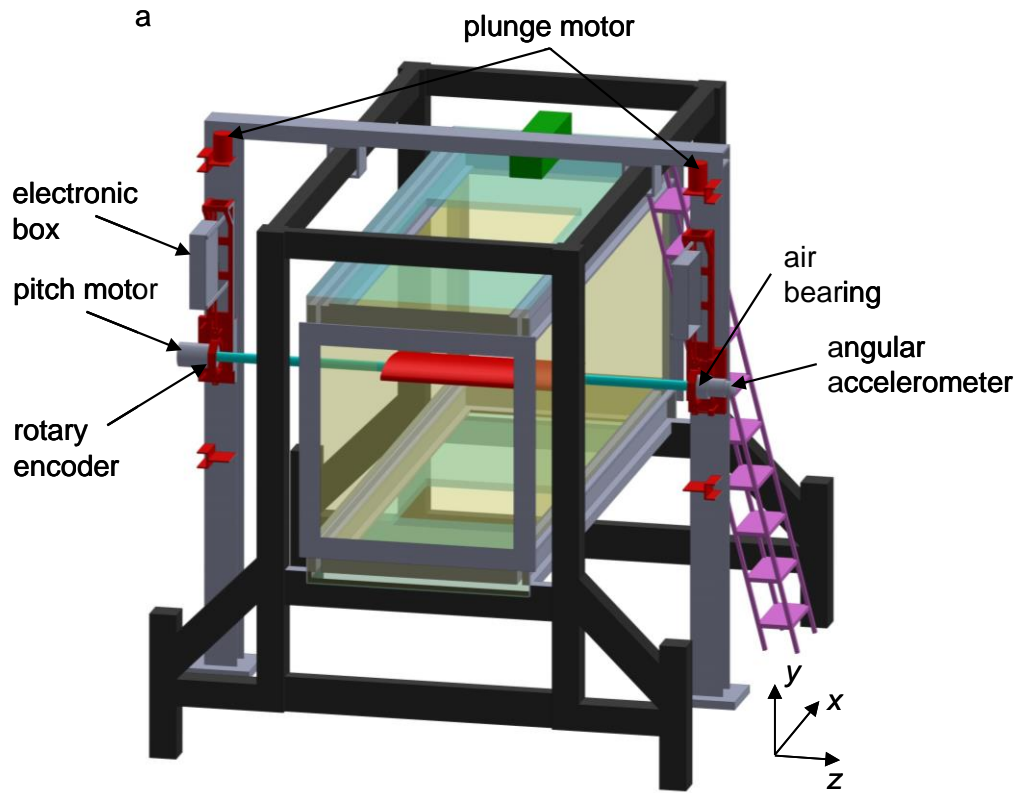


Figure 2.6: CAD model of the traverse mechanism: a) The front and back carriages with laboratory coordinates shown and b) The load cell mounted to the gimbal.

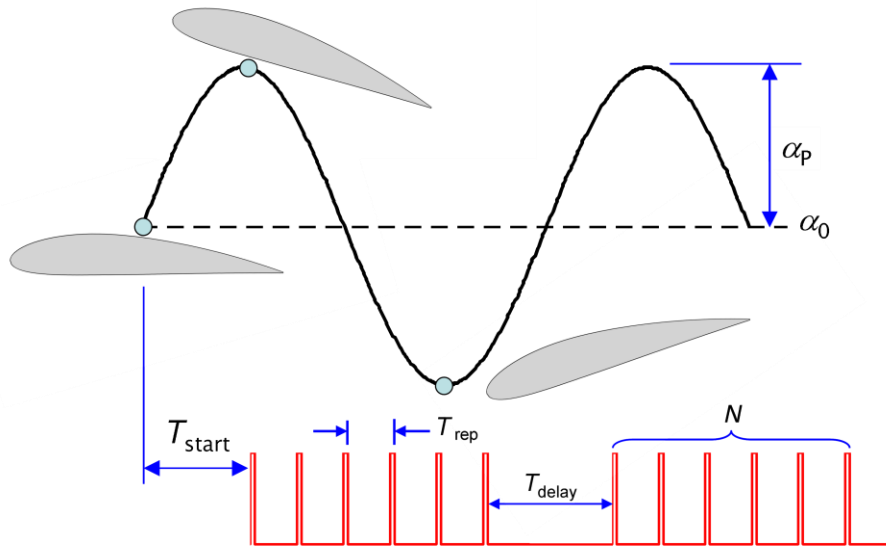


Figure 2.7: Timing of model pitch motion $\alpha(t) = \alpha_0 + \alpha_p \sin(\Omega t)$ and actuation.

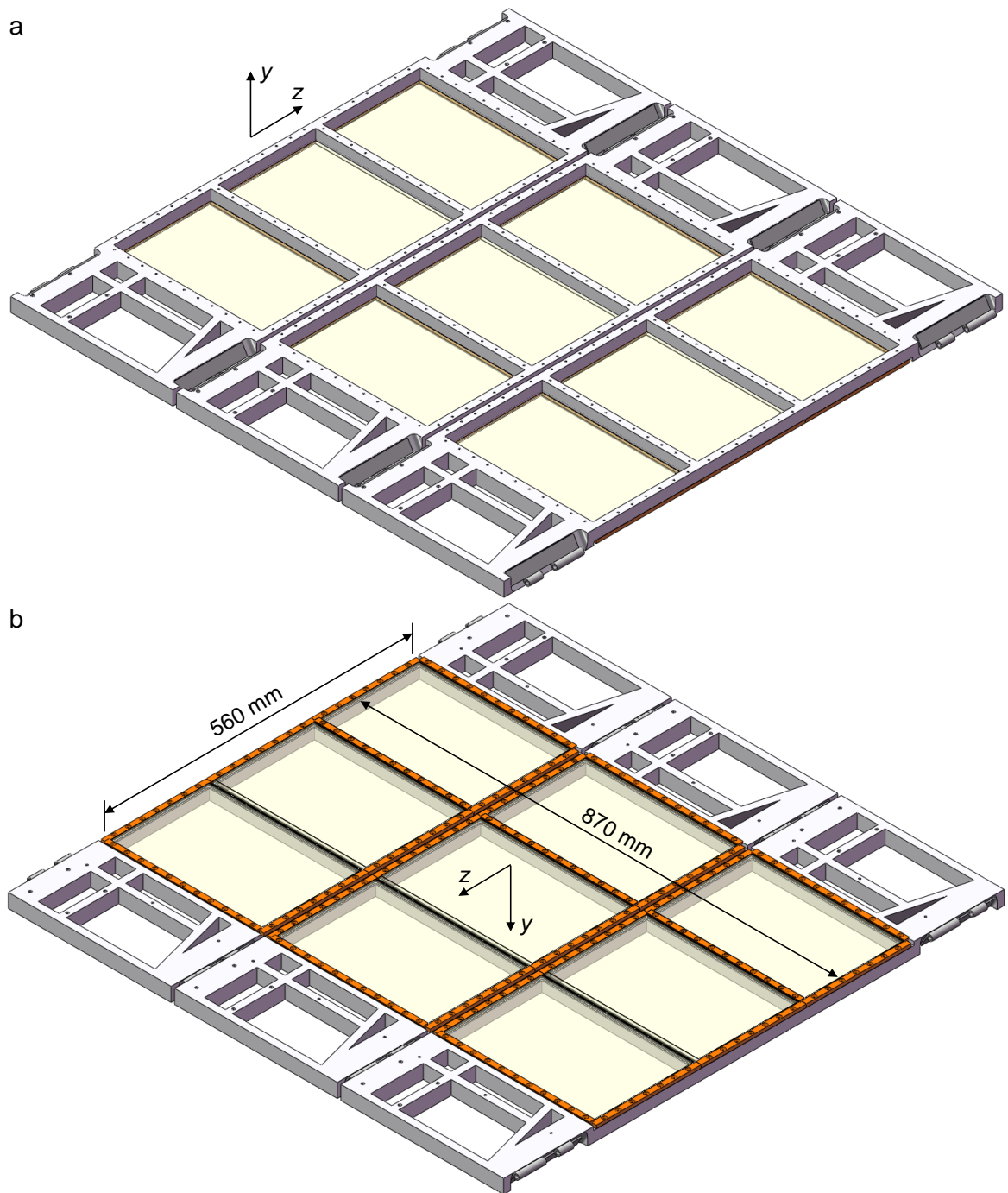


Figure 2.8: CAD model of PIV windows installed on the wind tunnel ceiling of the test section: (a) Viewed from above the tunnel and (b) Viewed from inside the test section showing the windows flush to the ceiling.

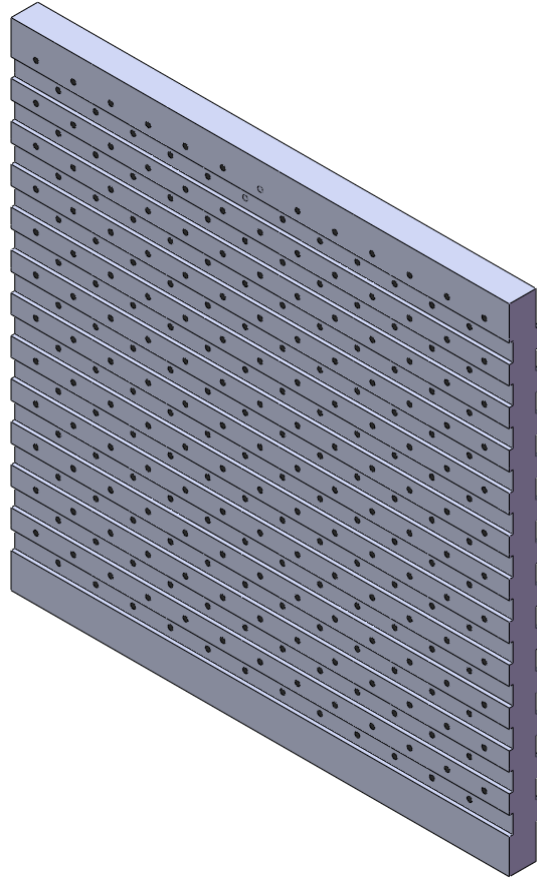


Figure 2.9: CAD model of dual-level calibration plate used for PIV showing the machined pattern of round dots.

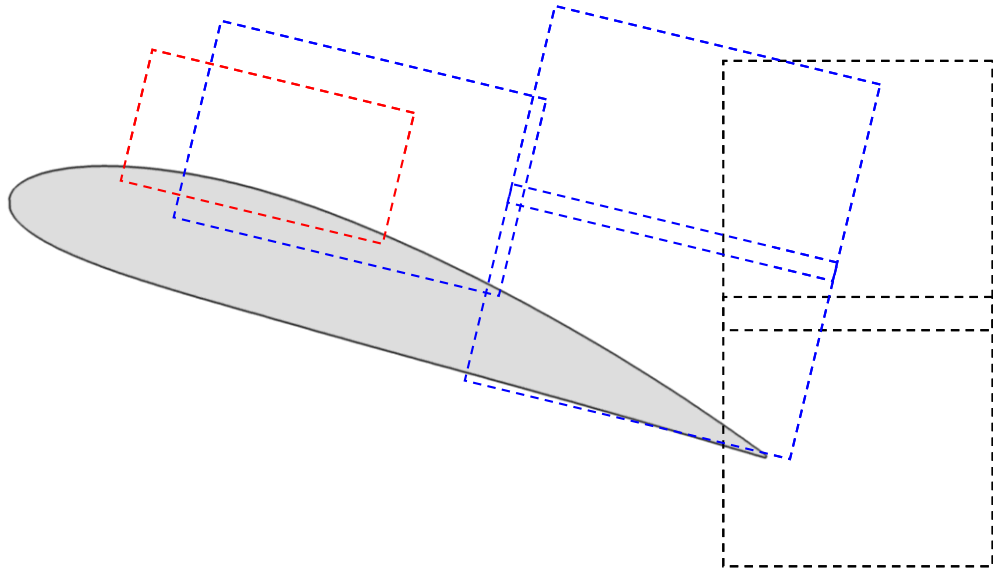


Figure 2.10: Schematic of overlapping PIV windows used. The different colors represent domains investigated in the different sections of the dissertation.

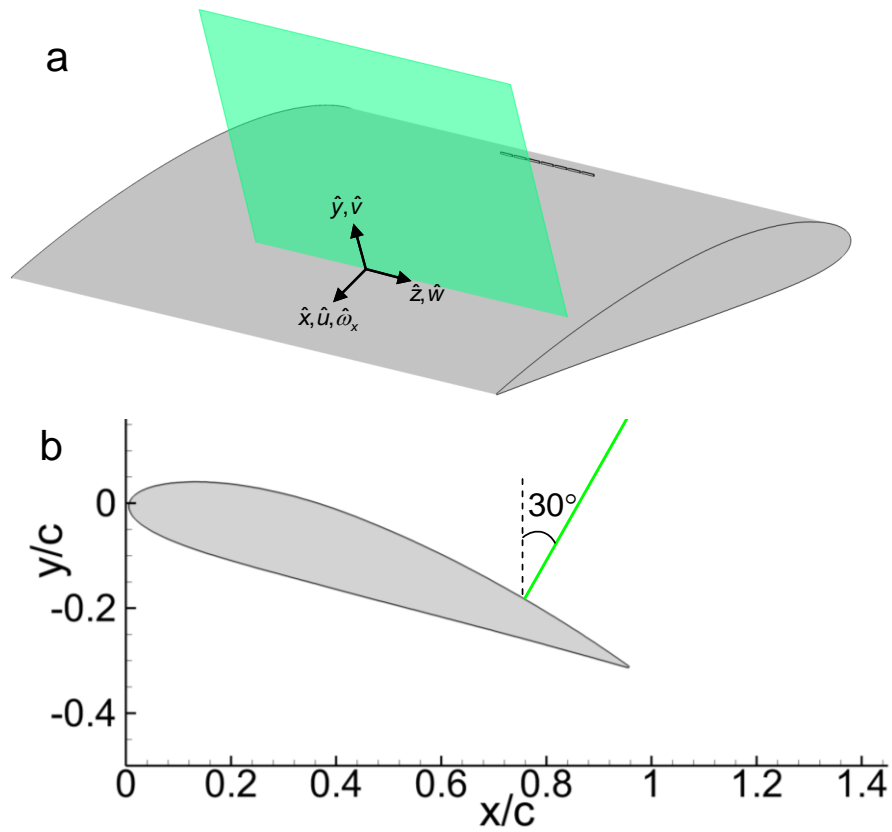


Figure 2.11: Setup of stereo-PIV showing (a) measurement coordinates and flow domain within laser sheet in green and, and (b) the relative angle of the measurement plane to the wind tunnel coordinates.

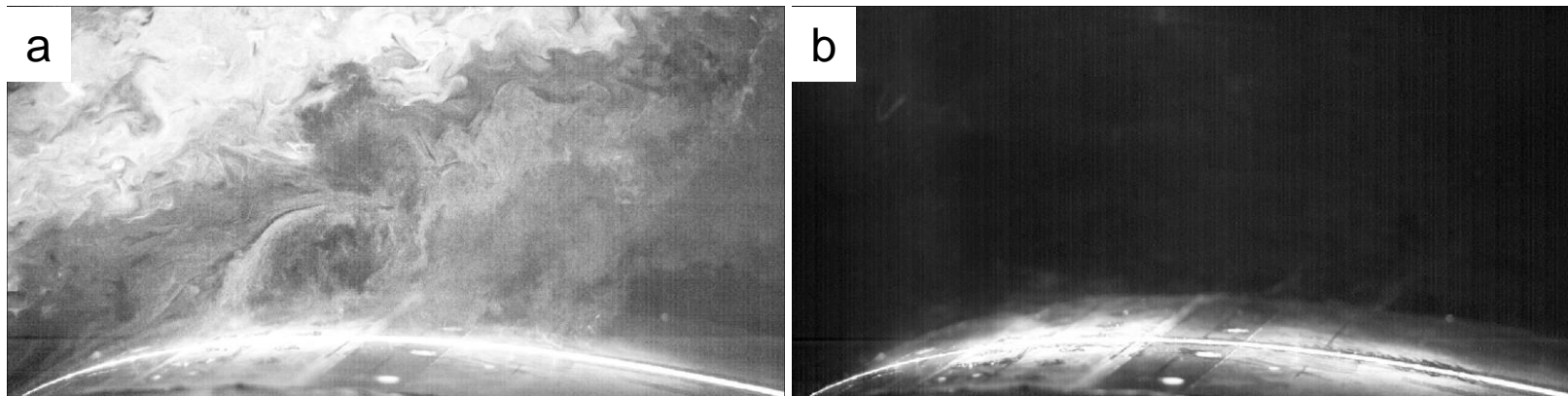


Figure 2.12: Sample images acquired using PIV camera above the airfoil illuminated using Nd:YLF laser: (a) Raw instantaneous phase-locked image of flow seeded with fog particles and (b) “Background” image averaged over 50 instantaneous realizations without fog particles.

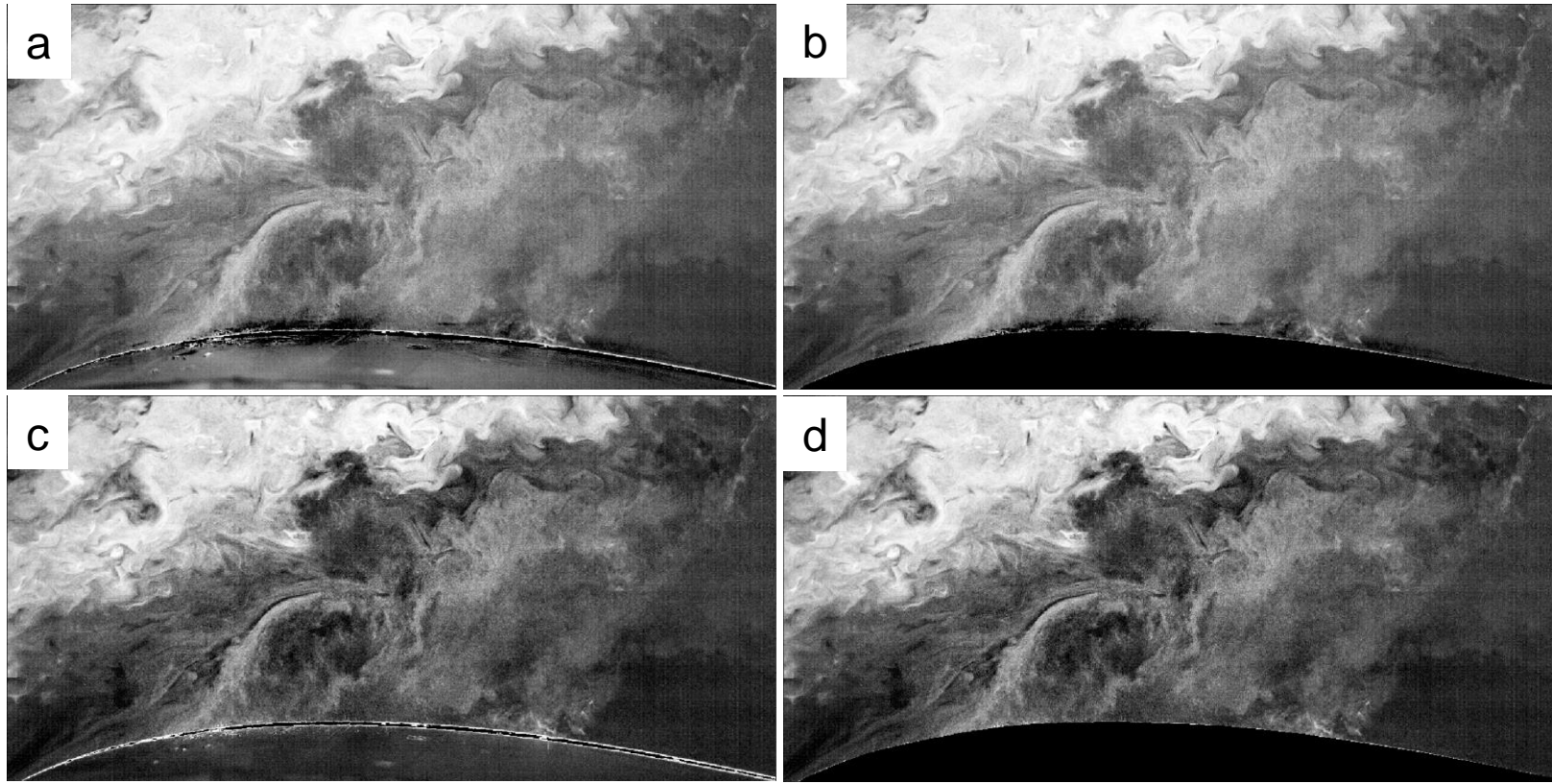


Figure 2.13: Pre-processed PIV images corresponding to Figure 2.11a. Background image in Figure 2.11b is subtracted (a) and with fixed mask applied (b). Minimum intensities from the sequence of 200 realizations are subtracted (c) and with fixed mask applied (d).

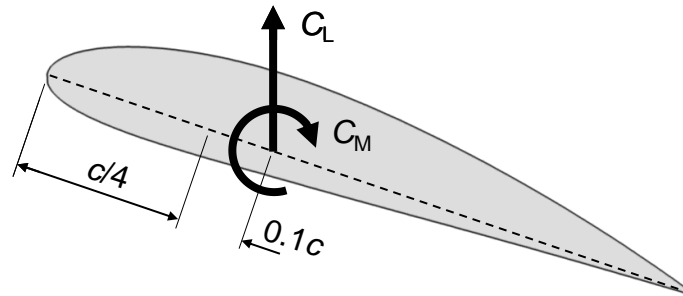


Figure 2.14: The measured lift and pitching moment coefficients acting at the pitch axis away from the reference quarter-chord location.

CHAPTER III

COMBUSTION POWERED ACTUATORS

3.1. Basic Concept

Combustion-powered actuation (COMPACT) for flow control was developed by Crittenden (2003) based on the principles of controlled, intermittent combustion to produce repetitive momentary pulsed jets that are each produced by ejection of combustion products through an orifice in a combustion chamber following the ignition of a combustible mixture within the chamber. Historically, pulsed combustion typically refers to the time-periodic pulsating combustion first developed in the late 1890s and implemented in industrial scale for heating and drying and later used for propulsion (e.g., the V-1 rocket since the 1930s), and is based on thermoacoustic combustion instability to repeatedly replenish and re-ignite the reactants (Ponizy and Wojcicki, 1985; Putnam et al., 1986; and Zinn, 1992).

The basic concept of the COMPACT utilizes the exothermal energy of the intermittent subsonic combustion (deflagration) process within a nearly fixed-volume combustion chamber to increase the pressure (and temperature) of the fuel-air mixture to generate a momentary jet through an exit orifice. This device is shown schematically in Figure 3.1. First, fuel and air are injected into a centimeter-scale chamber either independently or premixed, followed by the ignition of the reactant mixture. The activation energy for the combustion process is provided by a spark discharge controlled externally. Flow resistance elements in the reactant supply lines reduce the flow of the pressurized combustion gas products into the supply lines so the gases exhaust through

the exit orifice as a high-impulse, short-duration (~ 1 ms) high-speed jet (there are some pressure losses associated with the exit path of the jet). During the combustion and discharge, the flow of reactants into the chamber is momentarily stopped by the increased pressure. As the combustion process is concluded and the reaction products are vented through the orifice, the pressure in the chamber decreases. When the chamber pressure falls below that in the reactant supply lines, the flow of the reactants into the chamber resumes and helps evacuate the combustion products before the combustion process is repeated. This is shown in further detail by the pressure traces in Figure 3.7. This pulsed combustion can be triggered repetitively (T_{rep} apart, Figure 3.2) to form bursts of nearly arbitrary pulse trains of specified duration and number of pulses (N) that can be repeated with some delay T_{delay} .

The chemical kinetics of the combustion process are highly dependent on the fuel and air mixture inside the chamber. In addition, the discharge of the combustion products and the replenishing of the reactants that are both coupled to the combustion are also affected by the flow conditions in the supply lines and the exit orifice. There are several characteristic features of the COMPACT device that can alter the pulsed combustion process and therefore its performance. These include the shape (e.g., cuboid or cylindrical) and size of the chamber (e.g., internal volume, aspect ratio and surface area), and geometric parameters of its exhaust orifice (e.g., shape, size, aspect ratio, and exit flow path). A uniform mixture at a given overall equivalence ratio is usually desirable to avoid spatial and temporal variations in the combustion. Several of these parameters were studied in detail for different basic cylindrical chamber designs by Warta (2007) and later by Rajendar (2010) using cuboid chambers. Warta (2007) showed that the

combustion pressure build-up decreases with decreasing T_{rep} for different equivalence ratios (0.3 to 1.2), reactant flow rates (4 to 20 LPM) and chamber volumes (0.25 to 2 cm³). Rajendar (2011) constructed a cuboid chamber with 9 inlet air and fuel ports each, and investigated using PIV the flow effects of the different supply inlet configurations on the mixing of the fuel and air inlets, and concluded that the effective mixing of the reactants is affected by the spatial distribution of the internal flow (e.g., corner flows and counter-rotating cells) within the chamber.

It is noted that while the COMPACT and the larger scale pulse-combustors are similar in that both concepts consist of fuel and oxidizer supply inlets, a combustion chamber and an exit for exhausting the combustion products, there are some significant differences. Traditional pulsed combustion processes are designed to operate time-periodically and the fresh reactants are auto-ignited at the onset of each cycle. In the COMPACT process, the actuation is initiated (and in fact controlled) by spark ignition. Furthermore, as discussed in connection with Figure 3.4, COMPACT has no moving parts while conventional pulsed combustors often require mechanical (e.g., flapper) valves or resonance tubes. Finally, COMPACT actuators can be easily miniaturized and adapted for integration in complex hardware.

3.2. Structure of The Actuator Array

The present investigations use a design of a COMPACT array that is based on the earlier works of Brzozowski and Glezer (2006). These investigations successfully demonstrated the utility of this actuator array for transitory control of flow separation in wind tunnel experiments. The design of the combustion chambers in this actuator array is different

from earlier configurations and includes an array of chambers. However, the performance of the actuator array had not been characterized in detail.

In the present investigations, actuation is effected using an array of equally-spaced seven O[cm³] combustion chambers that, similar to the earlier design, are each equipped with a specialized, miniature (24 mm) spark plug (Rimfire V1 Viper in Figure 3.4a) that is driven by an electronic ignition module (*cf.*, Figure 2.14) using a 6 VDC automotive battery that can be wired in such a way that the combustion in each of the chambers is triggered individually from the laboratory computer (*cf.*, Figure 3.2). As noted in §II, this actuator array is mounted in the NACA 4415 airfoil model (Figure 2.3) with a flush-mounted cover plate that includes the orifices (Figure 2.4). The cover plate, the electrical connections and supply lines plumbing are omitted in Figure 3.3a to show the internal structure of the array (the cover plate and orifice are shown in a sectional view of the array in Figure 3.3b).

Following the earlier COMPACT investigations (e.g., Crittenden, 2003; Warta, 2007; and Rajendar, 2010) the fuel used in the present investigations is hydrogen which has a low ignition energy (less than 0.02 mJ) and fast laminar flame speed (about 3 ms⁻¹). Hydrogen (delivered from an ultra-high purity 5.0 Grade hydrogen 2,400 psig compressed cylinder) and air (available from the building's compressor at 100 kPa) enter each chamber from two separate cavities in the manifold (Figure 3.3a). Both supply line flow rates are measured and regulated using individual Aalborg Thermal Mass Flow Controllers and needle valves to ensure a prescribed equivalence ratio. In addition, particulate filters and a pressure regulator are installed in the air supply line to remove

contaminants. The flow conditioning and safety hardware are mounted on a dedicated cart next to the wind tunnel.

The mixing of these reactants take place inside the chamber before the combustion is initiated by the spark discharge. As shown in figure 3.3b, the hydrogen flows into each chamber through a fluidic valve that consists of a porous (or sintered) metal disk and then through holes in a thin plate, while air is injected into the chamber through a miniature needle valve (Figure 3.3a) to precisely control the equivalence ratio in each chamber. These porous, flow resistance disks limit the upstream flow of the combustion products and also act as flame arrestors. Downstream of the porous disk, the hydrogen is distributed into the chamber through a 0.1 mm thick brass orifice plate (Figure 3.4b) with a pattern of seven 0.4 mm diameter laser-cut holes, creating individual hydrogen jets that mix with the air. Figures 3.4c and d show examples of two porous disks that are cut using wire-EDM from a 6.35 mm thick 316 stainless steel rolled sheet of Mott porous Media Grade 2 and 10 that are rated to filter 99.9% of the nominal 2 and 10 micrometer solid particles in a gas stream, respectively. Figures 3.5a-c show examples of particulates that are likely burnt oil contaminants from the compressed air line deposited on the surface of the porous material over prolonged (about 6 months) use. The particulates degrade the performance of the actuation and can result in variations between the seven actuators. The porous disks are therefore regularly cleaned or replaced.

3.3. Bench Top Characterization of the Actuator Array

The operation of the actuator array was characterized on a bench top in the absence of a cross flow. A sequence of instantaneous images of a pulsed jet formed by the center actuator in the array that is visualized using a double-pass Schlieren system (Settles,

2001; and Davidhazy, 2006) are shown in Figures 3.6a-j. The jet discharges into a quiescent ambient, and the images are obtained phase-locked to the ignition trigger using a high-speed CMOS camera (Phantom V12.1) at 41,000 fps. The orientation of the actuator array is such that the long side of the rectangular orifice is aligned along the optical axis of the Schlieren system (the z axis in Figure 3.3). For the data in Figures 3.6 and 3.7, the chambers are equipped with the porous Media Grade 2 metal (Figure 3.4c) and the combustion in the center actuator is approximately at stoichiometric ratio with a nominal 0.36 LPM flow rate of reactants per chamber. The time-resolved pressure within the combustor is measured using a fast 100 psia Kulite XTEH high-temperature pressure transducer that is mounted on the chamber wall, and is sampled at 100 kHz phase-locked to the ignition waveform. Time traces of the phase-averaged (over 100 realizations) pressure within the combustion chamber are shown in Figure 3.7 for a range of T_{rep} . The black trace corresponds to Figure 3.6 and is marked with labels a – j for the timing of the individual images.

As shown for $T_{\text{rep}} = 0$ (Figure 3.7, black trace), the rise in chamber pressure for the single pulse due to combustion is first detected at $t = 0.28$ ms (with a brief delay from the ignition). The maximum pressure ratio, $P_{r,\text{max}} = p_{\text{chamber}}/p_{\text{atm}} \approx 3.8$, is reached at approximately 0.55 ms later, indicating that the combustion is mostly complete within less than 1 ms following trigger of the actuation. Note that even in the presence of exit losses, the present pressure ratios in Figure 3.7 suggest that the pulsed jet can reach a supersonic speed at the orifice. During the early stages of combustion, a weak starting vortex-like structure (marked by arrows in Figures 3.6a and b) and a following turbulent jet (Figure 3.6b – e) are discharged, corresponding to $P_r \approx 3.8$ in Figure 3.6c. The starting

vortex increases in size (Figures 3.6c and d) and becomes less distinguishable as it mixes with the ambient. The jet width continues to increase as it moves vertically above the orifice, eventually penetrating through the slower vortex structure (Figure 3.6d). The peak pressure corresponds to the peak in energy release, and it is assumed here that the characteristic time of the combustion can be represented by the elapsed time between the initial increase in pressure and the peak pressure (≈ 0.5 ms). Based on the Schlieren images it is assumed that during this time ($t < 0.8$ ms), the jet is therefore relatively weak compared to the discharge following the peak pressure (*cf.*, Figures 3.6d-h). The delay between the rise in internal pressure and the apparent strength of the jet in the Schlieren images may be attributed to compressibility effects which come into play when there is a rapid decrease in chamber pressure to atmospheric ($0.8 \leq t \leq 1.7$ ms). Finally, the conclusion of discharge is characterized by a brief vacuum (~ 0.95 atm for $t > 1.6$ ms) owing to inertial effects and cooling corresponding to the rapidly decaying jets in Figures 3.6i and j. As is evident in the pressure transients, the duration of the actuation jet (~ 1.3 ms total duration from Figure 3.7) is longer than the combustion, i.e., $T_{\text{discharge}} > T_{\text{combustion}}$. Note that although the “duration of the combustion” is simply estimated using this characteristic time from the pressure trace, the combustion does not necessarily end at the pressure peak.

The rise ($\sim 0.4 - 0.7$ ms) and decay ($\sim 0.8 - 1.2$ ms) time scales as characterized by the increase and decrease in the chamber pressure depend on the pulse repetition time, T_{rep} . This is shown in Figure 3.7 for the current example. As shown by Warta (2007) and Rajendar (2010), the decrease in performance as manifested by the reduced peak pressures of the pulsed combustion with decreasing T_{rep} for a given reactant flow rate is

caused by the decrease in the time available for replenishing the combustion chamber with fresh reactants following each discharge of the high temperature products and by incomplete scavenging of the exhaust from the previous cycle.

To demonstrate the variations in the instantaneous pressure measurements, Figures 3.8a-c show the phase-averaged pressure traces from Figure 3.7 of a single pulse repeated at $T_{\text{rep}} = 1000$ (a), 200 (b), and 100 (c) ms, each bounded by one standard deviation of the 100 instantaneous measurements. It is evident that at the current configuration, the variations in the pressure increase with decreasing T_{rep} due to the (fixed) time it takes to discharge the products and replenish them with fresh reactants. The data in Figure 3.8 show for example, the rms at the peak pressure of about ± 0.8 atm for $T_{\text{rep}} = 1000$ ms in Figure 3.8a increases by about 20% to about ± 1 atm for $T_{\text{rep}} = 100$ ms in Figure 3.8c.

It is noted that that there are also some variations in combustor pressure between the seven actuators within the array when they are operated simultaneously, even though the actuators are tuned to have similar performances across a wide range of operating conditions (up to $T_{\text{rep}} = 10$ ms). An example is shown in Figure 3.9 for the 1st, 3rd, 5th and 7th actuators in the array when the actuation is repeated at $T_{\text{rep}} = 200$ ms at a reduced equivalence ratio of 0.8 and an increased total supply flow rate of 3.5 LPM. The variations in the peak pressure are such that the pressures of the outboard actuators (1 and 7) are lower than the peak pressures of the inboard actuators (3 and 5) indicating that the flow rates to the individual chambers is affected by manifold losses that can be overcome with an improved design. The nominal rms variations for each chamber are relatively low [$O(0.03P_{r,\text{max}})$], but can reach as high as $0.2 P_{r,\text{max}}$ in this example. The increased flow rate is not expected to greatly affect the combustion performance at this low

repetition rate. A comparison of Figures 3.9a-d with Figure 3.8b at $T_{\text{rep}} = 200$ ms shows (as expected) that lean reactant mixture reduces the peak pressures. More importantly, it is also apparent from the standard deviation of the pressure traces that the variations in the instantaneous chamber pressures are noticeably reduced when the combustion is lean. The corresponding variations in the phase-averaged chamber pressure averaged over the 7-actuators are shown in Figure 3.9e, and indicates overall variation in performance between the actuators.

Although the focus of this thesis is on pulsed jets that operate at low repetition rates ($T_{\text{rep}} > 20$ ms), it is informative to demonstrate briefly that the current array of COMPACT actuators can be further tuned to operate at much shorter T_{rep} (Warta, 2007). Figure 3.10 shows that with further tuning of the existing actuator array including increasing the reactant supply to 10 LPM to each chamber, the performance and repeatability of the combustion are significantly improved. These improvements are evident by comparing the peak phase-averaged pressures of $p_{r,\text{max}} \approx 3 - 3.4 p_{\text{atm}}$ for $T_{\text{rep}} = 5 - 10$ ms in Figures 3.10a-c with the similar $p_{r,\text{max}}$ in Figures 3.7 and 3.8 for higher T_{rep} of up to 1000 ms. The increased supply flow rates achieve a faster refill time of the combustor with fresh reactants increases the baseline pressure from $1 p_{\text{atm}}$ to about $1.25 p_{\text{atm}}$, which is small compared to the transient pressure build-up from the combustion.

Earlier investigations of COMPACT actuators did not investigate the variation in the combustion pressure following the onset of repetitive actuation. An example of start-up transients of a sequence of actuation pulses is obtained from a set of instantaneous pressure measurements for 30 and 50 pulses repeated at $T_{\text{rep}} = 10$ and 6.67 ms (Figures 3.11a and b only show the first 10 and 15 pulses, respectively). These data show that

when the actuator is operating at $T_{\text{rep}} = 10$ ms (Figure 3.11a), the instantaneous pulsed combustion process is similar for the entire sequence of pulses following the onset of the first ignition trigger as is evidenced by the similarity of the pressure pulses. However, when T_{rep} is reduced to 6.67 ms (Figure 3.11b), the first combustion pulse has a higher pressure peak than subsequent pulses due to the ignition of fresh reactants. The peak pressures of the subsequent (up to the fifth) pulses are lower, but increase and appear to approach the quasi-steady values of the phase-averaged measurements in Figure 3.10b following start-up flow and thermal transients likely due to the refilling and combustion processes, respectively. Although Figures 3.11a and b only show a relatively small number of pulses, instantaneous data show that the actuation pulses are repeated consistently without misfiring, and therefore can be repeated in multiple bursts.

Following the bench top characterization, the pulsed jet actuators were operated in the present experiments (§IV-VII) at $T_{\text{rep}}/T_{\text{conv}} \geq 0.285$ with typical equivalence ratios of 0.6–0.8 and a total flow rate of reactants into each chamber of 6–8 LPM. This performance is similar to the data shown in Figure 3.10 above.

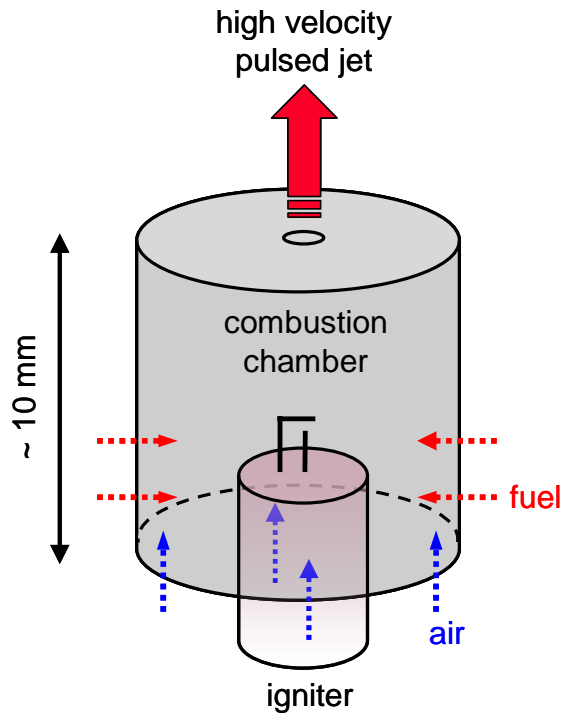


Figure 3.1: Basic concept of combustion-powered (COMPACT) actuator.

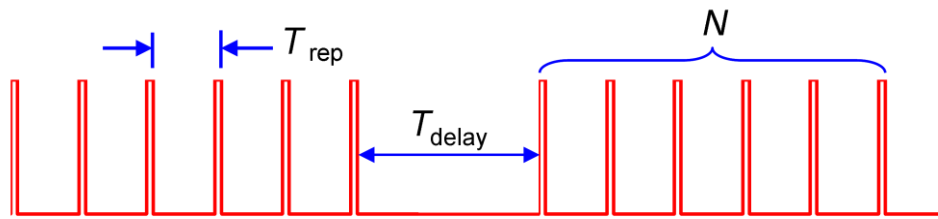


Figure 3.2: Actuation timing of a burst of N pulses separated by T_{rep} , followed by a second burst delayed by T_{delay} .

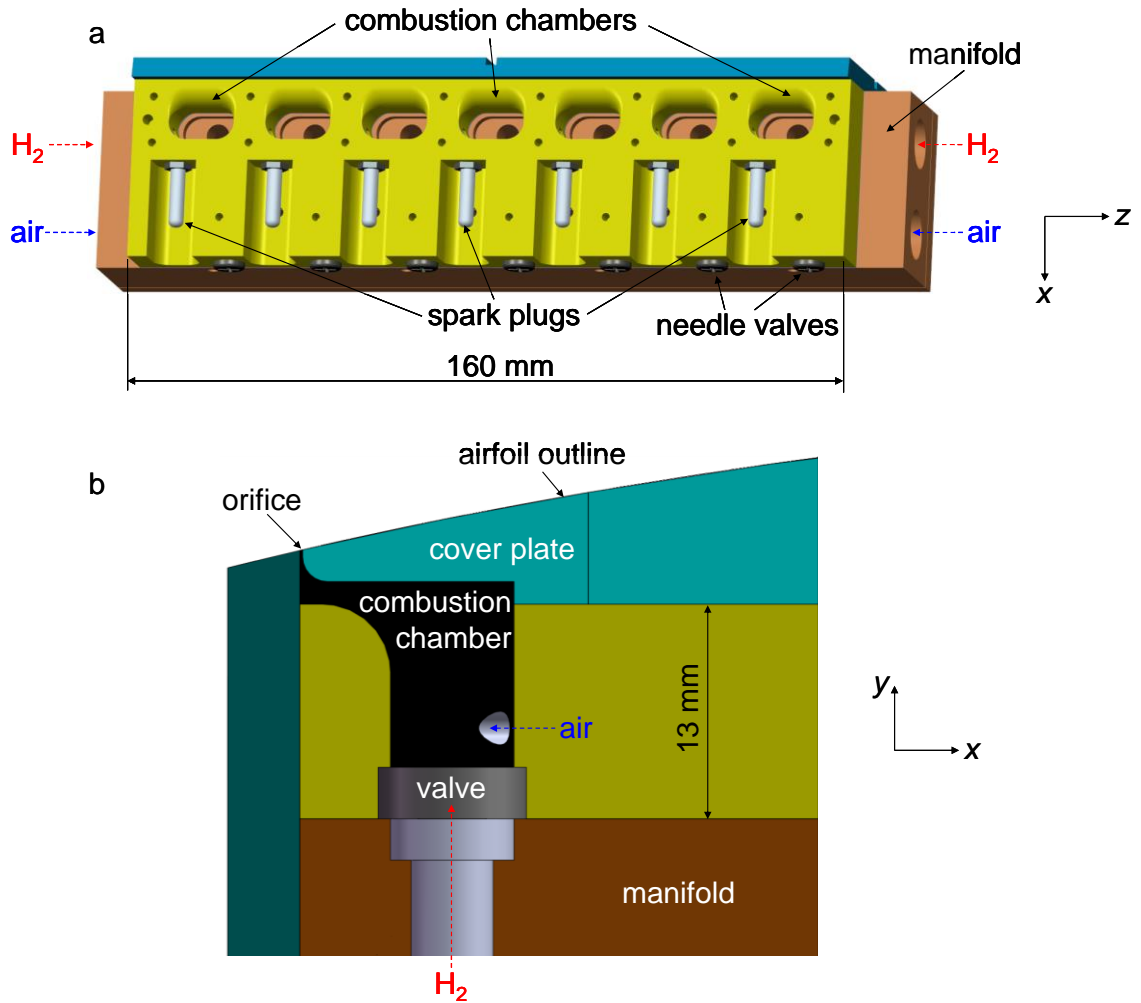


Figure 3.3: (a) CAD model of actuator module showing internal structure of the seven $O(1 \text{ cm}^3)$ combustion chambers, spark plugs and needle valves, and the manifold for the reactants, and (b) Cross-section view inside a chamber and its orifice showing reactant flow paths, and other manifold components. The airfoil coordinates are included.

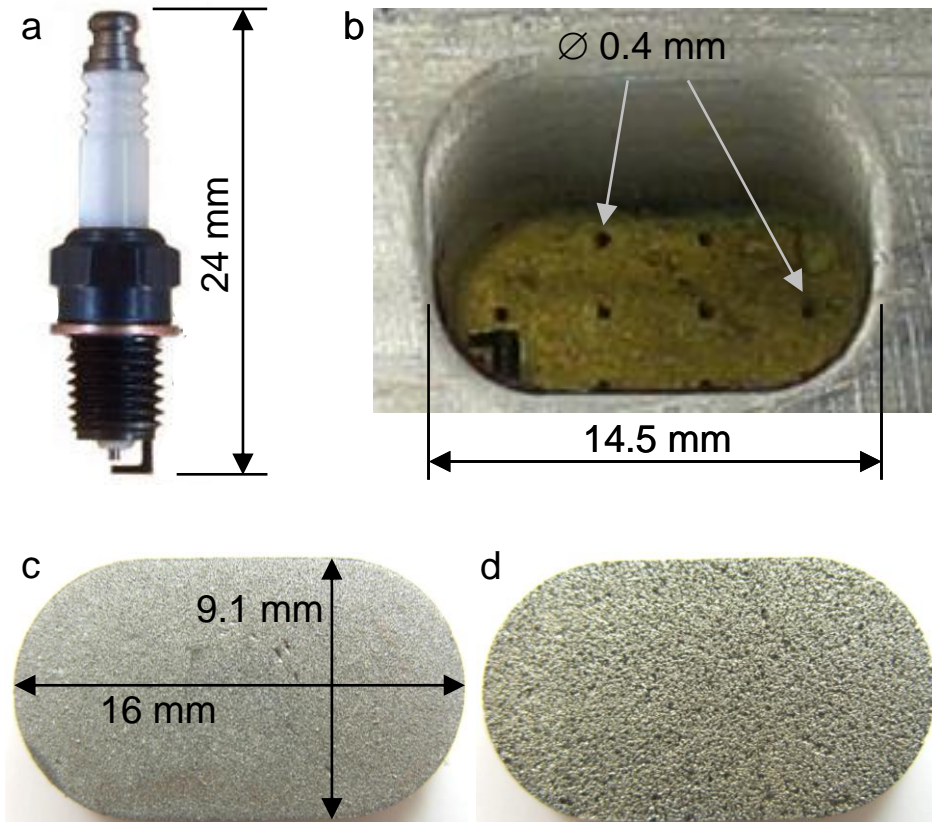


Figure 3.4: Photos of (a) Rimfire V1 Viper spark plug, and (b) Combustion chamber equipped with 0.1 mm thick brass shim insert with 7 laser cut holes. Two 6.35 mm thick 316SS fluidic valves wire-EDM from porous media grades; 2 (c) and 10 (d).



Figure 3.5: Particulate deposited on porous media following continual use in combustion chamber (a – c). These fluidic valves are identical in size with valves in Figure 3.4c & d.

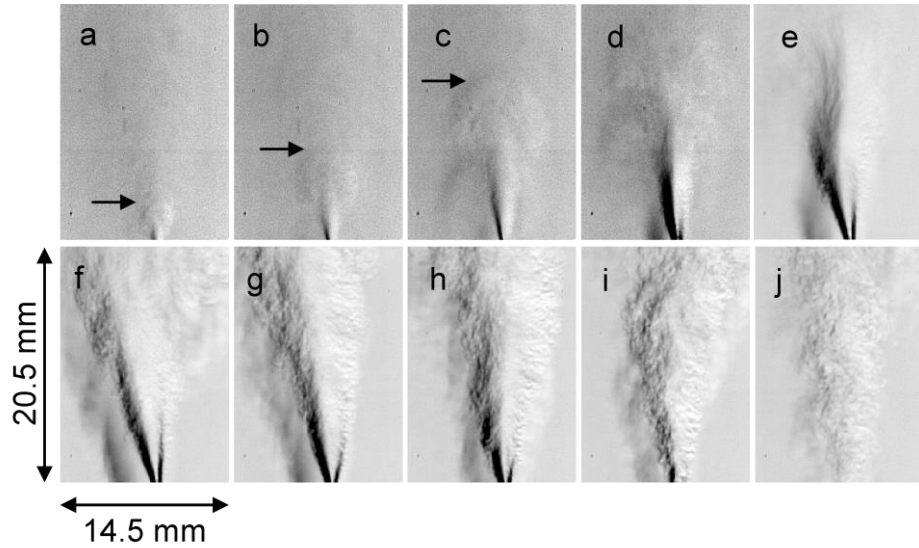


Figure 3.6: Phase-locked schlieren images of the pulsed jet emanating from the center actuator of the array following actuation (at $t = 0$): 0.49 (a), 0.61 (b), 0.73 (c), 0.80 (d), 0.85 (e), 0.98 (f), 1.22 (g), 1.46 (h), 1.71 (i), and 2.15 (j) ms. These phases correspond to the marked timings on the chamber pressure time traces in Figure 3.7

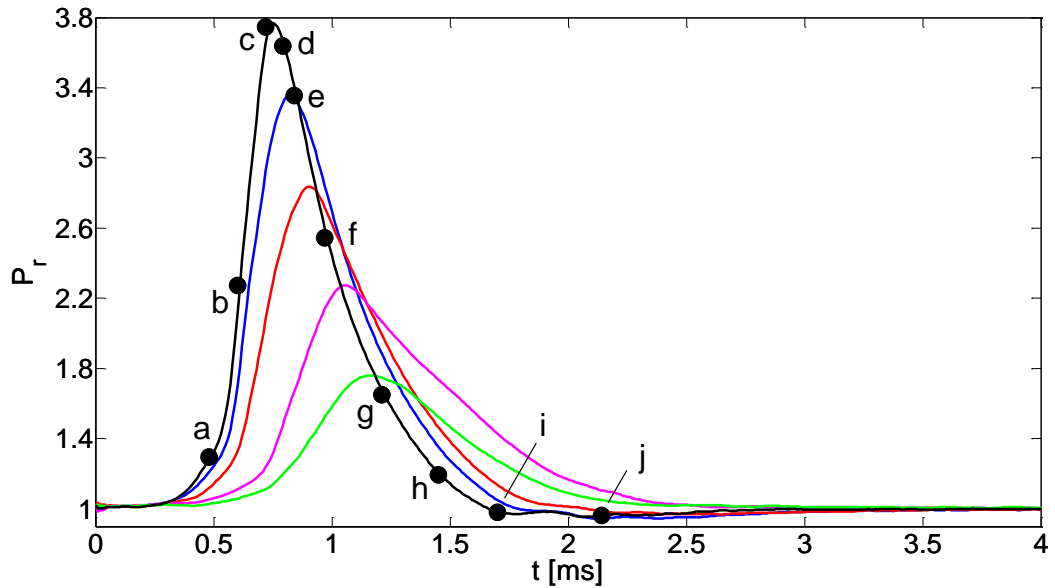


Figure 3.7: Phase-averaged, pressure-time history of the center combustor following the single pulsed jet triggered at $t = 0$ (—). The pulse is repeated with $T_{\text{rep}} = 200$ (—), 100 (—), 50 (—) and 33.3 (—) ms. The corresponding timings of the jet in Figures 3.6 are labeled (a) - (j) and marked (●).

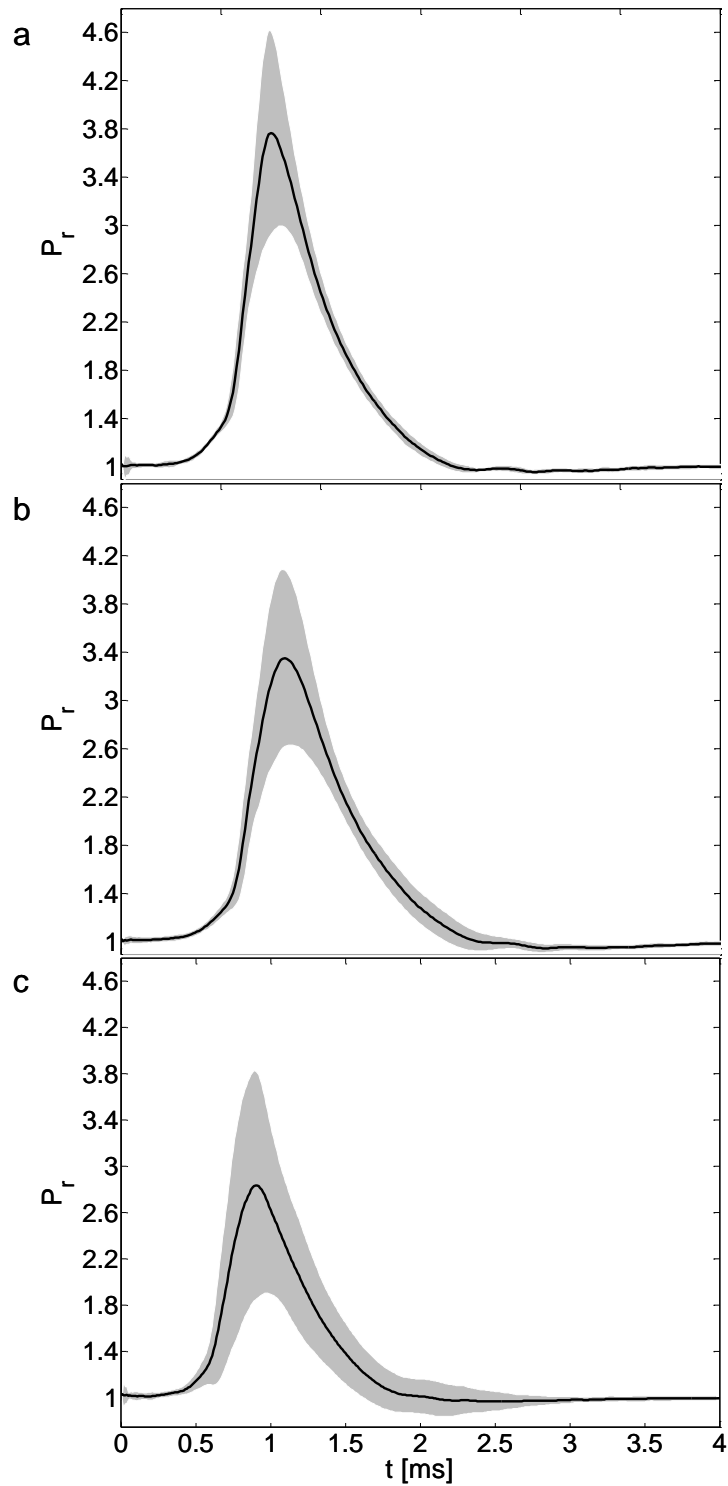


Figure 3.8: Phase-averaged pressure traces (–) and corresponding ± 1 standard deviation band (shaded) of center chamber in the array for repeated actuation: $T_{\text{rep}} = 1000$ (a), 200 (b), and 100 (c) ms. The combustion is stoichiometric with 0.36 LPM of reactants.

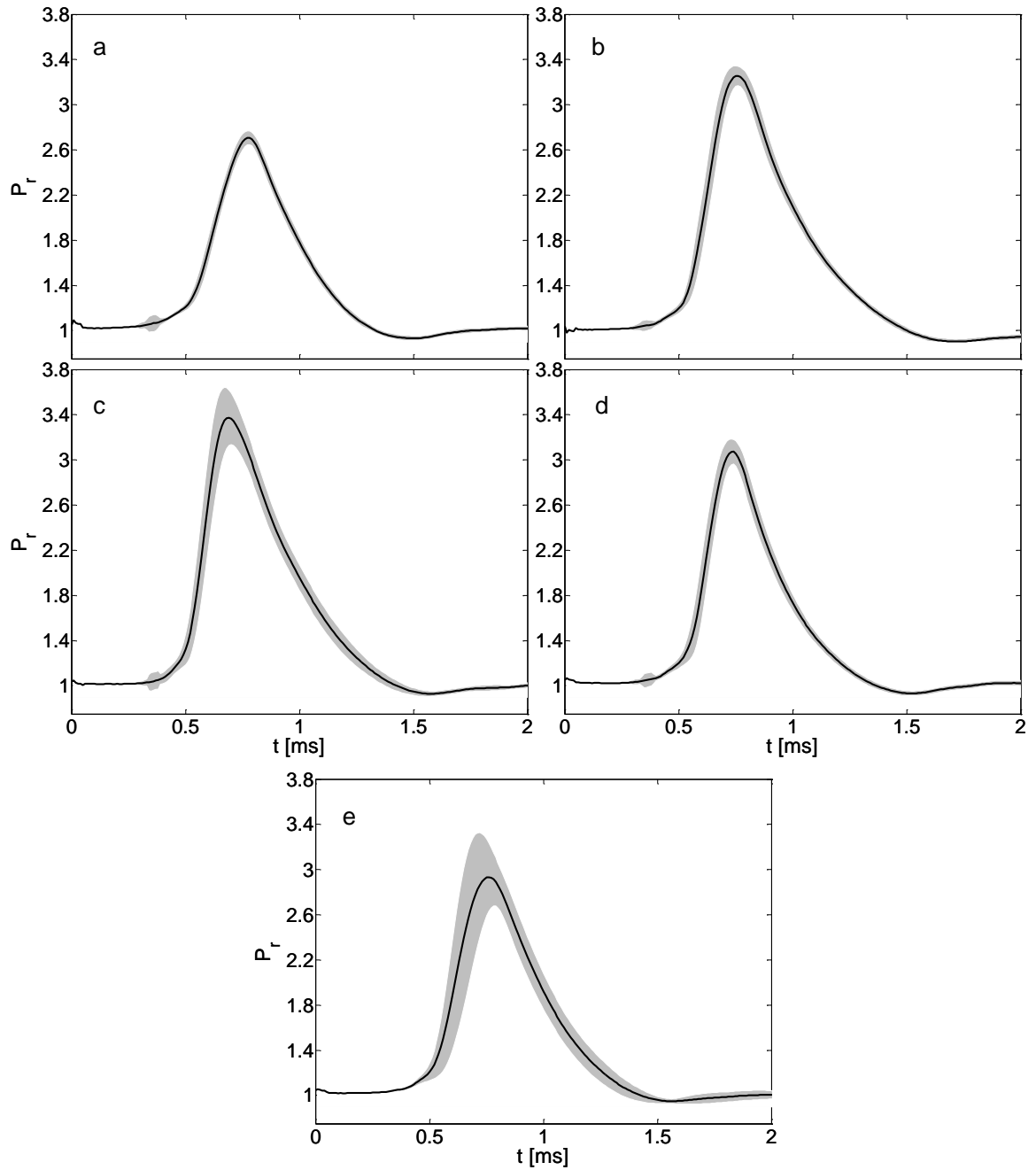


Figure 3.9: Phase-averaged pressure traces (–) and corresponding ± 1 standard deviation band (shaded) inside the 1st (a), 3rd (b), 5th (c), and 7th (d) actuators in the array for repeated actuation ($T_{\text{rep}} = 200$ ms), and the corresponding mean (–) and standard deviation across all seven actuators (e). The combustion equivalence ratio is 0.6 with 3.5 LPM of reactants.

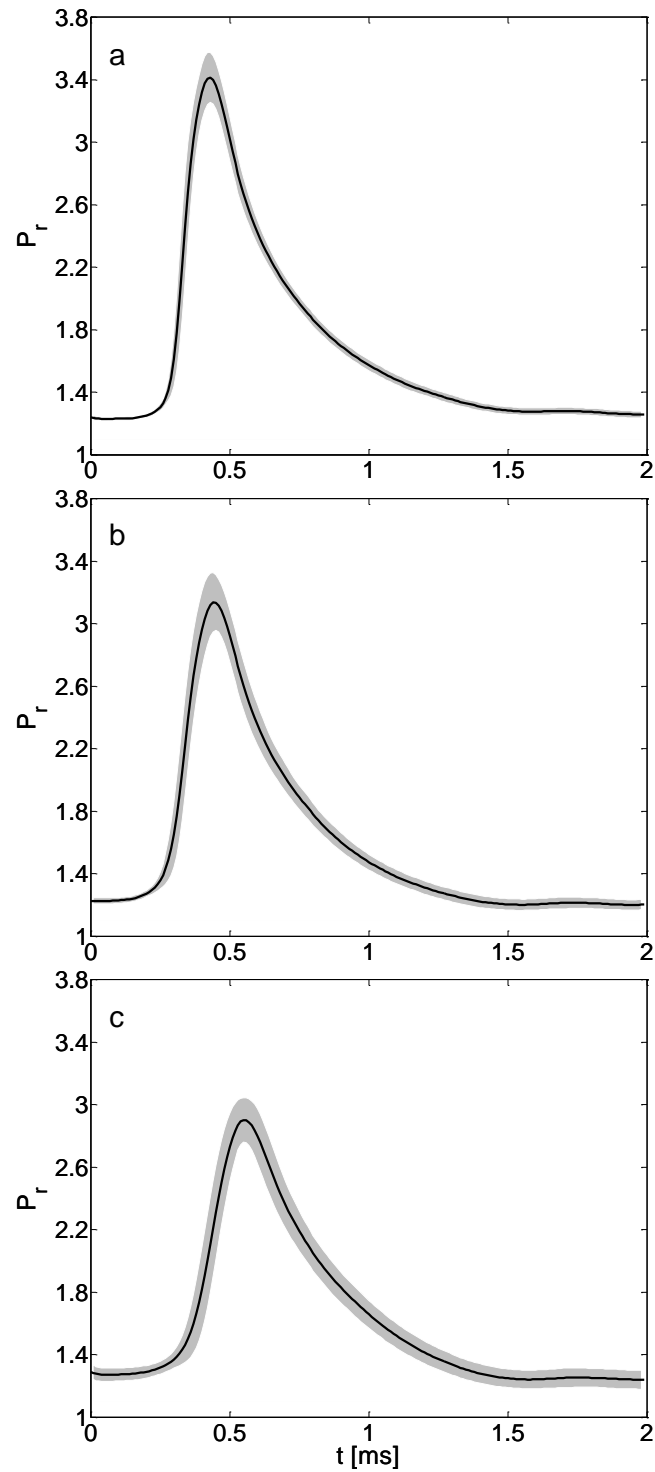


Figure 3.10: Phase-averaged pressure traces (–) and the corresponding ± 1 standard deviation band (shaded) inside center actuator for $T_{\text{rep}} = 10$ (a), 6.67 (b) and 5 (c) ms. The equivalence ratio is 0.6 with 10 LPM of reactants.

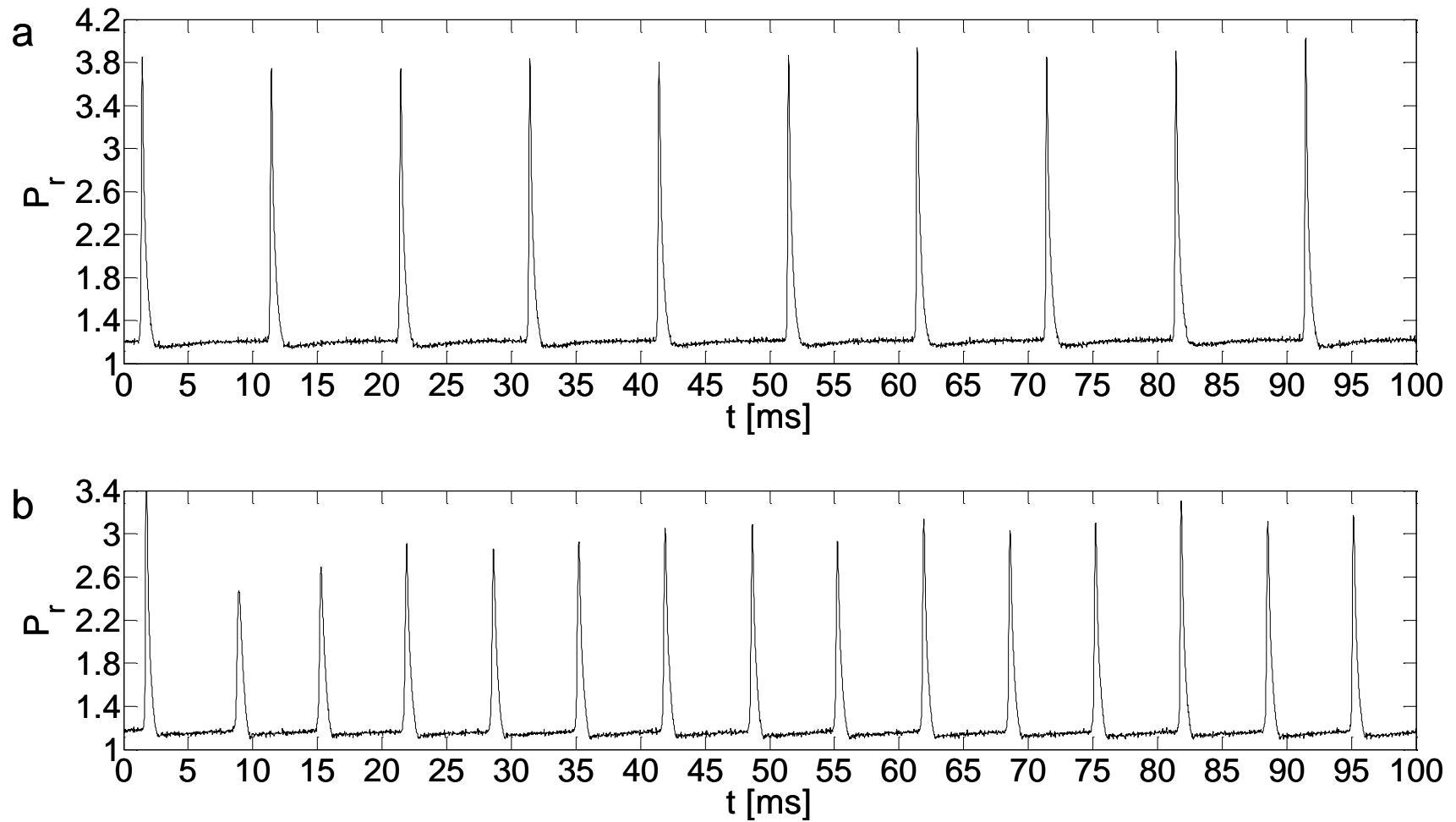


Figure 3.11: Examples of the instantaneous pressure start-up transients inside the center actuator following trigger at $t = 0$ and the pulses are repeated with $T_{\text{rep}} = 10$ (a), and 6.67 (b) ms under identical conditions in Figure 3.10.

CHAPTER IV

TRANSITORY PULSED ATTACHMENT

This section explores the dynamics of the nominally 2-D transient interactions between single pulsed actuation and the separated cross flow over a stalled NACA 4415 airfoil at $\alpha = 19^\circ$ and $Re_c = 5.7 \times 10^5$. The actuation is manifested as a single, brief jet effected simultaneously across an array of seven actuators that spans $S_{act} \approx 0.35c$ (§II) and its collinear orifices are aligned lengthwise with the airfoil span. As noted in §II, two streamwise fences are placed at each spanwise edge of the actuator array (i.e., $S_{fence} = S_{act}$) to confine the actuation effects to this nominally 2-D segment of the flow over the airfoil. The global effects on the airfoil of the single pulsed jet and the corresponding flow interactions near the actuators are first examined followed by investigations of the mechanism that leads to attachment.

4.1. Transitory Effects of Single Pulse Actuation

4.1.1. The Base Flow

Investigations of the baseline characteristics of the NACA 4415 airfoil are extensively documented in the literature (e.g., Graham et al., 1945; and Mukherjee and Gopalarathnam, 2006, *cf.*, §I) therefore only a few base flow results are presented for the current airfoil model configuration. The mid-span lift coefficient computed by integrating the time-averaged static pressure distribution (using trapezoidal formulation) at $z = 0$ in the absence of actuation,

$$C_L = \int_{\bar{x}_{LE}}^{\bar{x}_{TE}} C_p d(\bar{x}/c) \approx \frac{1}{2c} \sum_i \{ [C_p(\bar{x}_i) + C_p(\bar{x}_{i+1})] \cdot (\bar{x}_{i+1} - \bar{x}_i) \}$$

where $C_P = \frac{P - P_\infty}{0.5\rho U_\infty^2}$ and \bar{x} is the laboratory streamwise coordinate at each port location i , is shown in Figure 4.1a for $0 \leq \alpha \leq 24^\circ$. The locations of the pressure ports on the airfoil surface are tabulated in Table A.1 for $\alpha = 0^\circ$. Note that the pressure ports around the leading edge are closely-spaced. The monotonic increase in lift with the static pitch angle is nearly linear up to $\alpha \approx 12.5^\circ$, and then $dC_L/d\alpha$ diminishes and eventually changes sign when α exceeds 16.5° as the airfoil section begins to stall. The gradual stall in Figure 4.1a is characteristic of thick airfoils as described in §II.1.1. Note that the current stall angle of 16.5° and the corresponding $C_L = 1.69$ are somewhat higher than $\alpha \approx 12^\circ$ and $C_L = 1.4$ as reported by Abbott and von Doenhoff (1959) for the same airfoil having twice the aspect ratio (i.e., $S/c \approx 0.67$) at $Re_c = 3.0 \times 10^6$. This increased stall angle is likely due to increasing flow non-uniformities across the span for the higher aspect ratio model.

The pressure distributions for $\alpha = 14^\circ$, 16.5° and 19° are shown in Figure 4.1b corresponding to $C_L = 1.63$, 1.69 and 1.52 , respectively (there is no pressure port at the trailing edge where $x/c = 1$). The increase in the suction pressure from $\alpha = 14^\circ$ to $\alpha = 16.5^\circ$ near the leading edge for $x/c < 0.1$ (e.g., $C_{p,\min} \approx -3.76$ at $\alpha = 14^\circ$ to $C_{p,\min} \approx -4.4$ at $\alpha = 16.5^\circ$) explains the increase in C_L . On the other hand, the alternating differences in C_p further downstream (i.e., $C_{p,14^\circ} < C_{p,16.5^\circ}$ for $0.2 < x/c < 0.62$ and $C_{p,14^\circ} > C_{p,16.5^\circ}$ for $x/c > 0.62$) between these two angles represent flow changes that correspond to trailing edge separation as expected of this moderately thick airfoil. These differences in C_p contribute negligibly to the differences in C_L . More importantly, the small increase in suction pressure at $\alpha = 19^\circ$ (e.g., $C_{p,\min} \approx -4.65$ in Figure 4.1b) while C_L

in Figure 4.1b decreases confirms that this airfoil does not experience leading edge separation. The increase in the boundary layer thickness and the corresponding slower flow over the airfoil that are commonly associated with the increasing angle of attack are manifested by the increased adverse pressure gradient $dC_p/dx < 0$ in Figure 4.1b when α is increased from 14° to 19° . The nearly invariant pressure gradient ($dC_p/dx \approx 0$) for $x/c > 0.3$ at $\alpha = 19^\circ$ indicates separation and flow recirculation downstream of the maximum thickness of the airfoil. In the present flow control investigations in §IV and V, the static airfoil remains at the post-stall pitch angle of $\alpha = 19^\circ$.

The streamwise location of the actuator array orifices on the airfoil in Figure 4.1b ($x/c \approx 0.15$, marked by a green arrow) remains unchanged throughout the present investigations, and at $\alpha = 19^\circ$, the pulsed jet actuators are well within the region dominated by an adverse pressure gradient. As discussed in §II, the current fences are expected to have negligible effects on the flow over the center segment of the airfoil. For the present aspect ratio of $S_{fence}/c \approx 0.35$, the stalled base flow over the airfoil between the fences at $\alpha = 19^\circ$ is nominally 2-D as inferred from surface oil visualizations in Figure 4.2. The two images are obtained about 10 minutes apart and show that the progression of the separation line (marked by arrow in Figure 4.2a) is reasonably uniform across S_{fence} although there are some spanwise variations in the concentrations of the dye streaks owing to the local accumulation of oil that is likely somewhat affected by the use of slight excess amounts of oil. In Figure 4.2b, it can be argued that the separation is reasonably symmetric about mid-span as evident in the oil concentrations where the variations are limited to only local swirls near the fences (marked by arrows) similar to the observations of Zanin et al. (2008). Note that the downstream edge of the oil

accumulation in Figure 4.2b that represents the separation line is located downstream of the actuator array that is marked by the red dash line.

4.1.2. Global Characteristics of the Actuated Flow

A single, momentary and nominally 2-D actuation pulse that spans the entire distance between the fences and having a characteristic time scale that is approximately $0.05T_{\text{conv}}$ has a profound transitory effect on the flow field about the stalled airfoil. This is demonstrated in a sequence of contour plots (Figure 4.3) of the spanwise vorticity concentrations, ω_z , that are phase-averaged from 200 realizations of phase-locked (to the actuation trigger) PIV measurements in the center plane $z = 0$. Each image shown in Figure 4.3 is a composite of four partially-overlapping measurement domains with resolutions of 239 - 244 $\mu\text{m}/\text{pixel}$ that are recorded at an increasing time delay t/T_{conv} relative to the trigger.

As shown in Figure 4.3a, immediately following actuation at $t = 0$ and before there are any measurable changes in the flow, the streamwise onset of separation at $x/c \approx 0.3$ is downstream of the actuator orifice which is in agreement with the $dC_p/dx \approx 0$ in Figure 4.1b. The first and perhaps one of the more prominent effects of the actuation is the apparent “severing” of the separating shear layer by the pulsed jet. This effect is first observed within the domain $0.45 < x/c < 0.6$ at $t/T_{\text{conv}} = 0.32$ (Figure 4.3b). By $t/T_{\text{conv}} = 0.48$ (Figure 4.3c) there is a clear discontinuity in the shear layer at $x/c \approx 0.5$. This discontinuity becomes more noticeable in Figure 4.3d ($t/T_{\text{conv}} = 0.64$) as the separating layer is completely severed from the upstream flow resulting in two distinct flow regimes: an attached upstream boundary layer ($x/c < 0.6$) and a recirculation domain downstream. As was discussed by Brzozowski and Glezer (2006), the severed clockwise

(CW) vorticity concentration within the recirculation domain begins to roll up during this time and by $t/T_{\text{conv}} = 0.8$ (Figure 4.3e), the rolled up vortex is advected towards the trailing edge and its cross stream extent is commensurate with the cross stream width of the wake as it continues to move downstream (e.g., at $t/T_{\text{conv}} = 0.96$ and 1.12 in Figures 4.3f and g, respectively). The strength of this CW vortex is significantly reduced by $t/T_{\text{conv}} = 1.28$ as the vortex is almost completely downstream of the PIV field of view (Figure 4.3h). During this time and for $1.44 \leq t/T_{\text{conv}} \leq 1.6$ in Figures 4.3i and j, the downstream edge of the nominally-attached upstream boundary layer migrates towards the trailing edge, and effectively reduces the extent of the stalled flow as the separation point moves to $x/c \approx 0.6$ (compared to $x/c \approx 0.3$ in the absence of actuation). Figure 4.3k shows that the flow over the airfoil is vectored towards ($\Delta v/U_\infty > 0$) the surface (e.g., by as much as 20% at $x/c \approx 1.15$ compared to the flow in the absence of actuation in Figure 4.2a). Similarly, the cross stream extent of the near wake in Figure 4.3k estimated as the distance between the cross stream edges above and below the CW and CCW vorticity layers (where $\omega \approx 0$), respectively, is reduced by about 14% compared to the base flow, indicating some mitigation of the adverse effects of separation. The attached vorticity layer begins to lift off from the upper (suction) surface by $t/T_{\text{conv}} = 1.96$ (Figure 4.3l) and the flow slowly relaxes to the base stalled state as shown in Figures 4.3m and n at $t/T_{\text{conv}} = 3.2$ and 4.8 , respectively. By $t/T_{\text{conv}} = 6.4$ (Figure 4.3o), the flow is reasonably similar to the base flow (Figure 4.3a).

To further characterize the transitory flow response to pulsed jet actuation, instantaneous surface static pressure measurements are obtained phase-locked to the actuation waveform at five locations on the airfoil (Figure 4.4a). These are shown in

Figure 4.4b as time traces of the phase-averaged pressure increment ΔC_P relative to baseline for $t \leq 40T_{\text{conv}}$ with the locations of the pressure ports marked in an inset while the data are plotted using an expanded time scale (i.e., $t \leq 4T_{\text{conv}}$) in Figure 4.4c to show details at short times following the onset of actuation. The data in Figure 4.4b first demonstrate a significant disparity between the time scales that are associated with onset of the actuation and flow attachment effects, and their subsequent decay following a local suction pressure ($\Delta C_P < 0$) extremum. For example, the trace measured at $x/c = 0$ (●) clearly show that the rise time of the suction is nominally $2-4T_{\text{conv}}$ while the relaxation time is significantly longer or nominally $20T_{\text{conv}}$, indicating the significantly different flow mechanisms that are associated with each, as will be discussed in further detail in §IV.2. It is also important to note that most of the transitory changes in pressure are measured on the suction surface as compared to the relatively small changes in the time trace of ΔC_P on the pressure surface (●). The largest increase in suction of $\Delta C_P \approx -0.45$ is measured at the leading edge (Figure 4.4b), indicating a local increase in flow speed of the boundary layer flow over the leading edge even though the single pulsed actuation is generated further downstream. Similarly, as the boundary layer flow continues to grow further downstream and attaches to the upper surface of the airfoil due to the actuation, there is also a momentary increase in the local *suction* pressure (e.g., at $x/c = 0.24$ (●), 0.45 (●), 0.68 (●) in Figure 4.4b) and velocity (as demonstrated by the PIV data in Figure 4.12). The increased suction and velocity diminish in magnitude toward the trailing edge, indicating weaker flow attachment and the effects of the inherently high adverse pressure gradient. In conjunction with this, the ensuing gradual decay of the suction pressure following these peaks at each location appears to first occur and reach $\Delta C_P = 0$ for the

downstream ports. This suggests that the return to baseline upon the termination of actuation begins from the trailing edge, which can be inferred from the flow field as the flow separates in Figures 4.3m-o.

As discussed in connection with the attachment mechanism in §IV.2, the measured peak increments in suction appear increasingly delayed at the ports farther upstream from the trailing edge, and some of the pertinent flow dynamics immediately following actuation ($t \leq 4T_{\text{conv}}$) are examined closely in Figure 4.4c. The pressure traces measured at $x/c \approx 0.45$ (●) and 0.68 (●) are characterized by significant positive pressure peaks ($\Delta C_p \approx 0.4$) at $t/T_{\text{conv}} \approx 0.52$ and 0.92, respectively. These suggest that prior to the increased velocity of the attachment process; there is a reduction in the local velocity near the surface. At these two instances, the shed CW vortex in Figures 4.3c and f, is advected over these two locations and induces locally, flow in the upstream (negative x) direction over the surface that is associated with the momentary increase in pressure (or blockage effect). The pressure traces for the sensors located downstream of the actuator in Figure 4.4c each show a local increase in pressure that propagates downstream due to the CW vortex. For example at $x/c = 0.45$, the maximum pressure increase of $\Delta C_p \approx 0.4$ is evident at $t/T_{\text{conv}} = 0.52$ in Figure 4.4c while there are negligible effects (i.e., $\Delta C_p \approx 0$) further downstream at $x/c = 0.68$. Conversely, at $t/T_{\text{conv}} = 0.92$, the measured suction peak ($\Delta C_p \approx -0.3$) of the boundary layer at $x/c = 0.45$ corresponds to an increase in pressure at $x/c = 0.68$ as the CW vortex passes, increasing the adverse pressure gradient. In connection with the phase-averaged flow field shown in Figure 4.3, the progression and the opposite pressure gradients in Figures 4.4b and c of the attaching boundary layer and severed vorticity concentration suggest that the dominant flow dynamics of the

actuation are pressure-driven. More importantly, the increased magnitude of the transitory adverse pressure gradient with x in Figure 4.4c indicates that the flow structures over the airfoil induced by the pulsed actuation would act to amplify the boundary layer separation and therefore prevent attachment. However, the attachment and the streamwise growth of the boundary layer are apparent in Figure 4.3 even in the presence of this adverse pressure gradient. These contrasting effects are further discussed in §IV.2 in connection with the mechanism that leads to the pressure-driven flow attachment.

4.1.3. Near Wake Measurements

Contour plots of distributions of phase-averaged concentrations of spanwise vorticity and cross stream distributions of velocity vectors measured in the center plane of the near wake of the airfoil ($-0.05 < x/c < 0.5$ and $-0.1 < y/c < 0.6$ relative to the trailing edge) that complement the data in Figure 4.3 are shown in Figure 4.5. Each image in Figure 4.5 is stitched from data in two partially overlapping, independent PIV views that are averaged from over 200 instantaneous realizations and are captured at a given delay t/T_{conv} following the single-pulse actuation. The image at $t = 0$ (Figure 4.5a) with the large recirculation domain of the base flow above the airfoil corresponds to the onset of actuation waveform. In addition to the shedding of the severed CW vortex, the brief interruption of the flow over the airfoil also induces a discontinuity in the CCW vorticity layer that is shed from the pressure (bottom) surface of the airfoil as shown in Figures 4.5b-c, approximately $0.32 - 0.48T_{\text{conv}}$ following actuation. These data show the formation of a CCW vortex that is out of the field of view in Figure 4.5d at $t/T_{\text{conv}} \leq 0.8$, as well as the roll-up of an upstream CW that is clearly visible in Figures 4.5e-g ($0.96 \leq t/T_{\text{conv}} \leq 1.28$), and would indicate a momentary increase in circulation of the

airfoil as concentrations of the CCW vorticity bounded by the airfoil are reduced. These transitory flow details that occur near the trailing edge concomitantly with the severed domain in the separating shear layer on the airfoil are not captured by the lower resolution data of Figure 4.3.

The shedding of the CW vorticity concentration within the recirculation domain that forms the advected large-scale CW vortex is evident in Figures 4.5e-i for $0.96 \leq t/T_{\text{conv}} \leq 1.6$ and is associated with the transitory increase in cross stream width of the wake. As the vortex continues to be advected downstream in Figures 4.5h-k, the cross stream width of the wake decreases rapidly and the collapse leads to a slight downward deflection of the CCW vorticity layer from the bottom surface corresponding to the attachment in Figures 4.3j-l. By $t/T_{\text{conv}} = 2.4$ (not shown), the width of the wake decreases (narrows) by $0.2c$ compared to the base flow as also observed in the flow field downstream of the trailing edge in Figure 4.3. Following the momentary collapse (Figure 4.5k, $t/T_{\text{conv}} = 2.72$) the wake begins to open up along with the relaxation of the flow in Figures 4.5m-o, and eventually broadens as the flow separates again on the suction surface of the airfoil and returns to the stalled state by $11.04T_{\text{conv}}$ (Figure 4.5o).

Corresponding profiles of the phase-averaged u , v , and ω in the near wake at $x \approx 1.25c$ are presented in Figures 4.6a-c, respectively, at select time instances $t/T_{\text{conv}} = 0$ (—), 0.48 (—), 0.96 (—), 1.6 (—), and 2.72 (—) following the actuation. The initial (minor) effects on the CCW vorticity by the pulsed jet at $t/T_{\text{conv}} = 0.48$ as measured for the instance in Figure 4.5c are limited to the cross stream velocity, v , and the spanwise vorticity, ω , in Figure 4.6 (—). On the other hand, there are negligible alterations to the streamwise velocity, u . The most noticeable changes relative to the base flow (dashed —)

that are attributed only to the shedding of the CCW vortex ($t/T_{\text{conv}} \leq 0.48$) are in the increase in v confined to a narrow ($-0.1 < y/c < 0.1$) region in the wake (Figure 4.6b). Comparison of this small change in the flow with the large recirculation domain on the suction surface indicates that there are minimal contributions to the global attachment over the suction surface ($y/c < 0.3$) by this CCW vortex. Figure 4.6 shows that v is more sensitive to the roll-up of vorticity at $t/T_{\text{conv}} = 0.96$ (—) that leads to the shedding of the CW vortex as compared with u and ω . However, the passing of the CW vortex through the wake and the reduced shedding of CW concentrations over the suction surface clearly alters the profiles in Figure 4.6 (— and — at $t/T_{\text{conv}} = 1.6$ and 2.72 , respectively). The velocity components, u and v , and the vorticity, ω , at $t/T_{\text{conv}} = 2.72$ indicate a significantly narrower wake, the vectoring of flow towards the airfoil ($v < 0$), and the transport of CW vorticity toward the surface of the airfoil as is evidenced by flow attachment in Figures 4.3 and 4.5.

The global aerodynamic functionality of the static airfoil is quantified by considering the time-evolution of the phase-averaged cross stream distributions of the vorticity flux ($\omega_z \cdot u$) into the wake. The CW and CCW fluxes from the suction and pressure surfaces, respectively, are shown in a contour plot (Figure 4.7) as a function of y/c and t/T_{conv} at $0.25c$ downstream of the trailing edge. Since the direction of u can change across both the CW and CCW vorticity layers, it is necessary to distinguish the fluxes of these vorticity concentrations. The “wake center”, $y_{\text{wake}}(t)$ is estimated as the y elevation that marks the boundary between these two vorticity layers for which $\omega \approx 0$ (*cf.*, Figures 4.5). The cross stream elevation of $y_{\text{wake}}(t; x/c = 1.25)$ is marked in Figure 4.7 as a gray dash line, and the CW and CCW fluxes are plotted above and below y_{wake} , respectively. There

are two “weak” and two relatively “strong” flux layers in Figure 4.7 that straddle $y = y_{\text{wake}}$. These weaker (lightly-colored) layers correspond to cross stream contributions of CW and CCW flux where the flow (and flux) direction reverses (i.e., $u < 0$). The flux map highlights the time scales of the passage of the starting CCW and the CW vortices at the measurement location of Figure 4.6.

The cross stream distributions of the vorticity flux in the presence of actuation exhibit three notable features. To begin with, the (single) actuation pulse clearly affects or modulates the vorticity fluxes from *both* the suction and pressure surfaces of the airfoil. The present data also show three distinct disparate time scales (marked in shaded colors on the time axis of Figure 4.7) that are demonstrated by the temporal and spatial (cross stream) evolution of the vorticity flux (*cf.*, the pressure traces in Figure 4.4): the duration of (CW) vorticity shedding from the severing and the following flow attachment of 1 to $1.5T_{\text{conv}}$ are shaded in orange and green colors, respectively, and the longer time of over $9T_{\text{conv}}$ for the relaxation is represented in gray. Finally, the shedding of a CCW vortex (marked as red dashed oval) from the pressure surface into the wake that is followed by the shedding of a larger CW vortex (marked by dashed blue oval) on the suction surface is accompanied by the widening of the wake.

The flow behavior during the transitory attachment ($1.2 < t/T_{\text{conv}} < 2.5$) as marked on the time axis is manifested by concurrent narrowing of the wake (as shown in Figures 4.3 and 4.5), and the reduction in the flux of CW vorticity (red). Furthermore, the flux of CCW vorticity (blue) is deflected downward slightly during this time as an indication of a transitory increase in lift (and circulation) over the airfoil. Although the ensuing relaxation $t/T_{\text{conv}} > 2.5$ is slower than the attachment and less dramatic, and does not

involve shedding of large-scale vortical structures, the cross stream extent of the CW vorticity concentrations is nearly invariant ($\Delta y \approx 0.2c$) but is gradually displaced in y over $10T_{\text{conv}}$ as the width of the wake increases.

The time rate of change of the airfoil's circulation in the center plane is computed by integrating the streamwise flux of vorticity across the wake, $d\Gamma/dt = - \int_{y_0}^{y_1} u \cdot \omega_z dy$ where $\omega_z \approx 0$ at the limits of integration, y_0 and y_1 , which are the lower and upper edges of the PIV domain, respectively (the cross stream variation of the integrand is shown schematically in the inset to the left in Figure 4.8). Figure 4.8a shows the contributions to the normalized time rate of change of circulation, $(d\Gamma/dt)^* = \frac{d\Gamma/dt}{cU_\infty}$, from the top (●) and bottom (●) airfoil surfaces that are distinguished and arranged by the “wake center”, y_{wake} , such that

$$d\Gamma/dt_{\text{top}} = - \int_{y_{\text{wake}}}^{y_1} u \omega_z dy \quad \text{and} \quad d\Gamma/dt_{\text{bottom}} = - \int_{y_0}^{y_{\text{wake}}} u \omega_z dy,$$

and their total sum (●)

$$d\Gamma/dt_{\text{total}} = - \int_{y_0}^{y_1} u \omega_z dy = d\Gamma/dt_{\text{bottom}} + d\Gamma/dt_{\text{top}},$$

while the time-dependent change in circulation about the airfoil relative to baseline, $|\Delta\Gamma(t)| = \Delta\Gamma(t)/\Gamma_o$, following actuation is shown in Figure 4.8b. The change in circulation relative to the unforced flow is given by $\Delta\Gamma(t) = \Gamma(t) - \Gamma_o = \int_{t_o}^t \frac{d\Gamma}{dt} dt$, where $t_o = 0$ and $\Gamma_o = -\rho c U_\infty C_{L,o} = -5.30 \text{ m}^2/\text{s}$. To minimize integration errors in $d\Gamma/dt$ due to differences in the thickness of the CCW and CW vorticity layers, the spatial integration of the vorticity flux is computed at approximately $0.3c$ from the trailing edge where

$\int_{t_0}^{T^*} \frac{d\Gamma}{dt} dt \approx 0$, which is satisfied as the flow returns to the unperturbed base state by T^* .

In the present investigation for the static airfoil, the phase-locked PIV data are obtained until $T^* = 11.85T_{\text{conv}}$, which is judged to be sufficiently long following actuation.

In Figure 4.8a, the (integrated) vorticity flux contribution from the bottom surface increases for $0.4T_{\text{conv}} \leq t \leq 0.8T_{\text{conv}}$. Concomitantly, there is also a measured reduction in the CW vorticity flux across the wake, which appears to be a direct effect of the momentary interruption of the shear layer shedding by the pulsed jet. As a result of the shedding of the CCW vorticity and the reduction in CW vorticity flux, the bound circulation on the airfoil in Figure 4.8b increases by $|\Delta\Gamma(t)| \approx 0.03$. The increase in the flux of negative (CW, ●) vorticity from the top surface in Figure 4.8a for $1.3 \leq t/T_{\text{conv}} \leq 1.7$ corresponds to the shedding of the large scale CW vortex (*cf.*, Figure 4.3). More importantly, this momentary increase with a local maximum of $|d\Gamma/dt| \approx -1.15$ at $t/T_{\text{conv}} \approx 1.1$, indicates an accumulation of vorticity concentrations within this shed CW vortex resulting from the actuation-induced roll-up of the shear layer. As the vortex advects through the present survey location in the near wake, this peak in $d\Gamma/dt$ is followed by a rapid decrease with the CW vorticity flux returning to baseline levels $(d\Gamma/dt)^* \approx 0$ by $t/T_{\text{conv}} \approx 1.3$. The continued reduction in $d\Gamma/dt$ from the top surface is associated with the accumulation of CW vorticity concentrations over the airfoil by the increasing streamwise extent of the attaching flow (Figure 4.3h), resulting in the diminution in CW flux into the wake and subsequently the local minimum at $t/T_{\text{conv}} = 1.7$ as the wake begins to narrow (Figure 4.5). For $1.7 < t/T_{\text{conv}} < 2.5$, the flow above the airfoil continues to accumulate CW vorticity albeit decreasing slowly as the CW flux

from the top surface remains suppressed for about $0.9T_{\text{conv}}$, eventually relaxing to its stalled state for $t/T_{\text{conv}} > 2.5$. It is important to note the duration of the global attachment process over the airfoil is approximately $2-3T_{\text{conv}}$ as manifested by the downward deflection of the flow in the wake for $1.3 < t/T_{\text{conv}} < 2.6$ (Figures 4.5 and 4.7). During this time, the thickness of the CCW vorticity layer appears somewhat reduced as the corresponding flux is decreased, resulting in a local peak in $(d\Gamma/dt)^*$ at $t/T_{\text{conv}} \approx 1.8$ (•) in Figure 4.8a. The very slow relaxation process ($\sim 10T_{\text{conv}}$, *cf.*, Figures 4.3 and 4.7) is evident in the near zero increase in the CW vorticity flux.

The shedding of the CW and CCW vorticity concentrations are accompanied by significant changes in the global circulation relative to the baseline flow (Figure 4.8b): a 15% decrease at $t/T_{\text{conv}} \approx 1.1$ followed by a 22% increase at $t/T_{\text{conv}} \approx 1.8$. For $t/T_{\text{conv}} > 1.8$, following the transients associated with the attachment process, the flow slowly relaxes to its stalled state as the circulation gradually returns to the baseline value. This relaxation process exceeds $9T_{\text{conv}}$ compared to $2T_{\text{conv}}$ for the attachment process. Further discussion of the disparity between these transients are given in §V in conjunction with improved attachment by using repetitive actuation.

The alteration of the phase-averaged streamwise and cross stream momentum fluxes across the entire wake that are induced by the actuation are computed relative to the unforced flow $\Delta\mathcal{P}_x = \int \bar{u}^2 d\tilde{y} / (\frac{1}{2}\rho U_0^2 c)$ and $\Delta\mathcal{P}_y = \int \bar{u} \bar{v} d\tilde{y} / (\frac{1}{2}\rho U_0^2 c)$, respectively, and are shown in Figure 4.9. The integrations are described previously in connection with Figures 4.7 and 4.8, and are computed here at the same streamwise location ($x/c = 1.25$) with the same limits of integration, y_0 and y_1 . The changes in these momentum fluxes in the wake account for the largest variations between the baseline and transients in the

attachment and relaxation, and therefore represent an overall contribution to the streamwise and cross stream forces on the airfoil during the brief actuation. The actuation-induced changes in the streamwise momentum flux, $\Delta \mathcal{P}_x$, suggest a momentary increase in drag during the shedding of the CW detached vortex (when there is also a reduction in circulation), followed by a decrease in drag when the separation is momentarily reduced and as the vorticity layer migrates along the suction side of the airfoil. Concomitantly, $\Delta \mathcal{P}_y$ first increases suggesting a decrease in the normal force on the airfoil when there is a decrease in circulation, and then increases indicating a recovery of the normal force on the airfoil when the circulation increases.

4.2. The Interaction of a Momentary Pulsed Jet with the Cross Flow

As discussed in §IV.1, the interaction of the pulsed jet with the cross flow over the stalled airfoil has two, large scale and related effects. First, the severing of the separated shear layer and the formation and advection of a large scale CW vorticity concentration, and second, the attachment of the surface boundary layer that forms upstream of the jet. This section discusses the shear layer severing, the ensuing interaction of the jet starting vortex pair with the cross flow, and the role of these vortices in the attachment of the upstream boundary layer.

4.2.1. Severing of the Shear Layer and Formation of Vortical Structures

The flow field in the vicinity of the jet orifice prior to ($t = 0$), and shortly following actuation ($t = 0.2T_{\text{conv}}$) is depicted using phase-averaged color raster plots of spanwise vorticity concentrations superposed with streamlines in Figures 4.10a and b, respectively. As explained in §II, the streamlines are obtained as path coordinates computed from the phase-averaged PIV velocity data. In Figure 4.10a there is a dividing streamline (dashed

line) that connects the stagnation point “ SO ” on the surface (marked by white circle) where $u^2 + v^2 \approx 0$ (i.e., the stagnation point is located at $x/c \approx 0.3$, which is in agreement with the pressure distribution in Figure 4.1b). As noted in §III, the maximum duration of the actuation jet is about $0.08T_{\text{conv}}$. Although not included in Figure 4.10, the PIV data show no actuation-induced effects from the jet for $0 < t/T_{\text{conv}} < 0.2$. This $t/T_{\text{conv}} < 0.2$ includes the inherent trigger delay that includes the delay of the electronic ignition system (§II) and the combustion time prior to the pressure build-up in the actuator chambers. The temporal resolution for the present PIV data is $\Delta t = 0.04T_{\text{conv}}$, which is half the jet duration as estimated from the complete return of the chamber pressure ratio to pre-combustion levels (§III). It is therefore conjectured that at $t/T_{\text{conv}} = 0.2$, Figure 4.10b shows the cross flow effects during the jet flow and immediately prior to its completion with near maximum jet velocity that is likely supersonic at the exit plane of the orifice. As described in §II, the injection of this thin and high-velocity brief jet flow that is without particles seeding into the cross flow is not resolved by the present PIV measurements near the orifice due to limited resolution, resulting in the absence of velocity vectors within the near field region of the orifice in the instantaneous data. The phase-averaged flow field in Figure 4.10b therefore provides a lower estimate of the velocity immediately adjacent to the orifice, and in fact shows the effects on the surrounding cross flow rather than the jet itself. A comparison of ω and the streamlines between Figures 4.10a and b clearly reveals these jet-induced alterations to the surrounding cross flow.

At this stage ($t/T_{\text{conv}} = 0.2$) of the transient jet flow and for the present jet to free stream velocity ratio, the jet flow is expected to emanate normal to the cross flow with

minimal bending near the orifice due to the lower momentum boundary layer. Recall that as shown in the schlieren images in §III, the jet emanates over 25 mm ($\sim 0.05c$) in to quiescent flow. Figure 4.10b indicates that this jet penetration in the presence of the cross flow is similar and exceeds the boundary layer thickness ($\delta_{99} \approx 12$ mm at the orifice). The outer flow of the pulsed jet that penetrates beyond the boundary layer is therefore expected to bend in the streamwise direction by the higher velocity free stream and roll-up immediately downstream of the orifice. The presence of the pulsed jet acts as a local brief blockage to the approaching flow from the leading edge of the airfoil. This jet results in the cross stream deflection of the upstream flow as manifested in the dramatic spatial and temporal modifications in the streamlines between Figures 4.10a and b, and is accompanied by the formation of the opposite sense (CCW and CW upstream and downstream of the jet, respectively) vorticity concentrations in the cross flow that lead to a significant, albeit transitory distortion of the surface boundary layer. The deflected streamlines of the cross flow in Figure 4.10b show reasonable agreement with experimental (e.g., Kelso et al., 1996; and Hasselbrink and Mungal, 2001) and numerical (e.g., Sau et al., 2004; and Muppidi and Mahesh, 2005) investigations of the obstruction effected by a *steady* jet in cross flow (or transverse jet). The present jet-induced *momentary* blockage is precursor to the severing of the separating shear layer that leads to the global attachment over the airfoil demonstrated in connection to Figure 4.2. Although the blockage from the pulsed jet is brief, it leads to the development of large-scale vortical structures that persists beyond the termination of the jet flow as discussed in the following sections.

The flow field of Figure 4.10b is presented alternatively using velocity vectors and as vector differences relative to the base flow in Figures 4.11a and b, respectively. The contour plots of the changes in the streamwise and cross stream velocity components relative to the base flow are also shown in Figures 4.11c and d, respectively. The effects on the cross flow in the near ($\sim 0.05c$) field of the jet are represented by the direction and magnitude of the velocity vectors in Figure 4.11a where accelerated flow is clearly evident on the downstream side of the jet orifice while the flow from the leading edge is slowed by the actuation. The momentary blockage associated with the impulse of the jet penetrates through the local boundary layer into the free stream, slowing and deflecting the oncoming flow (upstream of the jet). These are further elucidated from the diminution of the streamwise velocity relative to the base flow upstream of the jet orifice in Figure 4.11c, and from an increase in both the streamwise and cross stream velocity components downstream of the jet orifice shown in Figures 4.11b and c. This is also observed with the near symmetrical displacement about the orifice of cross flow fluid by the jet ($\Delta v > 0$) in Figure 4.11d. Note also the small local entrainment of free stream flow towards the surface near the jet orifice into the windward portion of the jet, indicated by $\Delta v < 0$ in Figure 4.11d, in agreement with the curved streamlines near the orifice in Figure 4.10b. The flow disruption at the upstream edge of the orifice is expected to *increase the pressure in this region* with the decreasing velocity, which resemble the near-field behavior of a steady jet in the cross flow shown by Kamotani and Greber (1972) that acts as a *permanent* obstacle to the approaching flow.

The nominal symmetry of the Δu and Δv about the axis of the orifice (Figures 4.11c and d, respectively) represents the onset of the jet-induced CW and CCW vorticity where

the localized interactions of the cross flow with the jet at this stage of the actuation have limited effects on the airfoil as is also manifested in the reasonably undistorted vortex pair near the actuator's orifice in Figure 4.11a. This is also consistent with the minimal changes in the surface pressure in the vicinity of the jet orifice in Figure 4.4 for $t/T_{\text{conv}} < 0.4$. The CCW concentrations are distinct in the cross flow while the CW jet vortex, embedded within the same sense concentrations in the boundary layer, is less distinguishable. While the flow changes depicted in Figures 4.10 and 4.11 extend over $\sim 0.15c$ in both the streamwise and cross flow directions, there are negligible changes in the flow field farther downstream i.e., $x/c > 0.3c$ (Figures 4.11c and d), as is evident from the streamlines in Figures 4.10a and b.

The vorticity concentrations of these jet-induced vortices (and therefore their corresponding circulations relative to each other) are somewhat altered as visually evident during the jet penetration into the shear layer shown in Figure 4.11 and also as these structures continue to evolve downstream, which is discussed in connection with Figure 4.12. The CW vortex remains in the vicinity of the shear layer during the subsequent cross flow interactions associated with its downstream advection. The circulations and trajectories of the CW and CCW jet vortices are shown in Figure 4.12 to be different owing to their interaction with the predominantly CW vorticity layer next to the surface. A short time following the flow shown in Figures 4.10b and 4.11, the CW vortical structure concentrated near the orifice and airfoil surface at $t/T_{\text{conv}} = 0.24$ (Figure 4.12a) increases significantly in size, strength and spreading due to sustained interactions with the boundary layer. During the short time lapse of $0.04T_{\text{conv}}$, the CCW vortex of the upward-oriented jet vortices in Figure 4.10b is advected and located over the CW vortex

that is embedded in the shear layer in Figure 4.12a. The curved streamlines on the upstream side of the jet in Figure 4.10b suggest a decreasing pressure gradient in the streamwise direction induced by the onset of the pulsed jet, which helps reorient the vortices. It is also expected that during this time ($0.2 \leq t/T_{\text{conv}} \leq 0.24$), as the jet trajectory is continually deflected through interactions with the cross flow, the CCW vortex is transported at greater speeds than the downstream vortex due to its location in the faster free stream flow. The downstream re-orientation of the vortex pair in Figure 4.12a is owing to interactions with the approaching flow in the regions of high strain.

At the early times ($t/T_{\text{conv}} \leq 0.24$), the counter-rotating vortices grow in size and in circulation. In Figure 4.12a, the larger and stronger CW structure compared to Figure 4.11a extends into the free stream and partially envelopes the jet-induced CCW vorticity. The CW vorticity concentration continues to wrap around the CCW vortex in Figures 4.12b and c as these near-circular vortices also adjust to the induced strain field and their cores become increasingly elliptical. In particular, the CW structure is spread significantly and rapidly by the surrounding shear and boundary layer flows during its streamwise advection due to enhanced mixing. The distorted CW vorticity concentrations are evident in Figures 4.12c and d at $t/T_{\text{conv}} = 0.32$ and 0.36 , respectively.

As shown in Figure 4.11b, the penetration of the momentary actuation jet through the wall vorticity layer results in a diminution of CW vorticity that resembles a discontinuity in the local vorticity field at $x/c = 0.2$ (marked as † within the airfoil) of the shear layer as it advects downstream. As discussed in §IV.1, this discontinuity is the precursor to two significant processes that comprise the primary effects of the transitory actuation, namely the roll-up of a large-scale CW vorticity concentration whose advection marks the onset

of the momentary collapse of the separated flow domain, and the migration of an attached surface boundary layer well beyond the onset of separation in the base flow. In subsequent discussions throughout the dissertation, this low-concentration region of CW vorticity that becomes more noticeable in Figures 4.12c-f is referred to as the “severing” of the separating shear layer during the jet flow where vorticity concentrations in the base flow are transported by the CW vortex during its roll-up downstream of the orifice. Note that as previously discussed, this CW roll-up is first initiated by the high momentum of the pulsed jet column.

By $t/T_{\text{conv}} = 0.52$ following actuation (Figure 4.12f), the CCW vortex has moved beyond the measurement domain. As the CW vortex advects downstream, the upstream attached boundary layer continues to grow along the surface with its downstream leading edge moving towards the trailing edge (Figures 4.12g-h), creating a region of attached flow above the airfoil (compare Figures 4.12a and h) upstream of the severed CW vortex. As discussed further below, it appears that the shedding of the CW vorticity and the attachment are coupled.

As discussed in §IV.1, there is a significant disparity in the respective global attachment and relaxation time scales following the onset and termination of actuation where the rapid accumulation of CW vorticity concentrations during attachment subsequently takes significantly longer to advect into the wake, therefore increasing the circulation in Figure 4.8. These time scales are further elucidated from the spatial and temporal evolution of the cross stream integral of the vorticity flux $F_{\omega}(x,t) = \int (u\omega)dy$, which is computed from the phase-averaged velocity and vorticity fields across vertical cross stream sections over the suction surface following the actuation. An $x-t$ contour

plot of $F_{\omega}(x,t)$ in Figure 4.13 shows the celerity of the actuation-induced structures. The time and streamwise variations of F_{ω} for some fixed x_i and fixed t_i , respectively, are highlighted using traces of the vorticity flux increments at each location. These fluxes are normalized and computed relative to the flux at the actuator orifice (x_{act}) for the base flow ($t = 0$) as given by $\Delta F_{\omega}^* = [F_{\omega}(x, t) - F_{\omega}(x_{act}, t = 0)] / F_{\omega}(x_{act}, t = 0)$. Time traces of $\Delta F_{\omega}^*(t, x = x_i)$ are plotted for $x_i/c \approx 0.24, 0.28, 0.38$ and 0.48 (marked by vertical dash lines “i” - “iv” in Figure 4.13), and streamwise traces $\Delta F_{\omega}^*(x; t = t_i)$ are plotted for $t_i/T_{conv} \approx 0.28, 0.40, 0.52$ and 0.84 (marked by horizontal dash lines “v” - “viii”).

The contour plot distribution clearly shows the appearance and advection of the CW and CCW vortical structures induced by the pulsed jet in the PIV image of Figure 4.10b at $t/T_{conv} = 0.2$. The advection of the CCW vortex is apparent from patches of positive flux (marked in blue). These blue contour patches appear discretized due to the time resolution of the present PIV flow field measurements since at each time instance the phase-averaged vorticity concentrations occupy non-overlapping finite regions over the airfoil. If these regions overlapped (i.e., for higher PIV resolution), the CCW vorticity concentrations in Figure 4.13 would form a blue streak. It is evident from the absence of the blue patch at $x/c = 0.24$ (along the dash line “i”) on the contour plot that this vortex is not observed at this streamwise location. The passing of this CCW vortex also corresponds to the increase in the flux increment (i.e., $\Delta F_{\omega}^* > 0$) as shown in the “ii”, “iii” and “iv” time traces for $x/c = 0.28, 0.38$ and 0.48 where a negative peak is measured at $t/T_{conv} \approx 0.28, 0.35$ and 0.42 , respectively. The absence of this peak in the plot for $x/c = 0.24$ agrees with the contour plot where there are no distinct CCW flux along the vertical “i” dash line. A characteristic propagation velocity of the CCW vortex (marked

by a solid line in the contour plot), $u_{CCW}/U_\infty \approx 1$, is estimated from the loci of the maximum flux or from tracking the corresponding first peak in the time traces.

At the same time, as noted in connection with Figure 4.12, the CW vortex merges with the surface boundary layer moving within the shear layer and is not easily distinguishable from the “background” CW vorticity. However, the corresponding vorticity flux is increased by the actuation as shown in Figure 4.13, and the streamwise velocity of $u_{CW}/U_\infty \approx 0.75$ for this slower (compared to the CCW) vortex is estimated by tracking the highest concentration of the flux. This is also marked using a solid line in the contour plot.

Perhaps the most prominent feature in this $x-t$ diagram, is the appearance of a low-flux streak (having a characteristic propagation velocity of $u/U_\infty \approx 0.55$) that is associated with the severing and rollup of the separated CW vorticity as discussed in Figure 4.12. The four horizontal dash lines (“v” – “viii”) illustrate the flow structure that is associated with the severing. At $t/T_{conv} = 0.28$ (*cf.*, Figure 4.12b), the onset of the severed domain upstream of the counter-rotating vortices is manifested in the $\Delta F_\omega^* \approx 0$ domain in the “v” trace for $0.16 < x/c < 0.2$. This low-flux region becomes more prominent with increasing delays following the actuation pulse as evident from the increasing streamwise extent and magnitude of $\Delta F_\omega^* < 0$ in traces “vi” and “vii”. In addition, the severed region is stretched in the streamwise direction as indicated by its increasing width with t/T_{conv} in the contour plot. The boundary layer upstream of the severed region is represented by the increase in F_ω in Figure 4.13 that is associated with the CW vorticity following the low-flux region. It is important to note that the attached flow is slower than the severed flow and is estimated moving downstream at $u_{BL}/U_\infty \approx 0.36$.

4.2.2. Attachment Mechanisms

The accumulation and shedding of vorticity concentrations over the airfoil are not just the result of interactions with the actuation jet, but also due to accumulation associated with the attaching boundary layer (*cf.*, Figure 4.12). The time derivative of the phase-averaged spanwise vorticity, $d\omega/dt$, is calculated from the PIV measurements over the airfoil that are separated in time by 1 ms ($= 0.04T_{\text{conv}}$) to determine the local rate of change in vorticity concentrations induced by the actuation. This will determine the local contributions to the accumulation of vorticity over the airfoil associated with the changes in the circulation. A positive $d\omega/dt$ can represent an increase or decrease in CCW (“positive”) and CW (“negative”) vorticity concentrations, respectively, therefore the spatial distribution of $d\omega/dt$ over the airfoil is shown as color-filled contours in Figure 4.14 superimposed with dashed line contours of $\omega = -800$ (--) and 400 s^{-1} (--) of the CW and CCW concentrations, respectively. These values are chosen to represent the spatial extents of the (weaker) CCW vortex and the shear layer embedded with the (stronger) CW vortex. Figures 4.14a-d correspond to the flow in Figures 4.11a-c and g, respectively.

The complex interactions between the jet structures and the cross flow are manifested in the positive ($d\omega/dt > 0$) and negative ($d\omega/dt < 0$) vorticity variations at $t/T_{\text{conv}} = 0.24$ that are represented by the red (labeled “A” and “C”) and blue (labeled “B” and “D”) regions, respectively, in Figure 4.14a. In the “A” region immediately downstream of the orifice which is located completely within the CW concentrations bounded by $\omega = -800 \text{ s}^{-1}$ (--), the *decrease* in CW vorticity concentration ($d\omega/dt > 0$) is due, in part, to mixing from the entrainment of free stream fluid. The induced CW roll-up downstream of the orifice by the pulsed jet effectively enhances the transport of shear layer vorticity away

from the surface and into the adjacent domain of the rolled-up CW vortex. This plays an important role in the severing of the boundary layer flow demonstrated in Figure 4.11 and thereby increases the local strength (i.e., $d\omega/dt < 0$) of the CW vortex as manifested in the (blue) region “B” in the shear layer near the CCW vortex. Similarly, there is also reduction in concentration in the upstream vicinity of the CCW vortex within “B” i.e., $d\omega/dt < 0$ due to both the downstream convection of fluid within the upstream half of the CCW vortex (as marked by the yellow dashed line) and the increased mixing with the free stream fluid. Similar explanation can be made for the increase of CCW vorticity ($d\omega/dt > 0$) in the region labeled “C”. The region “D” of $d\omega/dt < 0$ in Figure 4.14a corresponds to the flow in Figure 4.12a - c where concentrations of CW vorticity are enveloped around the CCW vortex.

The transport of vorticity continues following the termination of the actuation pulse. The distance between regions “A” and “B” increases as shown in Figures 4.14b and c at $t/T_{\text{conv}} = 0.28$ and 0.32 , respectively, corresponding to the advection of the counter rotating vortex pairs. Most noticeable is the decreasing magnitude of $d\omega/dt > 0$ for the CW vorticity concentrations in region “A” that also spreads with the increasingly distorted CW vortex. The strength of the temporal variations in the CW vorticity in region “D” is evidently weaker in Figure 4.14b and appears undetectable by $t/T_{\text{conv}} = 0.32$ in Figure 4.14c. Of particular importance is the increasing rate of CW vorticity accumulated on the airfoil as manifested in the region “E” of $d\omega/dt < 0$ that is measured at the leading edge of the growing boundary layer in Figures 4.14b and c where CW vorticity concentrations generated from the upstream boundary flow are convected along the surface. The increasing concentrations of CW vorticity (region “E”) over the airfoil

that persist and continue to occupy a larger domain (e.g., Figure 4.14d at $t/T_{\text{conv}} = 0.76$) contribute directly to the enhanced lift and global circulation of Figure 4.8, and corresponds to the increased attachment shown in Figure 4.12g.

The analysis thus far provided details on the salient flow features following the onset of the pulsed jet. It is necessary to relate these features to understand the physical mechanisms of the ensuing transitory attachment. First, the phase-averaged flow over the actuator at select instances ($0.24 \leq t/T_{\text{conv}} \leq 0.76$) is shown in Figure 4.15. As discussed in §II, since the flow in the plane of symmetry is nominally 2-D, the “convergence” of streamlines located in regions of low velocity is likely a result of cumulative numerical errors. Some of these images were already shown in Figure 4.12 without streamlines. The streamlines in Figure 4.15 reveal the topological evolution of the reattaching boundary layer, the recirculation induced by the rolled-up CW vortex and the demarcation region of low vorticity concentrations. The accelerated flow downstream of the orifice enhances the roll-up process of the CW vortex as induced by the severing, increasing the reversed flow near the surface as shown in Figure 4.15a at $t/T_{\text{conv}} = 0.24$. This roll-up that induces upwash flow moving away from the surface opposes the approaching boundary layer flow and results in a stagnation region (“S1”) near the airfoil surface in addition to the stagnation point off the surface and farther downstream that is associated with separation of the base flow (“S0”) in Figure 4.15a.

As the CW vortex is advected downstream, the stagnation point “S1” between the two flow regions propagates with it along the airfoil surface and becomes more apparent as shown by the streamlines in Figures 4.15b-d ($t/T_{\text{conv}} = 0.28$ - 0.36). By $t/T_{\text{conv}} = 0.52$, the stagnation point “S1” has almost reached $x/c = 0.35$ in Figure 4.15e. It is conjectured that

the stagnation point “S0” of the base flow does not play an important role in the attachment however, it continues to move slowly downstream and away from the airfoil in response to the approaching CW vortex that eventually sheds into the wake. The presence of the two flow domains is obvious and the increased cross stream extent of the streamline that marks the separated flow domain and originates from the stagnation point “S1” suggests a corresponding increase in the obstruction of the free stream flow by the shed CW vortex. At $t/T_{\text{conv}} = 0.76$, “S1” moves off the surface as flow upstream increases in CW rotation. The streamlines in Figure 4.15 show that the effects of the single-pulse actuation manifested in the roll-up and advection of the CW vorticity concentrations displaces the stagnation point of the base flow toward the trailing edge. More importantly, the increase in circulation in association with the increased accumulation of CW vorticity on the airfoil (region “E” in Figure 4.14) and the corresponding attachment are connected to the presence of the new stagnation point “S1” that is first established by the actuation, and subsequently moves in the streamwise extent as it continues to modify the flow over the airfoil.

Whilst the CW vortex continues to interact with the separated shear layer and moves with increasing distance away from the airfoil surface, the cross stream extent of the blockage effect and therefore of its interactions with the free stream flow also increase (Figures 4.15a-d) as was discussed in connection with Figure 4.11. This is evident in the vectoring of the higher momentum free stream towards the airfoil surface in Figures 4.15b-e where the streamlines between the vortex and boundary layer are closely spaced. This free stream entrainment towards the airfoil coupled with the increased downward velocity (i.e. negative v) induced by the enhanced CW vorticity in the “bull-nose” leading

edge of the boundary layer promotes streamwise attachment. As the CW vortex moves downstream, it continues to sustain the stagnating flow region immediately upstream and thereby also the associated attachment.

To sum up, the stagnation flow region in Figure 4.15 plays a critical role in the attachment. First, the rolled-up CW vortex immediately following the onset of the pulsed jet induces velocity in the shear layer that opposes the upstream flow near the airfoil surface. This blockage enhances CW flow rotation upstream of stagnation as evident in the increased concentrations within the leading edge of the attaching boundary layer and in the accumulation ($d\omega/dt < 0$) in the region marked “E” in Figures 4.14b-d. As shown in connection to Figure 4.16, the pressure gradients associated with the stagnation induced by the CW vortex lead to the strengthening of the CW vorticity within the “bull-nose” of the attached flow.

Figure 4.16 shows the phase-averaged streamwise and cross stream pressure gradients, dC_p/dx , (a, c) and dC_p/dy , (b, d), respectively, that are computed from the PIV measurements using the Navier-Stokes equations following the procedure of Honohan (2003), and Liu and Katz (2006). The gradients in Figure 4.16 are computed at $t/T_{conv} = 0.52$ (a-b) and 0.76 (c-d). The alternating regions of adverse ($dC_p/dx > 0$) and favorable ($dC_p/dx < 0$) streamwise pressure gradients labeled “I” and “II”, respectively in Figure 4.16a clearly identify the stagnation region associated with the blockage induced by the CW vortex as shown in Figure 4.15e. The slowing of the approaching flow upstream and the recirculation downstream enhanced by the propagating stagnation that follows the rolled-up vortex results in these adverse and favorable streamwise pressure gradients, respectively.

Although the behavior at the stagnation region resembles a solid obstruction where flow diverges from the airfoil surface (e.g., Figure 4.15b above “S1”) and forms an adverse pressure gradient (Figure 4.16), the attaching boundary layer flow upstream of the stagnation point “S1” does not separate from the airfoil. In fact, immediately upstream of the stagnation region, the blockage induces a pressure gradient towards the airfoil surface (i.e., $dC_p/dy > 0$) as elucidated in the streamline curvatures in Figure 4.15. This increased cross stream pressure acting towards to the airfoil surface above the boundary layer is shown in Figure 4.16b at the stagnation region ($0.25 < x/c < 0.35$), supporting the attachment of the boundary layer. More specifically, the phase-averaged flow field data indicate that the positive dC_p/dy in Figure 4.16b is sufficient even in the presence of the opposing force of the adverse dC_p/dx in Figure 4.16a to successfully attach the flow and extend the boundary layer flow further downstream. These pressure gradients develop with the rolled-up CW vortex, and therefore the duration of the attachment process induced by the single pulse is commensurate ($\sim 1 T_{conv}$ as shown in the pressure traces and vorticity fluxes in Figures 4.4 and 4.7, respectively) with the convective time scale. Following this, in the absence of the pressure transients, the effects of actuation diminish gradually and flow eventually returns to baseline.

The pressure data in Figure 4.4b that show only the attachment transients ($t/T_{conv} < 4$) on the suction surface demonstrate that the effects of the jet as observed in Figures 4.15e for $t/T_{conv} = 0.56$ are not detectable as pressure effects at $x = 0$, suggesting that the flow transients are first concentrated only in the vicinity of the actuators and subsequently measured downstream. As shown in Figure 4.8b, the corresponding changes in mid-span circulation are also minimal and the majority of the increase in circulation ($t/T_{conv} > 1.8$)

is not measured until there are collective increases in suction pressure over the airfoil (also $t/T_{\text{conv}} > 1.8$ for all the sensors on the upper airfoil surface in Figure 4.4b). Figure 4.4b shows that the flow over the leading edge is accelerated for $t/T_{\text{conv}} > 0.6$ due to the attachment induced by the pulsed actuation as manifested in the suction pressure increments of $dC_p/dt < 0$. However, this increase ($dC_p/dt < 0$) appears to lag or is lower than the corresponding transients measured immediately downstream of the actuators (*c.f.*, the sensor at $x/c = 0.25$ until $t/T_{\text{conv}} \approx 2.2$). This delayed flow acceleration at locations upstream of the orifice that occurs following the completion of the pulsed jet flow is related to the fact that the attachment mechanism is driven by the (farther downstream) transitory CW roll-up of the attaching boundary layer flow that entrains free stream fluid at its “bull-nose” and subsequently increases the overall cross flow velocity further upstream over the airfoil surface.

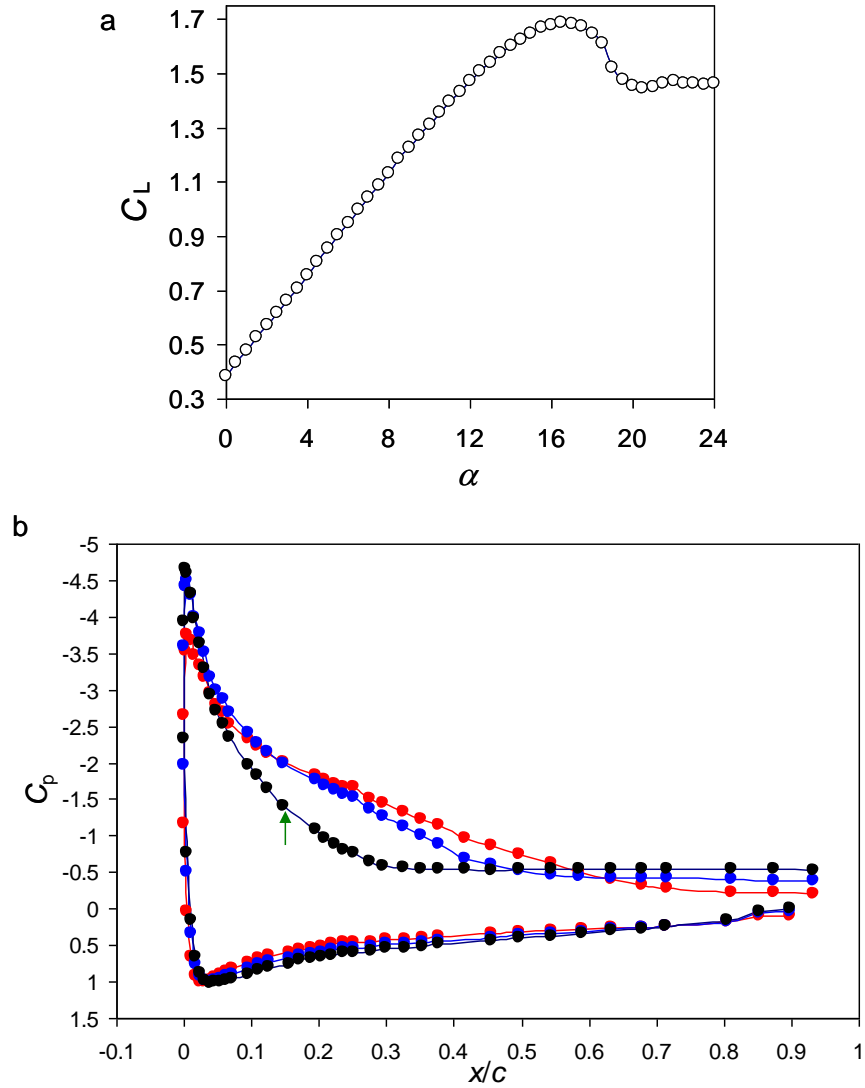


Figure 4.1: (a) Base flow lift coefficient, C_L , computed from mid-span pressure distribution C_p for $0 \leq \alpha \leq 24^\circ$ for current NACA 4415 airfoil configuration ($S_{\text{fence}} = 0.35c$) at $Re_c = 5.7 \times 10^5$, and (b) Distributions of C_p for $\alpha = 14^\circ$ (●), 16.5° (●) and 19° (●) (the green arrow shows the streamwise location of the actuator orifice).

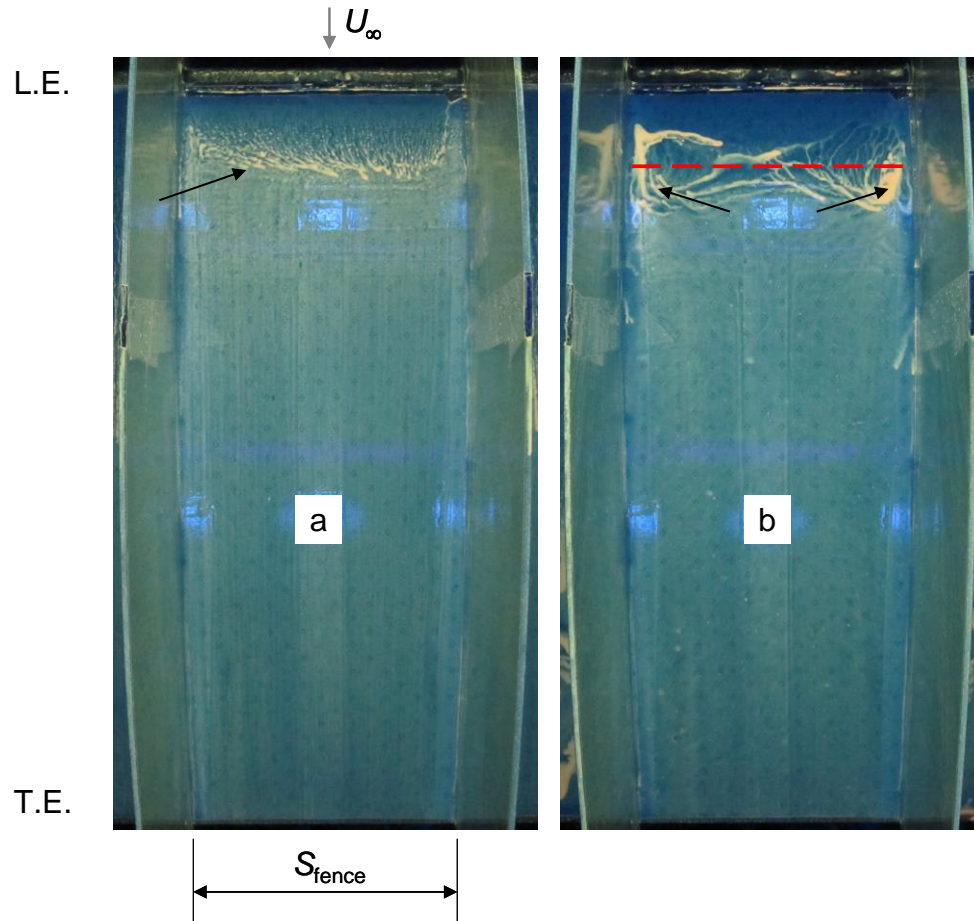


Figure 4.2: Surface oil visualizations obtained at 5 (a) and 15 (b) minutes following air flow show progression of nominally 2-D separation line on the airfoil spanwise-confined by fences at S_{fence} apart on the left and right sides of each image. The arrows mark local flow features and the actuators are also marked (-).

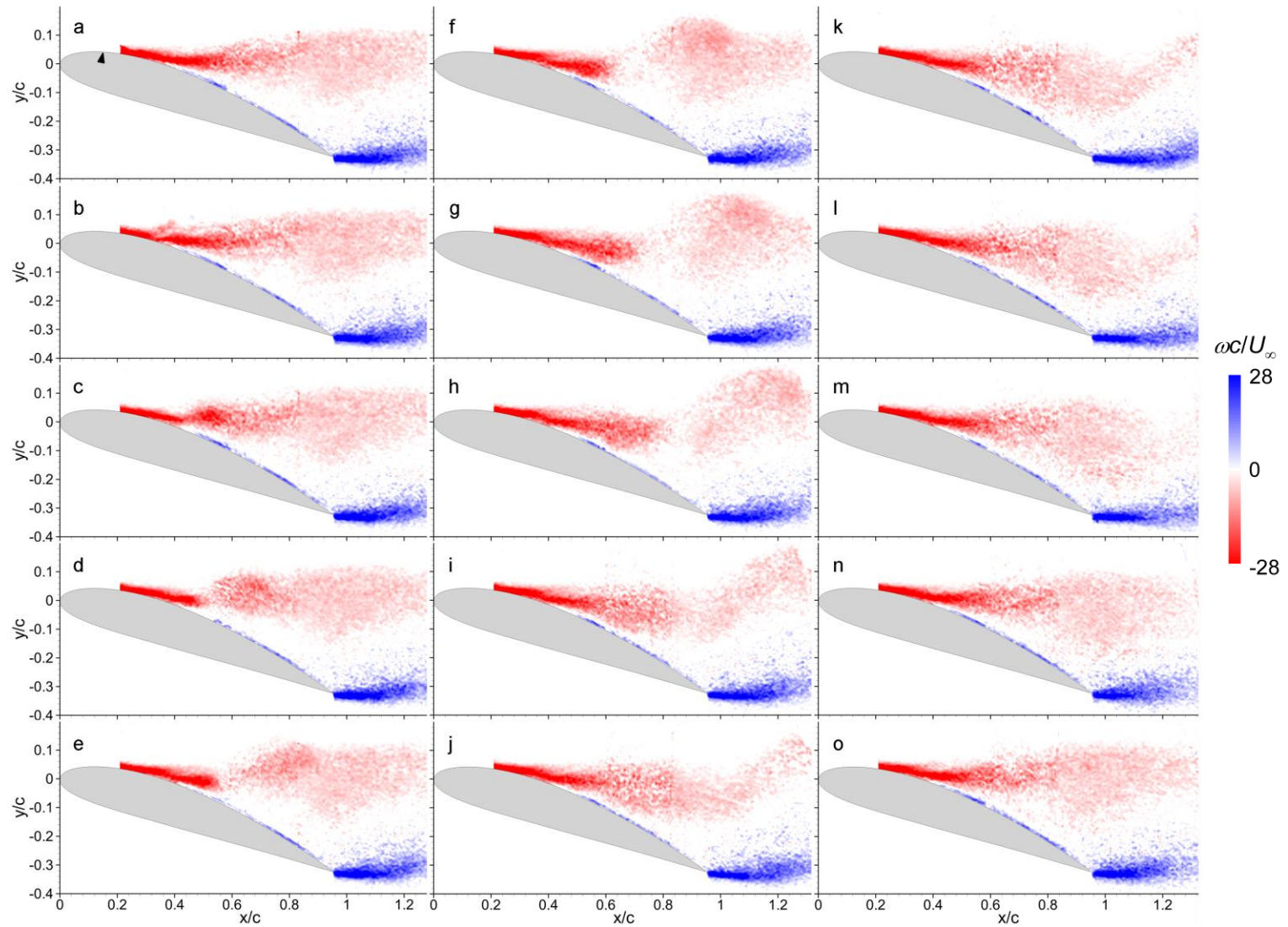


Figure 4.3: Time sequence of phase-averaged vorticity concentrations following single-pulse actuation at $t = 0$; $t/T_{\text{conv}} = 0$ (a), 0.16 (b), 0.32 (c), 0.48 (d), 0.64 (e), 0.8 (f), 0.96 (g), 1.12 (h), 1.28 (i), 1.44 (j), 1.6 (k), 1.76 (l), 1.92 (m), 3.2 (n) and 4.8 (o). Location of the jet orifice is marked by black triangle in (a).

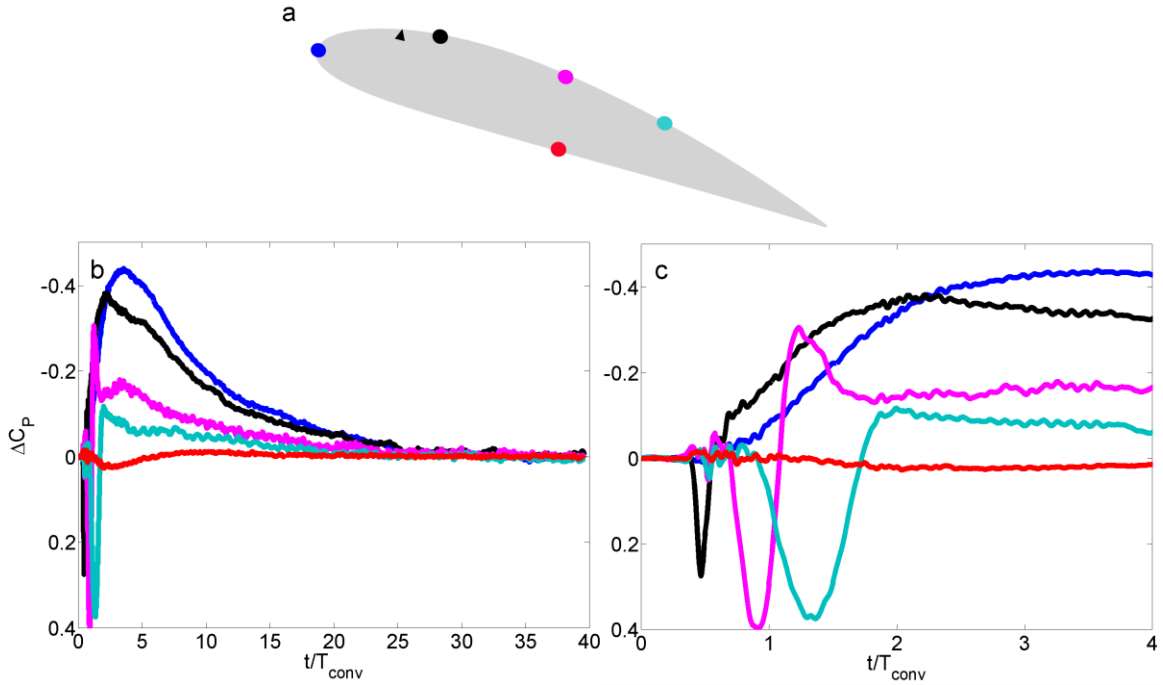


Figure 4.4: Phase-averaged changes in surface pressure measured by distributed sensors on airfoil (a) following single actuation pulse: b) $0 \leq t/T_{conv} \leq 40$, and c) and $0 \leq t/T_{conv} \leq 4$. Time traces shown at $x/c = 0$ (—), 0.25 (—), 0.45 (—) and 0.68 (—) on the pressure side, and 0.5 (—) the on suction side. The location of actuator array is marked by triangle in (a).

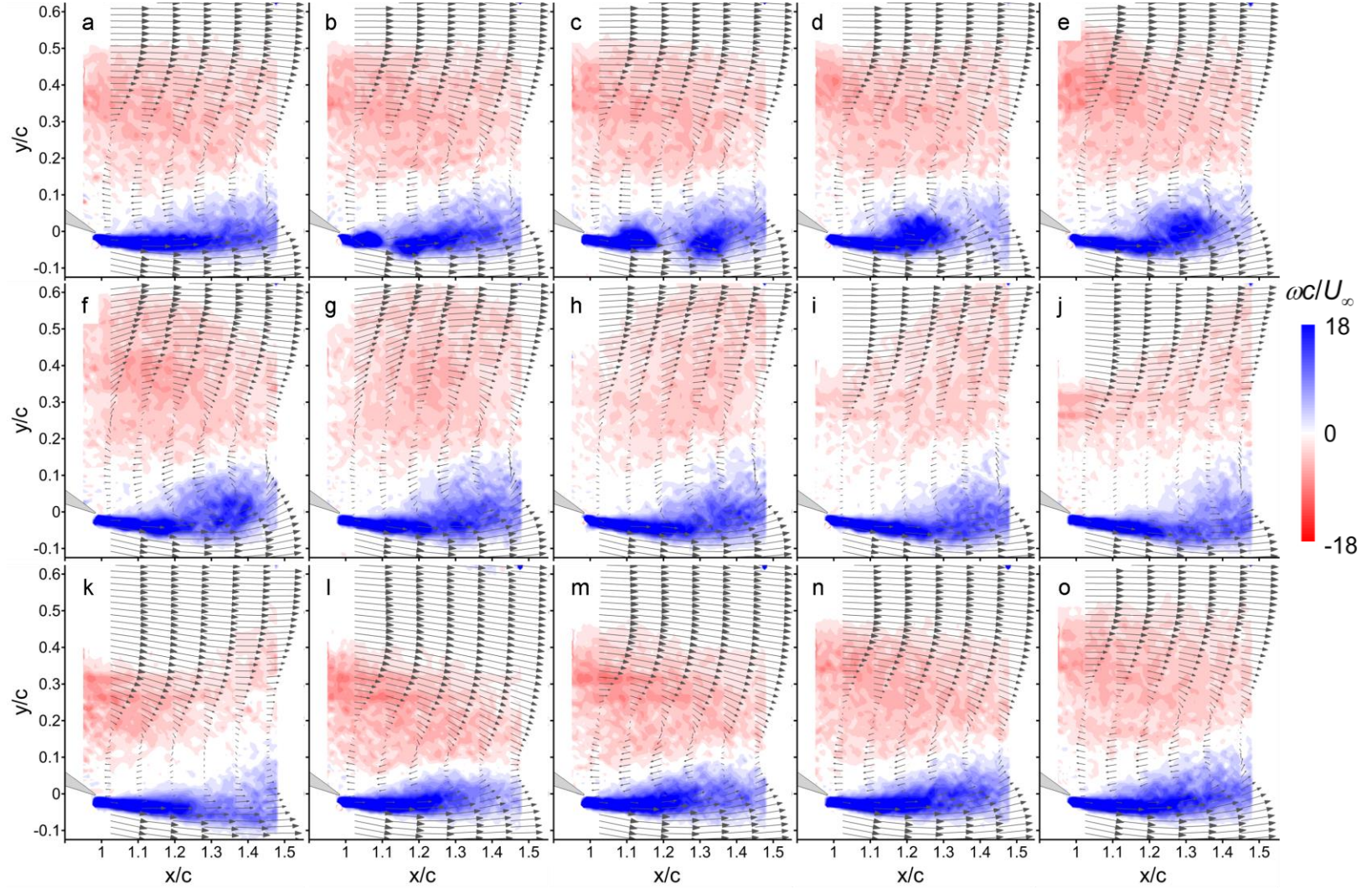


Figure 4.5: Flow field in the near wake (velocity vectors and vorticity concentrations) following single-pulse actuation at $t = 0$; $t/T_{\text{conv}} = 0$ (a), 0.32 (b), 0.48 (c), 0.8 (d), 0.96 (e), 1.12 (f), 1.28 (g), 1.44 (h), 1.6 (i), 1.76 (j), 2.08 (k), 2.72 (l), 4.64 (m), 6.24 (n) and 11.04 (o).

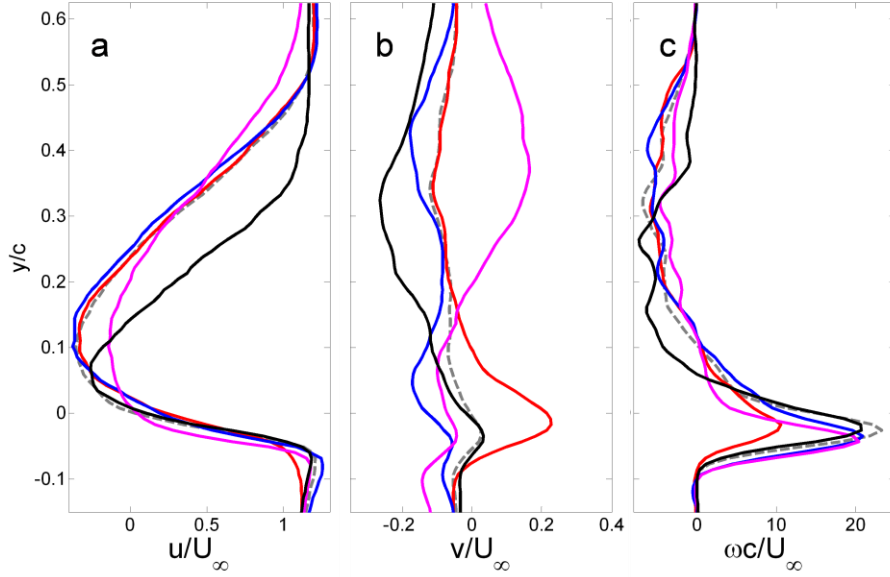


Figure 4.6: Cross stream distributions on the near wake of the streamwise, u (a), and cross stream, v (b) velocity components and of the spanwise vorticity, ω (c) measured at $0.25c$ downstream from trailing edge following single-pulse actuation at $t/T_{\text{conv}} = 0$ (—), 0.48 (—), 0.96 (—), 1.6 (—), and 2.72 (—).

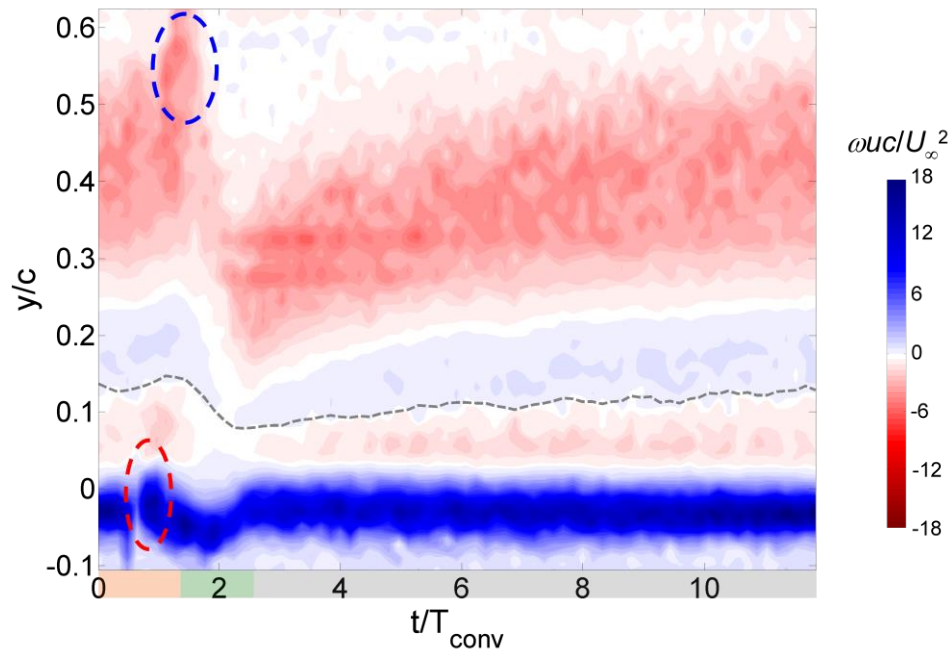


Figure 4.7: Time evolution of phase-averaged cross stream distribution of vorticity flux, $\omega_z u$, at $x/c = 0.25$ downstream of the trailing edge overlaid $y_{\text{wake}}(t; x/c)$, (—) following single-pulse actuation; CW ($y > y_{\text{wake}}$) and CCW ($y < y_{\text{wake}}$). Red and blue ovals mark the shedding of the CCW and CW vortices, respectively, as shown in Figure 4.5. The time axis colors represent the CW vortex shedding (orange), attachment (green), and relaxation (grey).

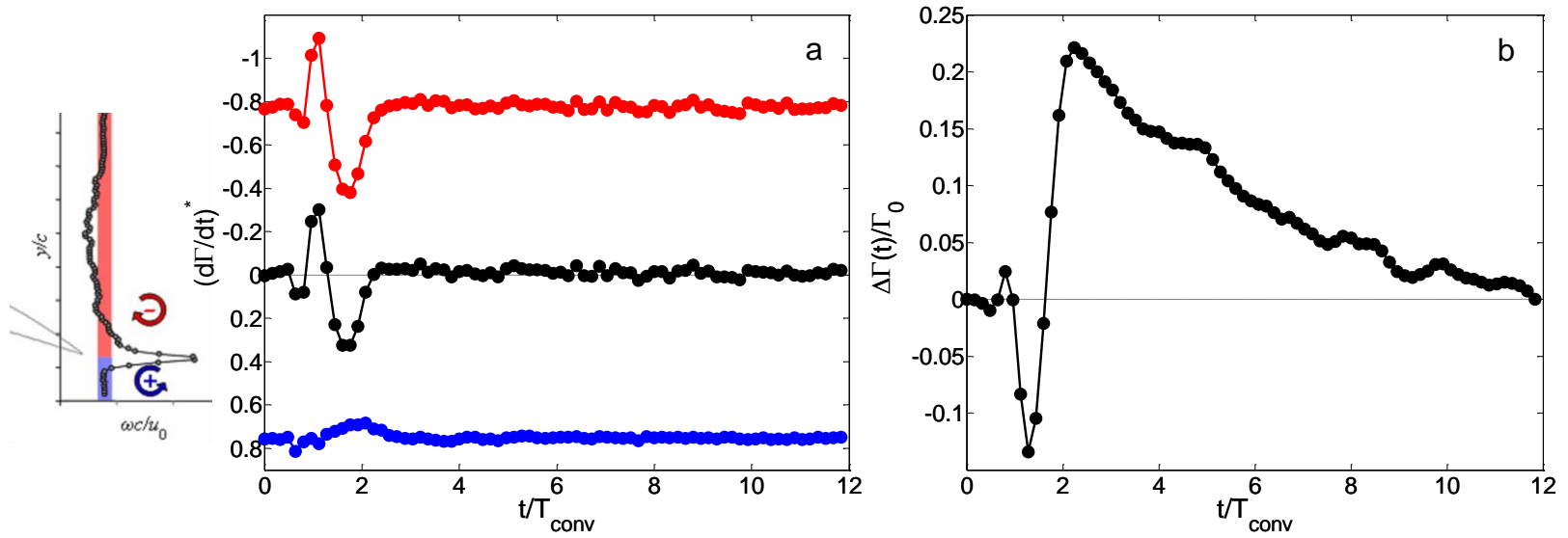


Figure 4.8: (a) Variation in the normalized vorticity flux $(d\Gamma/dt)^*$ in the near wake ($x/c = 1.25$, following an actuation pulse $[(d\Gamma/dt) = -(cU_\infty)^{-1} \int_{y_0}^{y_1} u \cdot \omega_z dy]$): top (\bullet , CW) and bottom (\bullet , CCW) surfaces, and their sum (\bullet), and (b) The corresponding incremental changes in circulation. The schematic on the left illustrates the cross stream vorticity distribution.

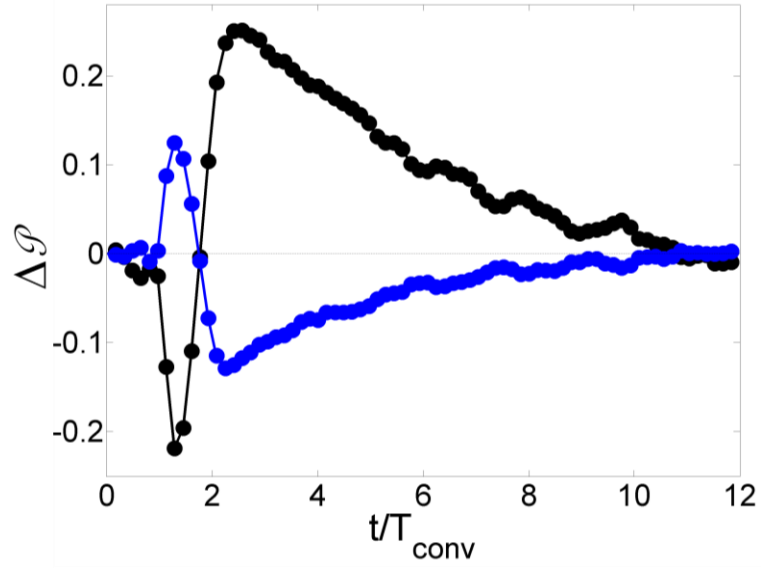


Figure 4.9: Time traces of the incremental changes (relative to the unforced flow) in streamwise (•) and cross stream (•) momentum fluxes across the wake.

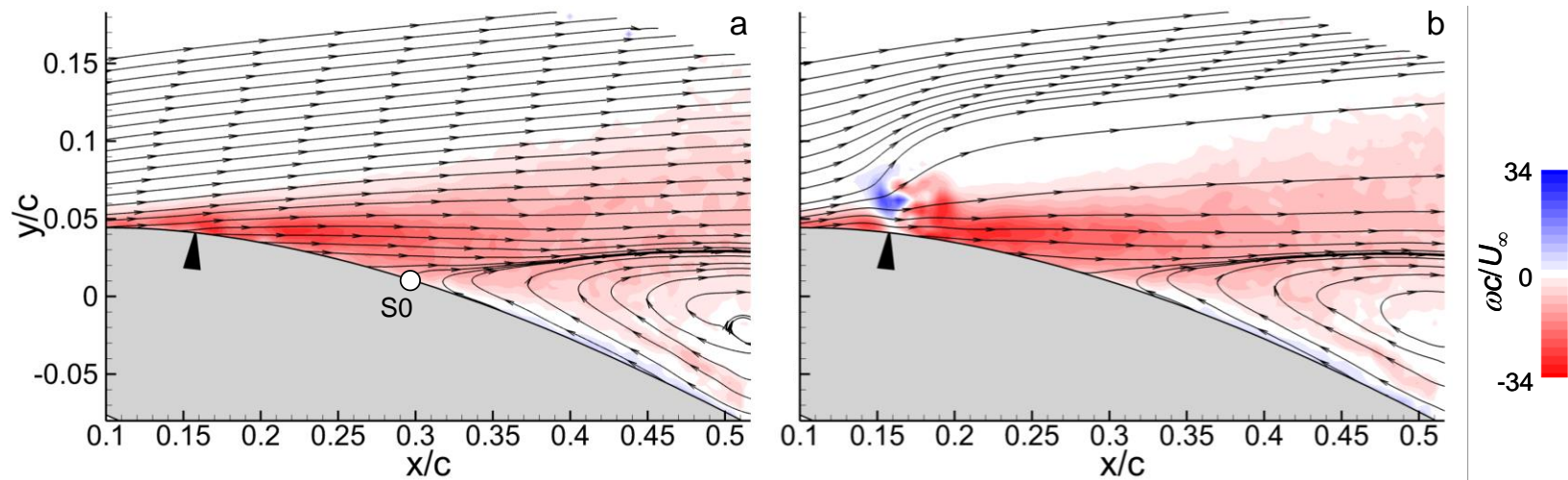


Figure 4.10: Raster plots of phase-averaged spanwise vorticity concentrations superimposed with streamlines following single-pulse actuation at $t/T_{conv} = 0$ (a), and 0.2 (b). The dividing streamline connects the stagnation point “S0”. Actuator location is marked with black triangle.

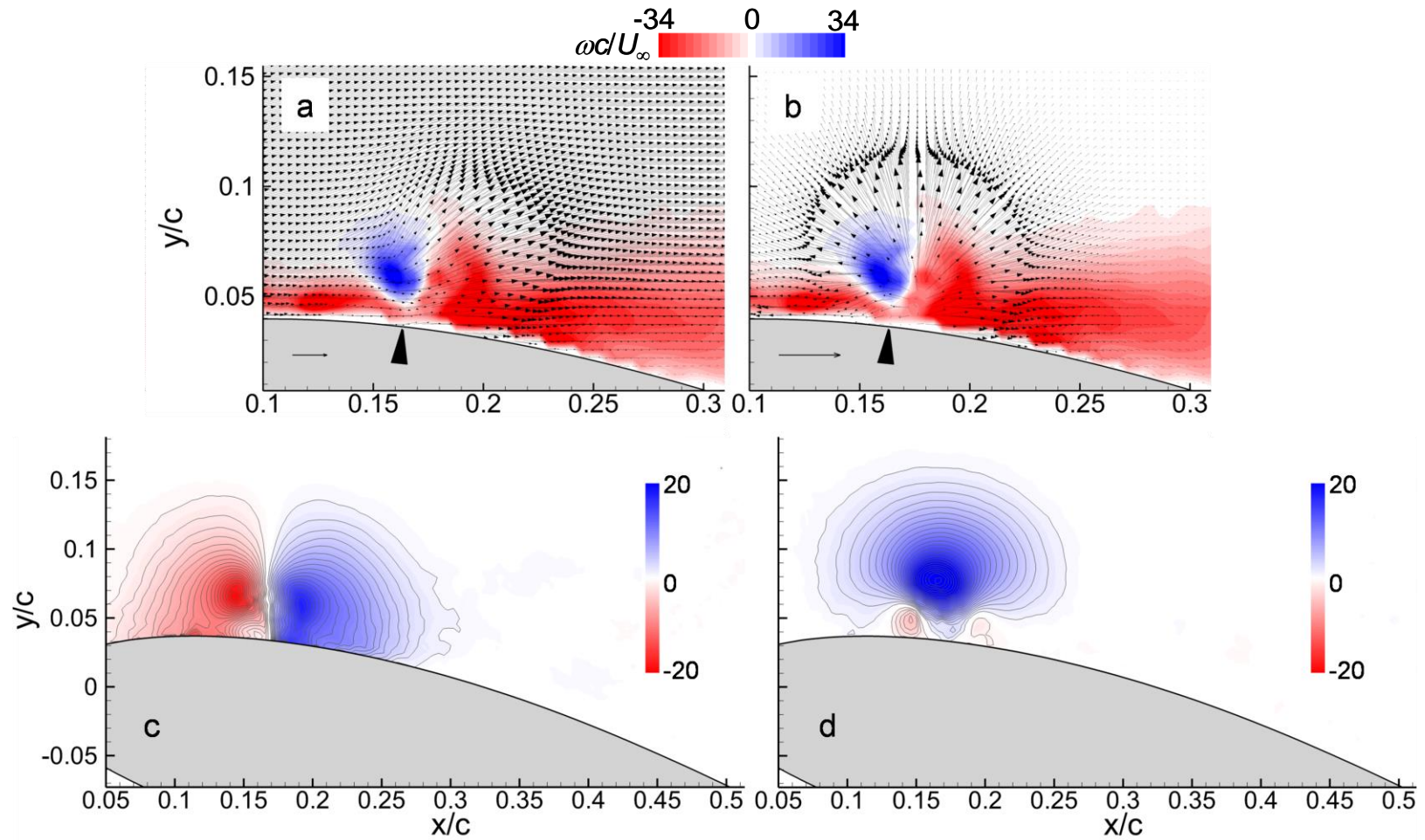


Figure 4.11: Raster plots of phase-averaged spanwise vorticity following a single-pulse actuation at $t/T_{\text{conv}} = 0.2$ superimposed with (a) velocity vectors and (b) velocity vectors relative to base flow. Corresponding contour of the changes in the streamwise, Δu (c) and cross stream velocity, Δv (d) relative to base flow.

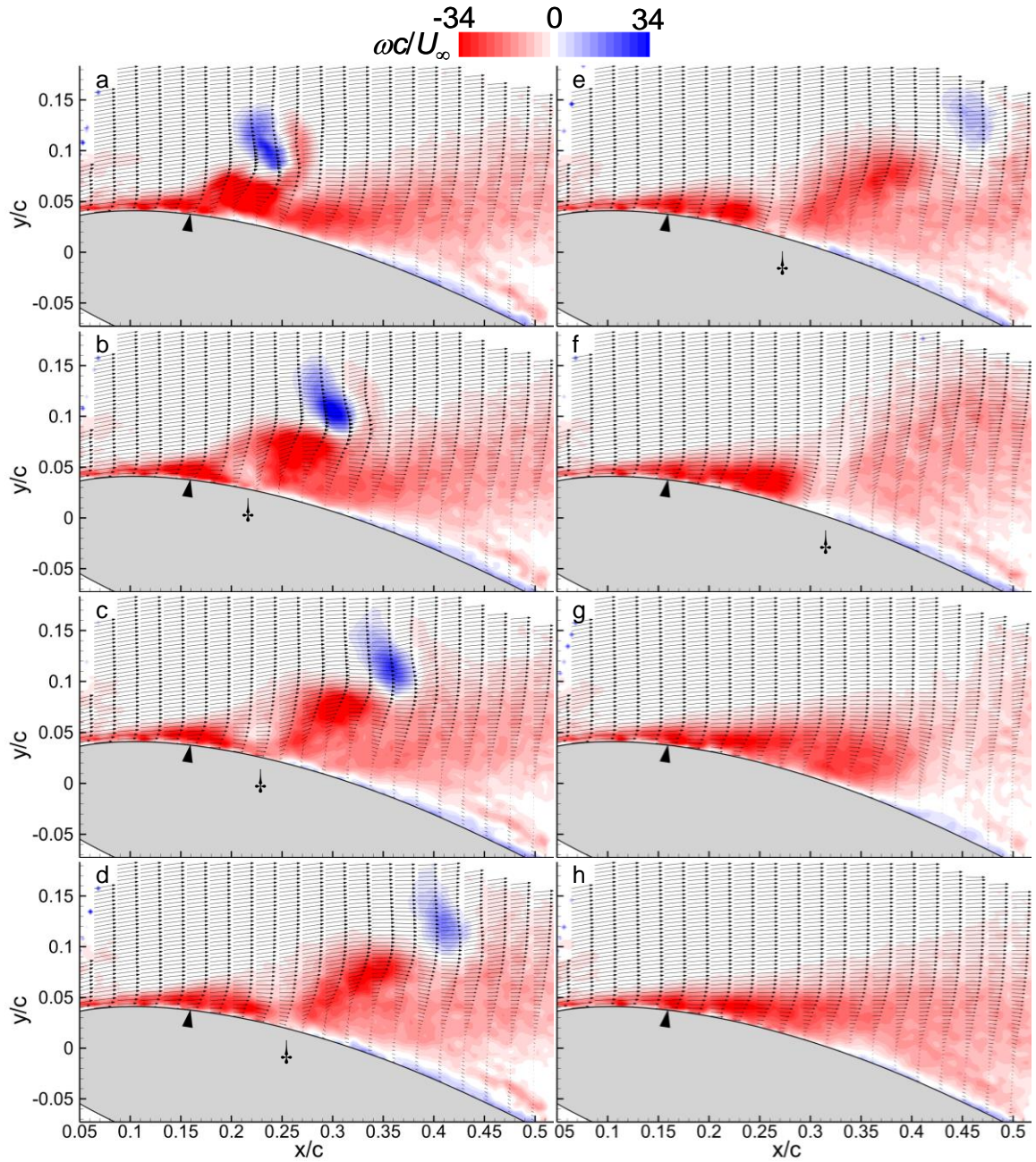


Figure 4.12: Raster plots of phase-averaged spanwise vorticity superimposed with velocity vectors following a single-pulse actuation at $t/T_{\text{conv}} = 0.24$ (a), 0.28 (b), 0.32 (c), 0.36 (d), 0.4 (e), 0.52 (f), 0.8 (g) and 1.16 (h). The “severed” region of low vorticity concentration is marked by †.

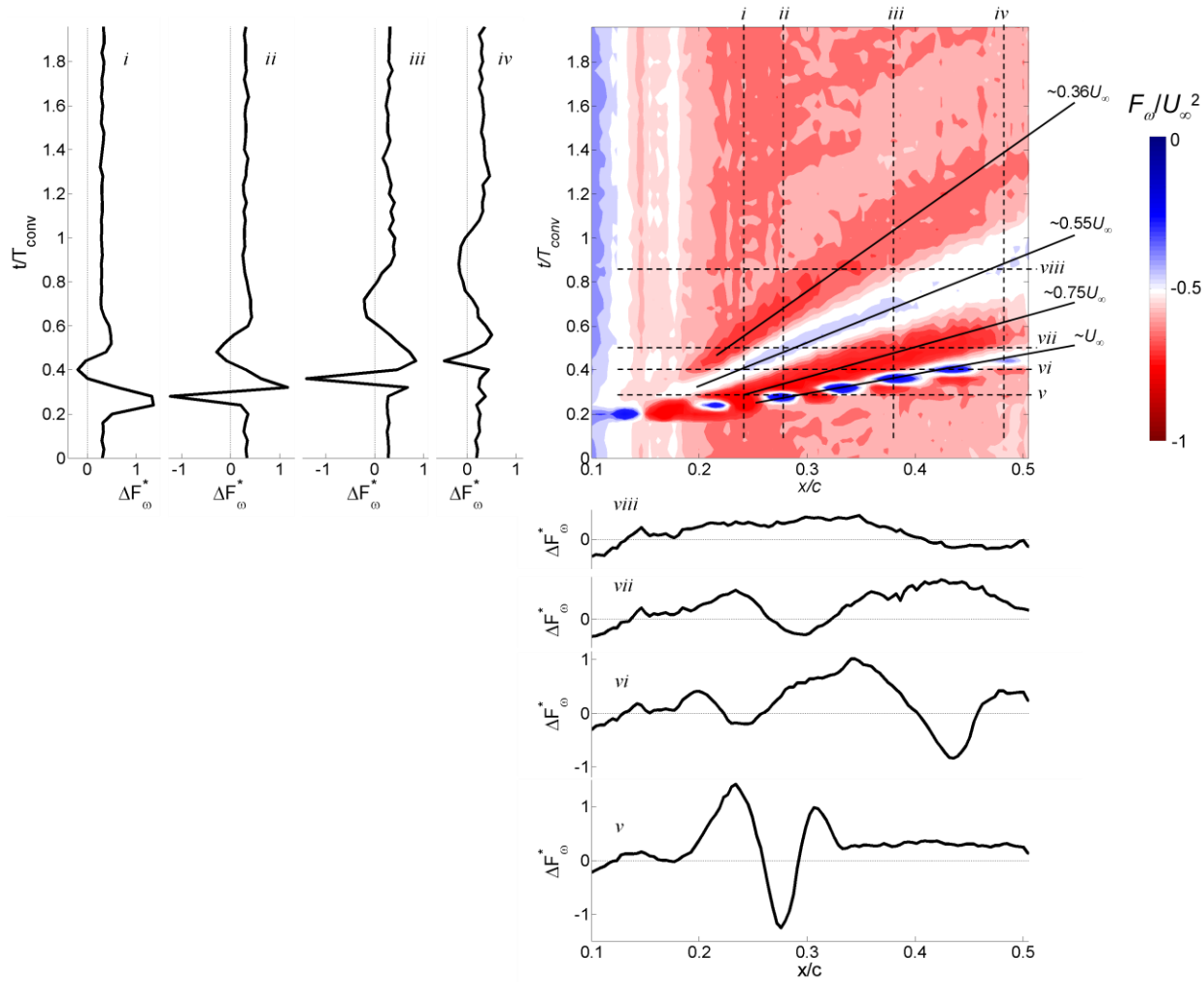


Figure 4.13: x - t contour plot of phase-averaged vorticity flux F_{ω} showing flow structure celerity over airfoil (-) and marked (--) corresponding to the time traces of vorticity flux relative to base flow, ΔF_{ω}^* , following single actuation pulse. at $x/c = 0.24$ (*i*), 0.28 (*ii*), 0.38 (*iii*) and 0.48 (*iv*), and at $t/T_{conv} = 0.28$ (*v*), 0.40 (*vi*), 0.52 (*vii*) and 0.84 (*viii*).

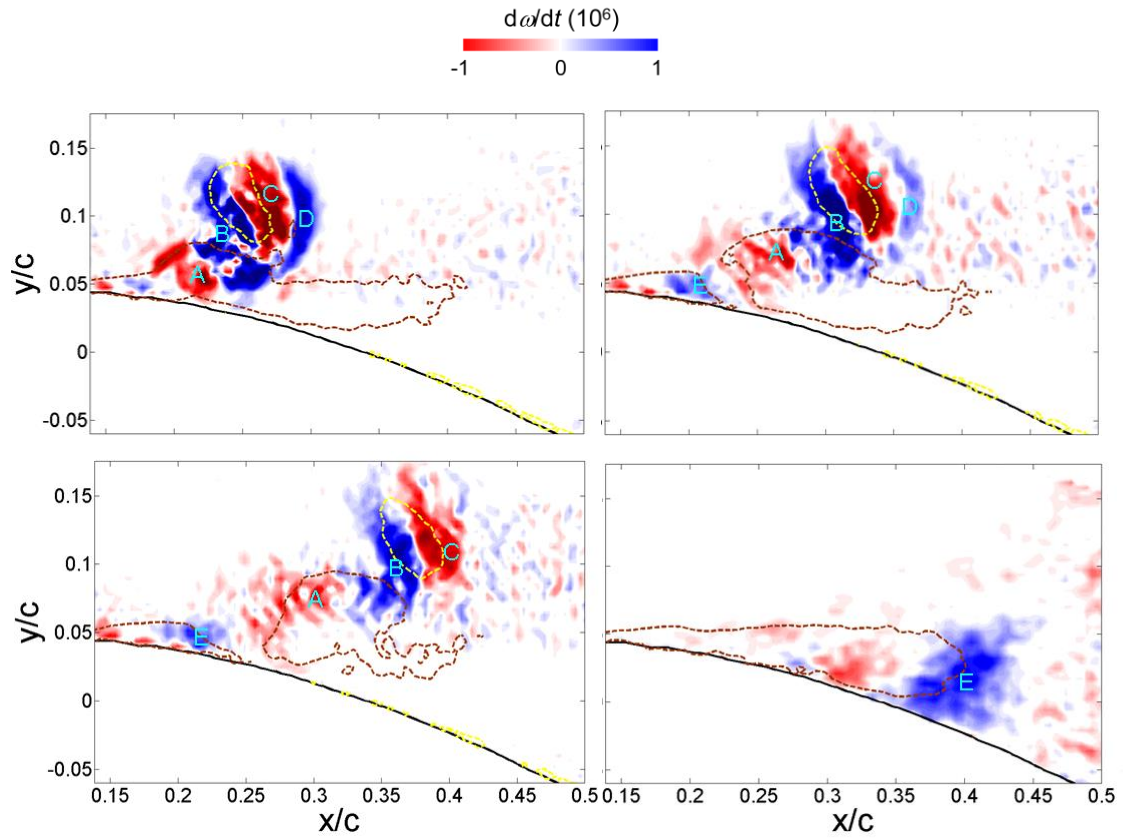


Figure 4.14: Phase-averaged raster plots of $d\omega/dt$ at $t/T_{\text{conv}} = 0.24$ (a), 0.28 (b), 0.32 (c) and 0.76 (d) with iso-contours of $\omega = 400$ (---) and -800 s^{-1} (---), and regions marked “A” – “E”.

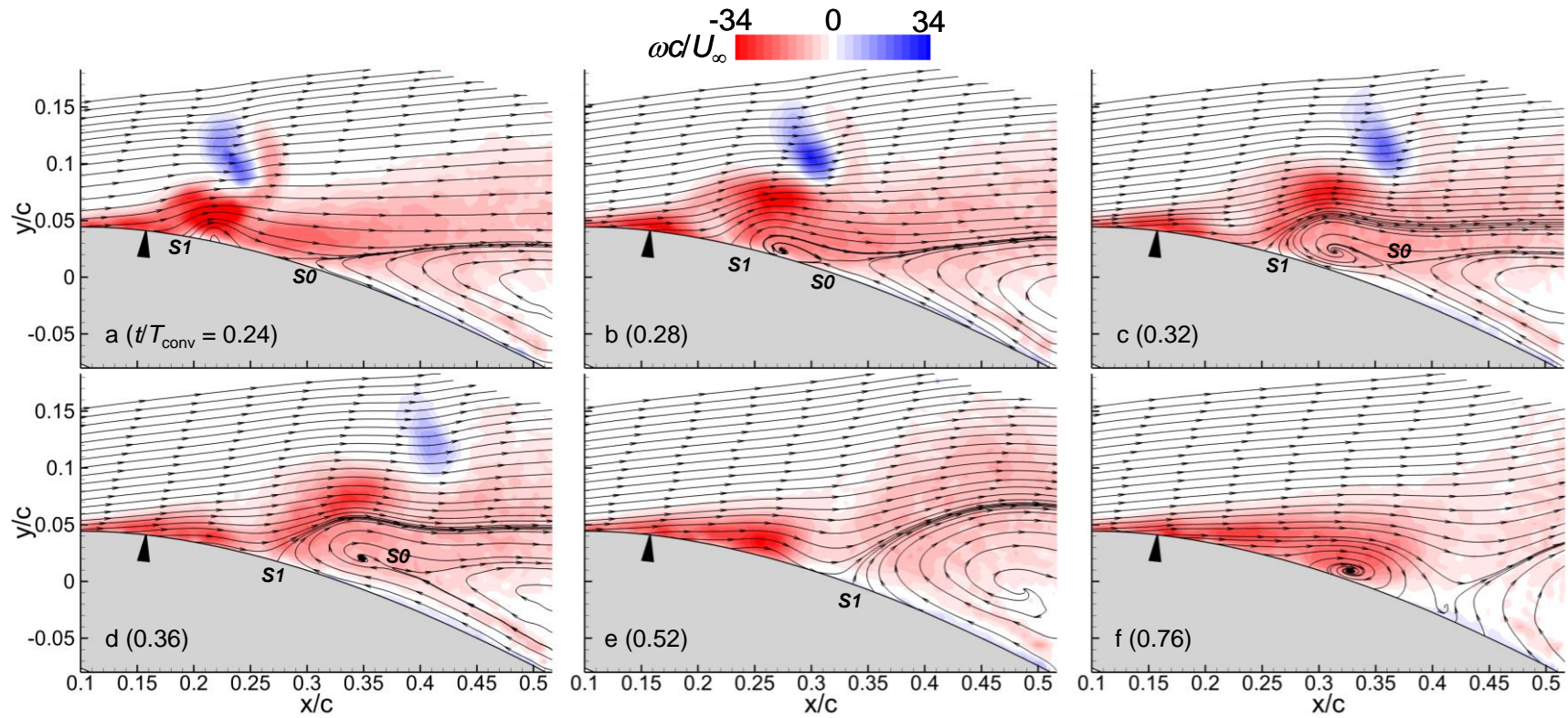


Figure 4.15: Raster plots of phase-averaged of spanwise vorticity superimposed with streamlines following actuation at $t/T_{\text{conv}} = 0.24$ (a), 0.28 (b), 0.32 (c), 0.36 (d), 0.52 (e), and 0.76 (f). Approximate locations of stagnation points are marked “S0” and “S1”.

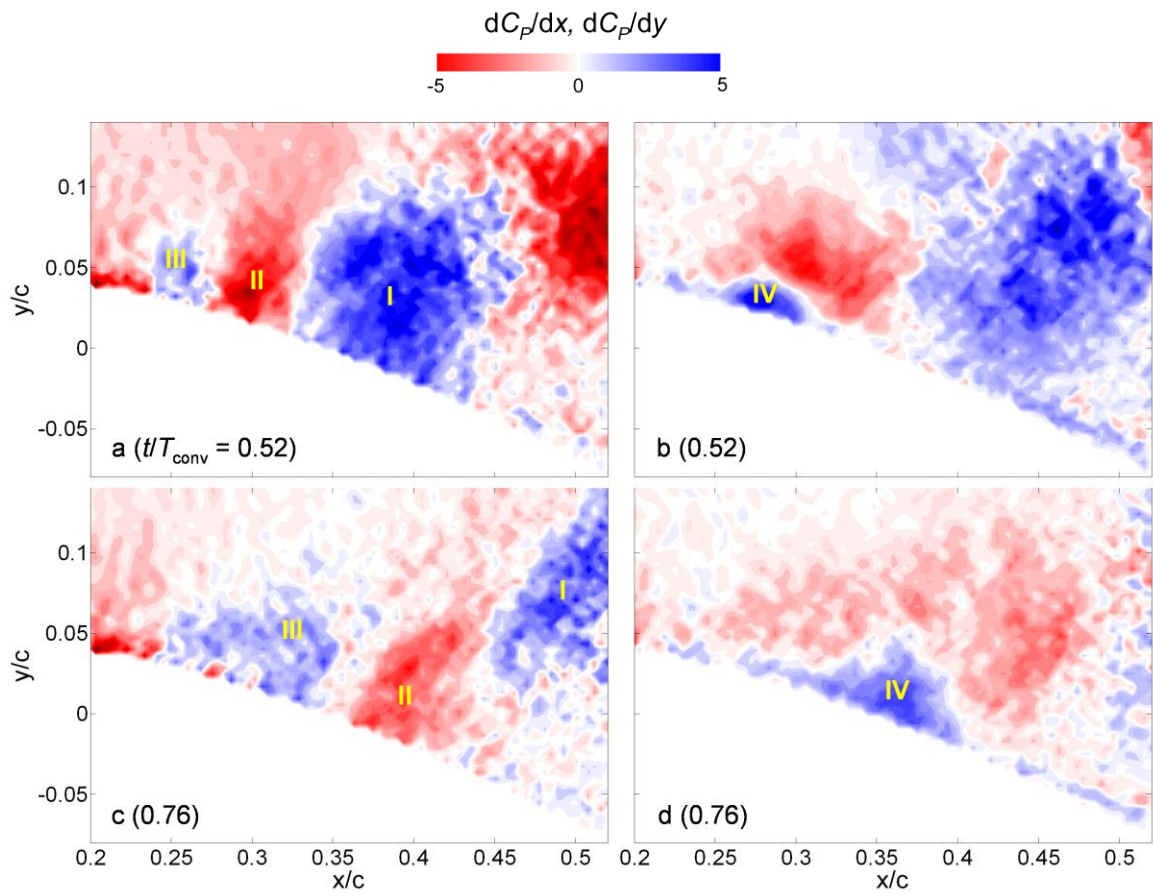


Figure 4.16: Phase-averaged raster plots of the pressure gradients, dC_p/dx (a, c) and dC_p/dy (b, d) following actuation at $t/T_{\text{conv}} = 0.52$ (a, b), and 0.76 (c, d) corresponding to the flow in Figures 4.15e and f, respectively.

CHAPTER V

SUCCESSIVE ACTUATION

This section demonstrates how the dynamics of single pulse jet actuation in the 2-D configuration of §IV can be extended to improve flow attachment over a stalled airfoil by repetitive application of the actuation to induce successive transitory interactions between the pulsed jet and the separated cross flow. The effects of variations of the actuation timing on the aerodynamic performance of the airfoil are explored first and are followed by an investigation of the flow mechanisms associated with the interaction of successive pulses with the cross flow.

5.1. Aerodynamic Performance Enhancement using Successive Actuation Pulses

5.1.1. Transitory Flow Attachment and Circulation Build-Up

The transitory increase in circulation over a stalled airfoil that is effected by single pulse actuation (*cf.*, §IV.1), can be significantly extended by exploiting the disparity between its characteristic rise and relaxation times. This is accomplished by successive actuation that is applied to take advantage of the increase in circulation that is already attained by an earlier pulse. Therefore, the objective here is to apply successive actuation to the partially-attached flow (and the recovered lift) and take advantage of the shorter characteristic response time associated with the attachment process to allow a faster buildup of circulation. Repetitive actuation can be effected either by successive pulses with a prescribed repetition rate (or period T_{rep}), or using “bursts” of N pulses each such

that the pulses within each burst have the prescribed repetition rate. The bursts can be applied either randomly or time-periodically.

To assess the effects of the repetition rate, on the lift, the pulsed actuation is repeated time-periodically with different T_{rep} or Strouhal numbers ($St_{\text{act}} = c/(U_{\infty}T_{\text{rep}})$ as based on the chord) and the lift is computed by trapezoidal integration of the time-averaged static pressure distributions on the airfoil (*cf.*, §IV.1). It is important to note that based on the pressure traces and the time-dependent circulation following single pulsed actuation (Figures 4.4 and 4.8, respectively), the highest frequency component in the pressure signal is attributed to the rise time during the attachment and is estimated to be at least 20 Hz. As described in §II, the pressure scanning system can measure at 100 Hz. However, the frequency response of the overall pressure measurement system including the tubing is estimated to be about 15 Hz and cannot resolve the rapid pressure changes. At the low pulse repetition rates (e.g., $St_{\text{act}} < 0.1$), the unsteady changes in the pressure return to baseline between successive pulses and therefore the magnitude of the measured time-averaged pressure at each port on the airfoil are underestimated. The pressure relaxation diminishes with increased repetition rate and so the measured time-averaged values are more representative of the true aerodynamic loads.. According to the traces in Figures 4.4 and 4.8, it is expected that for $St_{\text{act}} \approx 0.4$, the repeating cycles within the time-averaged pressure measurement are dominated by the actuation-induced flow dynamics that are of a similar time scale therefore only lift increments above this value are likely correct representations of the true aerodynamic loads and are shown in Figure 5.1. As shown in Figure 5.1, the increment in the time-averaged lift relative to the unforced flow, $\Delta C_L/C_{L,0}$, increases monotonically with increasing St_{act} (or decreasing T_{rep}), rapidly and

approximately linear up to $St_{\text{act}} \approx 0.4$ and ultimately asymptotes to a level that is about 36% above the lift of the unactuated (base) flow at $St_{\text{act}} \approx 1.2$. This asymptotic increase indicates that as the repetition rate of the actuation increases (or decreasing T_{rep}), its effectiveness appears to saturate.

When the actuation is applied at $St_{\text{act}} > 0.455$ the repetition period is shorter than the characteristic for attaining the peak increase in circulation following a single pulse actuation (about $2T_{\text{conv}}$ in Figure 4.8b). While it can be argued that following this characteristic time the effects of single pulse actuation begin to diminish (and fully subside within another $10\text{-}15T_{\text{conv}}$), this circulation peak may not necessarily mark the maximum extent of flow attachment to the airfoil. This timing suggests that if successive actuation is applied while the flow is still attaching as a result of an earlier pulse (e.g., $T_{\text{rep}} < 2$ for the earlier trigger), the transients associated with the attachment can be exploited to further increase the effectiveness of the actuation. However, if the repetitive actuation is applied such that the flow is able to relax between pulses (i.e., $St_{\text{act}} < 0.455$), its effectiveness may be reduced. Therefore, in what follows attention is first restricted to $T_{\text{rep}} = T_{\text{conv}}$ (i.e., $St_{\text{act}} = 1$) to elucidate these flow dynamics.

The changes in circulation relative to the base (unforced) flow, $-\Delta\Gamma(t)/\Gamma_o$, are computed from integration of the phase-averaged vorticity flux across the near wake using mid-span PIV measurements (*cf.*, §IV), and are shown in Figure 5.2 for $N = 5, 10$ and 25 (the first pulse in each sequence is triggered at $t = 0$). The time trace for $N = 1$ from Figure 4.8b is included for comparison. The changes in circulation for $N = 5$ and 10 demonstrate that the severing of the separated vorticity layer and the shedding of vorticity concentrations, that are modulated at the repetition period of the successive actuation

pulses, significantly enhance the buildup of circulation around the airfoil. The peak increases in circulation are about 41% for $N = 5$ (at $t/T_{\text{conv}} \approx 6$) and 52% for $N = 10$ (at $t/T_{\text{conv}} \approx 10$). The circulation begins to decrease monotonically thereafter as the flow begins to relax following the shedding of the last CCW vortex. A further increase in N leads to an extended duration of the flow attachment during which the circulation ultimately saturates and become “quasi-steady” at about 58% above baseline for $N > 25$, indicating that continual actuation only regulates the trapped, airfoil-bound vorticity while maintaining attachment.

The response of the flow to the actuation is demonstrated in Figure 5.3 using (PIV-measured) phase-averaged vorticity concentrations above the airfoil at $z = 0$ during the first five successive pulses with the stalled base flow shown in Figure 5.3a. As discussed in §IV, the application of the first pulse (Figure 5.3b-f) leads to the formation of a CW vortex that is induced by severing of the separating shear layer and is advected towards the trailing edge as the flow upstream attaches to the surface and results in the initial increase in circulation in Figure 5.2. The next (second) pulsed jet is triggered at $t/T_{\text{conv}} = 1$ and its effects on the flow field as measured at $t/T_{\text{conv}} < 1.28$ are shown in Figure 5.3g. It is important to note that the flow is already better attached as is evidenced by the concentrations of CW vorticity on the airfoil surface that extends to $x/c = 0.6$ compared to Figure 5.3a following the application of the first pulse, and therefore the actuation results in the rollup and shedding of a smaller CW vortex as observed in Figures 5.3h-k for $1.44 \leq t/T_{\text{conv}} \leq 1.92$. The timing of the severing of the vorticity layer by the second pulse explains the smaller circulation increment that is effected by the first pulse compared to the increment that can be achieved with a single (isolated) pulse as

shown in Figure 5.2. As expected, the attached boundary layer in Figure 5.3k following the second pulse is thinner than in Figure 5.3f (e.g., at $x/c = 0.5$). Similar shedding of a CW vortex by each of the subsequent third, fourth and fifth pulses (Figures 5.3l-p, q-u, and v-z, respectively) also leads to improved vectoring of the cross flow vorticity concentrations towards the surface. Another important feature of the successive actuation is there are no significant variations in the flow response beyond the second pulse as demonstrated by comparing vorticity distributions at the same relative time increments following each actuation pulse (e.g., compare Figures 5.3f, k, p, u and z). However, even though the evolution of the vorticity concentrations following successive actuation pulses appears similar, there is clearly accumulation of CW vorticity and shedding of CCW vorticity that contribute to the monotonic increase in circulation as shown in Figure 5.2, and is further discussed in §IV.2 using high-resolution PIV.

The flow transients associated with the actuation in Figure 5.3 ($N = 1, 5, 10$ and 25) are also observed in instantaneous pressure measurements on the airfoil using high-frequency pressure sensors (*cf.*, §II). Figure 5.4 shows the increments in the pressure coefficient, ΔC_p , relative to the static pressure in the base flow at five locations around the airfoil (marked in Figure 5.4a) following actuation at $t = 0$ (note that the pressure scales in Figures 5.4b-f are not identical). It is evident that upon actuation, the pressure on the airfoil is significantly altered. The transitory increase in suction at $x/c = 0$ and 0.24 (Figures 5.4b and c) following a single pulse is associated with the increased local velocity as the boundary layer is attaching and corresponds to the increased circulation in Figure 5.2, while the ensuing relaxation corresponds to reduction in circulation. The increases in suction at $x/c = 0$ and 0.24 are further enhanced as the number of successive

actuation pulses is increased to $N = 5, 10$ and 25 . The rate of increase in suction pressure at $x/c = 0$ and 0.24 is the same for all overlapping segments of the pressure traces indicating that the induced changes are indeed additive (as is also evident from the variation of the circulation). The pressure measurements at $x/c = 0.45$ and 0.68 on the suction surface (Figure 5.4d and e), and $x/c = 0.5$ on the pressure surface (Figure 5.4f) capture changes in pressure that are associated with the shedding of CW and CCW vorticity concentrations as a result of the induced changes in the circulation about the airfoil. Also, it should be noted that the extent of the increase in suction pressure is greatest near the leading edge as measured at $x/c \approx 0$ and 0.24 (downstream of the actuators) compared to $x/c \approx 0.45$ and 0.68 . The increases in suction at $x/c = 0.45$ follow a similar trend to the measurements upstream, although the overall increases are significantly lower (e.g., for $N = 25$, $\Delta C_p = -0.25$ in Figure 5.4d compared to $\Delta C_p \approx -1.1$ in Figures 5.4b-c). As expected, the rise in suction further downstream toward the trailing edge at $x/c = 0.68$ (Figure 5.4e) is somewhat less pronounced following each successive pulse compared to the corresponding measurements upstream owing to the diminishing local attachment effected by the pulsed actuation. However, the pressure effects associated with the passing of each rolled-up CW vortex as manifested in the fluctuations in C_p in Figure 5.4e are comparatively amplified during the local attachment of the boundary layer. In addition to the rapid attachment, the asymptotic variation of the pressure distribution on the suction surface with increased number of pulses (as evident for $N = 25$ in all the sensors for $t/T_{\text{conv}} > 10$), the transients associated with the relaxation upon termination of actuation and the oscillations associated with vortex shedding are in good agreement with measured changes in circulation as discussed in connection with

Figure 5.3 above. The increases in pressure measured by the sensor on the pressure surface at $x/c = 0.5$ as shown in Figure 5.4f are minimal compared to the suction pressures in Figure 5.4b-e. It is also interesting that the effects from increasing the number of pulses do not alter the flow over the pressure surface as manifested in the similar time traces in Figure 5.4f during the presence of actuation.

5.1.2. Burst-Modulated Pulses

The relaxation time following successive pulses as shown in the circulation and pressure transients in Figures 5.2 and 5.4, respectively, can be exploited by repeating a “burst” of N successive pulses at a low duty cycle, $D = NT_{\text{rep}}/(NT_{\text{rep}} + T_{\text{delay}})$, to maintain a desirable degree of attachment. Time-averaged pressure distributions over the airfoil (Woo et al., 2008) show that for $St_{\text{act}} = 1$ bursts, a 28% increase in lift is achieved with as little as $N = 5$ pulses (i.e., a 56% duty cycle). As an example to further elucidate the effects of pulsed “bursts”, the time-dependent vorticity flux and the corresponding change in circulation (relative to the stalled flow) are computed for two successive bursts of $N = 5$ pulses (at $T_{\text{rep}} = T_{\text{conv}}$ with $T_{\text{delay}} = 4T_{\text{conv}}$) as shown in Figures 5.5a and b. Figure 5.5a shows the phase-averaged vorticity flux at $z = 0$ from each surfaces of the airfoil (\blacktriangledown and \blacktriangle for the suction and pressure surfaces, respectively) and their sum (net flux, \blacklozenge). The vorticity flux from each surface is distinguished using the method described in connection with Figure 4.8a. It is important to note that the magnitudes of the oscillations (which correspond to the formation of vorticity concentrations that are associated with the pulses within each burst) are considerable higher on the suction surface (CW) flux, and is clearly attributable to the changes that are associated with the release and accumulation of CW vorticity within the stalled flow domain.

The corresponding flux that is associated with shedding of CCW vorticity is considerably smaller indicating that the increase in circulation during the burst (Figure 5.5b) is primarily connected with accumulation of CW vorticity on the suction surface. Time traces of the phase-averaged circulation (Figure 5.5b) show that the initial transients are similar to the circulation increment for a single burst ($N = 5$, included for reference in gray). As shown, once the actuation is terminated for a single (isolated) burst the flow begins to relax to the stalled state. However, when a second burst is applied, the circulation transients that are effected by the second burst are quite different. The second burst begins when the global circulation level is about 60% of the maximum circulation attained by the first burst and the flow is not fully separated and therefore, the second burst continues to increase the circulation (and unsteady lift). The start of the second burst is indicated by a (small) local circulation peak at $t/T_{\text{conv}} = 8$ (a similar small peak is also visible for the first burst at $t/T_{\text{conv}} \approx 0.8$). The circulation change affected by the second burst second reaches a somewhat higher peak (49%) than the first burst (45%). More importantly, the characteristic relaxation time when the actuation is terminated ($t/T_{\text{conv}} = 15$) is considerably longer than for a single burst ($16T_{\text{conv}}$ compared to $10T_{\text{conv}}$) due to the improved attachment induced by the increased N . The flow relaxation associated with the gradual lift-off of the attaching boundary layer persists longer following the second burst owing to the improved attachment.

5.2. Interactions of Repetitive Pulsed Actuation with the Cross Flow

Similar to the analysis of §IV, PIV measurements in the vicinity of the actuator orifice that are phase-locked to the actuation are used to provide some details of the boundary layer evolution and the shear layer characteristics induced by the multiple successive

pulses. These structures that are not captured in Figure 5.3 for $T_{\text{rep}} = T_{\text{conv}}$ are investigated using higher resolution PIV with emphasis on the attachment dynamics and the effects of T_{rep} .

5.2.1. Formation of Vortical Structures using Successive Pulses at $T_{\text{rep}} = T_{\text{conv}}$

The details of transitory manipulation of the separated shear layer above the airfoil are first investigated using 25 successive pulses ($T_{\text{rep}} = T_{\text{conv}}$ or $St_{\text{act}} = 1$) and phase-locked PIV measurements that are obtained at increasing delays relative to the actuation waveform. A sequence of the phase-averaged raster plots of vorticity concentrations and corresponding streamlines in Figure 5.6 show the flow transients immediately following the 1st, 5th, 10th, 15th, and 25th pulses in columns a – e, respectively. Each row (i – vi) in Figure 5.6 corresponds to the same elapsed time for each respective pulse. The separated base flow is shown in Figure 5.3a where the location of separation relative to the jet orifice is evident from the streamlines in the reversed flow.

The interaction of single pulse actuation with the cross flow is described in detail in §IV. Figure 5.6 shows that each CW vorticity concentration that is induced by the actuation merges with the vorticity layer over the surface and coalesces with the separated shear layer that ultimately rolls up to form a train of large-scale vortices. The discontinuity in the vorticity field of the shear layer due to the onset of the first pulse and the roll-up of its corresponding CW vortex is first observed at $t/T_{\text{conv}} = 0.2$ in Figure 5.6a-i and becomes more visible at $x/c = 0.25$ by $t/T_{\text{conv}} = 0.28$ (Figure 5.6a-iii). The separating layer is completely severed from the upstream attached boundary layer in Figure 5.6a-iv where the front of the attached segment of the boundary layer begins to advect towards the trailing edge (Figures 5.6a-iv to a-vi), creating a longer domain of

attached flow above the airfoil (compare Figure 5.6a-iv with a-i). The data in Figures 5.6a-i through a-vi are similar to corresponding data for single pulse actuation in Figure 4.12, demonstrating that the actuation effects of the pulsed jets in the present investigations are easily reproduced.

Similar flow dynamics repeat with the onset of successive actuation jets (Figures 5.6b-i through e-vi) where each subsequent pulse leads to additional severing of the vorticity layer near the surface and to the roll-up of the CW vorticity concentrations. As explained in §IV, the single pulsed jet acts as a transient obstruction to the approaching cross flow as clearly identified by the bending of the streamlines in the vicinity of the actuator orifice (Figures 5.6a-i, b-i, c-i, d-i and e-i). However, the progressively smaller recirculation elucidated from the streamlines (e.g., Figure 5.6e-i) and closer proximity of vorticity concentrations to the airfoil surface during these times indicate improved attachment. The large recirculation in the domain $x/c > 0.3$ at $t/T_{\text{conv}} = 0.2$ in Figure 5.6a-i is reduced in size prior to the onset of the 5th pulse in Figure 5.6b-i in addition to the movement of the separation farther downstream, and continues for the sequence of pulses. The counter-rotating vortices are increasingly more distinguishable from the shear layer vorticity probably due to decreasing interactions with the thinner, separating shear layer. The deflection of the cross flow as induced by the jet is therefore also altered as is evident in Figures 5.6a-i, b-i and c-i where the streamlines in the free stream (e.g., at $x/c = 0.3$ and $y/c = 0.15$) become increasingly vectored toward the airfoil's surface.

The ensuing interactions between the actuation-induced CW vortex and the separated cross flow during the burst that are pertinent to the attachment mechanism (§IV for the single pulse) are also observed in Figure 5.6 for the first and the repeated jets in the

sequence of pulses. Namely, the stagnation region (and $dp/dx > 0$) that is induced by the rollup of each severed CW vortex and therefore the corresponding cross stream pressure gradient dp/dy is positive, as evident from the curvatures in the streamlines near the vortex in Figures 5.6a-i, b-i, c-i, d-i, and e-i. The diminishing effects of attachment are apparent by comparing Figures 5.6a-iii & iv, b-iii & iv, c-iii & iv, d-iii & iv, and e-iii & iv. The vorticity concentrations and the streamlines in Figures 5.6a-v & vi, b-v & vi, c-v & vi, d-v & vi, and e-v & vi show that the ensuing attached boundary layer extends significantly downstream along the airfoil surface following the advection of each CW vortex induced by the first 15 pulses. This increasing attachment and the quasi-steady evolution of the flow for the subsequent pulses (e.g., Figures 5.6e-i to e-vi for the 25th pulse) are in agreement with the asymptotic increase in circulation in Figure 5.2. It is important to clarify that the performance of each actuation pulse repeated at $T_{rep} = T_{conv}$ is similar to that of a single pulse as shown in §III and that the diminishing actuation effects on the cross flow are primarily due to the fact that the shear layer over the suction surface is increasingly attached during the burst as shown in Figure 5.6. This indicates that the successive interactions between the jet and the cross flow can limit the effects of the next actuation pulse.

The evolution of multiple actuation pulses differs from that of a single pulse in several ways:

- 1 Successive actuation pulses (*cf.*, Figures 5.3 and 5.6) lead to multiple severing and rollup of the CW vorticity layer near the surface that results in cumulative improvement of boundary layer attachment and therefore of the circulation. These effects are proportional to the number of pulses within the burst;

- 2 As the attached boundary layer becomes thinner and extends farther downstream, the changes in the flow effected by subsequent pulses diminish as to the severing and rollup of the CW vortex weaken;
- 3 Despite these weakening effects, the streamwise-moving stagnation region induced by the roll-up of the CW vortex continues to entrain free stream fluid near the leading edge of the attached boundary layer to improve (or maintain) the attachment; and
- 4 These cumulative effects are directly related to the timing of each subsequent pulse (i.e., T_{rep}) or burst of pulses (i.e., T_{delay}) to enable the subsequent build-up before the effects of the previous pulses dissipate.

After the boundary layer becomes attached at the present repetition rate ($T_{\text{rep}} = T_{\text{conv}}$), subsequent pulses simply lead to modulation of the vorticity strength within the surface boundary layer downstream of the actuator. By the end of the 20th pulse at $t/T_{\text{conv}} = 19.96$ (not shown) the flow is almost fully attached within the present PIV measurement domain in Figure 5.6. In conjunction with each set of interactions between the pulsed jet and the cross flow, a pressure gradient that acts toward the airfoil surface ($dp/dy > 0$) and the accompanying adverse pressure gradient ($dp/dx > 0$) are induced by the propagating rolled-up CW vortex as discussed in §IV.

The time-evolution of the phase-averaged vorticity flux ($u\omega_z$) for the successive pulses ($T_{\text{rep}} = T_{\text{conv}}$) integrated across vertical cross stream sections of the measurement domain ($0.1 < x/c < 0.45$ comprised of three overlapping PIV windows each averaged from a data set of over 210 instantaneous realizations) are shown as an x - t contour plot of $\int(u\omega_z)dy$ in Figure 5.7 for $N = 25$. The present near-wake phase-locked PIV data are acquired in a

series of 225 equally-spaced time increments $\Delta t = 0.2T_{\text{conv}}$ that is sufficiently long to capture the attachment and relaxation processes during and following the 25 actuation pulses. This distribution clearly shows the contributions to the fluxes owing to the appearance and advection of the CW and CCW jet vortices of the first pulse at $t/T_{\text{conv}} = 0.2$ as already discussed in connection with Figure 4.13 (§IV). The advection of the CCW jet vortices is apparent from patches of positive (CCW) flux (marked in blue). As explained in connection with the single pulse actuation, these patches are discretized by the distinct time increments of the PIV measurements when the vortical structures are not present at some streamwise locations. The first pulse of the successive pulse sequence interacts with the separating cross flow in a manner that is similar to the transitory attachment induced by single-pulse actuation as manifested in the $x-t$ diagram for $t/T_{\text{conv}} < 1$. The successive severing and rollup of the large-scale CW vortices, are depicted by the streaks of low-level vorticity flux following each actuation pulse that are preceded by fluxes of strong vorticity concentrations, which appear to the left of each low-flux streaks in Figure 5.7. The severing and the associated diminution in flux become increasingly difficult to discern following the first few (≈ 5) pulses in Figure 5.7 (some low-intensity streaks are still visible for $N > 5$). Immediately downstream of the actuator $x/c > 0.15$, the flux becomes vanishingly small with time because the attached boundary layer becomes considerably thinner and cannot be sufficiently resolved by the present magnification. Similar interactions between the jet and the flow are observed for subsequent pulses ($N > 10$) in Figure 5.7 for up to the 25th pulse however, with increasing attachment as evidenced by the repeating flux streaks and the progressively (asymptotic) reduction in CW flux over the airfoil for $0.3 < x/c$. The temporal variations in the celerity

of these structures in Figure 5.7 do not appear to be directly coupled with the interactions between each successive pulse due to the sufficiently long time increment ($T_{\text{rep}} = T_{\text{conv}}$) between successive pulses.

5.2.2. Effects of Decreasing T_{rep}

As shown in Figure 5.2, a burst of successive actuation pulses with $St_{\text{act}} = T_{\text{conv}}/T_{\text{rep}} = 1$ results in a progressive increase in circulation. In this section, the changes in control effectiveness at a higher repetition rate ($T_{\text{rep}} = 0.4T_{\text{conv}}$ or $St_{\text{act}} = 2.5$) are compared with the $T_{\text{rep}} = T_{\text{conv}}$. The number of pulses is increased to $N = 50$ so that the two bursts have similar durations ($20 - 25T_{\text{conv}}$). The termination of actuation is followed by an idle period of $20T_{\text{conv}}$ to ensure sufficient time for the relaxation and separation of the attached flow. The global change in the airfoil's circulation relative to the base (unforced) flow, $-ΔI(t)/Γ_0$, is shown in Figure 5.8 for the two repetition rates. The PIV data for $St_{\text{act}} = 2.5$ are obtained using the same three overlapping views as for $St_{\text{act}} = 1$, and include a sequence of 525 phases (each phase-averaged over 200 realization) with equally-spaced time increments $Δt = 0.08T_{\text{conv}}$ (for $St_{\text{act}} = 1$, $Δt = 0.2T_{\text{conv}}$).

The circulation traces in Figure 5.8 consist of an initial period of rapid circulation buildup followed by a period of saturation at a level of approximately 55% above the stalled flow. Although the rate of increase in circulation for the initial evolution phase is somewhat faster for $St = 2.5$ ($T_{\text{rep}} = 0.4T_{\text{conv}}$) than for $St = 1$ ($T_{\text{rep}} = T_{\text{conv}}$), the duration of actuation needed to reach this maximum circulation level is similar for both repetition rates ($t/T_{\text{conv}} \sim 15$), hence it takes about 35 pulses at $St_{\text{act}} = 2.5$ compared to 15 pulses at $St_{\text{act}} = 1$. In addition to the initial transient increase in circulation, the coherent alternating CW and CCW concentrations that are from each actuation pulse and

contribute to the periodic reduction and increase (oscillations) in circulation are shown to be approximately 75% smaller for $St_{act} = 2.5$ than for $St_{act} = 1$ (Figure 5.8). The diminution in the magnitude of these oscillations in the circulation trace for $T_{rep} = 0.4T_{conv}$ is associated with the reduced circulations of each successive rolled-up CW vortex and since the performance of the actuation jet is similar for the two repetition rates as shown in §III, this reduction is due to the interactions between successive actuation vortices over the suction surface of the airfoil as shown in connection to Figure 5.9. However, the data in Figure 5.8 indicate that although modulation of vorticity concentrations over the suction surface between pulses is lower when the actuation rate is higher at $St_{act} = 2.5$ as evidenced by the shedding of vorticity into the wake, because this transient occurs at about twice the rate of $St_{act} = 1$, the total level of the induced saturated circulation by the two repetition rates are about the same. This helps explain the larger number of actuation pulses needed for $T_{rep} = 0.4T_{conv}$ to attain the same “plateau” level of the circulation for $T_{rep} = T_{conv}$ as the net effect of the each actuation pulse is somewhat diminished

While the characteristic relaxation time following the termination of the actuation is similar where both traces show a relaxation of about $15T_{conv}$ for the flow to return to the stalled state, the differences between both repetition rates are evident. There is a slight increase in circulation for $T_{rep} = 0.4T_{conv}$ immediately following the termination of actuation ($t/T_{conv} \approx 20$) that is not present in the corresponding circulation trace for $T_{rep} = T_{conv}$. As discussed in connection with the $x-t$ diagrams for these two Strouhal numbers, $T_{rep} = T_{conv}$ is sufficiently long for the boundary layer growth to be uninterrupted by the successive actuation unlike for $T_{rep} = 0.4T_{conv}$ where there are

interactions between the sequence of pulses that interrupt the streamwise development of the boundary layer as observed for the single pulse in §IV. This increase in circulation prior to relaxation (albeit brief) represents the continued build-up in CW vorticity that accompanies the streamwise growth of the attaching boundary layer following the last pulse in the sequence for $T_{\text{rep}} = 0.4T_{\text{conv}}$ that is uninterrupted in the absence of actuation. In addition to the observed differences in the circulation immediately following the termination of actuation burst in Figure 5.8, there are noticeable variations in the return to baseline for $T_{\text{rep}} = T_{\text{conv}}$ compared to the smoother relaxation process for the trace of $T_{\text{rep}} = 0.4T_{\text{conv}}$. It appears that these variations in the relaxation for $T_{\text{rep}} = T_{\text{conv}}$ are largely due to the abrupt termination of the actuation burst with a characteristic time scale between the successive pulses (and therefore the shedding of vortices) that may be commensurate with the natural wake shedding instabilities of the turbulent flow over the airfoil ($St_{\text{act}} \sim 1$). Other possible sources for the observed differences in the relaxation include the lower temporal resolution of the PIV data for $St_{\text{act}} = 1$. Another feature of these traces is the momentary increase in circulation when the higher repetition rate actuation burst is terminated. This increase is associated with the shedding of a final CCW vortex from the pressure side as the entire flow adjusts to abrupt termination of the actuation.

The differences in the evolution of multiple pulses with $T_{\text{rep}} = 0.4T_{\text{conv}}$ and T_{conv} , can be assessed from Figure 5.9 which shows the phase-averaged flow on the suction surface between $t/T_{\text{conv}} = 0.64$ and 1.12 (in increments of $0.04T_{\text{conv}}$) for $T_{\text{rep}} = 0.4T_{\text{conv}}$ (a-e, k-o and u-w) and $T_{\text{rep}} = T_{\text{conv}}$ (f-j, p-t and x-z). During this time interval, the onset of the second and third pulses are observed for $T_{\text{rep}} = 0.4T_{\text{conv}}$ while only the effects of the first

pulse are present for $T_{\text{rep}} = T_{\text{conv}}$. Note that the effects of the first pulse for $T_{\text{rep}} = 0.4T_{\text{conv}}$ are similar to $T_{\text{rep}} = T_{\text{conv}}$ in Figure 5.6. The emphasis here is on the transients between the 2nd and 3rd pulses for $T_{\text{rep}} = 0.4T_{\text{conv}}$.

It is interesting that due to the reduced pulse spacing, i.e., $T_{\text{rep}} < T_{\text{conv}}$, Figure 5.9a at $t/T_{\text{conv}} = 0.64$ clearly shows the severing and the beginning of the roll-up of the vorticity layer by the second pulse in conjunction with the streamwise growth of the boundary layer that was induced by the first pulse for $T_{\text{rep}} = 0.4T_{\text{conv}}$ (*cf.*, Figure 5.9f for $T_{\text{rep}} = T_{\text{conv}}$). This resulted in the formation of a third flow domain manifested as CW rotation concentrated within the boundary layer immediately downstream of the actuator orifice ($0.15 < x/c < 0.2$). The subsequent (faster) CW vortex advects downstream and eventually reaches the leading edge of the original boundary layer at $t/T_{\text{conv}} = 0.68$ and 0.72 (Figures 5.9b and c) while a new boundary layer is growing along the airfoil upstream of the severed layer. There is an additional stagnation region on the airfoil for the 2nd ($T_{\text{rep}} = 0.4T_{\text{conv}}$) pulsed jet within the measurement frame, which is apparent by comparing the streamlines in Figures 5.9b-e and k-o with Figures 5.9g-j and p-t. More importantly, it is conjectured that the $dp/dy > 0$ (§4) from this second stagnation combines with the previous stagnation located further downstream to contribute to the attachment, improving beyond that achieved within the same time lapse by only the first pulse of the $T_{\text{rep}} = T_{\text{conv}}$ configuration (*cf.*, Figures 5.9o and t). These flow dynamics, albeit gradually diminishing, repeat with the third pulse as shown in Figures 5.10u-w for $1.04 < t/T_{\text{conv}} \leq 1.12$ while the flow in Figures 5.9x-z for $T_{\text{rep}} = T_{\text{conv}}$ remains partially attached, but appears to begin relaxation just prior to the onset of the second pulse.

The continuing attachment induced by the subsequent pulsed jets for $T_{\text{rep}} = 0.4T_{\text{conv}}$ and T_{conv} are further compared. Figures 5.10a-e show the phase-averaged flow for $T_{\text{rep}} = 0.4T_{\text{conv}}$ as direct comparisons to Figures 5.6b-iv, c-iv, d-iv, and e-iv for $T_{\text{rep}} = T_{\text{conv}}$ following the onset of the 5th, 10th, 15th and 25th jet. The counter-rotating jet vortices appear more diffuse and distorted in Figure 5.10, suggesting increased mixing with and entrainment of the free stream flow for reduced temporal spacing between successive pulses. It is also expected that the downstream bending of the jet in the cross flow is amplified due to the increased momentum of the approaching flow, and that the pulsed jet is likely penetrating through the thinner boundary layer and further into the free stream. Perhaps more important is the improved attachment for $T_{\text{rep}} = 0.4T_{\text{conv}}$ as evidenced in the enhanced accumulation of vorticity and the noticeable flow vectoring towards the airfoil surface, although with twice the actuation pulses (e.g., compare the flow following the 25th ($T_{\text{rep}} = T_{\text{conv}}$) and 50th ($T_{\text{rep}} = 0.4T_{\text{conv}}$) pulsed jets at $t/T_{\text{conv}} = 24.96$ (Figure 5.6e-vi) and 20.24 (not included in Figure 5.10), respectively. .

The flow effects of the actuation burst that is triggered at $t = 0$ when T_{rep} is further reduced to $0.285T_{\text{conv}}$ (i.e., $St_{\text{act}} = 3.5$) are compared to $St_{\text{act}} = 2.5$ and 1. Although not shown, the flow effects of the first pulse in the $St_{\text{act}} = 3.5$ burst on the separated flow over the airfoil are similar to that of a single pulse (*cf.*, §IV) which is in agreement with the observations shown previously in connection with Figures 5.3, 5.6 and 5.9 for the corresponding first pulse with $St_{\text{act}} = 2.5$ and 1. The flow effects as manifested in the phase-averaged vorticity concentrations following the 2nd pulse within the $St_{\text{act}} = 3.5$ burst for $0.4 < t/T_{\text{conv}} < 0.8$ are shown in rows (i)-(vi) in Figure 5.11c. The corresponding phase-averaged data during this time for $St_{\text{act}} = 1$ and 2.5 that represent the effects

following the 1st and 2nd pulses in the burst previously discussed in connection with Figure 5.10 are shown for reference in Figures 5.11a and b, respectively. The notably earlier formation of the rolled-up CW vortex as induced by the second pulse owing to the reduction in T_{rep} for $St_{\text{act}} = 3.5$ in Figure 5.11c-i (*cf.*, Figure 5.11b-i) results in earlier interaction with the boundary layer, which occurs on significantly shorter time scale than following the first pulse (*cf.*, §IV and column a in Figure 5.11). The most apparent evidence of this earlier interaction (or interruption) is manifested in the absence of the bull-nose leading edge of the boundary layer in Figure 5.11c-i (*cf.*, Figure 5.11b-i). In the subsequent phase-averaged flow fields during the downstream advection of the CW (and CCW) vortex in rows (ii) – (vi) in Figure 5.11c, the flow induced by the CW vortex is significantly closer to the airfoil surface and occupies a smaller streamwise and cross stream extent in comparison to $St_{\text{act}} = 2.5$ in column (b) of Figure 5.11 where the CW vortex is shown to ultimately reach the bull-nose of the boundary layer. The pulsed actuation mechanism that lead to the continued flow attachment over the airfoil at the reduced timing T_{rep} of $St_{\text{act}} = 3.5$ remain unchanged from that of the single pulse in §IV and for $St_{\text{act}} = 1$ and 2.5. However, the data in Figure 5.11 suggest a subtle distinction in the mechanism. In addition to the CW vortex from the second pulse, the increasing CW flow at the bull-nose as the boundary layer grows downstream (e.g., Figures 5.11a-v and b-v for $St_{\text{act}} = 1$ and 2.5, respectively) that is absent for $St_{\text{act}} = 3.5$ in Figures 5.11c (i – vi) help delay the separation process by maintaining the stagnation point induced following the 1st pulse close to the airfoil surface (e.g., Figure 5.11c-v compared to Figure 5.11b-v), thereby enhancing the flow attachment. To further examine the actuation effects for the reduced T_{rep} in a burst, the phase-averaged PIV data following the 3rd pulse between

$St_{act} = 1, 2.5$ and 3.5 are compared in columns (a) – (c) of Figure 5.12, respectively. As discussed in connection with Figure 5.11, the CW flow over the airfoil is reduced as manifested by the minimal recirculation in the streamlines for $St_{act} = 3.5$ in column (c) of Figure 5.12 where the interruption of the boundary layer flow is clearly evident. Conversely, the corresponding effects following the 3rd pulse for $St_{act} = 1$ and 2.5 in columns (a) and (b), respectively, exhibit the CW flow that is induced by the previous (2nd) and the present (3rd) pulses.

The corresponding $x-t$ vorticity flux diagrams for the increased repetition rates $T_{rep} = 0.4T_{conv}$ and $0.285T_{conv}$ are shown in Figures 5.13a and b, respectively (*cf.*, Figure 5.7 for $T_{rep} = T_{conv}$). These $x-t$ plots demonstrate that for $T_{rep} < T_{conv}$, there are significant interactions within the measurement domain between the vortical structures induced by each repeated actuation pulse owing to their different propagation speeds as elucidated in Figure 5.7. Perhaps the most prominent feature is the fact that in Figure 5.7, the reduced CW flux associated with the severing of the vorticity layer and the roll-up of the CW vortices is the most prominent for the interaction between the first jet pulse and the cross flow. This is also in agreement with the corresponding increments in circulation effected by the first pulse as shown in Figure 5.2. Similarly, the rollup of successive CW vortices is less pronounced than the first although there is apparent modulation of the vorticity within the boundary layer. Furthermore, these $x-t$ diagrams indicate that the successive pulses begin to interact with each other over the airfoil within the streamwise extent of the present PIV window as marked by dashed region. These interactions are manifested by the rolled-up vortices reaching the attaching boundary layer induced by each previous pulse at locations downstream of the actuator. It is conjectured that these interactions

limit the circulation of the rolled-up CW vortices, as is evidenced by the reduced oscillations in the time traces of the phase-locked circulation at an increased repetition rate (Figure 5.8). The interactions also explain the higher initial circulation increments following a single pulse than for the first pulses of actuation burst at $T_{\text{rep}} = T_{\text{conv}}$, $0.4T_{\text{conv}}$, and $0.285T_{\text{conv}}$ ($St_{\text{act}} = 1, 2.5$ and 3.5 , respectively). Recall that for $St_{\text{act}} = 1$ (Figure 5.7), these interactions between two sequential actuation pulses are not evident in the measurement domain, but the differences in propagation velocities of the structures (i.e., the faster CW vortices and the slower attaching boundary layer) are expected to lead to the interaction between the jet-induced vortices of successive pulses downstream of the measurement domain. Due to the shorter delay between the pulses for $St_{\text{act}} = 2.5$ and 3.5 , the interaction domains are now within the measurement domain (Figure 5.13). The interaction region is closer upstream to the jet orifice for each pulse for $St_{\text{act}} = 3.5$ than it is for $St_{\text{act}} = 2.5$. From these observations, it is apparent that the reduced temporal spacing (T_{rep}) between successive pulses continues to limit the development of the rolled-up CW vorticity concentrations and the attaching boundary layer, and perhaps even interrupts the attachment induced by each pulse at the higher repetition rates (increasing St_{act}). This interaction between the successive pulses is not expected to have an adverse effect on the attachment and explains the correspondingly increased number of pulses required to attain similar increments in the circulation for lower St_{act} (*cf.*, the circulation traces in Figure 5.8).

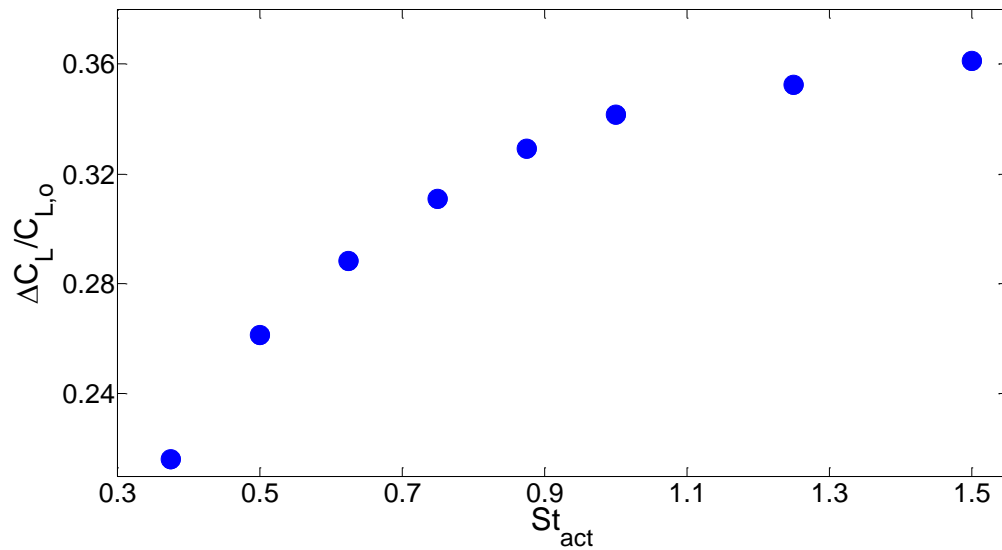


Figure 5.1: Lift increment induced by time-periodic pulse actuation with increased repetition rate St_{act} .

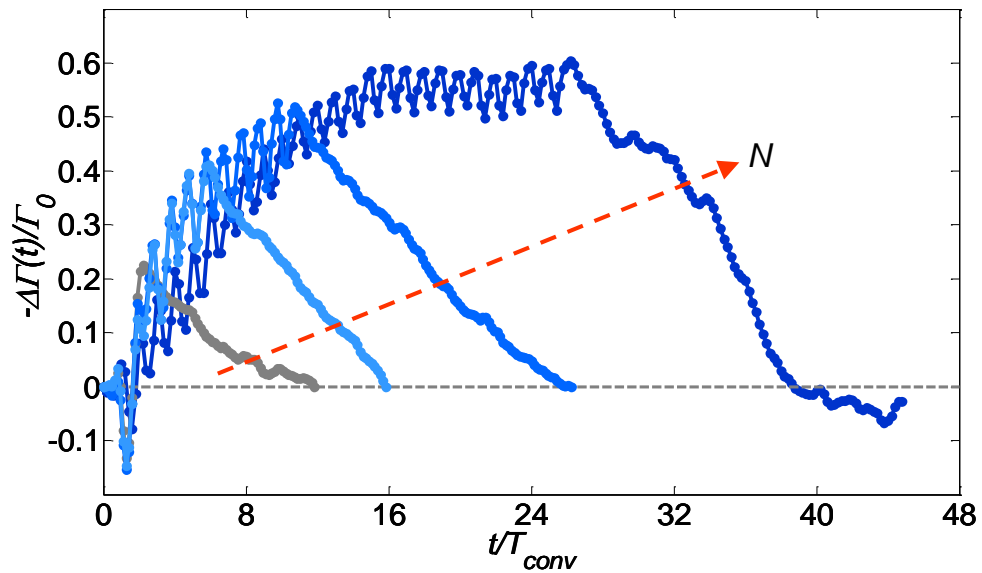


Figure 5.2: Time traces of the incremental change in circulation around a static airfoil following repetitive actuation with $N = 1$ (\bullet), 5 (\bullet), 10 (\bullet), and 25 (\bullet) pulses ($T_{rep} = T_{conv}$).

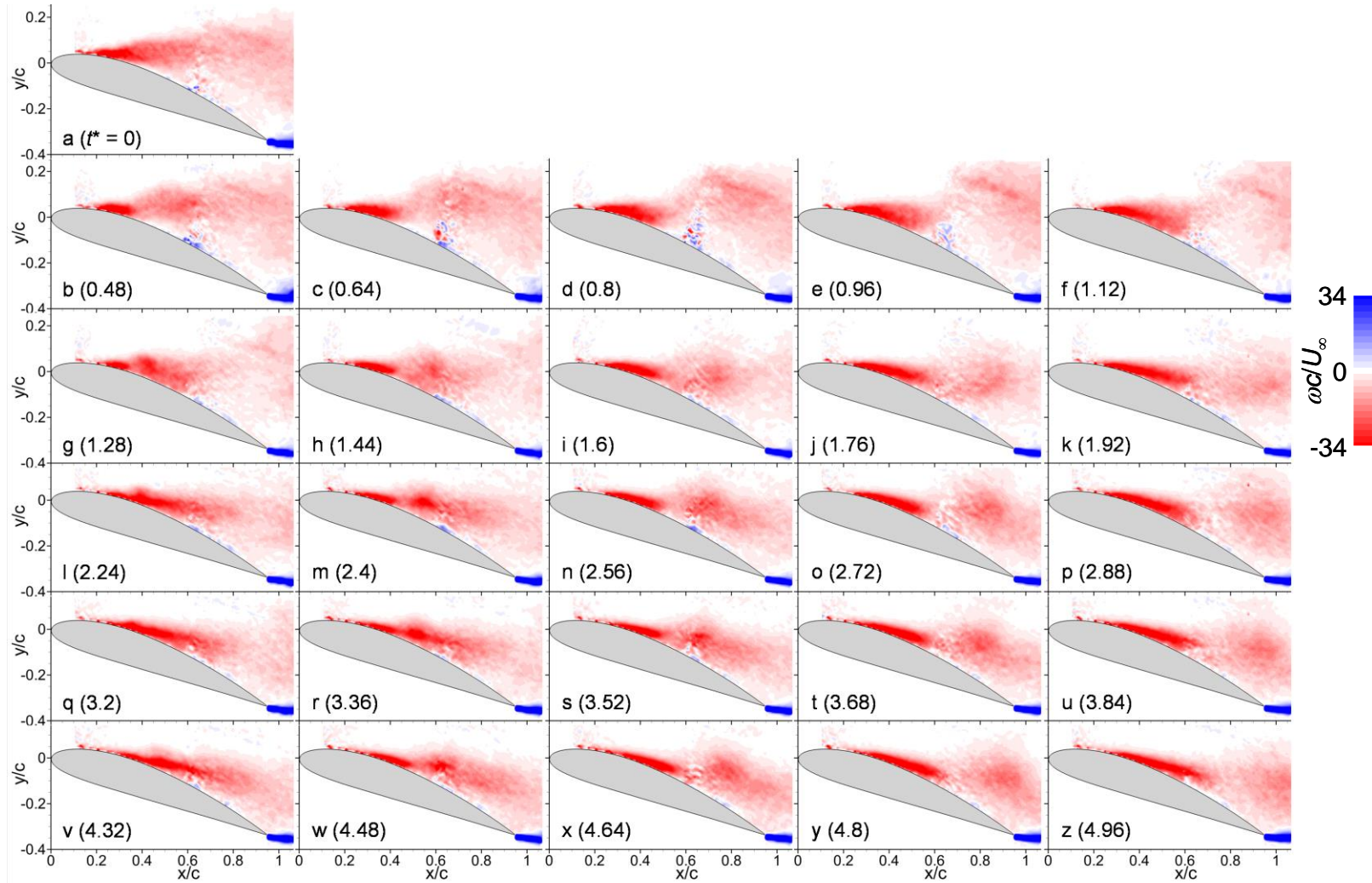


Figure 5.3: Phase-averaged vorticity over the airfoil following the 1st (b-f), 2nd (g-k), 3rd (l-p), 4th (q-u) and 5th (v-z) successive pulses separated ($T_{\text{rep}} = T_{\text{conv}}$). The base flow is shown in (a).

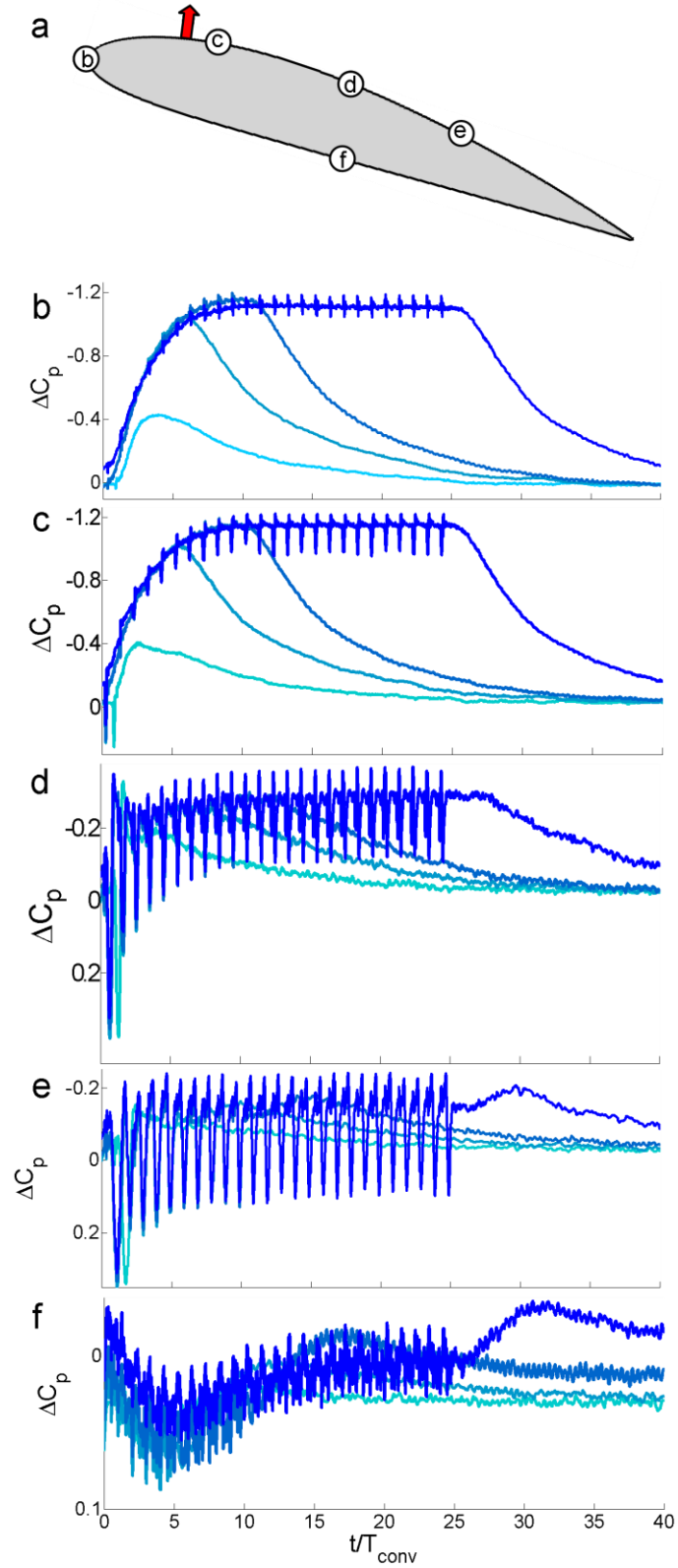


Figure 5.4: Instantaneous pressure distributions around the airfoil at $x/c = 0$ (b), 0.24 (c), 0.45 (c), 0.68 (d) on suction side and 0.5 (f) on pressure side for $N = 1$ (—), 5 (—), 10 (—) and 25 (—) pulses at $St_{act} = 1$. The pressure sensor locations (b - f) are marked in (a).

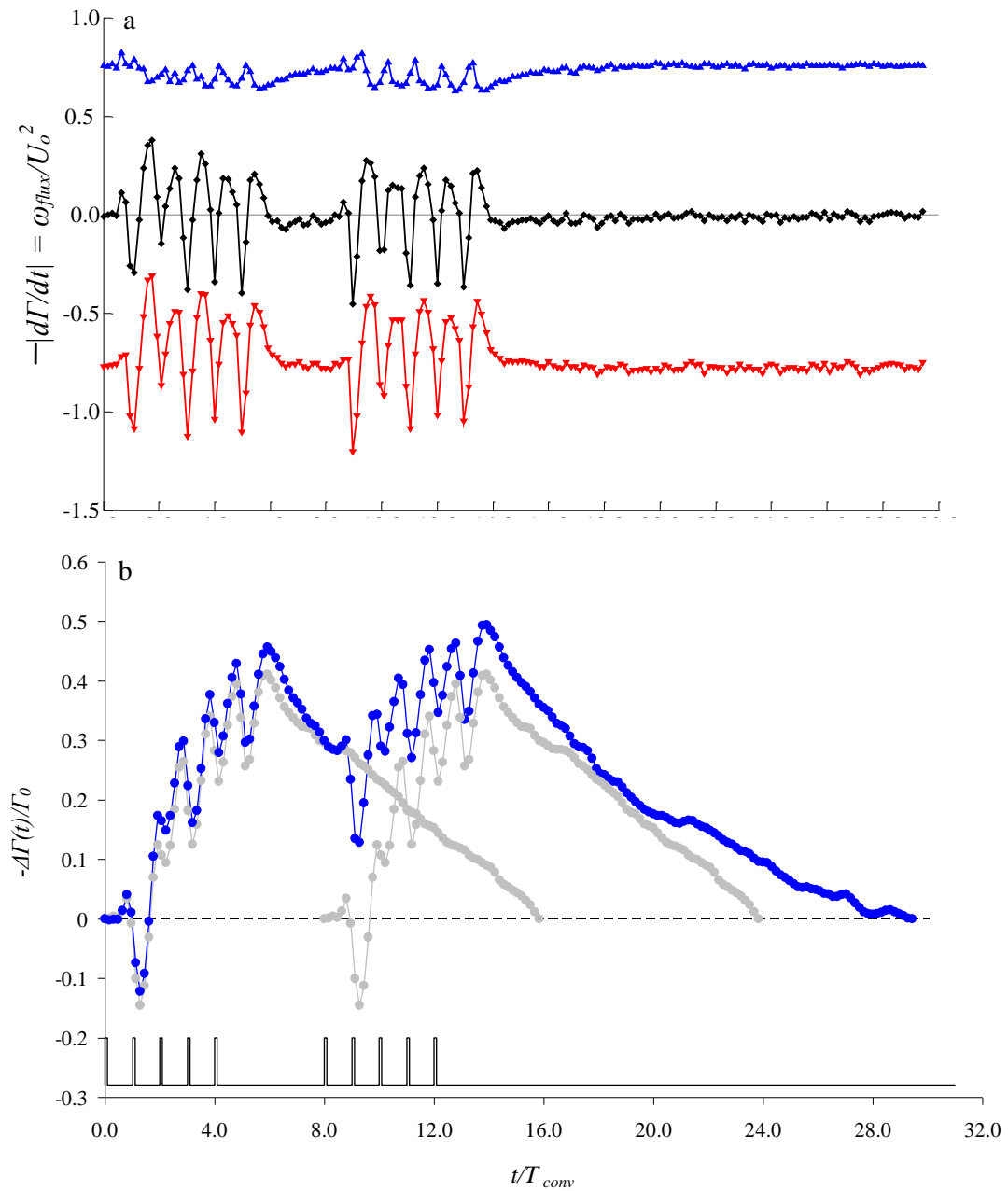


Figure 5.5: (a) Temporal variation of the normalized vorticity flux for two consecutive repeating actuation bursts ($N=5$) with $T_{\text{delay}}=4T_{\text{conv}}$: Suction surface (negative) flux (\blacktriangledown), pressure surface (positive) flux (\blacktriangle), and the net flux (\blacklozenge). (b) The corresponding incremental changes in circulation (\bullet). Circulation for a single burst ($N=5$) are shown for reference in gray (\bullet).

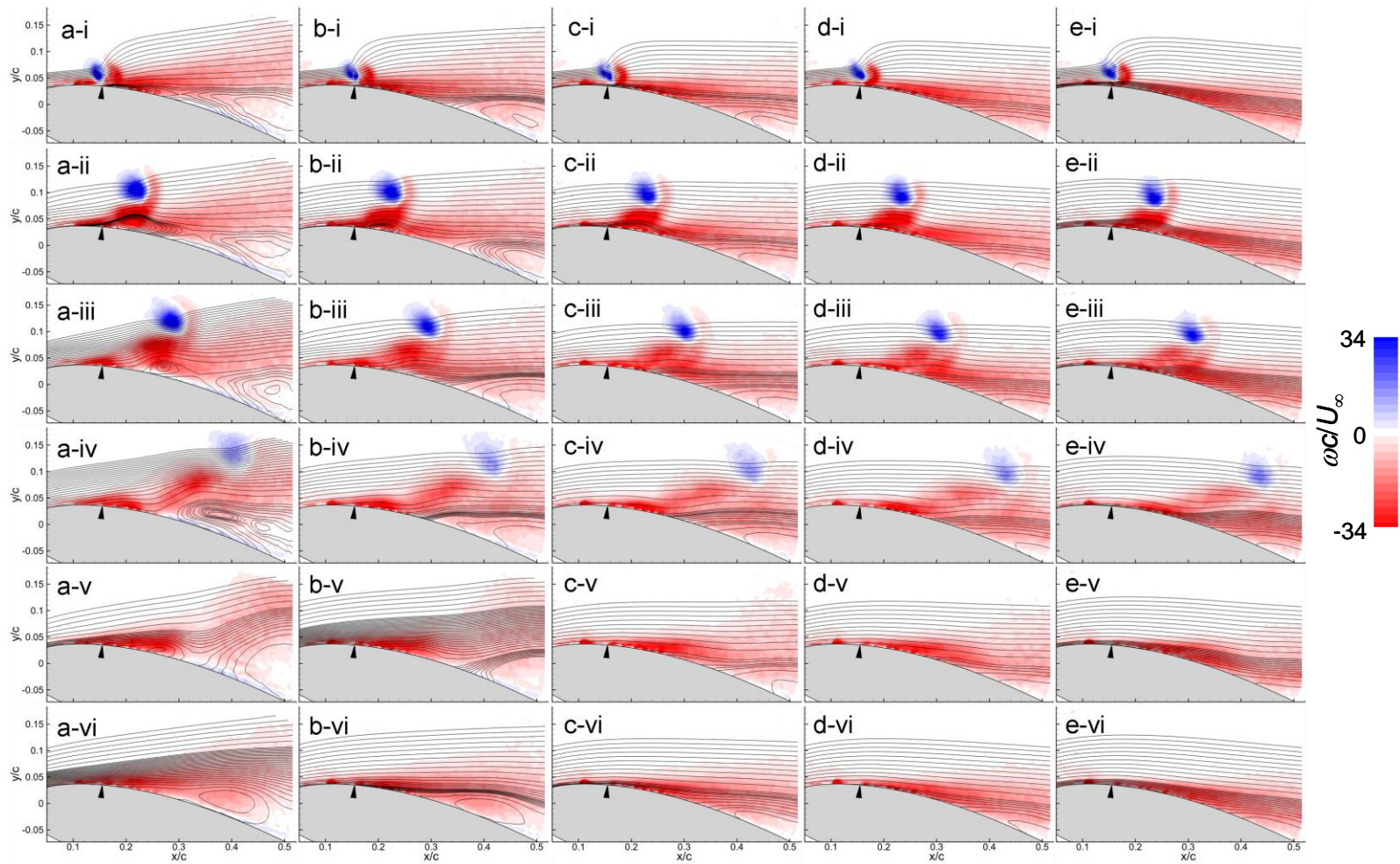


Figure 5.6: Phase-averaged vorticity in the vicinity of the actuator orifice showing the interactions between the actuation jet and the cross flow following the 1st (a), 5th (b), 10th (c), 15th (d), and 25th (e) pulses separated by $T_{\text{rep}} = T_{\text{conv}}$. The PIV timing is shown in Table 5.1. Streamlines are included and streamwise location of actuators is marked by triangle.

Table 5.1: Timing of PIV images in Figure 5.6 following the 1st (a), 5th (b), 10th (c), 15th (d), and 25th (e) pulses separated by $T_{\text{rep}} = T_{\text{conv}}$.

	a	b	c	d	E
i	0.2	4.2	9.2	14.2	24.2
ii	0.24	4.24	9.24	14.24	24.24
ii	0.28	4.28	9.28	14.28	24.28
iv	0.36	4.36	9.36	14.36	24.36
v	0.56	4.56	9.56	14.56	24.56
vi	0.96	4.96	9.96	14.96	24.96

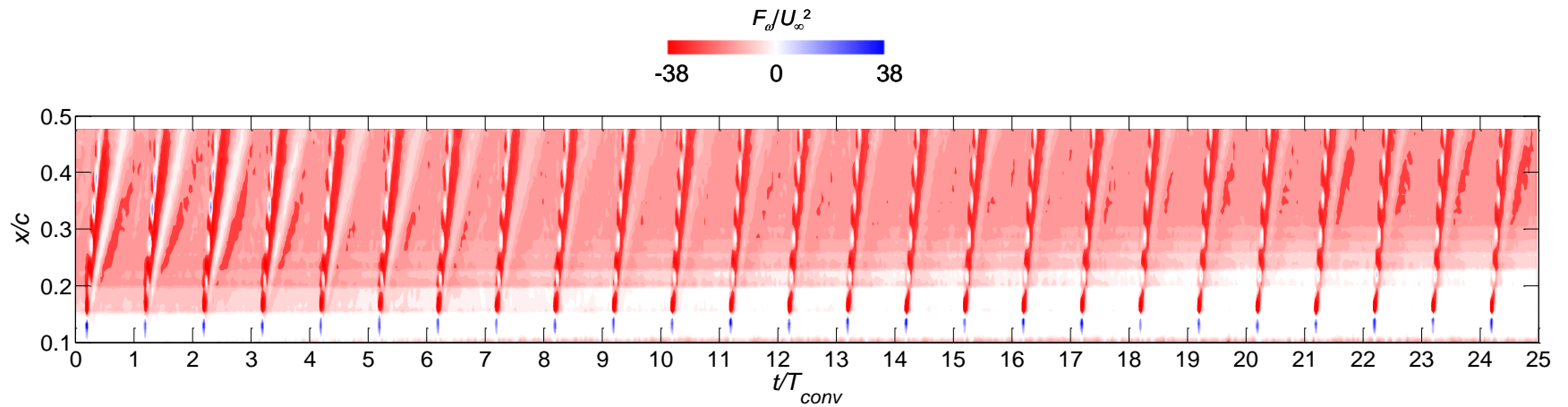


Figure 5.7: x - t raster plots of phase-averaged vorticity flux for 10 successive actuation pulses ($T_{\text{rep}} = T_{\text{conv}}$) showing the differences in propagation speeds of the induced vorticity concentrations. Vorticity flux levels are the same as in Figure 5. Arrows indicate location of the actuators.

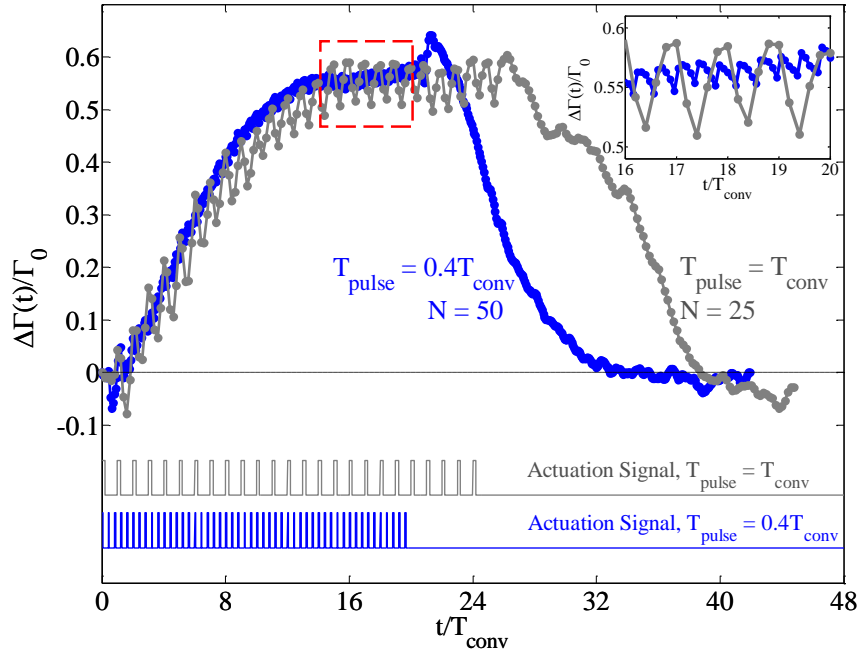


Figure 5.8: Phase-averaged circulation increments induced by repetitive burst actuation $N=50$ and $T_{\text{rep}} = 0.4T_{\text{conv}}$ (blue) and $N=25$, $T_{\text{rep}} = T_{\text{conv}}$ (gray). Actuation timing is shown below the traces.

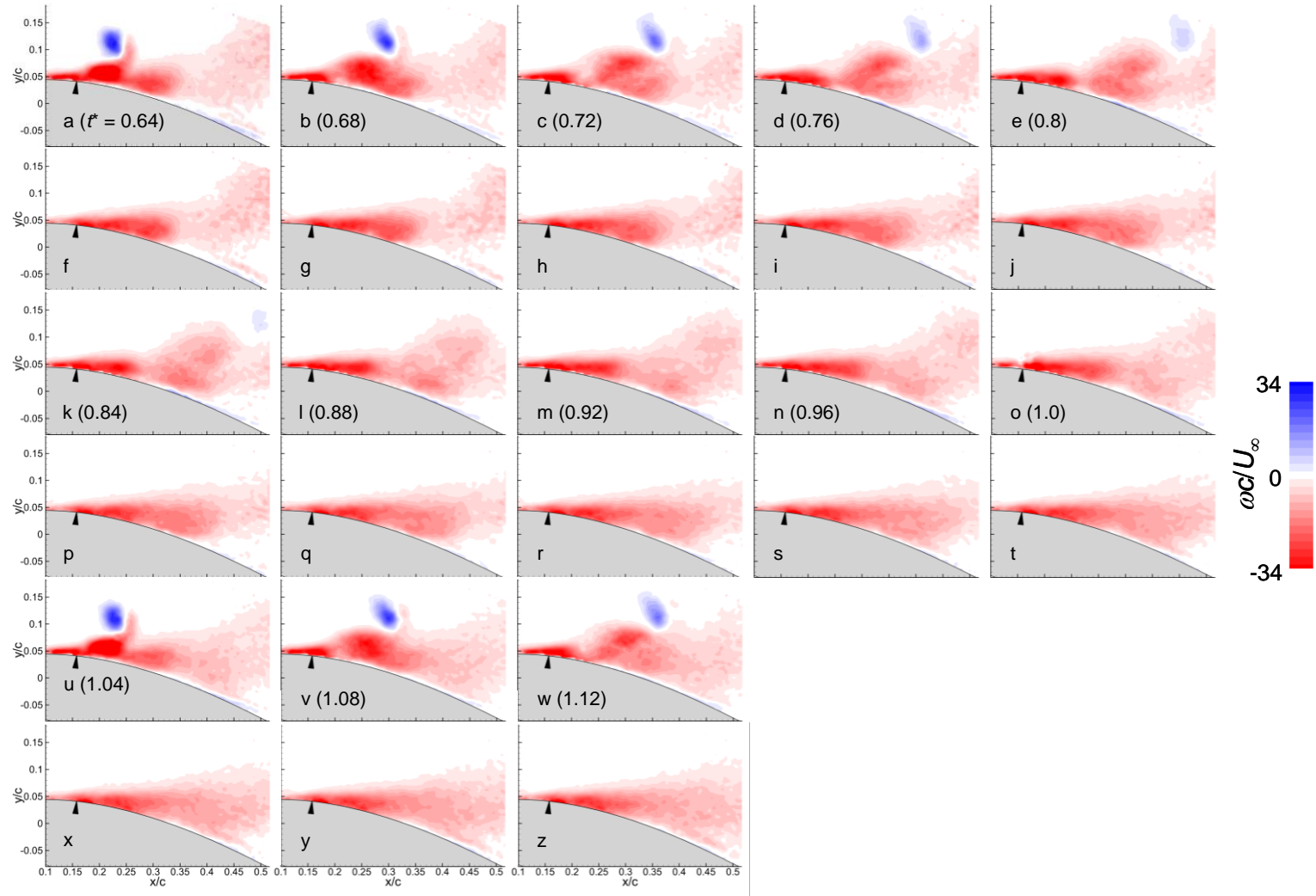


Figure 5.9. Phase-averaged vorticity in the vicinity of the actuator orifice showing the interactions between the actuation jet and the cross flow following the 1st pulse separated by $T_{\text{rep}} = 0.4T_{\text{conv}}$ (a-e, k-o and u-w) and $T_{\text{rep}} = T_{\text{conv}}$ (f-j, o-t and x-z).

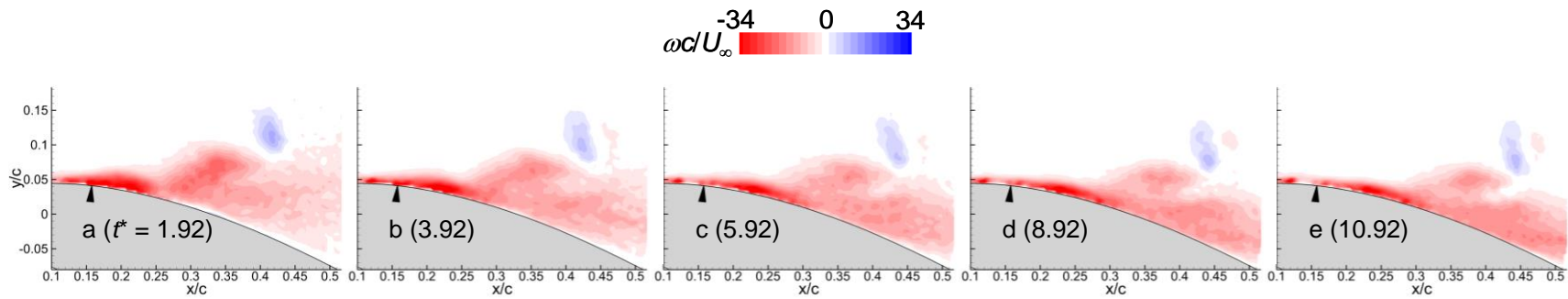


Figure 5.10: Phase-averaged vorticity in the vicinity of the actuator orifice showing the interactions between the actuation jet and the cross flow separated for $T_{\text{rep}} = 0.4T_{\text{conv}}$.

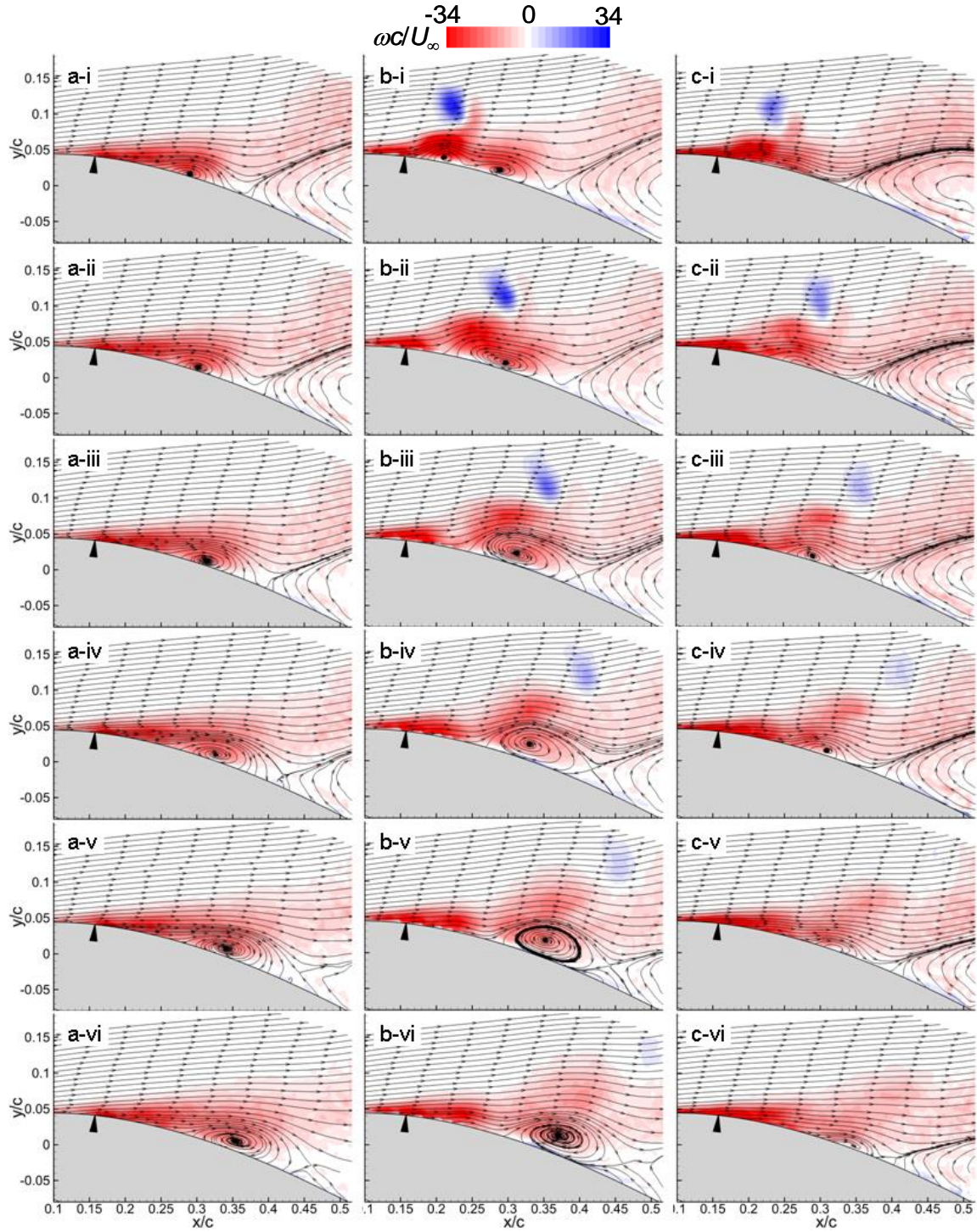


Figure 5.11: Phase-averaged vorticity superimposed with streamlines showing the successive actuation effects at $t/T_{\text{conv}} = 0.6$ (i), 0.64 (ii), 0.68 (iii), 0.72 (iv), 0.76 (v), and 0.8 (vi) for $St_{\text{act}} = 1$ (a), 2.5 (b) and 3.5 (c). During these times, the effects are following the 1st (a) and 2nd (b and c) pulses.

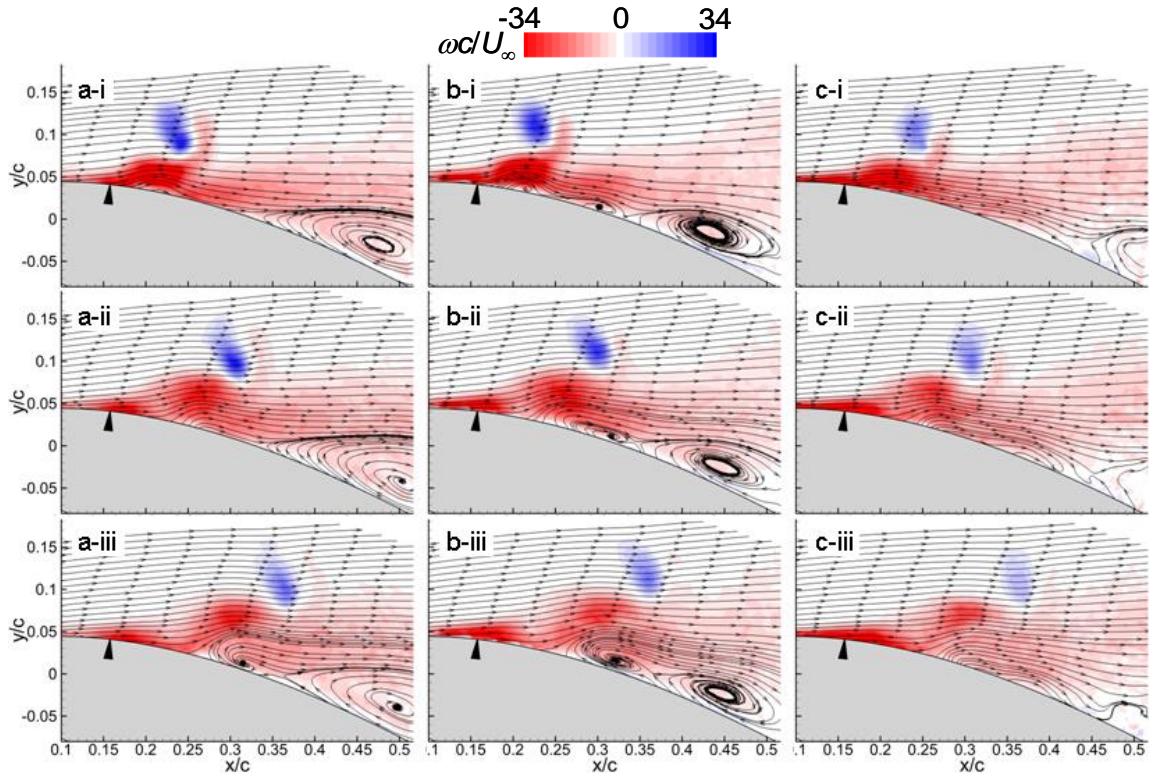


Figure 5.12: Phase-averaged vorticity superimposed with streamlines showing the successive actuation effects following the 3rd pulse for $St_{act} = 1$ at $t/T_{conv} = 2.24, 2.28$ and 2.32 (a-i to a-iii), $St_{act} = 2.5$ at $t/T_{conv} = 1, 1.04$ and 1.08 (b-i to b-iii), and $St_{act} = 3.5$ at $t/T_{conv} = 0.84, 0.88$ and 0.92 (c-i to c-iii).

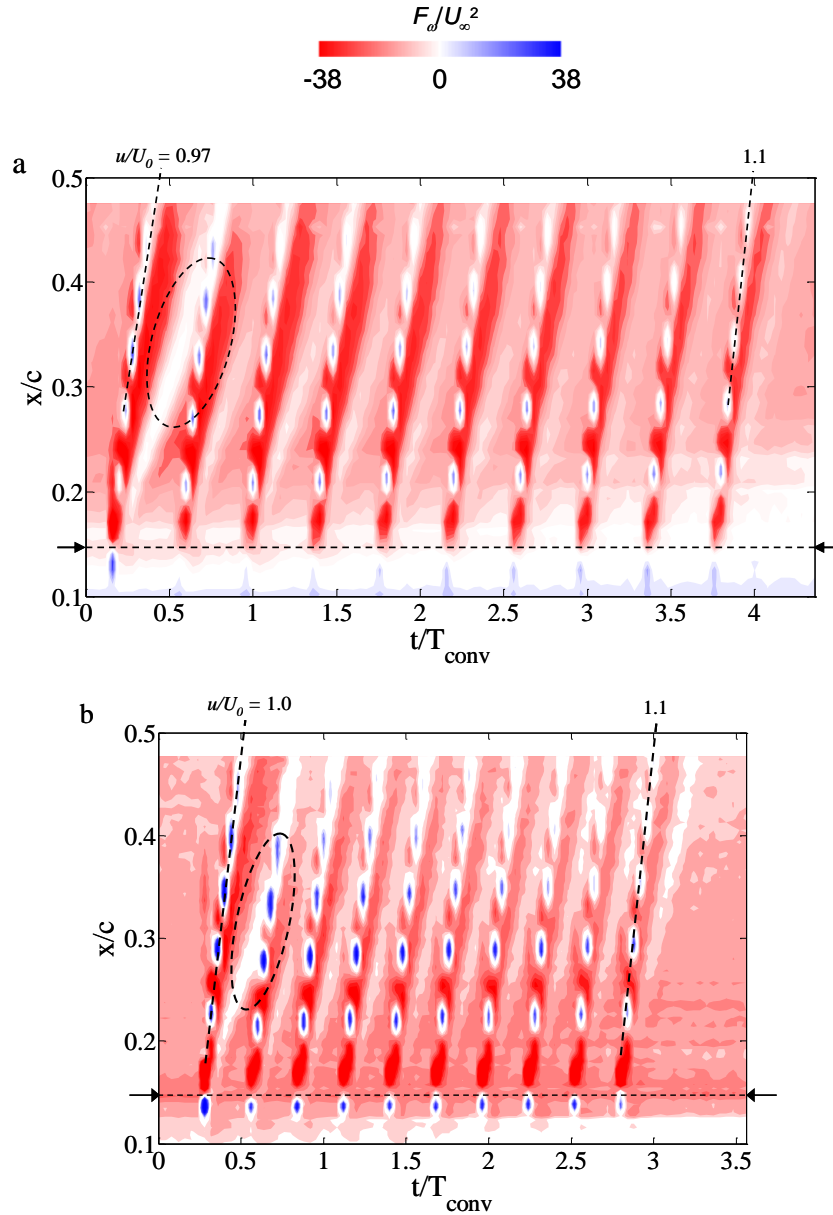


Figure 5.13: x - t raster plots of phase-averaged vorticity flux for 10 successive actuation pulses at $T_{\text{rep}} = 0.4T_{\text{conv}}$ (a) and $T_{\text{rep}} = 0.285T_{\text{conv}}$ (b), showing the differences in propagation speeds of the induced vorticity concentrations and the interactions between the vorticity concentrations within the measurement domain. Enclosed dashed region indicates the interaction between the first and second pulses. Arrows indicate streamwise location of the actuator array.

CHAPTER VI

FINITE-SPAN UNBOUNDED TRANSITORY ACTUATION IN A NOMINALLY 2-D SEPARATED FLOW

In §IV and V, nominally 2-D transitory attachment is effected by single and repetitive actuation pulses on a static airfoil along the entire span of the airfoil's center segment between two partitions such that $S_{\text{act}} = S_{\text{fence}} = 0.35c$. As shown, bounded pulsed actuation results in momentary flow attachment and in a corresponding increase in circulation. In this section, the dynamic effects of unbounded pulsed actuation on flow attachment are investigated when the airfoil partitions are extended ($S_{\text{fence}}/c = 1.07$), increasing the span of the separated flow domain over the center segment of the airfoil well beyond the width of the finite-span actuator array.

6.1. Unbounded Attachment

6.1.1. Characterization of the Separated Flow

The spanwise structure of the separated flow between the fences is characterized using PIV measurements in multiple equally-spaced ($\Delta z \approx 5 \text{ mm} \approx 0.011c$) cross stream (x - y) planes within the domain $0 \leq z/c \leq 0.295$ where each plane is comprised of two, partially-overlapping fields of view that cover the streamwise domain $0.47 < x/c < 1.46$. Owing to limited optical access, data at $z/c \approx 0.033, 0.066, 0.230, 0.241$ are not available, resulting in a total of 24 measurement planes. The distance between the outermost spanwise plane at $z = 0.295c$ and the nearby fence ($z/c \approx \pm 0.54$) is $0.24c$. As noted in §II, the laser optics,

cameras and fog sheet are moved in 5 mm increments for each plane of PIV measurements, and the camera views are recalibrated following each adjustment.

The PIV data in five of the cross stream planes at $z/c = 0, 0.08, 0.175, 0.219,$ and 0.284 (the last two planes are located beyond the spanwise edges of the actuator array at $z/c = \pm 0.175$) are shown in Figure 6.1. The spanwise uniformity of the flow is illustrated using overlaid cross stream line distributions of the time-averaged streamwise velocity, u , that are measured at three streamwise locations $x/c = 0.64, 0.94,$ and 1.23 (Figures 6.1a-c, respectively). The streamwise onset of flow separation appears to be somewhat delayed as z increases as evidenced by the corresponding decrease in the magnitude of the reversed flow ($u < 0$) at $x/c = 0.64$ (Figure 6.1a). This reversed flow in Figure 6.1a decreases by about 20% from the center plane ($z = 0$) to the outermost plane ($z/c = 0.284$) where there is little to no reversed flow with $u \approx 0$ and the velocity distribution is almost invariant with y near the surface, indicating that the instantaneous flow fluctuates between attached and separated states.

Although the magnitude of the reversed flow decreases with increasing z from the mid-plane, the cross stream width of the separated flow as measured by the cross stream width, Δy , of the reversed flow domain is nearly spanwise-invariant (e.g., $\Delta y \approx 0.15c$ in Figure 6.1a). By comparing Figures 6.1a-c, it is apparent that the separation (as measured by flow reversal) intensifies further downstream towards the trailing edge. Domains of $u < 0$ are pronounced for $x/c = 0.94$ and 1.23 (Figures 6.1b and c) while only partially noticeable across the span further upstream at $x/c = 0.64$ (Figure 6.1a). For example, the measured peak of $u/U_\infty \approx -0.25$ and the cross stream width of reversed flow, $\Delta y \approx 0.3c$, in the center plane at $x/c = 0.94$ (Figure 6.1b) increase by nearly 50% and

100% from $x/c = 0.64$, respectively. The u velocity deficit is clearly apparent in the near wake at $x/c = 1.23$ (Figure 6.1c) where the peak magnitude of the reversed flow decreases by up to $0.2U_\infty$ between $z = 0$ and $0.284c$. Similar to Figure 6.1a, the cross stream widths of the separated flow in Figures 6.1b and c remain almost invariant with z , indicating that the shear layer flow is reasonably spanwise uniform. Although there are some measurable spanwise variations in u within the reversed flow (20%) that exhibit a decrease in the strength of the separation with increasing z , these variations are reasonably small. Moreover, *the velocity distributions across y outside of the reversed flow domain are nearly identical at all spanwise planes of a given streamwise station.* Therefore, the time-averaged base (separated) flow may be taken to be nearly two-dimensional. This notion is further supported by considering the spanwise distribution of the time-averaged spanwise vorticity, ω_z , in the 24 planes of PIV data ($z/c = 0$ to 0.295), which is shown as iso-surfaces (mirrored about $z = 0$) in Figure 6.1d. Although no surface oil visualization was performed for the current base flow with $S_{\text{fence}}/c \approx 1$, the flow visualization for the expanded center segment ($S_{\text{fence}}/c \approx 1.7$) in Figure 7.1 indicates that the flow is reasonably symmetric about the center plane. Furthermore, in connection to Figure 7.2, the present flow results are mirrored about $z = 0$ to help visualize the 3-D flow features, albeit the flow physics of the actuation are assumed independent of the symmetry. These iso surfaces of the CW and CCW vorticity concentrations in Figure 6.1d clearly exhibit reasonable spanwise-uniform distributions over the airfoil and in the near wake for both the pressure and suction surfaces. As shown in the following sections, the unbounded “spanwise-limited” or “finite-span” ($S_{\text{act}} < S_{\text{fence}}$) pulsed actuation effects transitory attachment on this nearly 2-D base flow similar to the 2-D

bounded actuation in §IV, albeit with significant amplification of three-dimensional effects, namely in the spanwise non-uniform attachment.

6.1.2. Single Pulse, Spatially-Compact Actuation

The flow dynamics induced by a single unconfined actuation pulse are assessed from phase-locked PIV measurements in the near wake obtained at successive time increments relative to the onset of the actuation where each phase is averaged over 200 realizations. Figure 6.2 shows color raster plots of spanwise vorticity concentrations superimposed with velocity vectors in the near wake of the airfoil ($0.95 < x/c < 1.45$, $-0.2 < y/c < 0.6$). The 3-D actuation effects are elucidated from measurements in the cross stream planes $z/c = 0$ and 0.22 (rows b and c in Figure 6.2, respectively), and are compared with the corresponding 2-D effects from the bounded actuation discussed in §IV that are shown for reference in row a in Figure 6.2 at the same phase delays relative to the actuation trigger. The illustrations to the left of each row show the position of the PIV plane relative to actuators marked as arrows and the fences. Note that the off-center ($z = 0.22c$) flow field in Figures 6.2c-i to c-vii is measured beyond the spanwise edges of the actuator array at $z \approx \pm 0.18c$.

Figures 6.2a-i, b-i and c-i show the stalled flow at the actuation trigger ($t = 0$) and, as noted in §IV, the onset of the pulsed jets that are located at $x/c = 0.15$ follow about $0.2T_{\text{conv}}$ later. There are subtle differences between these two nominally 2-D base flows as manifested by the increased concentrations of the CW vorticity when the fences are farther apart, $S_{\text{fence}}/c = 1.07$, in Figures 6.2b-i and c-i compared to $S_{\text{fence}}/c = 0.35$ in Figure 6.2a-i. In addition, it appears that the cross stream and streamwise extents of the

recirculation flow at the center plane in Figure 6.2a-i ($S_{\text{fence}} = 0.35c$) are smaller than in Figure 6.2b-i ($S_{\text{fence}} = 1.07c$).

The advection of a rolled-up CW vortex owing to the transitory disruption and severing of the separating shear layer by the unbounded actuation jets is evident in the near wake (e.g., $t/T_{\text{conv}} = 1.28$, Figures 6.2b-ii and c-ii), which is similar to the near-wake effects of the spanwise bounded actuation in §IV (e.g., Figure 6.2a-ii). The vortex induced by the 3-D actuation appears to be somewhat more concentrated and occupies a smaller region in the wake than the vortex that is induced by the 2-D actuation. More importantly, the shedding of the CW vortical structure observed off-center in Figure 6.2c-ii does not diminish beyond the spanwise edges of actuator, indicating that the effects of the *unbounded* actuation extend to the unactuated flow domain over the airfoil.

From $t/T_{\text{conv}} = 1.6$ (Figures 6.2a-iii, b-iii and c-iii) and by $t/T_{\text{conv}} = 2.08$ (Figures 6.2a-iv, b-iv and c-iv), the CW vortex is advected downstream out of the field of view and the flow fields induced by the two actuation configurations are distinctly different. As shown in Figure 6.2a-iv (and in §IV), 2-D actuation leads to partial flow attachment over the airfoil where the associated downstream propagation of vorticity concentrations follows closely with that of the severed CW vortex. However, 3-D actuation results in relatively slower advection of the attaching boundary layer over the airfoil as observed at mid-span ($z = 0$) and also in the off-center plane at $z/c = 0.22$ (Figures 6.2b-iv and c-iv, respectively, *cf.*, Figure 6.2a-iv). The differences in advection celerity between the CW vortex and the upstream boundary layer are evidenced by the extent of streamwise domain within the wake that is almost void of CW vorticity (Figures 6.2b-iv and v, and 6.2c-iv and v, *cf.*, Figures 6.2a-iv and v). These images also show the “braid” of the CW

vortex and the downstream edge of the CW (“bull-nose”) vortex of the attaching boundary layer (*cf.*, §IV) at the downstream and upstream edges of Figures 6.2b-iv and c-iv. This gap in the concentration of CW vorticity indicates a prolonged accumulation of CW vorticity over the airfoil compared to the 2-D counterpart in Figures 6.2a-iii and a-iv. The bull-nose vortex is clearly evident just above the trailing edge in Figures 6.2b-v and c-v at $t/T_{\text{conv}} = 2.24$, albeit the intensity of its CW vorticity concentration is somewhat reduced in the off-center plane.

During the time interval $1.6 < t/T_{\text{conv}} < 2.56$, the evolution of the CCW vorticity layer induced by the 3-D (unbounded or finite span) single-pulsed actuation (Figures 6.2b-iii to c-vi and c-iii to c-vi) is significantly different from that of the bounded actuation (Figures 6.2a-iii to a-vi). The most notable differences in the effects of the unbounded actuation are the additional downward deflection of the CCW vorticity layer (rows iv and v in Figure 6.2) and its concomitant “pinching off” that resulted in a dramatic and abrupt discontinuity in shedding of the CCW vorticity into the near wake at $t/T_{\text{conv}} = 2.56$ (row vi in Figure 6.2). These alterations of the CCW vorticity in the near wake (e.g., Figure 6.2b-vi and c-vi) compared to its 2-D counterpart indicate that the momentary unbounded flow attachment is accompanied by regulation of vorticity concentrations over the both sides of the airfoil and likely leads to some accumulation of CCW vorticity (there is no evidence of a similar effect with the 2-D actuation). These data also indicate that the unbounded actuation pulse accentuates the disparity between the advection time scales of the rolled-up CW vortex and the attaching boundary layer. It is conjectured that it prolongs and enhances the rate of accumulation of CW vorticity over the airfoil that ultimately yields a larger increase in the airfoil circulation (*cf.*, Figure 6.3). Finally, for

$2.56 < t/T_{\text{conv}} < 4.64$ the flow response to the 2-D actuation begins to slowly relax to the stalled state as the cross stream extent of the wake increases (Figures 6.2a-vi and a-vii), while it appears that the corresponding relaxation following the 3-D actuation is perhaps somewhat delayed as evident in the narrower cross stream width of the wake in Figures 6.2b-vi to b-vii and c-vi to c-vii. Corresponding phase-locked PIV data that were acquired further away from the actuation in a third off-center x - y plane at $z = 0.33c \approx 0.95S_{\text{act}}$ (not included in Figure 6.2) show similar attachment effects of the CW vorticity (albeit with some reduction in concentration magnitude) and unsteady features of the CCW vorticity in the near wake.

Similar to the analysis of Figure 4.7, the global aerodynamic characteristics of the static airfoil are assessed by considering the time-evolution of the phase-averaged cross stream distributions of the vorticity flux ($\omega_z \cdot u$) into the wake. The CW and CCW fluxes from the suction and pressure surfaces, respectively, are shown in a contour plot for the planes $z/c = 0, 0.22$ and 0.33 (Figures 6.3a-c, respectively) as a function of y/c and t/T_{conv} at $0.25c$ downstream of the trailing edge as identical to Figure 4.7. Note that the slightly decreasing cross stream extent of the wake with increasing z is evident by comparing the corresponding locations of the CW vorticity flux concentrations at $t = 0$ in Figures 6.3a-c. In addition to the noticeable shedding of the CCW and the CW vortices, and the narrowing and widening of the wake during attachment and relaxation (*cf.*, Figure 4.7), the flux maps in Figure 6.3 highlight the differences observed in Figure 6.2 between the unbounded and bounded actuation configurations.

To begin with, the region of low concentrations of CW vorticity on the suction surface that follows the shedding of the CW vortex and ahead of the attaching bull-nose

vortex of the boundary layer is clearly evidenced by the duration of low flux (marked by black oval) in Figure 6.3a for $z/c = 0$ and in the off-center planes at $z/c = 0.22$ (Figure 6.3b) and $z/c = 0.33$ (Figure 6.3c), which was not discernable in Figure 4.7. Secondly, the flow attachment over the suction surface induced by the single pulse as manifested in the decreasing distance between the two streams of vorticity fluxes appear to increase in duration by about $0.5T_{\text{conv}}$ for the finite-span actuation in Figure 6.3a as compared with Figure 4.7. In addition to modulating the vorticity fluxes from both surfaces of the airfoil, the downward deflection of the CCW vorticity layer (shown in Figure 6.2) and the abrupt (brief) suppression of the CCW flux effected by the finite-span actuation that are not present in §IV are clearly observed for $0 \leq z/c \leq 0.33$. The improved attachment effects discussed in Figure 6.2 are shown by the fact that the two vorticity layers meet and effectively closes the wake (as marked by red oval in Figure 6.3a). Lastly, the prominent attachment effects of the finite-span actuation and the subsequent relaxation of the base flow are extended beyond the spanwise extent of the actuation in the outboard flow regions (i.e, $z/c > 0.5St_{\text{act}}$) in Figures 6.3b and c. This is not achievable in §IV due to the confined flow between the fences.

The differences between the transient flow response measured in the center plane and beyond the spanwise edge of the unbounded actuation in Figure 6.2 are further quantified by computing the phase averaged changes in sectional circulation about the airfoil (Figure 6.4). The changes in the circulation of the 2-D bounded flow (*cf.*, Figure 4.8b) is included for comparison and exhibits the typical reduction in circulation that is associated with the severing and shedding of the 2-D vortex at $t/T_{\text{conv}} = 1.5$ followed by a local peak of $|\Delta I/\Gamma_{\text{o}}|_{\text{max}} \approx 20\%$ at $t/T_{\text{conv}} = 2.5$ from the attachment where CW vorticity is

accumulated within the boundary layer on the suction side of the airfoil, before the final, slow return to stall. The variations of the sectional circulation in the planes $z/c = 0, 0.22$ and 0.33 following 3-D actuation are evident. To begin with, the initial loss in circulation due to the shedding of the severed CW vortex ($t/T_{\text{conv}} = 1.5$) is larger (commensurate with the stronger vortex in Figure 6.2b-ii and c-ii). Furthermore, the circulation peaks for the 3-D configuration ($t/T_{\text{conv}} = 2.5$) are nearly 200% larger than the peak associated with the 2-D actuation. This indicates that the control authority of pulsed actuation is enhanced through the shedding and accumulation of increased concentrations of CW vorticity.

Although the rise times of the three traces in Figure 6.4 are similar, the steeper traces for the 3-D actuation compared to the effect of the bounded actuation correspond to an increase in the rate at which CW vorticity is accumulated owing to the prolonged reduction in the flux of CW vorticity in Figures 6.2b-iv and c-iv. Furthermore, there is a somewhat small ($\sim 10 - 20\%$) and brief ($\sim 0.3T_{\text{conv}}$) decrease in the sectional circulation of the unbounded actuation that precedes a second peak at $t/T_{\text{conv}} \approx 3$ that is about 10% higher than the first peak (neither of these features are observed for the bounded actuation). This second peak is likely an indirect effect of the brief termination of the CCW vorticity layer as shown in Figures 6.2b-vi and c-vi and in Figure 6.3 that contributes to a lift-reducing change in the circulation. Figures 6.2 and 6.3 also indicate that there are spanwise variations in the flow during relaxation to stalled flow. The second peak in the mid-span circulation is somewhat higher and its rate of increase is slower with a noticeable delay compared to the corresponding off-center traces in Figure 6.4. These slower and larger transients at $z = 0$ are likely due to the enhanced CW vorticity concentrations within the “bull-nose” vortex of the attaching boundary layer that

are coupled to the slower CCW vortex dynamics as suggested by flux evolution in Figure 6.3a. This also explains the differences in the flow relaxation to the base flow as shown in Figure 6.4 where the off-center ($z/c = 0.22$ and 0.33) traces indicate that the circulation begins to decrease earlier than at $z = 0$.

It is interesting to note that the circulation trace in Figure 6.4 for $z/c = 0.33$ (black) decreases below the baseline value by about 15% for $7 < t/T_{\text{conv}} < 14$ during the relaxation. Comparison with the flux plot in Figure 6.3c indicates that for $t/T_{\text{conv}} = 5 - 7$, the CW flux from the suction surface at the off center plane is distributed across a larger cross stream width than in the base flow, indicating that the CW vorticity layer is wider as a result of the spanwise spreading of the actuation effects.

6.2. The Interface between the Actuated and Unactuated Flow Domains

As demonstrated in §VI.1, the noticeable effects of the unbounded, finite-span pulsed actuation ($S_{\text{act}} \approx 0.35S_{\text{fence}}$) are measured even at $z = 0.95S_{\text{act}}$ i.e., extending well beyond the spanwise edges of the actuator array. In order to characterize the spanwise and cross stream spreading of the interface between the actuated and unactuated flow domains, the spanwise width of the actuation is reduced by using only the center three actuators in the array ($S_{\text{act}} \approx 0.13S_{\text{fence}}$) while the locations of the fences remain unchanged. The transient flow field during $0 \leq t/T_{\text{conv}} \leq 16$ is obtained from PIV measurements phase-locked to the actuation in the 24 cross stream planes as described in §VI.1 which occupy within $0 \leq z \leq 0.295c$ where the outermost plane is about $0.26c$ or $4S_{\text{act}}$ beyond the extent of the actuators that are at $z = \pm 0.5S_{\text{act}} = \pm 0.065c$.

6.2.1. Global Flow Structures

The raster plots in Figure 6.5 show phase-averaged spanwise vorticity concentrations in five select planes $z/S_{\text{act}} = 0, 0.42, 1.25, 1.67,$ and 2.24 (columns a-e, respectively) at increasing time delays following the actuation pulse $t/T_{\text{conv}} = 0, 1.12, 1.52,$ and 2.32 (rows i-iv). Streamlines for $z/S_{\text{act}} = 0$ are also computed based on the particle-trace method described in §II and are superimposed in row “a” of Figure 6.5 (streamlines in the off-center planes are not included due to the out-of-plane flow). For formatting purposes, Figure 6.5 is divided into two primary sets that depict columns a-c, and a, d-e, respectively. Each set includes a four-row panel. Figures 6.5a-i, b-i, c-i, d-i, and e-i show the similar base flow in the different measurement planes across the span when actuation is triggered ($t = 0$) and prior to the onset the pulsed jets (some of the base flow data are discussed with Figure 6.1).

The streamlines in rows ii and iii at mid-span that pass through the domain that is straddled upstream and downstream by the bull-nose vortex of the attaching boundary layer and the rolled-up CW vortex, respectively (e.g., at $x/c \approx 0.7$, near the surface in Figure 6.5a-ii) reveal a stagnation region induced by the actuation effects (*cf.*, §IV). This transient blockage effect results in the attachment over the airfoil (as previously shown in §IV) as evidenced by the vectored streamlines in Figure 6.5a-iv compared to the base flow in Figure 6.5a-i. Similar to the effects described in connection to Figures 6.2 and 6.3, the spanwise variations in the flow attachment induced over the airfoil by the actuation are clearly evident for $t/T_{\text{conv}} \geq 1.12$. At $t/T_{\text{conv}} = 1.12$ and 1.52 (rows ii and iii in Figure 6.5, respectively) where the characteristic shedding of a spanwise CW vortex induced by the actuation pulse is clearly observed at as far as $z/c = 1.25$ in column c. The corresponding severing of the shear layer and the ensuing roll-up of this CW vortex at the

same instances are also present in Figure 6.5 at $z/c = 1.67$ and 2.24 (Figures 6.5d-ii & iii, and e-ii & iii), but appear to weaken with outboard distance from the three-module actuator.

In addition, during attachment ($t/T_{\text{conv}} = 1.12$ and 1.52 , rows ii – iii), the CW vorticity concentrations of the attaching boundary layer spread from the inner planes at $z/S_{\text{act}} = 0$, 0.42 and 1.25 (columns a – c in Figure 6.5) beyond the spanwise edges of the actuation and are gradually displaced into the shear layer with increasing distance from the mid-span. These flows in the outer planes (columns d and e) remain separated, characterizing the spanwise-limited flow attachment. This is more noticeable at $t/T_{\text{conv}} = 2.32$ where the attached flow that extends further downstream (Figures 6.5a-iv and b-iv) is confined mainly to the spanwise extent of the actuators while the outboard domain remains separated (Figures 6.5d-iv and e-iv). Rows d and e in Figure 6.5 show limited roll-up in the outer flow, indicating that the control authority (i.e., the extent of $dp/dy > 0$ induced by the roll-up of CW vorticity and the corresponding stagnation region as described in §IV) is diminished, with decreasing effects on the attachment as the blockage moves away from the surface in the outboard regions. It is shown in connection with §VII that the proximity of the blockage to the airfoil surface is important for the spanwise spreading of attachment beyond the actuation.

As suggested in connection with Figure 6.2, the data in Figure 6.5 show differences in the vortical structures between the inner (e.g., at $x/c \approx 0.7$ near the surface in Figure 6.5a-ii) and outer (e.g., at $x/c \approx 0.7$ above the surface in Figure 6.5e-ii) planes that further indicate the development of an “interface” between the (inner) attaching flow and the (outer) separated flow. This transitory interface region above the airfoil is characterized

by the nominal 2-D base flow (Figures 6.5a-i through e-i) that is first modified by the subsequent passing of the rolled-up CW vortex and then by the attachment as manifested by the increased non-uniform distribution of spanwise (namely, CW) vorticity concentrations across the span in rows ii – iv in Figure 6.5. In connection with Figure 6.9, the development of this interface is in conjunction with a corresponding development of velocity (spanwise) gradients that would encompass a spanwise domain in the flow over the airfoil beyond the edges of the actuation where the rolled-up CW vortex weakens across the span.

To isolate the severing of the separating shear layer that leads to the shedding of the rolled-up vortex shown in Figure 6.5, and more importantly to reveal spanwise variations during its evolution, vorticity concentrations over the suction surface in 13 measurement planes ($0 \geq z/c \geq 0.265$) are shown in Figure 6.6 (mirrored about the center plane) viewed in the streamwise direction from the airfoil's leading edge. The grey line segments at the bottom of each image mark the locations of the three actuator orifices. A comparison between the flows at $t = 0$ and $0.72T_{\text{conv}}$ (Figures 6.6a and b, respectively), shows that the severing is observed in the center plane and in only six of the adjacent off-center planes ($z/c \leq 0.09 = 0.68S_{\text{act}}$) somewhat farther upstream as evidenced by the distinct concentrations of vorticity from the rolled-up vortex. At $t/T_{\text{conv}} = 0.72$, the spanwise edge of this vortex as induced by the actuation is therefore estimated to be in the vicinity of the sixth off-center plane and is marked by an arrow in Figure 6.6b.

A short time later, at $t/T_{\text{conv}} = 0.8$, a *discontinuity in the shear layer* is present in the 7th off-center plane ($z/c = 0.1$) in Figure 6.6c although it is somewhat difficult to discern at this early stage of the local roll-up. This discontinuity in the shear layer as induced by

the roll-up continues to spread into the outer planes (Figures 6.6e-i) and eventually reaches the outermost plane at $z/c = 0.265$ which is far beyond the edges of the actuator array ($\pm 0.5S_{\text{act}} \approx \pm 0.065c$). It is conjectured that the severing of the separated shear layer is initially seeded only by the transitory, finite-span pulsed jet. However, despite the finite severing, the ensuing roll-up of the CW vortex within the severed vorticity layer downstream of the actuator proceeds to spread in the spanwise direction as the spanwise edges of this vortex cannot end in the cross flow following the termination of the pulsed jet flow. Owing to the increasing spanwise extent of the vortex, the corresponding spanwise development of the interaction of the CW vortex with the separating shear layer is unbounded and therefore protrudes beyond the edges of the actuation unlike the 2-D bounded actuation (*cf.*, §IV).

The rolled-up vortex and the attaching boundary layer flow are highly 3-D as manifested by the spanwise variations in the two structures in Figure 6.6 that form into crescent shapes of opposite directions. The downward-facing crescent-shaped CW vortex is characterized by the vorticity concentrations in the vicinity of the center plane that are displaced farther away from the airfoil surface and into the free stream than in the outer flow regions (e.g., Figure 6.6g at $t/T_{\text{conv}} = 1.12$). It is conjectured that this shape from the spanwise and cross stream distributions of the CW vorticity scales with the spanwise width of the pulsed actuation jets as evidenced in the spanwise extent of the farther-displaced rolled-up concentrations in Figure 6.6b, that is commensurate with S_{act} . The curvature of this downward-crescent shape appears to decrease across its span with increasing elapsed time as the magnitude of the CW vorticity concentration diminish over a larger core size at each spanwise (x - y) plane (e.g., Figure 6.6i).

Conversely, the upward-facing crescent corresponds to the spanwise distribution of the CW vorticity associated with the attachment in the vicinity of the center region and the separated outer flow. As discussed above, the spanwise extent of the flow attachment first scales with the actuator (S_{act} , e.g., Figures 6.6d and e). However, as time elapses and the attaching boundary layer grows in both streamwise and spanwise directions, the curvature of the corresponding crescent-shaped distribution of CW vorticity appears more pronounced due to the fact that the outer, separated shear layers (e.g., Figures 6.6h and i) are located farther from the attaching flow on the surface of the airfoil.

6.2.2. The Effect of the Severed CW Vortex on Attachment

The evolution of the spanwise vorticity, ω_z , is investigated here to further elucidate details of the 3-D interface that separates between the attaching boundary layer in the inner (center) region and the almost unaltered separated shear layer in the outer region. Figures 6.7a-o show contours of $\omega_z(y, z)$ at $x/c = 0.76$ over the airfoil (at $t/T_{\text{conv}} = 0.72, 0.88, 0.96, 1.12, 1.36, 1.52, 1.68, 1.92, 2.32,$ and 3.12 , respectively), that are interpolated from the 24 planes of phase-averaged data described above (a spatial Gaussian filter is used to remove vertical striations from minor mismatches in the data planes). The surface of the airfoil at $y/c \approx 0.16$ is marked with a horizontal dash line.

The attachment across the span as observed at this x -location is manifested in the transport of vorticity from the 2-D separating shear layer at $y/c > 0.3$ in Figure 6.7a towards the airfoil surface as shown in Figures 6.7h-m. The passing of the CW vortex through this spanwise plane leads to the reduction in CW vorticity in the shear layer in Figures 6.7d-g owing to the accompanying roll-up process of the vortex. The spanwise distribution of the CW concentrations within the vortex in Figure 6.7c are farther away

from the surface across the inner region ($z/c < 0.1$) compared to the outer region. This corresponds to the lift-off associated with the CW vortex that is clearly most prominent close to the mid-span, resulting in the upward-bending distribution in Figure 6.7c that is followed by an opposite (downward bending) shape for the distribution in Figures 6.7e-f. The flow attaches upstream of the CW vortex, resulting in the distribution of CW vorticity above the surface ($y/c < 0.3$) in the center region ($|-0.2 < z/c < 0.2$) that is evolving during $1.28 < t/T_{\text{conv}} < 2.32$ in Figure 6.7h-n. Also, these inner CW vorticity concentrations that are associated with the attaching boundary layer and the outer flow concentrations of the separated shear layer ($|z/c| > 0.2$) in Figures 6.5d-n clearly show the presence of the interface within a spanwise region that occupies $|z/c| \approx 0.1 - 0.2$ and develops during this time, and evolves with the attachment before disappearing by $t/T_{\text{conv}} = 3.12$ in Figure 6.7o.

These flow structures are also present further downstream at $x/c = 0.85$ and 0.95 (Figures 6.8a-e and f-j, respectively) following a short convective time lag. For example, the distribution of vorticity at $x/c = 0.76$ in Figure 6.7i that corresponds to the early stages in the evolution of the attaching boundary layer at $t/T_{\text{conv}} = 1.36$ is measured later at $t/T_{\text{conv}} = 1.68$ and 1.92 in Figures 6.8b and h, respectively. By comparing Figure 6.8 with 6.7, the concentrations of CW vorticity on the surface from the transitory attachment occupy a cross stream (y) and spanwise (z) domain that decreases in the streamwise direction. In addition, the effects of the actuation persist longer at the upstream location in Figure 6.7 compared to in Figure 6.8. For example, the residence time of the CW vorticity transported toward the airfoil surface as observed in Figures 6.7f-n, is estimated to be approximately $1.2T_{\text{conv}}$ while for $x/c = 0.95$ in Figures 6.8h-i, the corresponding

duration is about $0.4T_{\text{conv}}$. This is indicative of the diminishing effects of attachment toward the trailing edge, and is apparent from the levels of vorticity concentration in Figure 6.7 that are noticeably reduced in Figures 6.8a-e and f-j for $x/c = 0.85$ and 0.95 at the same instances. This reveals the streamwise variations in the spanwise spreading of the attaching flow.

Next, the ensuing attachment effected by the large-scale global features in Figure 6.6 is analyzed using the cross stream velocity, v , induced by the CW vortex as it advects over the airfoil. The phase-averaged and spatially-filtered contour plots of v in Figure 6.9 for the streamwise position at $x/c = 0.76$ correspond to the flow in Figure 6.7. The separated base flow at $t = 0$ is shown in Figure 6.9a and the flow as the CW vortex arrives at $x/c = 0.76$ at $t/T_{\text{conv}} = 0.72$ is shown in Figure 6.9b where the effects of the downstream edges of the vortex are minimal. However, as shown in Figures 6.5 (e.g., at $t/T_{\text{conv}} = 1.12$ in a-ii, b-ii and c-ii), the CW vortex induces a significant upwash on its upstream side. A comparison between the base flow in Figure 6.9b with the upwash ($v \sim 0.5U_\infty$, colored blue) of the passing CW vortex at $t/T_{\text{conv}} = 0.88$ and 0.96 in Figures 6.9c and d, respectively, reveal the large ($\Delta z \sim \pm 0.2c$ cf., $S_{\text{act}} = \pm 0.07c$) spatial changes to the global flow at $\Delta y \approx 0.1c$ away from the airfoil surface ($y = 0.15c$). The majority of the increased (positive, blue) cross stream velocity persists only for $t/T_{\text{conv}} \leq 1.04$ in Figures 6.9c-e, which is commensurate with the convective time scale associated with the streamwise extent of the CW vortex. This transient variation of v is related to the reduced concentrations of the CW vorticity in Figures 6.7 and 6.8 for $-0.2 < z/c < 0.2$ owing to the transport of vorticity within the shear layer of the base flow through the roll-up and concomitant advection of the CW vortex into the wake. The most intense upwash is

concentrated in the vicinity of the center plane and diminishes in magnitude with increasing variations in v across the cross stream (y) toward the outer flow, resulting in an oblong region of influence for $-0.2 < z/c < 0.2$ and $y/c < 0.3$ as outlined in Figures 6.9c and d. Note that this contour domain is a representation of the 3-D vortex observed in Figure 6.6 where the effects shown in Figure 6.9 are for a fixed y - z section through the spanwise extent of the vortex. More importantly (*cf.*, the streamlines in Figure 6.5), the upwash is a result of the blockage that is precursor to the attachment mechanism as discussed in §IV, therefore its spanwise distribution in Figures 6.9c-e may point to the corresponding flow regions across the span where unbounded attachment is expected to occur.

Immediately following the CW vortex, a significant spanwise extent of downwash (colored red) is first measured and shown in Figure 6.9f at $t/T_{\text{conv}} = 1.12$, and continues to amplify rapidly over a short elapsed time through to $t/T_{\text{conv}} = 1.52$ in Figure 6.9k. Furthermore, the increased downwash velocity (e.g., $v \sim 0.5U_\infty$ in Figure 6.9i) covers an area that is commensurate with the width of the CW vortex that has expanded spanwise beyond the actuation extent. Not surprisingly, these flow regions of upwash (blue) and downwash (red) occupy a similar, but opposite kidney (or crescent) -shaped region (*cf.*, Figures 6.9c and g) that are attributed to the spanwise structure of the vortex and the boundary layer (also discussed in connection to Figure 6.6). As mentioned earlier, the blockage effect from the actuation pulse is initiated via the stagnation region induced by the rolled up vortex which induces a cross stream pressure gradient $dp/dy > 0$ near the bull-nose vortex of the attaching boundary layer flow. It is therefore conjectured that the spanwise limits and magnitude of the pressure gradient from the attachment are

commensurate with the spanwise ($-0.2 \leq z/c \leq 0.2$ in Figure 6.9) influence of the CW vortex that extend well beyond the spanwise edges of actuation. This indicates that the pressure gradient is also expected to spread in the spanwise and streamwise directions in conjunction with the evolution of the flow. This helps explain the improvements in attachment and circulation over the bounded 2-D actuation described in §IV and V. The spanwise variations in the distribution of $v < 0$ (red) in Figures 6.9f-k for $1.12 \leq t/T_{\text{conv}} \leq 1.52$ demonstrate that the strongest effects of $dp/dy > 0$ are near the center plane, corresponding to the peak strength of the shed CW, which is in agreement with the spanwise variations in the stagnation region shown in Figure 6.5. The pressure gradient is expected to eventually decay for $1.92 \leq t/T_{\text{conv}} \leq 3.12$ at this streamwise location following the termination of the pulsed jet as the downwash over the airfoil diminishes in Figures 6.9m-o.

6.2.3. Spanwise Spreading of Attachment

The integrated streamwise flux of the spanwise vorticity $F_{\omega}(x,t) = \int (u \cdot \omega_z) dy$ is computed at each streamwise location x in each of the 24 cross stream planes. The flux over the airfoil ($x/c < 1$) is integrated between the surface of the airfoil and the upper cross stream boundary of the PIV data, and between the lower and upper boundaries in the near wake ($x/c > 1$). Contour maps of the flux computed *relative to the flux of the base flow* at $t = 0$ $\Delta F_{\omega} = F_{\omega} - F_{\omega_0}$ are shown in Figure 6.10 in the x - z plane at multiple time delays relative to the onset of actuation $0.64 < t/T_{\text{conv}} < 1.84$ (the data are mirrored about $z = 0$, and the location of the actuator array is labeled in Figure 6.10a and marked in each image).

Figure 6.10a ($t/T_{\text{conv}} = 0.64$) shows the response of the flow shortly after the onset of the pulsed jet. The formation of a domain of increased CW vorticity flux (labeled “I”)

with a span of $\Delta z \approx 0.3c$ is evident upstream over the suction surface of the airfoil at $0.5 < x/c < 0.6$. This domain represents the accumulation of CW vorticity by the rolled-up vortex that spreads beyond the actuated domain. Figure 6.10a also show alternating regions of enhanced and attenuated CCW vorticity flux (blue and red, respectively) that span the measurement domain downstream of the trailing edge ($x/c > 1$). These fluxes are attributed to the characteristic shedding into the wake of a spanwise CCW vortex from the pressure side. This vortex is induced by the pulsed actuation but is smaller and weaker compared to the CW vortex that is shed by the severed shear layer from the suction surface. This CCW vortex that corresponds to a brief increase in circulation is also observed in several mid-span PIV data (Figures 4.8b, 5.2, and 6.3), and its size and shape remain unchanged as it continues to advect downstream in Figures 6.10b-d while the CW vortex evolves. It is somewhat unexpected, however, the shedding of CCW vorticity is near simultaneous across all the PIV measurement planes and is nominally spanwise uniform as evidenced by the negligible spanwise variations at the trailing edge in Figures 6.10a-d. The evolution of the CW and CCW vorticity fluxes implies that the transient flow disruption induced by the unbounded pulsed jet has an instantaneous effect on the global flow, leading to the starting vortex shed in the wake ($x/c > 1$), whilst the ensuing interactions on the suction surface ($x/c < 1$) are localized, perhaps first seeded by the pulsed jets and therefore are initially commensurate with the actuation span. These differences in the flow dynamics between the airfoil surfaces are owing to the separated and the attached conditions of the base flow on the suction and pressure sides, respectively.

The domain of reduced flux of CW vorticity in the severed region over the airfoil (Region “II”, blue) is first observed at $0.72T_{\text{conv}}$ in Figure 6.10b and corresponds to the stagnation flow between the CW vortex and the bull-nose vortex at the leading edge of the attaching boundary (*cf.*, Figure 6.5). The spanwise spreading of regions “I” and “II” is estimated from the spanwise edges of the contours and are marked by the green and white circles, respectively, in Figures 6.10b-g. These data indicate that these contrasting regions of vorticity fluxes spread nearly linearly at short times, and ultimately the spanwise growth rate decreases by $t/T_{\text{conv}} = 1.12$ (Figure 6.10g) although these changes in the fluxes continue to spread in the spanwise direction at streamwise locations through the trailing edge. The edges of the present vorticity level appear to spread spanwise and extend streamwise linearly (Figure 6.10g) with an estimated ratio of $\Delta x/\Delta z \approx 3.5$. These disturbances in the vorticity concentrations induced by the single pulse develop into the alternating (up and downstream-facing) kidney-shaped domains “I” and “II” for $0.64 < t/T_{\text{conv}} < 0.96$ (Figures 6.10a-e) with well-defined spanwise edges that are marked by the circles adjacent to the unactuated domain.

The streamwise extent of the red (I) domain is reasonably uniform across most of its span during the roll-up and advection of the CW vortex that is dominated by the direct interactions of the pulsed jet with the separating shear layer. On the other hand, the corresponding streamwise extent of the blue (II) domain decreases noticeably at the outer spanwise edges for $-0.15 > z/c > 0.15$ in Figures 6.10f-k for $1.04 < t/T_{\text{conv}} < 1.44$, suggesting that in comparison with the effects of the CW vortex (“I”), the ensuing reduction in vorticity flux (“II”) is strongly influenced by the surrounding flow owing to

the larger spanwise gradients in the vorticity concentration as indicated in Figures 6.6 and 6.8.

After a short time lapse, a domain of increased CW vorticity flux (marked “III” in Figure 6.10h) indicating the attaching flow first appears immediately upstream of region “II” at $t/T_{\text{conv}} = 0.96$ in Figure 6.10e and continues to propagate downstream with regions “I” and “II” and also extends in the spanwise direction beyond the edge of the actuators. By $t/T_{\text{conv}} = 1.36$, the region of reduced CW vorticity flux (II) in Figure 6.10j has reached the wake. Note that in Figures 6.10k-p, the vorticity flux over the airfoil is significantly altered as manifested in the region “III” that stretches outboard away from the center plane with distinct spanwise edges, representing the spanwise limits of the accumulation of CW vorticity attributed *mostly* to the attaching boundary layer. It is argued that beyond these edges the flux is nominally unchanged from the base flow as these outer flows remain separated. The leading edge of this region continues to propagate towards the trailing edge and outwards toward the streamwise partitions spanning $z = \pm 0.25c$ at $t/T_{\text{conv}} = 1.76$ in Figure 6.10o (almost reaching the edges of the PIV measurement domain). The outer spanwise edges of the enhanced flux of region “III” remain almost unchanged over the suction surface in Figure 6.10p at $t/T_{\text{conv}} = 1.84$ and for $t/T_{\text{conv}} < 2.16$ (not included) as its leading edge reaches the trailing edge. Thereafter, although not shown, the spatial extent of region “III” begins to recede while a region of decreased CCW vorticity flux is observed to spread across the wake for $2.16 \leq t/T_{\text{conv}} \leq 2.4$, which corresponds to the noticeable deflection of the CCW vorticity layer and the ensuing shedding of a CCW vortex in Figures 6.2b-vi and c-vi that is not present in the 2-D pulsed actuation. These events correspond to the peaks in the sectional circulation that

are similarly observed in Figure 6.3, before the flow relaxes as region “III” recedes upstream.

To estimate the spatial evolution and, in particular, the spanwise spreading of the vorticity layer near the surface of the airfoil, it is desired to consider planform, vorticity concentrations that capture the transient vorticity concentrations near the surface during the attachment induced by the rolled-up CW vortex. To this end, the phase locked CW vorticity concentrations are averaged within the cross stream domain $0.05c$ centered at $y \approx y_\delta$ that corresponds to the nominal elevation of the boundary layer edge ($\delta_{99} \approx 0.05c$) at mid-span and $x/c = 0.4$ (the upstream edge of the present PIV measurement domain). This cross stream-averaged distribution is computed at each x - z grid point of the available 24 planes of phase-averaged PIV data.

As an example, this process is illustrated in Figure 6.11 using raster plots of the spanwise vorticity concentrations $\omega(y, z; t)$ at $t/T_{\text{conv}} = 1.68$ in three planes $x/c = 0.76$, 0.85, and 0.95 (from Figures 6.7l, 6.8b and 6.8g, respectively). The horizontal dashed line at the elevation Δy above the airfoil suction surface at each streamwise station represents the spatially-averaged domain of the vorticity distribution within $y_\delta \pm 0.025c$ above the airfoil surface for each of the planes. A given level $\omega(z, y) = \omega_o$ is also illustrated as a solid contour line in each streamwise location in Figure 6.11, and may be present within the segment at Δy such that $\omega(z, \Delta y) = \omega_o$ yields z_o (marked by closed circles). This contour line is used to first identify the presence of the attaching boundary layer at this instance and second, its spanwise edges in response to the actuation at each streamwise location. Although it is likely that at each x there are multiple locations of z_o

where ω_o may fall somewhere else along z at Δy (e.g., closer to the center plane $z = 0$), the present algorithm only uses the maximum z_o (i.e., the spanwise edge of ω_o).

The streamwise distribution of these intersections $(\Delta y, z_o)$ forms an instantaneous measure of the outline of the flow interface between the attaching inner flow and the separated outer flow. This outline is expected to change with time following the temporal and spatial evolution of the vorticity distribution on the airfoil. In the illustration of Figure 6.11 near the trailing edge the prescribed level of ω_o cannot be found at $y = \Delta y$ (i.e., within $y_\delta \pm 0.025c$) along the entire range of z , indicating that there is no flow attachment at this streamwise location and instance, albeit there are measurable changes in the local vorticity concentrations as shown in Figure 6.10n.

Figure 6.12a shows the contours in the x - z plane for $1.12 \leq t/T_{\text{conv}} \leq 2.32$ where each blue contour represents the locus of $z_o(x)$ within $0.05 \leq \Delta y/c \leq 0.1$ for which $\omega_o = -300 \text{ s}^{-1}$ as described above. These loci represent the spanwise and streamwise development of the effects of the actuation on the boundary layer above the airfoil's surface. The spreading of the interface between the attached and outer flow is estimated by the celerity of the edges of the contour lines as marked using closed symbols (\bullet) in Figure 6.12a. It is argued that this estimate of the interface captures the spatial and temporal evolution of the vorticity concentrations near the surface, which are associated with the attachment. The spanwise spreading of vorticity following the onset of attachment as the boundary layer increases in the streamwise direction as is evident for $1.12 \leq t/T_{\text{conv}} < 1.44$ in Figure 6.12a.

Although the current PIV measurements only reveal the flow dynamics for $x > 0.4c$ downstream of the actuators, the data can provide the celerity at different spanwise

locations as shown in Figure 6.12b where the x and z positions of the vorticity edges from Figure 6.12a are plotted. It is interesting to note that the rates of spanwise ($\Delta z/\Delta t$, ●) and streamwise ($\Delta x/\Delta t$, ○) spreading for the boundary layer interface are similar (about $0.11U_\infty$) for $t/T_{\text{conv}} \leq 1.44$. At $t/T_{\text{conv}} = 1.44$, the enhanced CW vorticity flux in region “III” of Figure 6.10k begins to deflect outwards. In addition, the “origin” of the attaching boundary layer as extrapolated upstream (marked by the pink line in Figure 6.10g) is aligned with the span of the actuator array ($\Delta z \approx \pm 0.15c = 1.06S_{\text{act}}$). On the other hand, the streamwise growth of the downstream edge of the boundary layer at $z = 0$ is included in Figure 6.12b (●) for comparison, and it propagates faster toward the trailing edge ($0.2U_\infty$). This is in agreement with the analysis of Figure 6.10 where it is noted that the spanwise spreading of regions “I” – “III” are slower than its downstream advection. More importantly, the data in Figure 6.12 supports the notion of increased accumulation of CW vorticity by unbounded actuation compared to bounded actuation by prolonged reduction of CW vorticity flux over the suction surface owing to the lower celerity of the leading edge “bull nose” vortex.

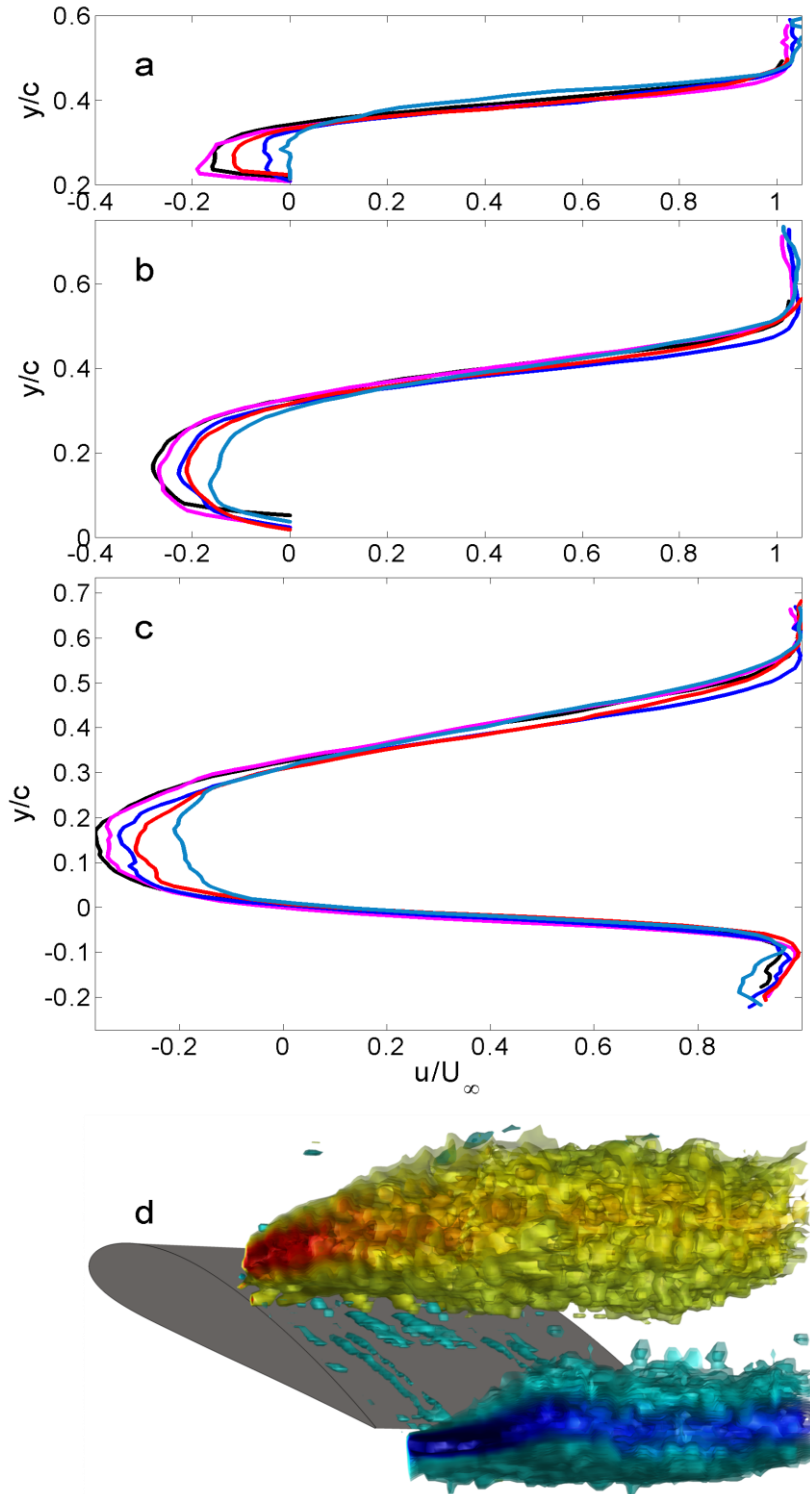


Figure 6.1: Cross stream distributions of streamwise velocity, u , in the base flow over the airfoil ($S_{\text{fence}}/c = 1.07$) at $x/c = 0.64$ (a) and 0.94 (b), and in the near wake at $x/c = 1.23$ (c) in the spanwise planes $z/c = 0$ (—), 0.088 (—), 0.175 (—), 0.219 (—) and 0.284 (—). The corresponding iso-surface contours of the spanwise vorticity over the airfoil without showing the fences (d).

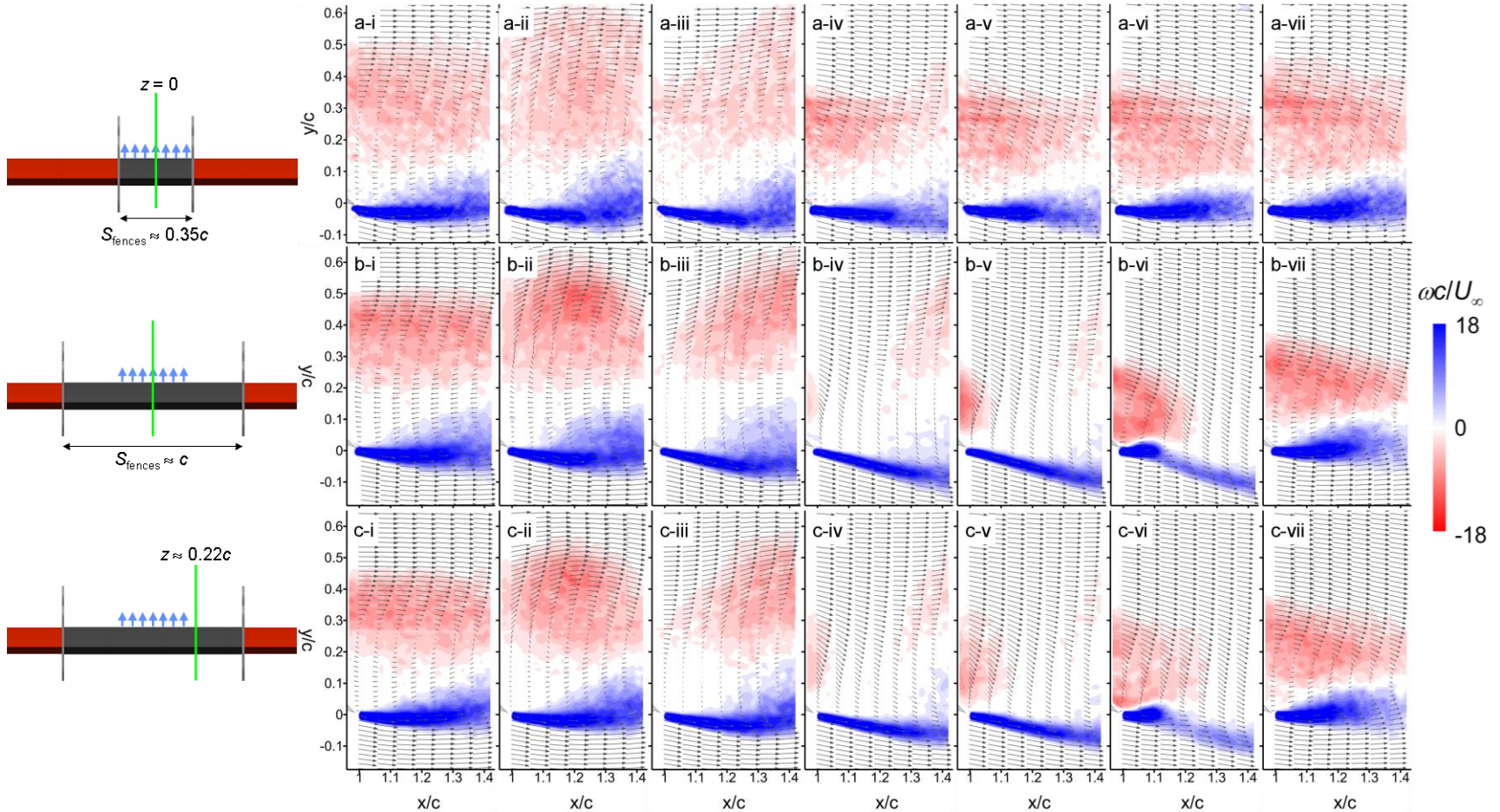


Figure 6.2: Phase-averaged vorticity and velocity maps in the cross stream planes $z/c = 0$ (a & b) and 0.22 (c) in the near wake at $\alpha = 19^\circ$ following single pulse actuation for the bounded (2-D, a-i to a-vii) and the unbounded (3-D, rows b and c) configurations: $t/T_{\text{conv}} = 0$ (i), 1.28 (ii), 1.6 (iii), 2.08 (iv), 2.24 (v), 2.56 (vi) and 4.64 (vii). The spanwise extent of the pulsed jet actuation (blue arrows) and the PIV plane ($\color{green}{\rule{0.5pt}{1cm}}$) are shown schematically on the left side of each sequence.

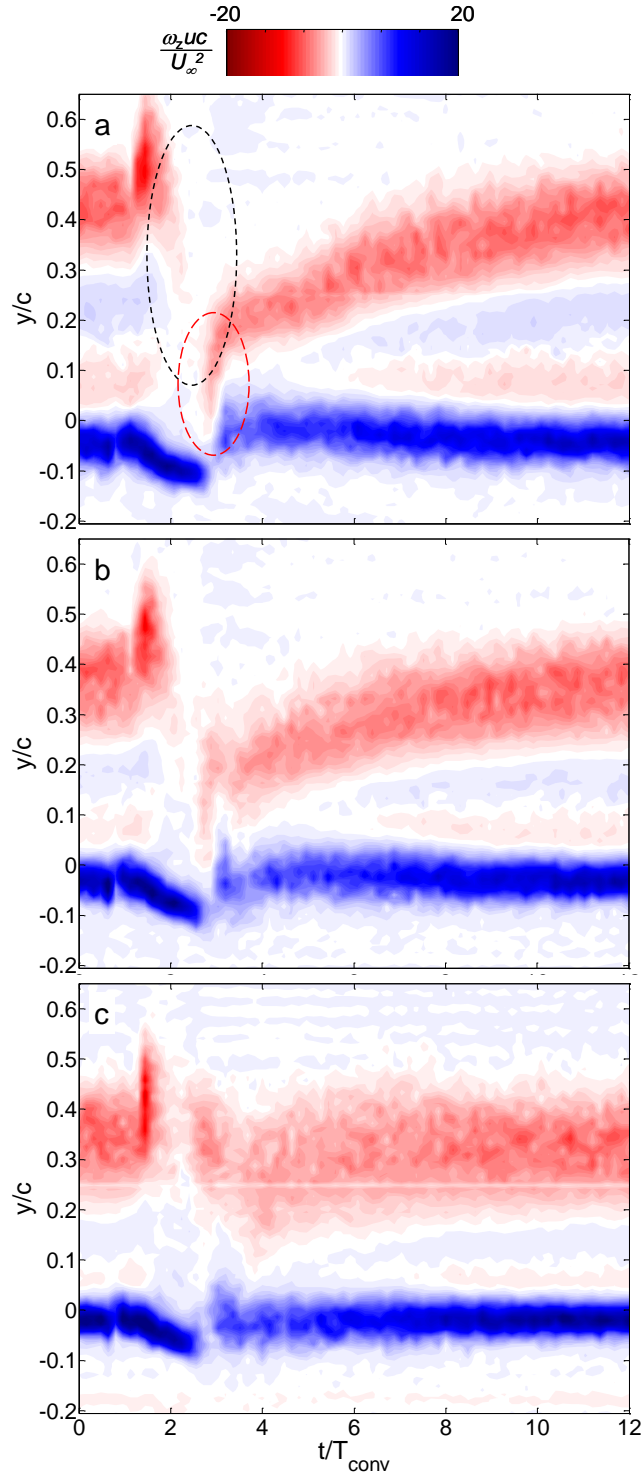


Figure 6.3: Time evolution of phase-averaged cross stream distribution of vorticity flux, $\omega_z \mu$, at $x/c = 0.25$ downstream of the trailing edge following single-pulse finite span actuation at spanwise planes; $z/c = 0$ (a), 0.22 (b) and 0.33 (c). Black and red ovals in (a) mark the low-vorticity region between shed CW vortex and attaching boundary layer, and modification to the CCW and CW layers, respectively, as shown in Figure 6.2.

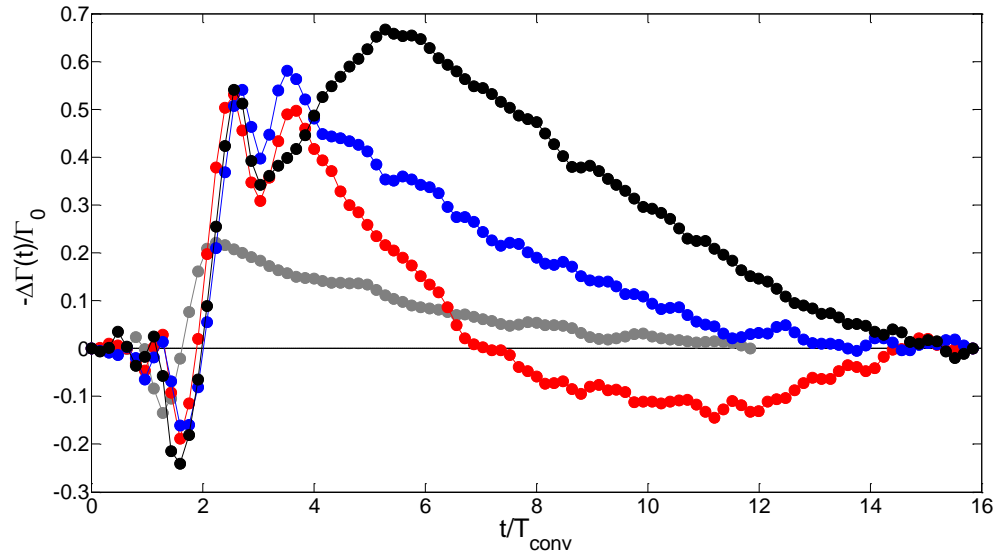


Figure 6.4: Phase-averaged incremental change in circulation following a single actuation pulse for 2-D (\bullet at $z = 0$) and 3-D finite span (\bullet , \bullet and \bullet at $z = 0, 0.22c$ and $0.33c$, respectively) actuation configurations.

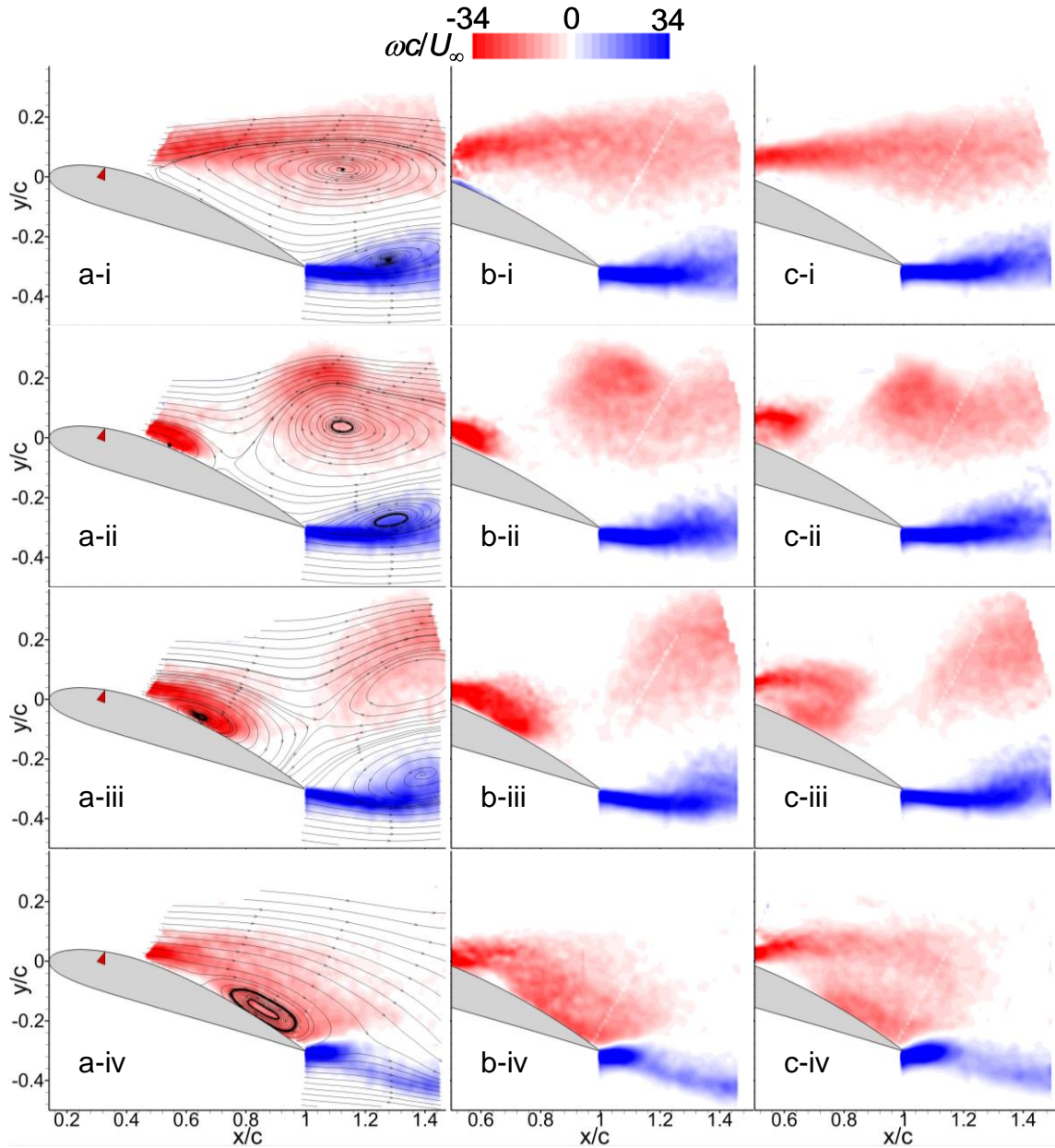


Figure 6.5: Phase-averaged vorticity and streamlines following single spanwise-unbounded ($S_{\text{act}} \approx 0.13c$ and $S_{\text{fence}} \approx c$) pulsed actuation in the cross stream planes shown as columns: $z/S_{\text{act}} = 0$ (a), 0.42 (b), 1.25 (c), 1.67 (d), and 2.24 (e). The measurement times are constant in each row; $t/T_{\text{conv}} = 0$ (i), 1.12 (ii), 1.52 (iii), and 2.32 (iv)

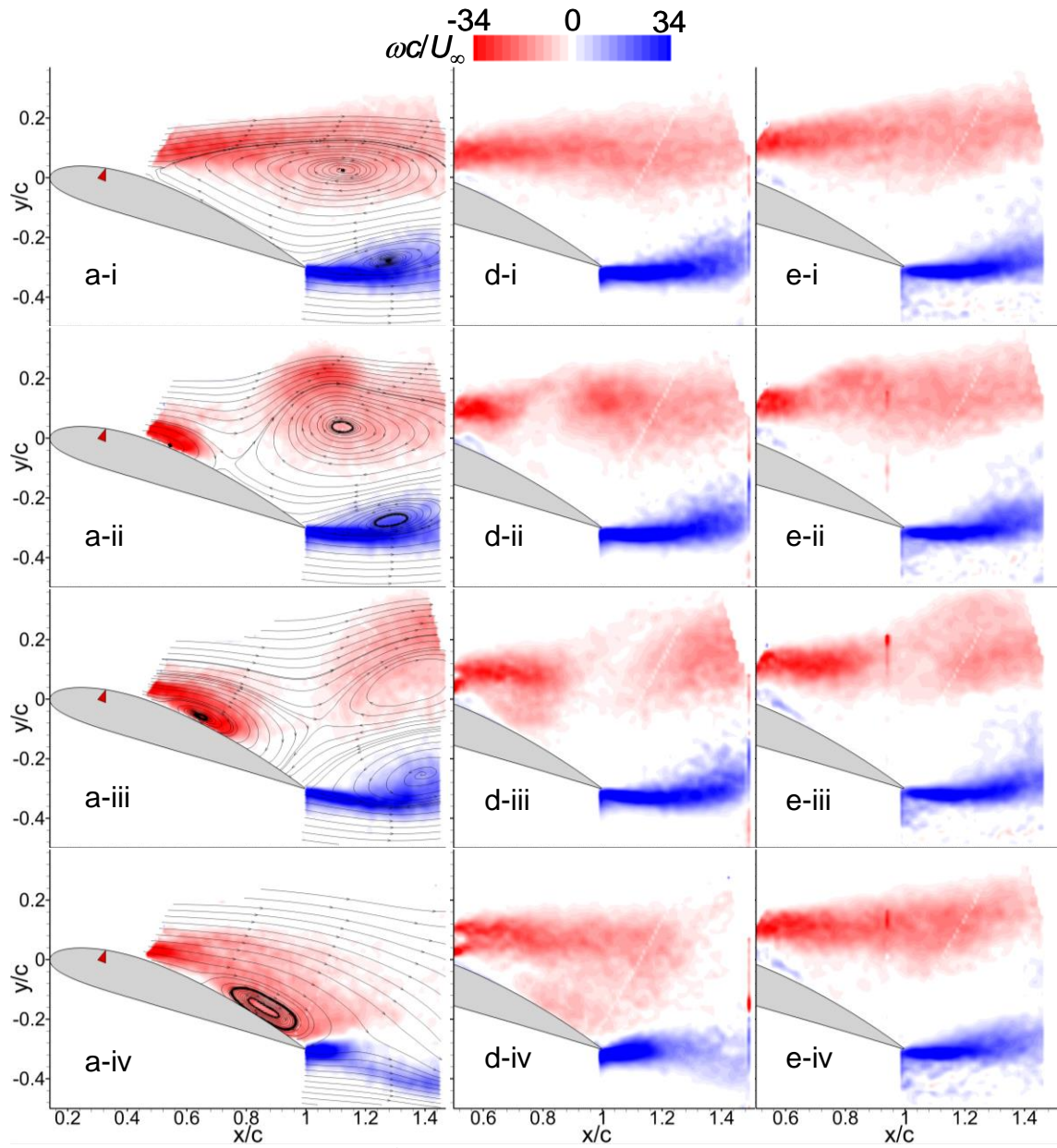


Figure 6.5: (Continued)

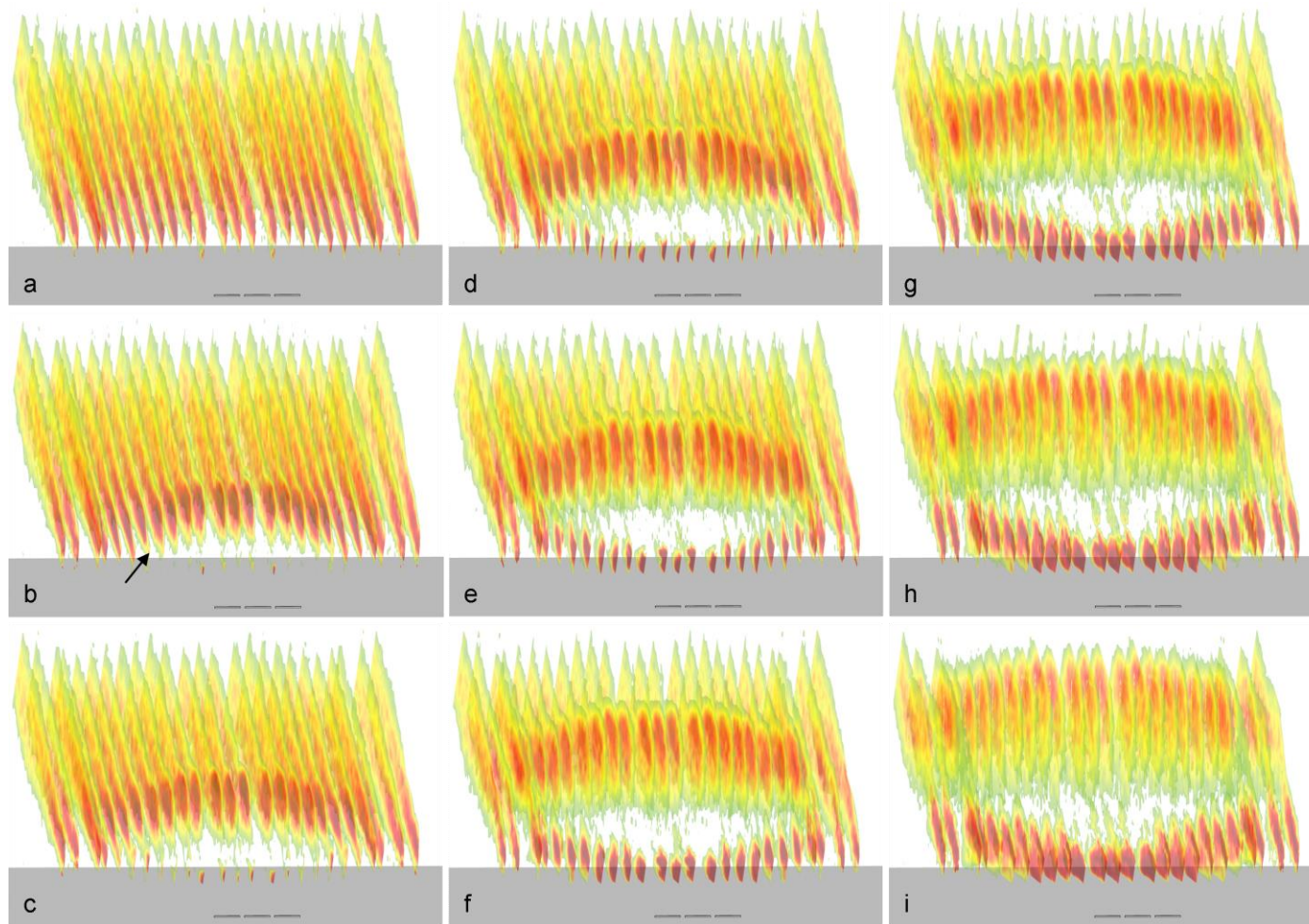


Figure 6.6: Distributions of phase-averaged spanwise vorticity in multiple cross stream planes spaced 5 mm apart ($0 \leq z/c \leq 0.265$) mirrored about $z = 0$ and viewed downstream from the leading edge at $t/T_{\text{conv}} = 0$ (a), 0.72 (b), 0.8 (c), 0.88 (d), 0.96 (e), 1.04 (f), 1.12 (g), 1.2 (h) and 1.28 (i). The three actuator array is marked at the upstream edge. The arrow in (b) marks the outermost severing of the shear layer at that instance.

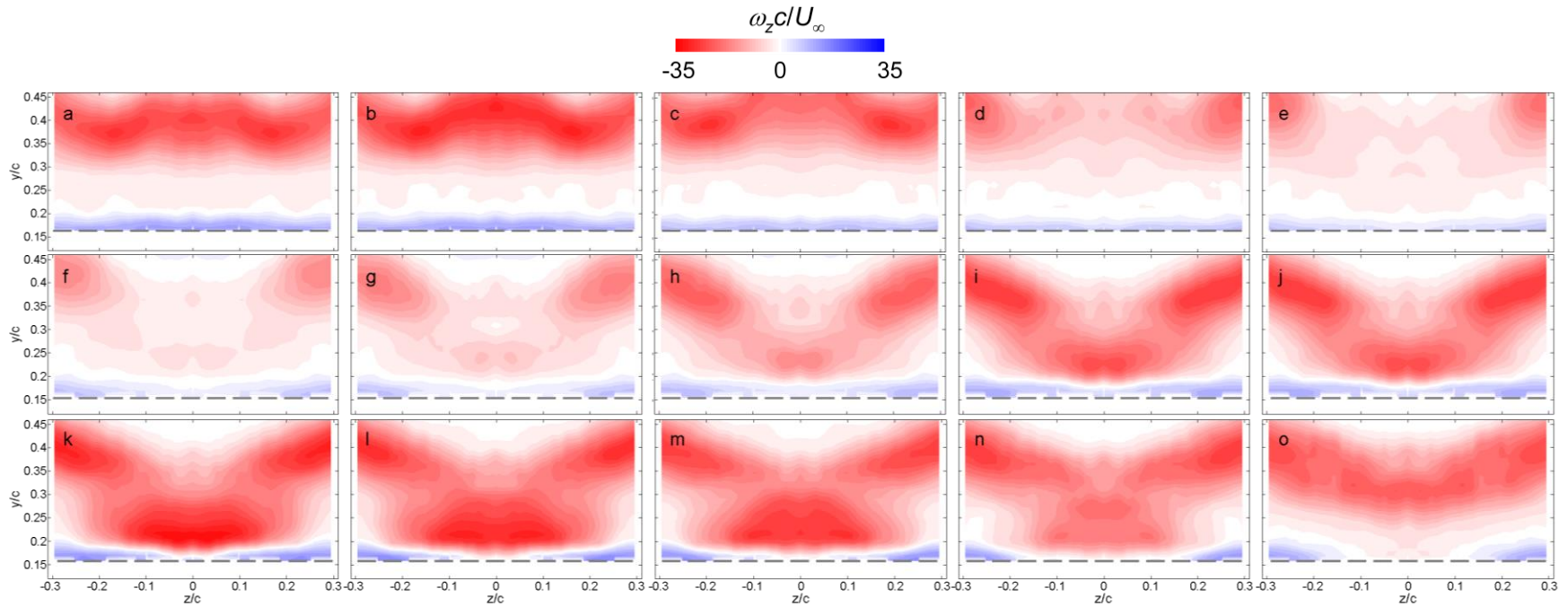


Figure 6.7: Distribution of phase-averaged spanwise vorticity, ω_z , across the span at $x/c = 0.76$ mirrored about $z = 0$ at $t/T_{conv} = 0$ (a), 0.72 (b), 0.88 (c), 0.96 (d), 1.04 (e), 1.12 (f), 1.2 (g), 1.28 (h), 1.36 (i), 1.44 (j), 1.52 (k), 1.68 (l), 1.92 (m), 2.32 (n) and 3.12 (o). The airfoil surface is shown as dashed line.

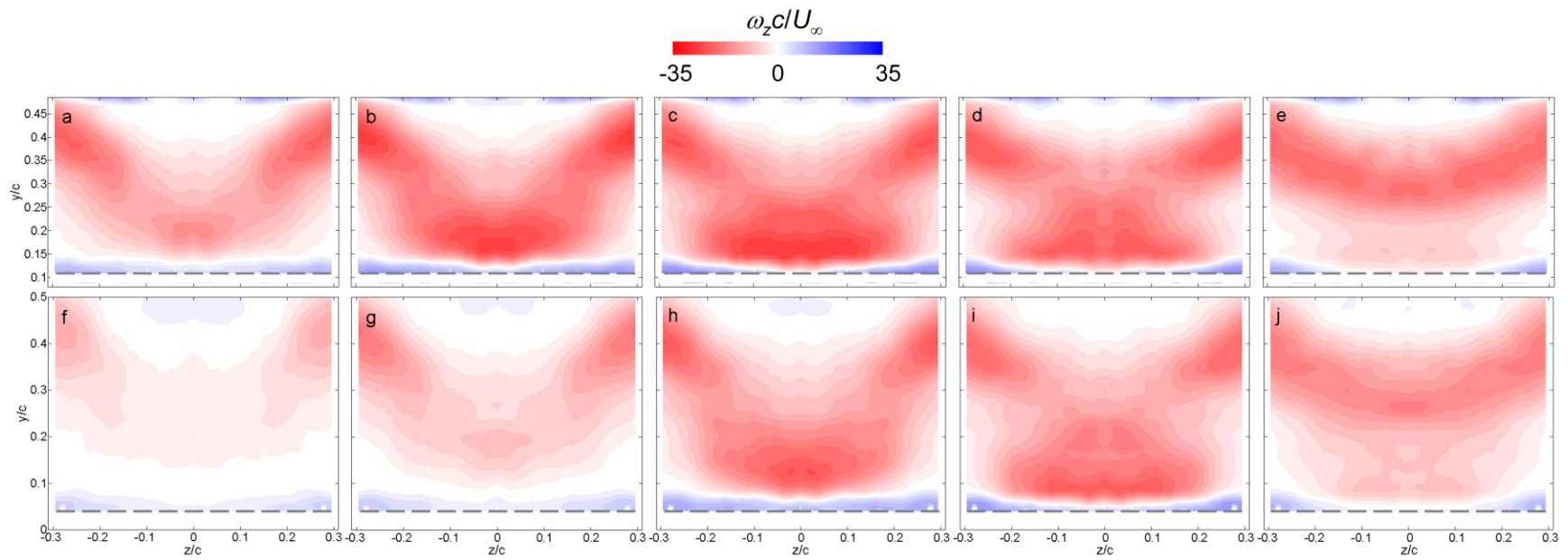


Figure 6.8: Distribution of phase-averaged spanwise vorticity, ω_z , across the span at $x/c = 0.85$ (a-e) and 0.95 (f-j) for the flow in Figure 6.5 mirrored about $z = 0$ at $t/T_{\text{conv}} = 1.52$ (a, f), 1.68 (b, g), 1.92 (c, h), 2.32 (d, i), and 3.12 (e, j). The airfoil surface is shown as dashed line.

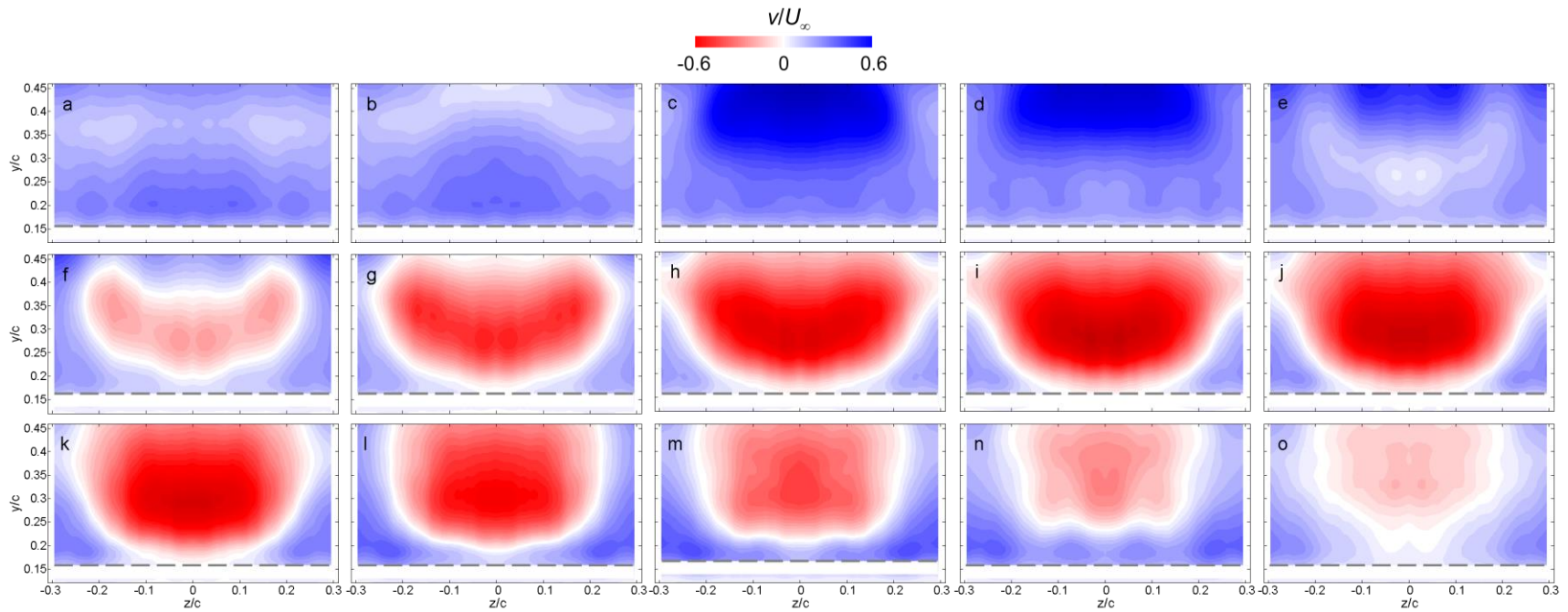


Figure 6.9: Distribution of the phase-averaged cross stream velocity, v , across the span at $x/c = 0.76$ for the flow in Figure 6.8 mirrored about $z = 0$ at the same timing t/T_{conv} as in Figure 6.7.

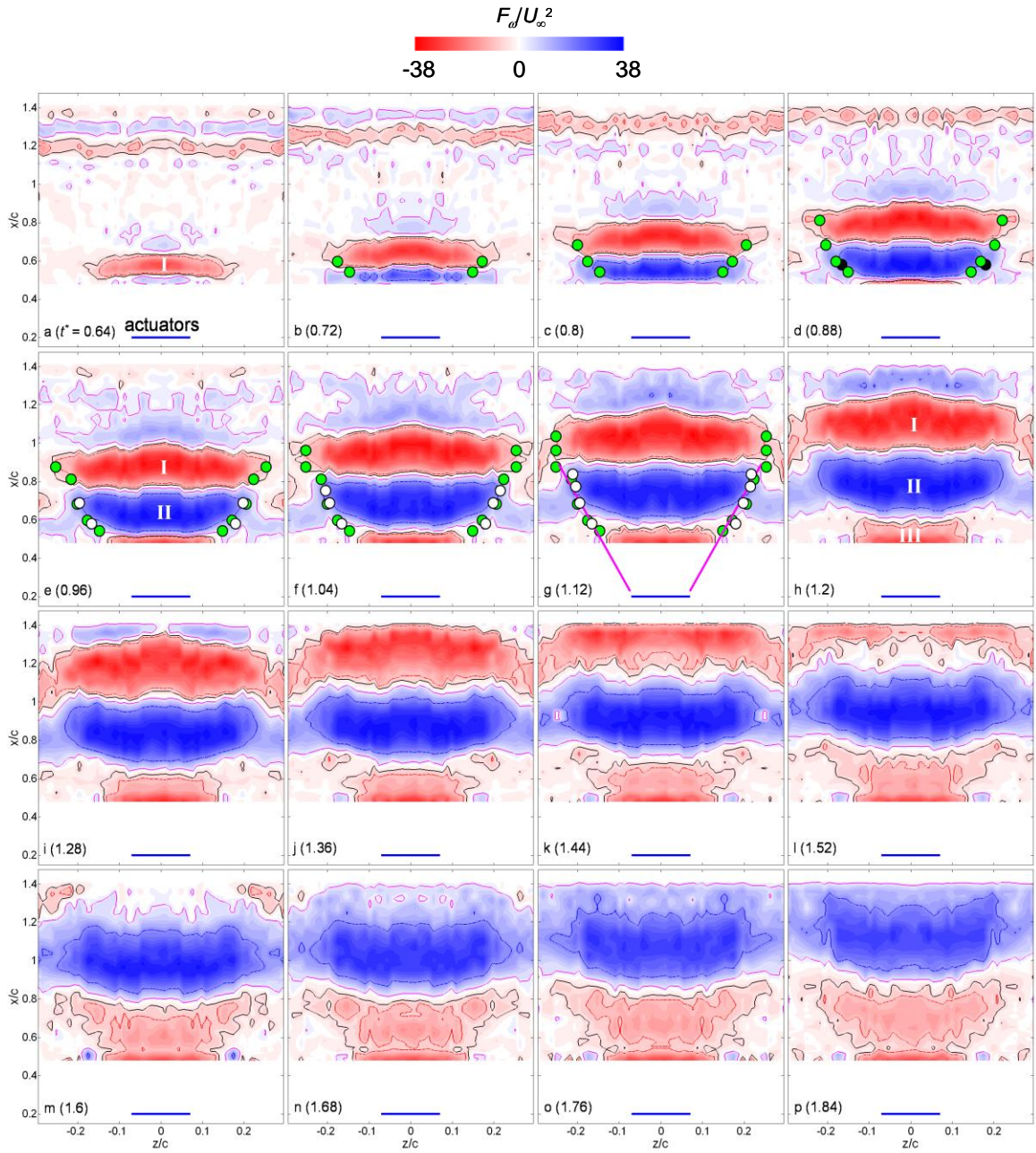


Figure 6.10: Phase-averaged contours of streamwise flux of vorticity, $\int \omega u \, dy$, computed at each location x from the PIV planes for $t/T_{\text{conv}} = 0.64$ (a), 0.72 (b), 0.8 (c), 0.88 (d), 0.96 (e), 1.04 (f), 1.12 (g), 1.2 (h), 1.28 (i), 1.36 (j), 1.44 (k), 1.52 (l), 1.6 (m), 1.68 (n), 1.76 (o) and 1.84 (p). The spanwise actuator array is shown for reference at the bottom of each plot. The labeled contours represent increased (“I” and “III”) and decreased (“II”) CW vorticity flux. The circles represent the spanwise edges of “I” (○) and “II” (●) at the previous instance. The data are mirrored about $z = 0$.

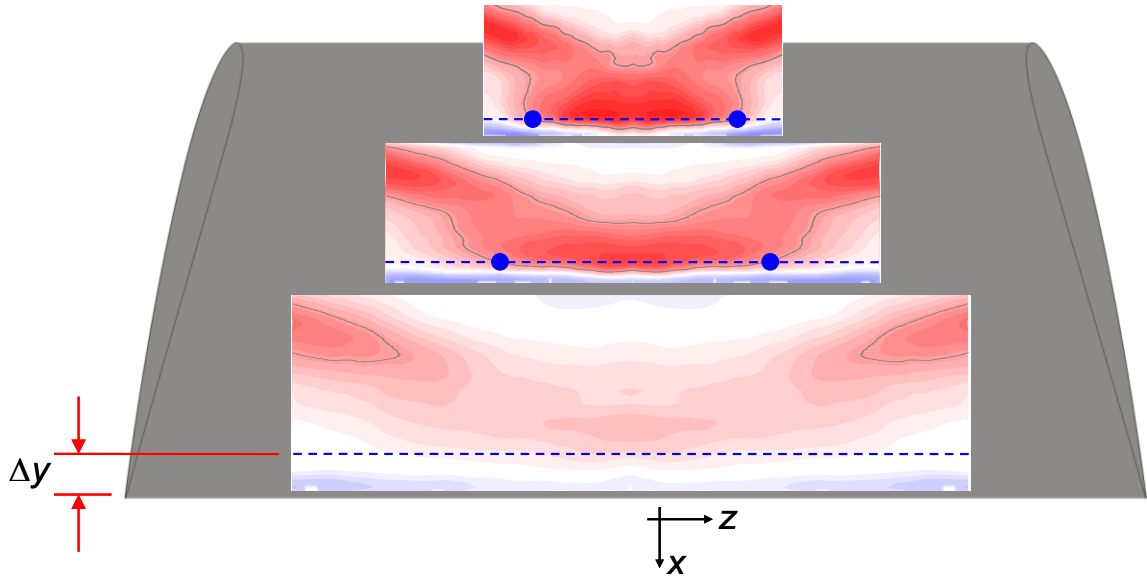


Figure 6.11: Raster plots of spanwise vorticity in three y - z planes overlaid on the airfoil illustrating averaging of $\omega(y, z; t)$ within the domain $0.05 \leq y/c \leq 0.1$ above the surface that is represented by the dashed lines located at $y = \Delta y$ at each x . The location $z = z_0$ along the dash lines for which $\omega(\Delta y, z) = \omega_0 = -300 \text{ s}^{-1}$ is marked by (\bullet). The data are mirrored about $z = 0$.

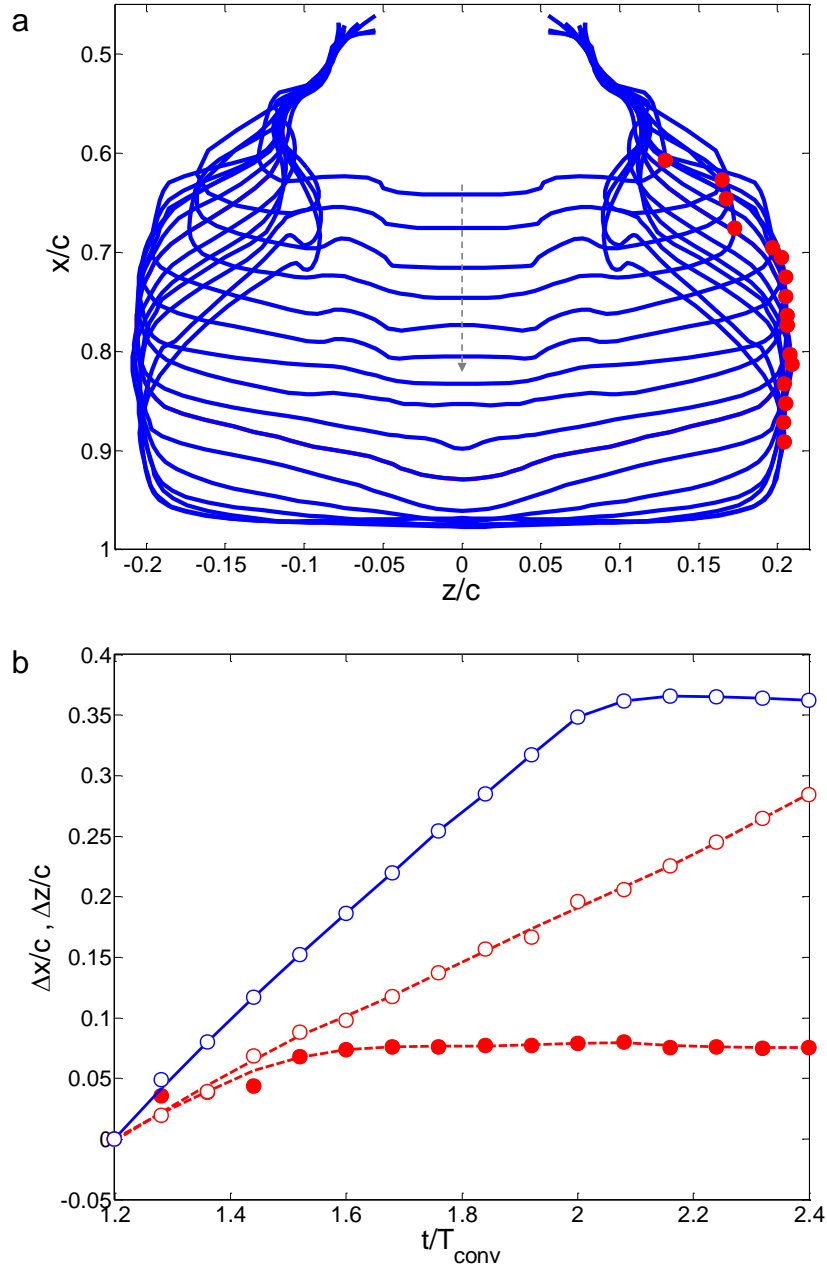


Figure 6.12: (a) Phase-averaged contours in the x - z plane for $1.12 \leq t/T_{\text{conv}} \leq 2.32$ where each contour represents the loci of $z_0(x)$ within $0.05 \leq y/c \leq 0.1$ above the surface for which $\omega = \omega_0 = -300 \text{ s}^{-1}$ (*cf.*, Figure 6.11). These loci represent the spanwise and streamwise development of the effects of the actuation on the boundary layer above the airfoil's surface. The spanwise edge of each contour is marked by (\bullet). (b) The spreading rate of the interface between the attached and outer flow is estimated by the celerity of the edges of the contour lines in (a) in the streamwise (\circ , Δx) and spanwise (\bullet , Δz) directions, and are compared with the streamwise growth rate of the loci on the centerline (\circ , Δx). The data are mirrored about $z = 0$.

CHAPTER VII

UNBOUNDED ACTUATION IN A NOMINALLY 3-D SEPARATED FLOW

This section builds on the findings of §VI in which spanwise unbounded (3-D) actuation is applied in a 2-D separated base flow. In this section, the actuation is extended to a nominally 3-D base flow that extends over the full spanwise width of the wind tunnel model.

7.1. The Base Flow Field

As the spanwise spacing between the partitions is increased, the base flow develops a local 3-D stall region that is characteristic of high span-to-chord aspect ratio airfoils (e.g., Winkelmann and Barlow, 1980). The 3-D features of the separated flow domain at $\alpha = 19^\circ$ when the partitions are placed at the tips of the airfoil ($S_{\text{fence}}/c = 1.68$) are demonstrated first using a time-sequence of surface oil visualization (Figure 7.1) that show the development of oil patterns with time following the start of air flow. Figure 7.1a shows minor changes in the oil distribution near the leading edge of the airfoil after one minute. The image in Figure 7.1b is taken after seven minutes of air flow and shows accumulation of oil (marked by arrow) downstream of the curved separation line indicating that separation begins at center span ($z = 0$) about $0.15c$ downstream of the leading edge, and then progresses in the spanwise direction towards the outboard sections of the span. The separation line is reasonably symmetric about $z = 0$ and does not appear to change further with time as evident from the similar oil patterns in Figure 7.1c (after

36 minutes of air flow). Figure 7.1c shows a region of oil accumulation upstream of the trailing edge and approximately symmetric about center span, that continues to develop as shown in Figure 7.1d (after 105 minutes) indicating a domain of recirculating flow and the presence of a local, 3-D separation bubble or stall cell. In addition, streaks of oil in Figure 7.1 (marked by arrow in Figure 7.1c) upstream of the separation line indicate that flow from the leading edge approaching the curved separated flow domain turns towards the spanwise edges of the model. Note that the actuator array marked with a red dash line in Figure 7.1d is located upstream of the separation line.

The surface flow features in Figure 7.1 are in qualitative agreement with the observations of Winkelmann and Barlow (1980) who reported stall cells on finite span airfoils of different aspect ratios ($S/c = 3$ to 9) and noted that the formation and evolution of the trailing edge “mushroom-shaped” stall cells depend strongly on the airfoil's aspect ratio, and that the number of these cells typically increases with S/c . Although $S_{\text{fence}}/c = 1.68$ in the present investigation is somewhat lower than the lowest aspect ratio of Winkelmann and Barlow (1980), the present visualization is in qualitative agreement with their findings. The oil patterns in Figure 7.1 show variations across the span and some asymmetry about $z=0$ which may be attributed to a random deflection by the separated flow. The spanwise variations in the separation over the baseline airfoil are further examined using planar and stereo-PIV, as shown by the green line segments in Figure 7.1d. Planar measurements are taken in the x - y planes $z/c = 0, 0.16, 0.27,$ and 0.39 (lines $i - iv$) and stereo measurements across the airfoil span are taken in the $\hat{y} - \hat{z}$ plane (*cf.*, §II.3.2) that intersects the airfoil surface at $x/c \approx 0.78$ (line v).

The spanwise variations and symmetry of the flow about mid-span ($z = 0$) is demonstrated using spanwise distributions of the streamwise (u) and spanwise (w) velocity components in the domain $-0.27 \leq z/c \leq 0.76$ ($S_{\text{fence}} \approx 1.7c$) shown in Figures 7.2a and b, respectively. These distributions are measured at three cross-stream elevations ($\Delta y/c = 0.074, 0.17$ and 0.233) above the airfoil surface that represent the lower, mid and upper cross stream regions of the stereo-PIV data. Within the limited extent of the spanwise measurement domain, the streamwise velocity profiles in Figure 7.2a display reasonable symmetry about $z = 0$ as suggested by the oil visualization in Figure 7.1. Although the velocity profiles in Figure 7.2a are not identical about $z = 0$, the largest differences between u with the same $|z|$ for $-0.27 \leq z/c \leq 0.27$ are smaller than $0.08U_\infty$. Similarly, the maximum differences in the v (not included in Figure 7.2) and the w (Figure 7.2b) velocity components are less than $0.04U_\infty$ and $0.06U_\infty$, respectively. Furthermore, the spanwise velocity distribution in Figure 7.2b show that $w < \pm 0.03U_\infty$ at $z = 0$ and $w(z) \approx -w(-z)$. Therefore, although *the present measurements clearly do not include direct evidence that the flow is fully symmetric about the center plane, it is nevertheless assumed that the flow is symmetric within $|z|/c \leq 0.76$* so that the complex 3-D flow structures can be visualized using mirrored PIV measurements about the center plane to help explain some of the intricate 3-D features of the flow field.

The 3-D features of the stalled domain are manifested by the spanwise reduction in the cross stream extent of the reversed flow. Cross stream distributions of the streamwise velocity component from the planar PIV data at multiple spanwise ($z/c = 0, 0.16, 0.27$, and 0.39) and streamwise ($x/c = 0.46, 0.71, 0.96$, and 1.22) stations are shown in Figures 7.3a-d. Near the center plane ($z = 0$ and 0.16), the 3-D base flow is reasonably similar to

the 2-D base flow ($S_{\text{fence}}/c = 1.07$, Figure 6.1), although the cross stream width of the recirculation domain in the 3-D configuration is somewhat smaller. However, in contrast to the velocity distributions in the 2-D base flow (Figure 6.1), in the 3-D flow the magnitude of the peak reversed flow decreases with spanwise distance from the centerline due to the increased span between the fences. For example, at $z/c = 0.39$ the peak decrease is about 50%, 50%, and 66% for $x/c = 0.71$, 0.96, and 1.22, respectively. The corresponding distributions at $x/c = 0.46$ indicate that at $z/c = 0.27$ and 0.39, the flow is attached. Finally, distributions of spanwise vorticity in the cross stream planes ($z/c = 0, 0.16, 0.27, \text{ and } 0.39$) are shown in two perspective views in Figure 7.4 (the off-center data are mirrored about $z = 0$, and the partitions are not included) and illustrate the displacement of the vorticity concentrations away from the airfoil as a result of the 3-D separation, and the spanwise decrease in the cross stream extent of the separated flow (*cf.*, the nominally spanwise uniform distribution in Figure 6.1d). The structure in the near wake exhibits cross stream spreading of the CW and CCW wake vorticity concentrations.

7.2. Pulsed Transients in 3-D Separation on a Static Airfoil

The temporal and spatial variations of the flow over the static airfoil following finite-span, single pulsed actuation using the entire seven actuator segments ($S_{\text{act}}/S_{\text{fence}} \approx 0.21$) are examined at $\alpha = 19^\circ$. The flow attachment is investigated within the four cross stream (x - y) planes $z/c = 0, 0.17, 0.27, \text{ and } 0.39$ (*cf.*, Figure 7.1d) and within the \hat{y} - \hat{z} plane using phase-locked planar and stereo-PIV measurements, respectively.

7.2.1. Actuation Effects

The effects of the single pulse, unbounded actuation in the presence of the 3-D base flow is examined using time-sequences of phase-averaged PIV measurements as shown in Figure 7.5 at four cross stream planes $z/c = 0$ (column a), 0.17 (b), 0.27 (c), and 0.39 (d) (the off-center planes are located beyond the spanwise edges of the actuator array $z = \pm 0.5S_{\text{act}} \approx 0.18c$), at $t/T_{\text{conv}} = 0$ (row i), 0.4 (ii), 0.64 (iii), 0.88 (iv), 1.12 (v), 1.52 (vi), 1.76 (vii), and 2.64 (viii).

Figures 7.5a(i-vii) show that the transitory effects induced by single pulse actuation in 3-D at the centerplane $z = 0$ of the base flow are similar to the effects of bounded (§IV) and unbounded (§VI) single pulse actuation in a 2-D base flow in terms of the severing of the shear layer ($x/c \approx 0.38$, $t/T_{\text{conv}} = 0.4$, Figure 7.5a-ii) and the roll-up and shedding of the CW vortex (Figures 7.5a(iii-v)). The 3-D base flow leads to several small differences in the details of the flow attachment including a more coherent bull-nose vortex in the attaching boundary layer (Figure 7.5a-iv) that remains attached through the trailing edge, and a larger streamwise distance between the severed CW vortex and the attaching boundary layer. Owing to the arrival of the attaching boundary layer at the trailing edge, there is noticeable regulation of the CCW vorticity layer in Figure 7.5a-viii at $t/T_{\text{conv}} = 2.64$ that is characteristic of unbounded actuation only (*cf.*, §VI). Although not included in Figure 7.5, the relaxation process in which the attached flow gradually returns to its base flow is significantly slower compared to the bounded actuation in 2-D base flow (§IV) owing to the prolonged accumulation of CW vorticity during the attachment.

The 3-D effects associated with the separation cell in the base flow result in a spanwise reduction in the extent of flow separation (Figures 7.5b-i, c-i and d-i) compared

to the center plane (Figure 7.5a-i) as noted in connection with Figures 7.2 – 7.3. The differences between the outboard planes in the severing of the shear layer and the onset of the rolled-up CW vortex are evident in Figures 7.5. First, as noted in §VI (Figure 6.5), the spanwise spreading of the actuation effects namely the severing of the separating shear layer that is first measured at $t/T_{\text{conv}} = 0.4$ at $z/c = 0$ and 0.17 (Figures 7.5a-ii and b-ii) are somewhat delayed to $t/T_{\text{conv}} = 0.64$ and 0.8 for $z/c = 0.27$ and 0.39 (Figures 7.5c-ii and d-ii, respectively). As a result of the 3-D base flow the spanwise spreading rate of the vortex is faster than in the 2-D base flow, and is estimated as $\Delta z/\Delta t \approx 0.75U_\infty$ compared to $\Delta z/\Delta t \approx 0.5U_\infty$ (§VI, Figure 6.5). Although the actuation span in the 3-D flow is larger, it is noted that the ratios of the actuation span to the fence spacing is nearly the same for the 3-D ($S_{\text{act}}/S_{\text{fence}} = 0.21$) and 2-D ($S_{\text{act}}/S_{\text{fence}} = 0.17$) base flows. The CW vortex continues to grow and accumulates vorticity as it advects downstream (Figures 7.5b-, c- and d-iv) while the leading edge “bull-nose” vortex of the upstream boundary layer continues to attach in the planes $z/c = 0.17$ and 0.27 (Figure 7.5b and c). In the outermost ($z = 0.39c$) plane, the leading edge of the upstream severed vorticity layer does not become attached to the surface at $t/T_{\text{conv}} = 0.88 - 1.12$, and subsequently attaches over the airfoil with the upstream flow ostensibly as a result of the strengthening of the CW vortex, and along with the flow in $z/c = 0.17$ and 0.27 (rows b and c) the attachment reaches the trailing edge at $t/T_{\text{conv}} = 1.76$ and 2.64. The attaching flow over the airfoil and the changes in the CCW vorticity in the near wake are almost identical at the four spanwise locations (e.g., rows vii and viii in Figures 7.5a, b, c and d). These data indicate that the attachment of the outboard flow well beyond the spanwise edge of the actuator

array appears to be primarily affected by spanwise evolution and spreading of the rolled-up CW vortex, and its proximity to the local separated flow.

The spanwise variations in the flow response are visualized using a perspective view of the phase-averaged concentrations of spanwise vorticity in the four PIV planes (mirrored about center-span) in Figure 7.6 at $t/T_{\text{conv}} = 0.1$ (a), 0.56 (b), 0.72 (c), 1.2 (d) and 2.08 (e). The severing of the separating shear layer and the formation of a CW vortex is initially observed near $x/c \approx 0.4$ ($t = 0.4T_{\text{conv}}$, Figure 7.6a) only in the center three planes ($-0.17 \leq z/c \leq 0.17$) over the full width of the actuator array ($0.34c$). The vortex continues to roll up along the span of the flow and severs the separating shear layer as it is advected downstream ($t/T_{\text{conv}} = 0.56$ and 0.72 for $z/c = 0.27$ and 0.39 , respectively, in Figure 7.6b and c), indicating that the flow disruption and instability induced by the actuation continues to propagate along the vortex core. The rate of spanwise spreading is clearly affected by the advection speed or celerity of the “primary” CW vortex that is first induced by the actuation (as apparent from the presence of the vortex only for $z/c < 0.5S_{\text{act}}$). The data in Figure 7.6 also show that similar to the 2-D base flow (§VI), the severed flow is three-dimensional as depicted by the spanwise structure of the CW vortex over the airfoil (e.g., in Figure 7.6c at $t/T_{\text{conv}} = 0.72$), although the spanwise variations appear to be accentuated by the 3-D base flow. More importantly, as the effects of actuation extend beyond the actively-actuated domain, the attached flow in all the z -planes upstream of the vortex are similar (Figures 7.6d and e at $t/T_{\text{conv}} = 1.2$ and 2.08), indicating a flow interface region between the attaching and separated flows that is less distinguishable in contrast to the strong spanwise variations in the distribution of vorticity across the span in Figure 6.5.

7.2.2. 3-D Velocity and Vorticity Field

The spanwise evolution of the 3-D base flow following actuation is investigated using phase-averaged stereoscopic PIV measurements obtained in the \hat{y} - \hat{z} plane that is normal to the surface of the airfoil and tilted streamwise at 30° (*cf.*, §II). It is noted that the seeding density in the free stream was sparse compared to the recirculation domain over the airfoil, and, as a result, the PIV data shown in Figures 7.7 - 7.9 has a (time-dependent) spanwise boundary above the airfoil beyond which velocity vectors could not be computed with sufficient fidelity. Figure 7.7 shows color raster plots of the plane-normal vorticity, $\omega_{\hat{x}}$, superimposed with planar projection of the velocity vectors (\hat{v} , \hat{w}) (the PIV data are mirrored about $z = 0$). The data plane is viewed in the streamwise direction and red and blue mark concentrations of CW and CCW plane-normal vorticity, respectively.

A striking feature of the flow prior to the onset of the actuation is the presence of adjacent, opposite-sense streamwise vorticity concentrations over the airfoil (Figure 7.7a, $z > 0.4c$, and $z < -0.4c$) that are associated with the formation of spanwise (symmetric) outboard wall-jets that are associated with spanwise spreading of the 3-D flow over the stalled airfoil. The wall jets are accompanied by the formation of a lower-tier (CCW) and upper-tier (CW) streamwise vorticity concentrations adjacent to the surface and near the cross stream edge of the separated flow. Note that the inner spanwise edges ($z/c \approx 0.4$) of the streamwise vorticity concentrations in Figure 7.7a are close to the outermost x - y PIV plane in Figure 7.6, and are in the vicinity of the oil build-up near the trailing edge that corresponds to the 3-D flow features in Figure 7.1d.

By $t/T_{\text{conv}} = 0.88$ (Figure 7.7b), the severed CW spanwise vortex (Figure 7.5a-iv) is slightly downstream of the measurement plane and induces an upwash as it is advected through the present measurement plane ($0.88 \leq t/T_{\text{conv}} \leq 1.12$) that is manifested by an increase in the magnitude of the cross stream velocity component \hat{v} in Figures 7.7b-d. Streamwise tilting of the spanwise edges of the severed CW vortex that merge into the separating shear layer in the outboard flow domains are tilted upstream and toward the airfoil surface in a manner that is commensurate with the spanwise curvature of the base flow, and therefore briefly intensify and attenuate the lower- and upper-tier wall jet vorticity, respectively. The approaching attached boundary layer begins to induce downwash that is already measured at $t/T_{\text{conv}} = 1.2$ (Figure 7.7e) and is manifested by the cross stream narrowing of the separated flow and by reduction on the magnitude of the cross stream velocity. The attachment of the upstream flow is clearly evident by $t/T_{\text{conv}} = 1.36$ (Figure 7.7g). As the attachment progresses the speed of the wall jet increases with the diminution in its cross stream extent and the upper-tier CW vorticity concentrations intensify significantly. At the same time, the streamwise vorticity layer near the surface is squashed and as a result of the narrowing cannot be resolved by the present measurements (even though the cross stream shear near the surface increases significantly). The intensification of the spanwise wall jets indicates that the 3-D spreading of the base flow is not suppressed by the attachment of the upstream boundary layer and by the spanwise spreading of the attaching CW vorticity layer in Figure 7.5. As the attachment progresses ($1.2 \leq t/T_{\text{conv}} < 1.6$, Figures 7.7e-j), each of the streamwise vortices induces spanwise velocity distributions that is commensurate with its sense of rotation. During the transition from attachment to relaxation ($1.84 \leq t/T_{\text{conv}} < 2.96$,

Figures 7.7m-q), the spanwise wall jets weaken and ultimately, the streamwise vorticity concentrations vanish in 7.7q rendering the nominally attached flow nearly 2-D. During the relaxation as the streamwise flow begins to lift of the surface, the wall jets reverse their direction (i.e., towards the center plane) and the outer flow streamwise vorticity concentrations reappear and lift off the surface while concentrations of opposite sense are induced near the surface (Figures 7.7r-t, $5.12 \leq t/T_{\text{conv}} \leq 6.56$). The data in Figure 7.7 indicate that as the separation finally reaches a nominally stable state, the spanwise wall jets reverse their direction as shown in Figure 7.7a.

Figures 7.8 and 7.9 show color raster plots of the plane-normal (\hat{u}) and cross stream (\hat{v}) velocity components, respectively, corresponding to the velocity vectors in Figure 7.7. The spanwise distributions of the base flow in Figures 7.8a and 7.9a clearly show that the reversed ($\hat{u} < 0$) flow away from the airfoil surface ($\hat{v} < 0$) is diminishing towards the fences (the white contour in Figure 7.8a corresponds to $\hat{u}/U_{\infty} \approx 0$). At $t/T_{\text{conv}} = 0.8$ (Figure 7.8b), the presence of the CW spanwise vortex results in minimal measurable changes in u (Figure 7.8b) while the upwash induced upstream of the vortex (*cf.*, 7.7b) is evident for $-0.6 < x/c < 0.6$ and continues to intensify in Figure 7.9c ($t/T_{\text{conv}} = 0.88$) leading to a decrease in the magnitude and spatial extents of the separated flow in Figure 7.8c. As expected, the reduction in the cross stream width of the flow during attachment is accompanied by an increase in u , while the evolution of the two intensified streamwise vortices (Figure 7.7j) results in typical induced cross stream velocity (negative inboard and positive outboard, $0.2 < z/c < 0.6$, Figures 7.9d-f). These distributions of the cross stream velocity component enable a direct comparison with the corresponding data for the 2-D base flow in Figure 6.9 that shows that during attachment

the distribution of the cross stream velocity is nominally uniform within the domain of influence of the actuation ($-0.2 < z/c < 0.2$). As the attachment progresses, the attached layer becomes thinner and more 2-D at $t/T_{\text{conv}} = 1.92$ and 2.96 in Figures 7.8g-h and 7.9g-h when the streamwise vortices vanish (Figure 7.7q).

The flow dynamics following an unbounded actuation pulse in the 2-D base flow (*cf.*, §VI, $S_{\text{fence}}/c \approx 1$, $S_{\text{act}}/S_{\text{fence}} \approx 0.17$) and 3-D base flow ($S_{\text{fence}}/c \approx 1.7$, $S_{\text{act}}/S_{\text{fence}} \approx 0.21$) are compared using iso-surfaces of the phase-averaged spanwise vorticity interpolated from the planar PIV measurements in cross stream (z) planes. The iso-surfaces are viewed from above (Figures 7.10) and in a perspective view (Figure 7.11). Note that the iso-surfaces of the 2-D base flow are obtained from 24 PIV planes and therefore have significantly higher spatial resolution compared with only four planes in the 3-D base flow. Although the limited number of cross stream planes limits resolution and fidelity of the iso-surfaces for the 3-D flow, it is nevertheless instructive to compare the dynamics of the two flows while supplementing the 3-D flow surfaces with the stereo-PIV data in Figures 7.7 – 7.9.

In Figures 7.10 and 7.11, the effects of the actuation following the trigger are shown in columns “i”– “ix” for $0.56 \leq t/T_{\text{conv}} \leq 1.2$ (equal time steps $\Delta t/T_{\text{conv}} = 0.08$) where the 2-D ($S_{\text{fence}}/c \approx 1$) and 3-D ($S_{\text{fence}}/c \approx 1.7$) base flows are shown in rows “a” and “b” respectively. Column “x” in Figure 7.11 shows the flows at $t/T_{\text{conv}} = 2.4$. Several features of the spanwise vorticity concentrations point to similar features of the enhanced spanwise attachment in the two base flows. To begin with, the similar severing of the separating shear layer and the roll-up of CW vorticity on the suction surface are visible in Figures 7.10 and 7.11. These images show the spanwise spreading and intensification of

the CW vortex as it is advected towards the trailing edge, and the concomitant appearance and spreading of the low CW vorticity domain upstream. The corresponding flow attachment upstream of the low vorticity domain is also visible in Figures 7.10 and 7.11. Downstream of the actuator array, the spanwise extent of the attached domain scales with the width of the actuator array about the mid-span indicating that the effects of the actuation pulse are not substantially changed by the differences in the base flows as long as the same ratio between the actuators and spanwise spacing of the fences S_{act}/S_{fence} is maintained.

The iso-surfaces in Figures 7.10 and 7.11 also show some of the differences between the attachment processes in the two base flows. The resultant flow interface at the spanwise edges between the inner, attached and the outer, separated flows is prominent in Figures 7.11a-vii to a-x where the attachment in the outer flow regions is diminished. Conversely, attachment is observed as far as $z/c = 0.39$ in Figures 7.11b-vii to b-x, which demonstrate the discussion of Figure 7.6 that the spreading of the flow attachment to the unactuated domain when the base flow is 3-D (row “b” in Figure 7.11) is enhanced when compared to the 2-D base flow counterpart (row “a” in Figure 7.11). Although a similar S_{act}/S_{fence} is maintained between the two unbounded actuation, the attachment effects continue in the off-center regions of the 3-D base flow and results in the absence of the interface between the attached and the separated flows as shown in Figure 7.11b-x (*cf.*, Figure 7.11a-x).

7.3. Controlled, Transitory 3-D Attachment on a Dynamically-Pitching Airfoil

The control authority of the unbounded, pulsed jet was explored by coupling the actuation to time-periodic separation on an airfoil that is oscillating time-periodically

beyond its stall margins [$\alpha(t) = \alpha_0 + \alpha_p \sin(\Omega t)$ where α_0 is the nominal average angle of attack, α_p is the oscillation amplitude]. The reduced pitch frequency is $k = \Omega c / 2U_\infty = 0.115$ for which the pitch cycle period is $T_p = 625$ ms, the pitch excursion is $\alpha_p = 4^\circ$ around $\alpha_0 = 14^\circ$ (the airfoil pitches up through 14° at $t = 0$). An important parameter of the coupling of a single-pulse actuation to the flow is the timing of the actuation pulse (T_{start}) relative to the pitch cycle (and thereby to the separation). The effects of a single pulse actuation during the pitch cycle on the time-periodic aerodynamic lift and pitching moment are examined for a range of T_{start} . These effects are then extended by using multiple, successive pulses (*cf.*, §V) during the cycle.

7.3.1. Timed-Interactions of a Single Actuation Pulse with Time-Periodic Separation

The phase-averaged lift $C_L(t)$ and pitching moment $C_{M,c/4}(t)$ are measured for several T_{start} relative to the pitch cycle in the absence (base flow, gray) and presence of single pulse actuation (red) and shown in Figures 7.12a-h, and 7.12i-p, respectively (the onset of the pulse is marked). As a result of the time-periodic pitch, separation in the base flow occurs at higher angle of attack than for the static airfoil (α_{stall} and $C_{L\text{stall}}$ are 13° and 1.45, and 17° and 2.2 for the static and dynamic airfoils, respectively). As can be seen in Figure 7.12a, the onset of dynamic stall occurs near $\alpha = 17^\circ$ on the upstroke, and is followed by large-scale separation and significant loss in lift ($\Delta C_L = 0.6$) that is associated with the shedding of the dynamic stall vortex and separation during the downstroke. The lift hysteresis in the base flow is characteristic of light dynamic stall.

The corresponding curve for the pitching moment during the oscillation cycle is shown in Figure 7.12i. The phase-averaged pitching moment during the oscillation cycle

exhibits an undesirable pitch instability or a “negative damping” of the aerodynamic moment (e.g. Carta, 1967; McCroskey, 1982; and Carr, 1988) when the airfoil extracts energy from the flow, inducing structural oscillations and vibrations whose amplitude can increase with time (flutter) and can result in possible structural damage. A CW loop in the pitching moment trace when plotted with α during the pitching cycle is indicative of negative damping. As shown in Figure 7.12i, the pitching moment of the base flow leads to negative damping for $\alpha > 15.5^\circ$ when $C_{M,c/A}(t)$ exhibits rapid CW increase ($\Delta C_{M,c/A}(t) = 0.08$) after being nearly time-invariant during most of the upstroke (shown as a CW cross-hatched loop in Figure 7.12i). This increase in C_M continues through the onset of the downstroke ($\alpha = 18^\circ$). The negative pitching moment subsequently decreases in magnitude as the airfoil continues to pitch down through $\alpha < 15.5^\circ$, and the sense of $C_{M,c/A}(t)$ is reversed to CCW.

When the pulse is applied during the upstroke but before the onset of dynamic stall (Figures 7.12a-e for $0 \leq T_{start}/T_P \leq 0.192$) as the thickness of the suction surface boundary layer increases, $C_L(\alpha)$ first exhibits a small decrease relative to the unactuated curve ($17^\circ < \alpha < 18^\circ$) similar to the shedding of CW vorticity as discussed extensively in §IV for the static airfoil. This decrease in $C_L(\alpha)$ is followed by an immediate increase beyond the corresponding base flow levels ($\Delta C_L \approx 0.2$) for the remainder of the upstroke, resulting in the crossover loops in the traces for $C_L(\alpha)$ of the actuated flows in Figures 7.12d and e, that continue for an extended fraction of the downstroke. It appears that during this time the actuation delays the onset of separation momentarily. The timed interactions of the pulsed jets as manifested in the lift and pitching moment curves in Figure 7.12 are highly sensitive to the pitch angle and pitch rate, illustrating the strong

coupling of the production and accumulation of vorticity on the airfoil induced by its motion with the interactions of the pulsed jets. For example, even when the pitch rate is near zero at $\alpha \approx 17 - 18^\circ$, pulsed actuation triggered at $T_{\text{start}}/T_P = 0.128$ and 0.16 (Figures 7.12c and 7.12d, respectively) results in opposite effects on the lift immediately following the actuation, namely $C_{L,\text{upstroke}} > C_{L,\text{downstroke}}$ and $C_{L,\text{upstroke}} < C_{L,\text{downstroke}}$ respectively.

When the actuation is applied ahead of the downstroke (through Figure 7.12e), the ensuing decrease in $C_L(\alpha)$ during the downstroke due to the unsteady separation is lower than in the base flow. On the other hand, when the actuation pulse is delayed until the downstroke begins (e.g. $T_{\text{start}}/T_P = 0.24$ and 0.32 in Figure 7.12f and g) when the flow is already separated, there is a momentary ($\sim 0.05T_P$) and significant increase in the unsteady lift relative to the base flow during the downstroke (for $T_{\text{start}}/T_P = 0.24$, $\Delta C_L \approx 0.55$ for $17^\circ < \alpha < 17.5^\circ$) which relaxes within $0.24T_P$ (by $\alpha = 12^\circ$) thereafter. Note that for $T_{\text{start}}/T_P = 0.24$ the lift on the downstroke following actuation (that is effected over only 20% of the span) reaches nearly the same level as on the upstroke at the same angle, thereby reduces the lift hysteresis.

It is also evident that single pulse actuation can induce significant effects on the pitching moment. For $0 < T_{\text{start}}/T_P < 0.16$ (Figures 7.12i-l), the extent of negative damping is reduced as manifested by the reduction in the CW hysteresis loop over a range of pitch angles (e.g., $T_{\text{start}}/T_P = 0.128$ and 0.16 in Figures 7.12k and l, respectively). In Figures 7.12k and l, when the actuation pulse is applied at $T_{\text{start}}/T_P = 0.128$ and 0.16 , respectively, the extent of negative damping is significantly reduced as manifested by the reduction in the hysteresis loop over the large pitch angles indicating improvements in

pitch stability. On the other hand, when actuation is applied at $T_{\text{start}}/T_P = 0.24$ and 0.32 (Figures 7.12n and o), the effectiveness of the actuation for reduction of negative damping is significantly diminished. In fact, in Figure 7.13c, the negative damping is increased for $T_{\text{start}}/T_P > 0.4$. It should be borne in mind that the changes in lift and pitching moment discussed above are measured over the *entire* airfoil while the actuation is effected over only 20% of the span.

The timing effects on the transient response to pulsed actuation on the airfoil are computed from phase- and time-integrals of the unsteady lift,

$$L^* = \frac{\oint (C_L - C_{L,o}) d\alpha}{\oint C_{L,o} d\alpha} \quad \text{and} \quad L_{\text{cycle}}^* = \frac{\int_0^{T_p} (C_L - C_{L,o}) dt}{\int_0^{T_p} C_{L,o} dt},$$

and phase- and time-integrals of the pitching moment,

$$E^* = \frac{\oint (C_M - C_{M,o}) d\alpha}{\oint C_{M,o} d\alpha}, \quad \text{and} \quad M_{\text{cycle}}^* = \frac{\int_0^{T_p} (C_M - C_{M,o}) dt}{\int_0^{T_p} C_{M,o} dt}$$

relative to the base flow. The variation with the actuation timing T_{start} of these integral measures of the global lift, L^* and L_{cycle}^* , and of the pitching moment, E^* and M_{cycle}^* , are shown in Figures 7.13a-d, respectively. The phase-integral of the lift provides an estimate of the extent of cyclic hysteresis in the lift while the time-integrals provide an estimate of the cumulative changes in C_L and $C_{M,c/4}$ over the pitching cycle [the background colors mark the upstroke (pink) and downstroke (blue) segments of the pitching cycle, respectively].

The receptivity to actuation with increasing T_{start} is demonstrated in Figures 7.13a and b. These data show that the extent of lift hysteresis (L^*) is reduced by almost 30% over the range $0.2 < T_{\text{start}}/T_P < 0.4$, and that cumulative lift improvements above the base flow are achieved for $T_{\text{start}} > 0$ with maximum increase in L^*_{cycle} when $T_{\text{start}} \approx 150$ ms ($0.24T_P$ *cf.*, the cycle lift in Figure 7.12f). Figure 7.13a shows that the range of T_{start} with the maximum reduction in L^* ($0.2 < T_{\text{start}}/T_P < 0.4$) is also the range for which the reduction in hysteresis is nearly invariant with T_{start} . The increase in L^*_{cycle} with T_{start} for up to 0.2 - $0.22T_P$ (Figure 7.13b) results from the increased effectiveness of the pulsed actuation in delaying the onset of unsteady stall on the upstroke, and in attaching the separated flow following the onset on the downstroke. The abrupt decrease in L^*_{cycle} for $0.25 < T_{\text{start}}/T_P < 0.55$ is due to the lower C_L associated with the lower α on the downstroke. Although the maximum L^*_{cycle} is only 3% above the base flow, this is equivalent to a 3% increase in C_L during the entire pitching cycle that is attained with a single actuation pulse effected across only 21% of the airfoil span. The control authority of the single pulse diminishes as the actuation delay increases (e.g., $T_{\text{start}} = 0.48T_P$ in Figure 7.12h) as shown in Figures 7.13a and b where L^* and L^*_{cycle} returns to base levels for $0.4 < T_{\text{start}}/T_P < 0.6$ and $0.24 < T_{\text{start}}/T_P < 0.6$, respectively. Thereafter, the effectiveness of actuation is negligible as the flow over the airfoil at low α is attached.

Pulsed actuation can also effectively control the cumulative pitching moment. Figure 7.13c shows that the change in $\int C_{M,c/4} dt$ is maximum when the actuation is effected at $T_{\text{start}}/T_P = 0.128$ which coincides with the largest suppression of negative damping as shown in Figure 7.12a. For $0 < T_{\text{start}}/T_P < 0.128$, as the airfoil pitches up through the high angles but with a decreasing positive pitch rate, Figure 7.13c shows improved control

authority in effecting pitch stability. This suggests that the delayed interactions of pulsed actuation (as influenced by the onset of hysteresis due to the increased residence time of the airfoil's leading edge at these high angles) can prevent the onset of moment stall. The delayed severing of the boundary layer (before separation occurs) can lead to the formation of a fresh, thinner boundary layer that continues to grow temporarily. During this time, as the controlled flow interacts with the moving airfoil surface, the mitigation of the pitching moment hysteresis (as related to the negative damping) is effected by the accelerated flow and the corresponding time modulation of the vorticity concentrations near the leading edge as suction pressure over the airfoil is expected to increase.

The response of the flow to single-pulse actuation applied at $T_{\text{start}}/T_P = 0.24$, which yields the largest momentary increase in unsteady lift (Figure 7.12f) is further investigated using sectional circulation computed (relative to $t = 0$) using PIV measurements that are acquired phase-locked to the airfoil's motion at the planes $z/S_{\text{act}} = 0, 0.47, 0.78, \text{ and } 1.11$ (Figure 7.14). Note the distance between these PIV planes relative to the actuator edges at $z = \pm 0.5S_{\text{act}}$. Variations in the phase-averaged incremental changes in circulation with time in each of the planes (relative to $\Gamma_0(z)$ at α_0) are shown in Figure 7.14a for the base flow and 7.14b following the actuation.

In the absence of actuation (Figure 7.14a), the sectional circulation of the base flow increases during the upstroke until $t/T_P \approx 0.1-0.15$ which correspond approximately to the onset of dynamic stall (*cf.*, Figure 7.12), and thereafter the circulation and lift decrease rapidly and remain low during the downstroke. It is noted that both the magnitude and timing of the peak circulation increment increase with spanwise distance from the center plane as a result of 3-D effects in the base flow. The following shedding of the dynamic

stall vorticity concentration and the precipitous decrease in lift as the flow separates on the downstroke ($0.24 < t/T_P < 0.74$) also increases with spanwise distance from the center plane which is commensurate with the spanwise variation in the strength of the dynamic stall vortex. Thereafter, the circulation begins to increase nearly monotonically at all spanwise planes as the flow re-attaches.

Prior to the onset of actuation (Figure 7.14b), at $T_{\text{start}}/T_P = 0.24$, the increase in $\Delta\Gamma$ in each of the cross stream planes as the airfoil pitches up is similar to that of the base flow (Figure 7.14a). The initial decrease in circulation in following actuation ($t/T_P = 0.26 - 0.3$) is the result of the shedding of the severed CW vortex, and it is followed by a rapid increase due to attachment (up to $t/T_P = 0.36$) with minimal spanwise variations in the characteristic rate of change of the sectional circulation (Figure 7.14b, $0.32 < t/T_P < 0.4$). The data indicate that although the local minima in $\Delta\Gamma$ increase in magnitude with z , the increase following attachment is nearly spanwise invariant. It is important to note that following the actuation-induced temporal peak in circulation, the circulation decreases in all spanwise positions as the effects of the actuation relax, and the airfoil continues its downstroke motion, and a local minimum is reached at $t/T_P \approx 0.6$ indicating secondary shedding of vorticity as the induced flow attachment readjusts to the actual angle of attack during the downstroke. Such a pronounced secondary minimum is not prevalent in the base flow except perhaps at $z/S_{\text{act}} = 1.11$.

The variation of the circulation with $\alpha(t)$ following the actuation is shown in Figures 7.15a-c that compare the traces in the four spanwise planes (the direction of the airfoil motion is marked with arrows, and $\Delta\Gamma = 0$ at $\alpha = 14^\circ$ on the upstroke). At the center plane (Figure 7.15a), the circulation decreases abruptly at the end of the upstroke when

the flow over the airfoil stalls, but the actuation at $T_{\text{start}}/T_P = 0.24$ results in steep increase (at $\alpha = 17.3^\circ$ above the level during the upstroke) followed by a gradual relaxation as the downstroke continues. A similar pattern is also evident at $z/S_{\text{act}} = 0.47$. However, even though the increment in circulation following the actuation is nearly the same as in $z = 0$, the peak level at $z/S_{\text{act}} = 0.47$ is lower, and as a result during the relaxation the sectional circulation is also lower. A similar pattern is visible at $z/S_{\text{act}} = 0.78$ (Figure 7.15b), and 1.11 (Figure 7.15c). The global lift trace for the entire airfoil (Figure 7.12-f) shows a peak change in lift at about 17° on the downstroke that includes the contributions from actuated and unactuated segments. This trend is similar to the circulation increments in Figures 7.16a-c that occur at $\alpha = 17.3 - 17.5^\circ$ in that the actuation results in a significant (and rapid) increase in lift and circulation that are followed by the relatively gradual relaxation which also leads to a significant reduction in cycle hysteresis (almost 30%, in Figure 7.13a). The dependence of the increments in lift and circulation on the timing of the actuation pulse during the pitch cycle indicates that controlled timed interactions of discrete actuation pulses with the unsteady flow can effectively enhance the overall unsteady lift on the airfoil (*cf.*, 3% increase in Figure 7.13b).

7.3.2. Multiple Pulses and Staged-Actuation

The control authority of single pulse actuation is extended by using repetitive actuation (multiple pulses) during the pitch cycle. The first approach is to use N actuation pulses that are equally spaced in time during the pitch period. The actuation is synchronized to the airfoil's motion such that the first pulse is triggered at $t = 0$ when the airfoil crosses $\alpha = 14^\circ$ during upstroke. The resulting lift and pitching moment during the pitch cycle are shown in Figures 7.16a and b (the timing of the actuations is shown in Figure 7.16a)

for $N = 5, 10, 15$ and 20 such that the time between successive pulses is $T_{\text{pulse}} = 125, 62.5, 41.6,$ and 31.25 ms, respectively. It is evident from the oscillations in lift and pitching moment for $N = 5$ that the actuation results in large, time-dependent changes in the flow field over the airfoil. The limited effects of the first two pulses applied during the upstroke segment of the cycle following α_0 are similar to the results shown in Figure 7.12 where the pulsed jets interact with the flow ahead of separation. However, the third and fourth pulses are applied during the downstroke during the onset of stall ($\alpha \approx 18^\circ$), resulting in oscillations in the C_L and C_M .

The unsteady effects owing to the 3-D interaction with the uncontrolled segments of the airfoil are significantly mitigated when the number of actuation pulses is increased to $N = 10$, and as shown in Figure 7.16, there are no large lift and moment oscillations during the pitch cycle. Furthermore, the lift during the entire downstroke segment of the cycle is above the lift of the base flow indicating that dynamic stall is significantly suppressed and this effect persists throughout the entire downstroke. At the same time, the undesirable effects of “negative damping” in pitch are significantly reduced. The improvement in control authority as the number of pulses increases from $N = 5$ to 10 is due to the reduction in the elapsed time between successive pulses from $T_{\text{pulse}}/T_{\text{conv}} = 5$ to 2.5 (as can be seen in Figure 7.16, the flow reaches full stall within $4 - 5 T_{\text{conv}}$ on the downstroke). However, further increases in the number of pulses to $N = 15$ or 20 result in relatively small additional changes in C_L and $C_{M,c/4}$. In fact, as shown in connection with Figure 7.16, as few as $N = 8$ pulses equally distributed through the pitch cycle are sufficient to achieve the majority of the same increments in C_L and $C_{M,c/4}$. These results indicate that even in the presence of strong 3-D effects, tuning the timing of the actuation

pulses during the cycle can lead to an “optimal” actuation sequence that can effectively control and prevent the abrupt shedding large concentrations (dynamic stall) vorticity and minimize the required actuation power.

Further tuning of the actuation timing during the pitch cycle is shown in Figure 7.17. To begin with, comparison of the flow response to sequences of 8- and 20- actuation pulses that are equally distributed through the pitch cycle ($T_{\text{pulse}} \approx 78 \text{ ms}$, $3.1T_{\text{conv}}$, and $T_{\text{pulse}} \approx 31 \text{ ms}$, $1.25T_{\text{conv}}$) demonstrates that there are only minor differences in C_L and $C_{M,c/4}$ during the downstroke. The data in Figure 7.17 also shows a “rapid” 8-pulse actuation sequence that is triggered (relative to $\alpha = \alpha_0 = 14^\circ$ on the upstroke) at $T_{\text{start}} = 0$, but for which the pulses are spaced at $T_{\text{pulse}}/T_{\text{conv}} = 1.4$ and therefore the actuation terminates before the airfoil returns to the reference start of the pitch cycle ($\alpha = \alpha_0 = 14^\circ$). Figure 7.17 shows that this “rapid” 8-pulse sequence suppresses the effects of stall in both the lift and moment.

The effects of the actuation on the flow dynamics over the model during the pitch cycle are captured using PIV measurements in the cross stream x - y plane at center span ($z = 0$). The measurement domain is $-0.15 < x/c < 1.25$ and $-0.4 < y/c < 0.15$ above the airfoil and in the near wake, and PIV data are acquired phase-locked to the oscillation cycle. The PIV images shown in Figure 7.18 are color raster plots of the phase-averaged spanwise vorticity concentrations with superimposed velocity vectors. The evolution of the flow during five instances of the oscillation cycle in Figure 7.17 (upstroke: $\alpha = 15$, 17.2 and 18° , and downstroke: $\alpha = 15.7$ and 11.2°) in the absence and presence of actuation are shown in the two left columns of Figure 7.18 [Figures 7.18a($i - v$) and 7.18b($i - v$)], respectively. The images in Figures 7.18b($i - v$) are captured $\Delta t = 0.024T_p$

following the 1st, 3rd, 5th, and 8th actuation pulses while the images in Figures 7.18a-v and b-v are captured at $t = 0.621T_p$ when the airfoil pitches down through 11.2° for the two flows. The images in the third and fourth columns of Figure 7.18 [Figures 7.18c(i - v) and 7.18d(i - v)] are also of the actuated flow, but the five images in each column are captured at a fixed delay relative to the corresponding images in Figure 7.18b. These delays are $\Delta t = 0.016T_p$ (Figure 7.18c) and $= 0.032T_p$ (Figure 7.18d).

In the absence of actuation, the flow at $\alpha(t/T_p = 0.038) = 15.0^\circ$ (Figure 7.18a-i) appears to be attached over most of the suction surface although the boundary layer thickens considerably towards the trailing edge while the corresponding flow over the static airfoil is stalled (*cf.*, Figure 7.17a). As the airfoil continues to pitch up through $\alpha(t/T_p = 0.150) = 17.2^\circ$ (Figure 7.18a-ii), a recirculating flow domain appears at $x/c > 0.6$ and extends beyond the trailing edge of the airfoil. The base flow (at center span) is fully separated at $\alpha(t/T_p = 0.261) = 18^\circ$ (Figure 7.18a-iii). Although the base flow separation over the airfoil is three-dimensional and appears first near center span, the measured C_L in Figure 7.17a indicates a characteristic feature of dynamic stall in that concentrations of CW vorticity accumulated during pitch up cycle are still present and the loss in lift is minimal. At $t/T_p = 0.429$, as the airfoil pitches down through $\alpha = 15.7^\circ$, the flow above the airfoil remains separated (Figure 7.18a-iv) although the separating shear layer and the flow above it appear to be deflected towards the airfoil. However, the massive shedding of vorticity following the onset of stall results in a significant reduction in C_L and in ‘negative damping’ in pitch (Figure 7.17). Finally at $t/T_p = 0.621$ (pitch down through $\alpha = 11.2^\circ$), the flow re-attaches over the entire surface of the airfoil (Figure 7.18a-v) although C_L is lower than during the upstroke (Figure 7.18a).

Actuation has a profound effect on the evolution of the flow as shown in Figures 7.18b, c, and d. Figures 7.18b-*i* ($\alpha = 15^\circ$), 7.18c-*i* ($\alpha = 15.3^\circ$) and 7.18d-*i* ($\alpha = 15.7^\circ$) show the flow response to the first actuation pulse and the rollup and advection of a CW vortex that is embedded within the surface vorticity layer as the airfoil continues to pitch up. These images indicate that the boundary layer upstream of the CW vortex is somewhat thinner than in the absence of actuation (Figure 7.18a-*i*). The advection speed of the vortex is such that its interaction with the upstream boundary layer promotes flow attachment and therefore indicates that the interaction results in a favorable pressure gradient. By the time the vortex is shed (Figure 7.18d-*i*) the boundary layer upstream of the trailing edge is clearly thinner than in the base flow. The advection of the CW vortex that is formed following the third actuation pulse is shown Figures 7.18b-*ii* ($\alpha = 17.2^\circ$), 7.18c-*ii* ($\alpha = 17.5^\circ$) and 7.138-*ii* ($\alpha = 17.6^\circ$). Again, in comparison to the base flow (Figure 7.18a-*ii*) which is close to stall, the boundary layer upstream of the CW vortex in Figures 7.18b- and c-*ii* is much thinner. Of particular note is the CW vorticity concentration accumulated upstream of the trailing edge after the shedding of the actuation-induced vortex which is similar to, though smaller in extent than the trailing edge vortex in the base flow that is associated with dynamic stall. Furthermore, the controlled shedding of CW vorticity apparently suppresses the abrupt changes in the pressure distribution on the suction surface and hence significantly reduces the extent of “negative damping”. A similar pattern continues following the fifth actuation pulse in Figures 7.18b-*iii* ($\alpha = 18^\circ$), 7.18c-*iii* ($\alpha = 17.9^\circ$) and 7.18d-*iii* ($\alpha = 17.8^\circ$) which highlight the significant suppression of separation in comparison to the base flow (Figure 7.18a-*iii*). Also, it should be noted that the actuation-induced CW vortex is significantly larger

than at lower angles of attack. The evolution of the flow following the eighth (and last) actuation pulse is shown in Figures 7.18b-*iv* ($\alpha = 15.7^\circ$), 7.18c-*iv* ($\alpha = 15.4^\circ$) and 7.18d-*iv* ($\alpha = 15^\circ$). While the extent of the separation in the base flow is beginning to diminish as the downstroke progresses, the actuation still results in transitory, progressive flow attachment (Figures 7.18b- and c-*iv*), but following the shedding of the CW vortex, the extent of the vortex near the trailing edge increases significantly. Finally at $t/T_p = 0.621$ (pitch down through $\alpha = 11.2^\circ$), following the termination of the actuation, the actuated flow [Figures 7.18b-*v* ($\alpha = 11.2^\circ$), 7.18c-*iv* ($\alpha = 11^\circ$) and 7.18d-*iv* ($\alpha = 10.7^\circ$)] is reattached over the entire surface of the airfoil and is very similar to the base flow (Figure 7.18a-*v*). However, the C_L in the presence of actuation is higher than at the corresponding downstroke angle in the base flow (Figure 7.17a). This indicates that in the presence of actuation the cycle-averaged accumulated vorticity is higher than for the base flow.

The dynamics of the vortices that are formed by the actuation can be assessed from an $x-t$ diagram of evolution of the phase-averaged vorticity flux through vertical cross stream sections of the measurement domain above the airfoil ($0 < x/c < 1.2$) as shown in Figure 7.19, similar to the analysis of Figure 4.12. This distribution clearly shows the advection of the CW vortices that are induced by the interaction of the actuation jet with the surface boundary layer, and the changes in the advection speed following successive actuation pulses. For the first pulse, the CW vortex remains close to the suction surface and has a characteristic propagation velocity of $u_{adv}/U_\infty \approx 0.75$, for a single pulse over a static airfoil $u_{adv}/U_\infty \approx 0.75$]. These data show that the CW vortex induced by the 4th actuation pulse is advected at a higher speed ($u_{adv}/U_\infty \approx 0.97$) due to its closer proximity to the free stream flow while the flow over the airfoil appears to be separated (*cf.*, Figure

7.18c). As expected, the vortex induced by the last (8th) pulse is advected at a lower speed ($u_{adv}/U_\infty \approx 0.95$) due to the pitch-down motion of the airfoil. Perhaps the most prominent feature in the $x-t$ diagram, is the appearance of streaks of low vorticity flux that is associated with the severing and rollup of the separated CW vorticity layer. The characteristic speeds of the streaks following the 1st, 4th and 8th actuation pulses are $u_{adv}/U_\infty = 0.47, 0.65$ and 0.67 , respectively. It is owing to the differences in the characteristic propagation velocities that the severed region is stretched in the streamwise direction as indicated in Figure 7.19 by the increase in its width with t/T_p . This streamwise stretching represents the growth of the upstream boundary layer following each pulse, and the disparity between the amount of CW vorticity shed by the vortices and the accumulation of CW vorticity on the suction surface. This $x-t$ diagram indicates that there are no pairings or amalgamations of the CW vortices within the measurement domain (*cf.*, §VI for repeated pulses). The accumulation of vorticity over the airfoil during the oscillation cycle is regulated by the actuation to maintain a thin boundary layer during the upstroke through the high pitch angles.

To complement the data in Figure 7.18, the transitory alteration of the flow dynamics and stall during the pitch cycle by the 8-pulse “rapid” actuation sequence is further assessed using higher-resolution center span ($z = 0$) PIV measurements taken phase-locked to the pitch cycle. Raster plots of the phase-averaged velocity field and vorticity distributions in the near wake during the pitch cycle of the airfoil are shown in Figure 7.20 in the absence (top row, a-e) and presence (f-j, bottom row) of actuation (the measurement domain $0 < x/c < 0.4, 0 < y/c < 0.75$ is constructed from two, partially overlapping PIV frames). The cross stream height of the top (base flow) and bottom

(actuated flow) rows are $0.1 < y/c < 0.6$ and $0.1 < y/c < 0.75$, respectively. The timing of the images in each row is measured relative to t_0 when the airfoil is pitching up through $\alpha_0 = 14^\circ$ ($t/T_{\text{conv}} = 0$ (14° upstroke), 2.8 (16.5° upstroke), 9.4 (16.8° downstroke), 14 (12.5° downstroke), and 19 (10.1° upstroke). The data for the base flow show that at $\alpha(t) = 14^\circ$, the flow is still attached and that the cross stream extent of the near wake is $0.2 < y/c < 0.4$ at $0.3c$ downstream of the trailing edge. By $t = 2.8 T_{\text{conv}}$ [$\alpha(t) = 16.6^\circ$ upstroke, Figure 7.20b], when C_L approaches $C_{L,\text{max}}$ (*cf.*, Figure 7.17) the vorticity layer on the suction surface of the airfoil is considerably thicker (indicating an increased in accumulated vorticity), but the velocity distributions show only slight reversed flow upstream of the trailing edge. That the cross stream width of the near wake for $x/c > 0.25$ is still comparable to the wake in Figure 7.20a indicates that the bulk of the accumulated vorticity has not advected into the wake. By $t/T_{\text{conv}} = 9.4$ (16.8° downstroke), the dynamic stall vortex is shed into the near wake and, as shown in Figure 7.20c, the airfoil becomes stalled ($C_L \approx 1.44$). Thereafter, the flow slowly attaches as the airfoil continues to pitch down. At $t \approx 17 T_{\text{conv}}$, the wake is much narrower and as shown in connection with Figure 7.21a the less diffused vorticity flux distributions compared to $t = 0$ are connected to the motion of the airfoil in Figure 7.20d, and in agreement with the corresponding larger force and moment measurements. The flow remains attached for the remainder of the pitching cycle as indicated by the wake that extends $0.2 < y/c < 0.3$ in the cross stream direction at $x/c = 0.3$ (Figure 7.20e).

The 8-pulse “rapid” actuation sequence (triggered at the start of the pitching cycle, $T_{\text{start}} = 0$ and lasting $9.8T_{\text{conv}}$, *cf.*, Figure 7.17) leads to considerable alteration of the flow in the near wake (Figures 7.20f–j). These images show that the actuation effectively

prevents massive shedding of the dynamic stall vorticity concentrations during the pitch cycle. Although it appears that some vorticity is shed by the onset of the actuation as is evident for example by the difference between Figures 7.20g and b ($t = 2.8 T_{\text{conv}}$). Of particular note is the difference between the images in Figures 7.20c and h ($t/T_{\text{conv}} = 9.4$, $\alpha(t) = 16.8^\circ$ downstroke), where in the absence of actuation the dynamic stall vortex is shed into the near wake, but the actuation results in considerably flux of vorticity into the wake as discussed in connection with Figure 7.21 below and C_L in the presence of actuation is 1.71 compared to 1.44 for the baseline flow. A short time later following the termination of the 8-pulse “rapid” actuation sequence at $9.8T_{\text{conv}}$, the flow relaxes, but does not stall again as it is now pitching down through smaller angles (Figures 7.20i and j). These observed wake characteristics are clearly shown by the time-evolution of the vorticity fluxes (Figure 7.21b).

The effects of the actuation on the global aerodynamic performance of the moving airfoil are quantified by considering the time-evolution of the phase-averaged cross stream distributions of the vorticity flux $\omega_z \cdot u$ (CW and CCW from the suction and pressure surfaces) downstream of the trailing edge (at $x/c = 1.25$) as shown in color raster plots of Figure 7.21. The “positive” and “negative” fluxes are distinguished based on the method described in §IV when either ω_z or u can be positive or negative. The time rate of change of the airfoil’s circulation is computed for the base and actuated flows by integration of vorticity flux across the wake $d\Gamma/dt = -\int(\omega \cdot u)dy$, and traces of normalized $(d\Gamma/dt)_{\text{CW}}$ and $(d\Gamma/dt)_{\text{CCW}}$ are also shown in Figures 7.21a and b as time traces in the same colors. Time instances i through v in Figure 7.18 are also marked by the vertical dashed lines in Figure 7.21 for reference. In the absence of actuation (Figure 7.21a), the changes

in the cross stream width of the wake for $t < 0.18T_p$ are relatively small indicating a reasonably attached flow during this part of the upstroke. However, when the flow begins to separate, the cross stream extent of the wake increases rapidly along with the magnitude of the flux of CW vorticity which is associated with the shedding of the vorticity concentration that is associated with the dynamic stall (at about $t/T_p = 0.18$ $\alpha \approx 17^\circ$ during the down stroke, *cf.*, Figure 7.17). The maximum broadening of the wake as marked by the cross stream separation between the CW and CCW fluxes occurs at $0.36 \leq t \leq 0.38 T_p$ corresponding to full stall. Thereafter, the flow slowly reattaches as the airfoil continues to pitch down. At $t \approx 0.68T_p$, the wake is much narrower than during stall and the distributions of vorticity flux appear to be more concentrated than at $t = 0$ as the airfoil pitches through the smallest angles. It is interesting to note that in the absence of actuation, the magnitudes of $(d\Gamma/dt)_{CW}$ and $(d\Gamma/dt)_{CCW}$ are similar and that the vorticity flux from the suction surface intensifies during the downstroke.

The corresponding cross stream distributions of the vorticity flux in the presence of actuation (Figure 7.21b) exhibit two striking differences compared to the base flow. First, the sequence of eight actuation pulses clearly modulates the vorticity fluxes from *both* the suction and pressure surfaces of the airfoil. This indicates that the actuation regulates the instantaneous vorticity distribution about the airfoil through trapping and shedding with minimal fluctuations in lift (*cf.*, Figure 7.17). Second, and perhaps more striking, is the absence of massive stall as indicated by the widening of the wake, corresponding to the large reduction in the lift hysteresis in Figure 7.17a.

It is evident that the sum $(d\Gamma/dt)$ is associated with a net increase in circulation as shown in Figure 7.22. As noted above, the vorticity flux into the wake is altered

significantly in the presence of actuation. The time rate of change of the circulation that is associated with the shedding of the discrete vortices induced by the actuation pulses increases as the actuation progresses and appears to reach a maximum level around $t/T_p = 25$ when the airfoil attains its largest angle of attack before the beginning of the downstroke. The successive increases in the peaks of $(d\Gamma/dt)_{CW}$ is connected with the increased thickness of the boundary layer on the suction surface and therefore the stronger shed vorticity concentrations as a result of the actuation. Each of the shed vortices is followed by a significant reduction (or deficit) in CW vorticity concentration that is associated with the severing the vorticity layer by the actuation on the airfoil and the build-up of vorticity in the upstream boundary layer indicating a concomitant increase in CW vorticity (or positive $d\Gamma/dt$) on the airfoil that contribute to the increases in circulation as shown in Figure 7.23. The strength of the shed CW vortices (which is clearly coupled to the motion of the airfoil) is nearly invariant during the downstroke. The data in Figure 7.21 also show that the corresponding flux of CCW vorticity from pressure side of the airfoil has similar (but opposite) effects on $(d\Gamma/dt)_{CCW}$. Finally, the raster plots of vorticity flux and the traces of $(d\Gamma/dt)_{CW}$ and $(d\Gamma/dt)_{CCW}$ also show an intricate effect that is associated with the severing of the CW vorticity layer on the airfoil. Following the reduction in flux of CW vorticity, the flux resumes before the next actuation pulse and, as a result, the shed vorticity concentrations (CW and CCW) exhibit two adjacent vortices.

It is instructive to compare $(d\Gamma/dt)_{CW}$ and $(d\Gamma/dt)_{CCW}$ directly by superposing them in Figure 7.22. The traces in the absence and presence of actuation are virtually identical ahead of and following the actuation. It is evident that the actuation primarily modulates

the vorticity fluxes and that the overall time rate of change in $(d\Gamma/dt)_{CW}$ is larger so that the actuation results in a net increase in circulation as shown in Figure 7.23.

The time-dependent circulation increment that is computed relative to the circulation when the airfoil pitches up through $\alpha = \alpha_o$ at $t = 0$, $-\Delta\Gamma(t)$, is shown in Figure 7.23a in the absence and presence of the staged actuation. The initial rise in circulation ($0 \leq t \leq 0.16T_p$) for the base flow (unactuated) motion corresponds to the accumulation of CW vorticity during the formation of the dynamic stall vortex ($-\Delta\Gamma_{max}/\Gamma_o \approx 0.09$ at $t \approx 0.12T_p$). As noted above, the accumulation is not necessarily restricted to the circulating domain near the trailing edge (Figure 7.17), but can also occur in the vorticity layer near the surface. The subsequent reduction in circulation ($0.16 \leq t \leq 0.56T_p$) is due to the shedding of accumulated dynamic stall vorticity and the onset of stall over the airfoil at ($-\Delta\Gamma_{min}/\Gamma_o \approx -0.2$ at $t \approx 0.56T_p$) before the flow reattaches again ($-\Delta\Gamma$ vanishes) as the pitching cycle continues. In the presence of actuation, the circulation exhibits some oscillations (10 - 15%) that are induced by the actuation pulses as the circulation level increases relative to $\alpha = \alpha_o$ from $t = 0$, but the overall increase is significantly larger compared to the base flow ($-\Delta\Gamma_{max}/\Gamma_o \approx 0.25$ at $t \approx 0.3T_p$) and lasts for the duration of the actuation through $t \approx 0.52T_p$. This increase is the result of trapping of vorticity in the surface layer and in the recirculation domain near the trailing edge (Figure 7.18d-iv) that are likely associated with the dynamic stall vortex. Following the termination of the actuation as the airfoil continues to pitch, there is a reduction in circulation ($-\Delta\Gamma_{min}/\Gamma_o \approx -0.13$ at $t \approx 0.64T_p$), but this reduction is significantly smaller than the corresponding reduction of the base flow pitch indicating that the effects of the actuation

last beyond its termination and consequently there is a cycle-averaged increase in circulation owing to the actuation.

The control authority of pulsed actuation is evident in Figure 7.23b that shows the phase-averaged net change in sectional circulation in the center plane due to the actuation relative to the base flow pitching cycle. *Even though the circulation is only computed at center span and the effects of the actuation clearly vary across the span owing to the 3-D stall, it is remarkable that an 8-pulse sequence that is applied during the upstroke and lasts for about 40% of the cycle period leads to an increase in circulation through almost the entire cycle. The net circulation build-up during actuation is rapid, reaching a maximum (at $t \approx 0.3T_p$) which is equivalent to an increase of 44.7% when normalized by $\Gamma_o(t_o)$, before decreasing upon termination of actuation and the end of the pitch cycle.*

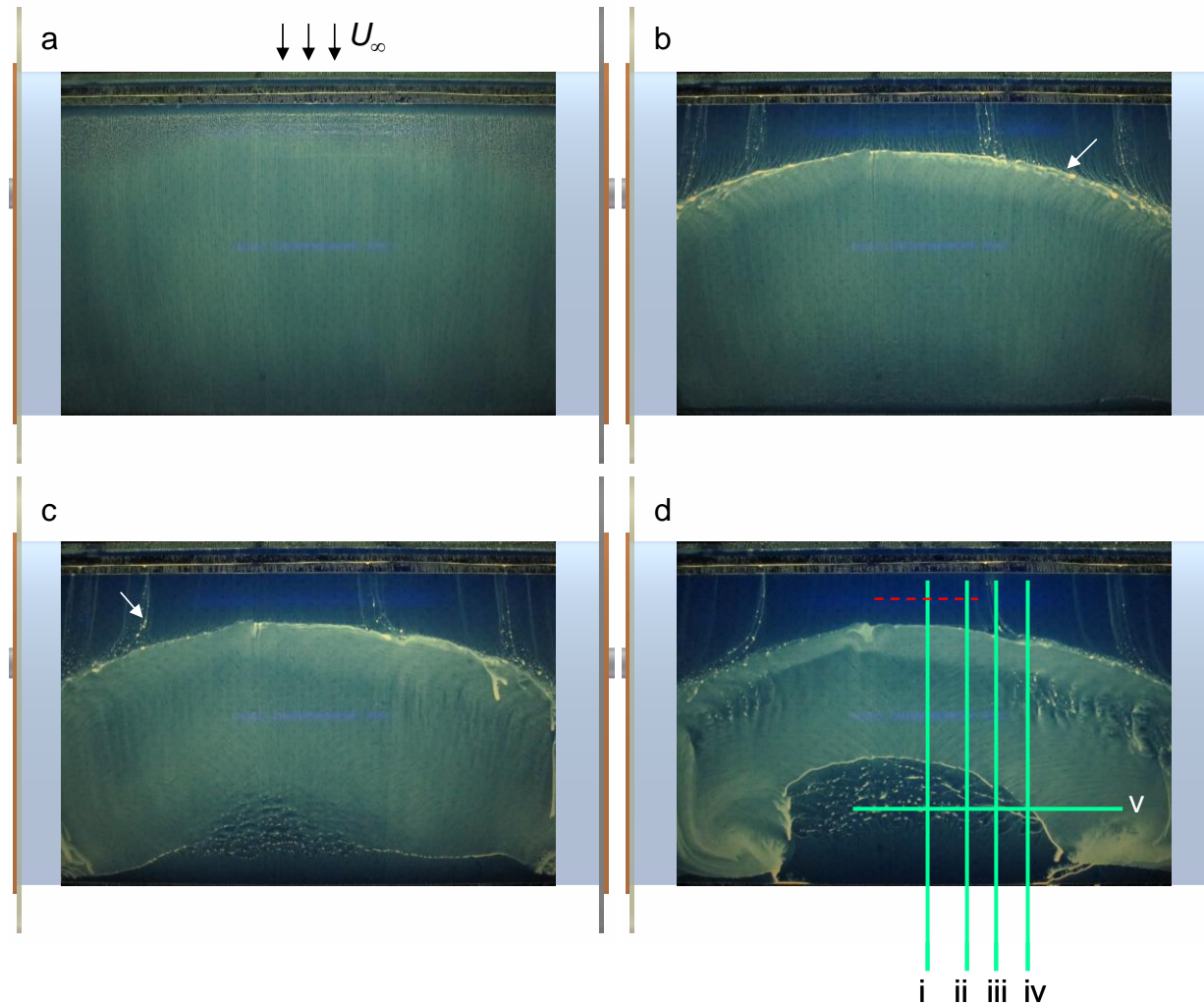


Figure 7.1: Surface oil visualization of base flow over airfoil at 1 (a), 7 (b), 36 (c) and 105 (d) minutes. Arrows mark free stream flow direction (a), separation line (b), spanwise flow (c), and counter-rotating swirl (d). Green lines (d) show measurement locations of planar-PIV at $z/c = 0$ (i), 0.16 (ii), 0.27 (iii) and 0.39 (iv), and stereo-PIV at $x/c = 0.78$ (v). Location of actuators is marked (- -).

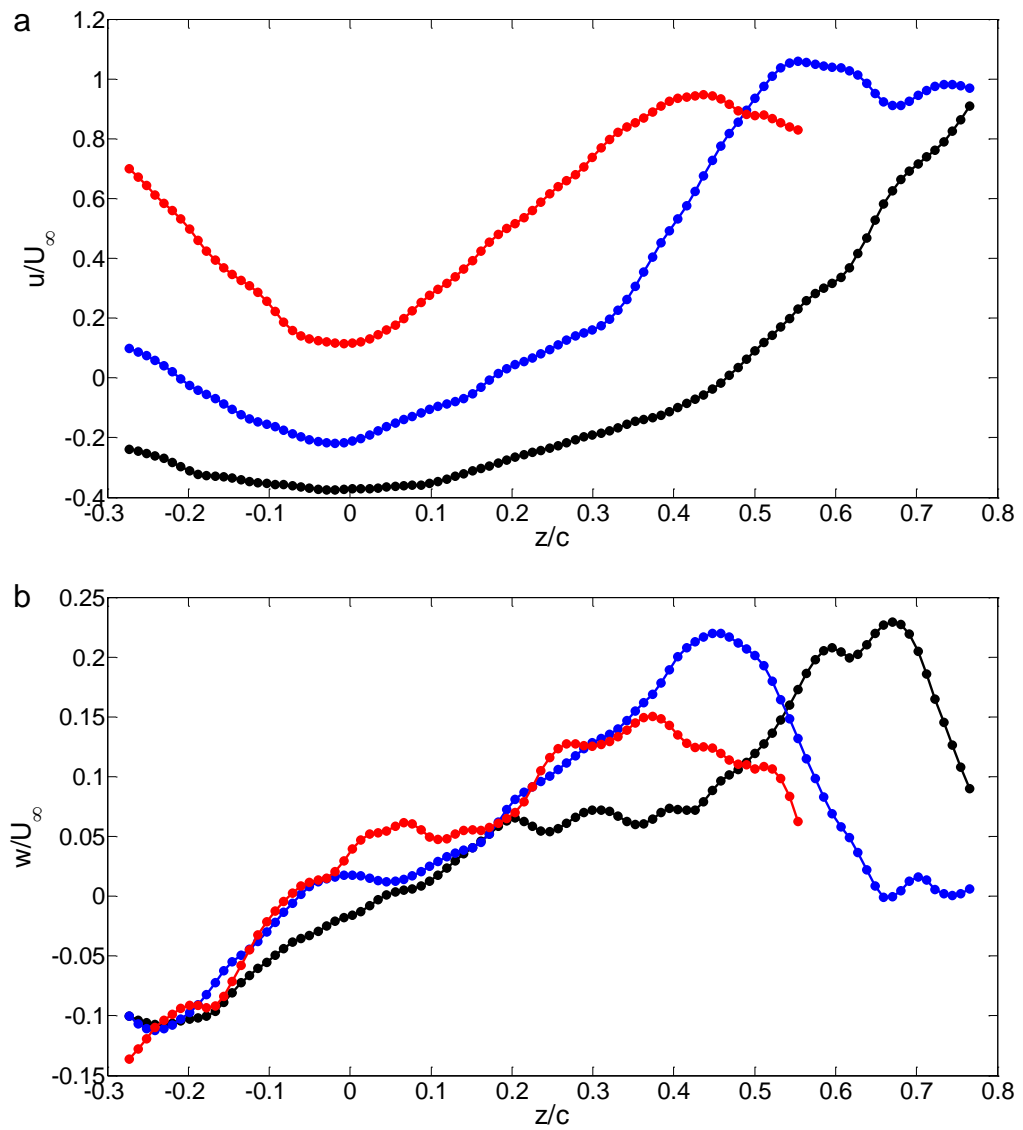


Figure 7.2: Base flow velocity profiles of u (a) and w (b) obtained from stereo-PIV at $x/c = 0.78$ and above airfoil surface; $\Delta y/c = 0.074$ (\bullet), 0.17 (\bullet) and 0.233 (\bullet). Symmetry plane is at mid-span ($z = 0$).

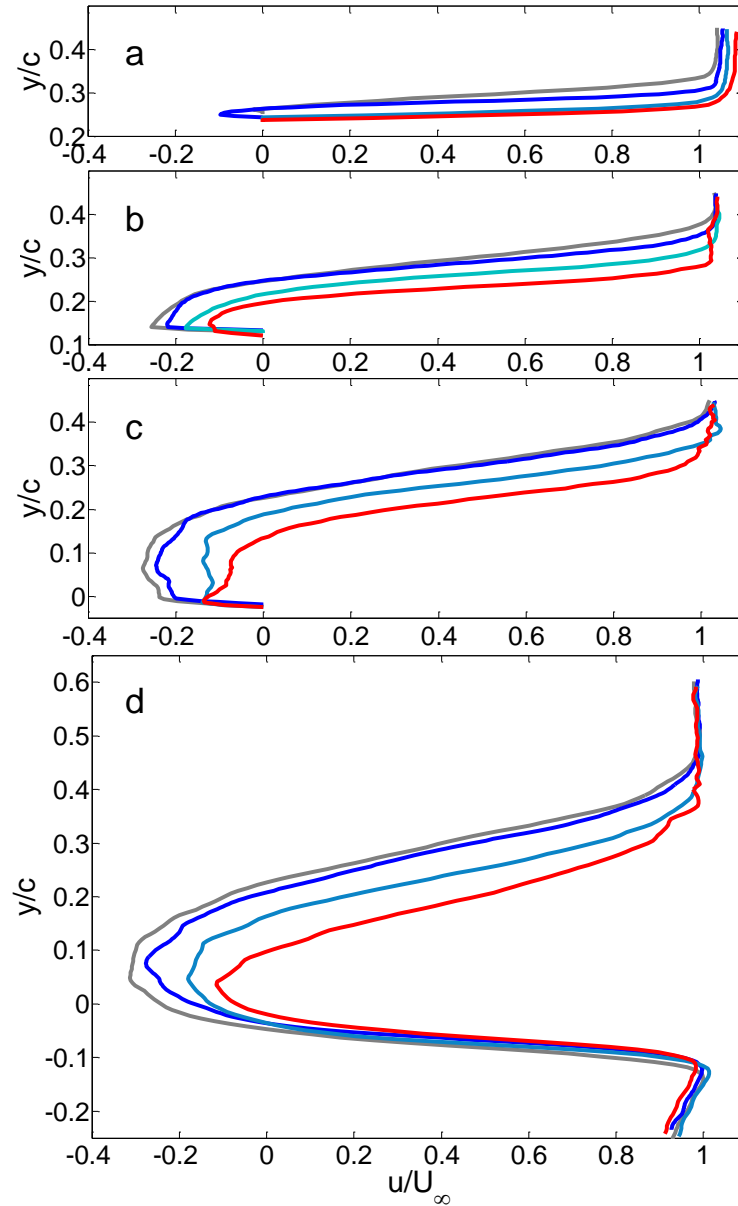


Figure 7.3: Cross stream distribution of streamwise velocity, u , in the base flow over the airfoil at $x/c = 0.46$ (a), 0.71 (b), 0.96 (c) and in the near wake at $x/c = 1.22$ (d) in the spanwise planes: $z/c = 0$ (\blackline), 0.16 (\bluearrow), 0.27 (\cyanarrow) and 0.39 (\redarrow).

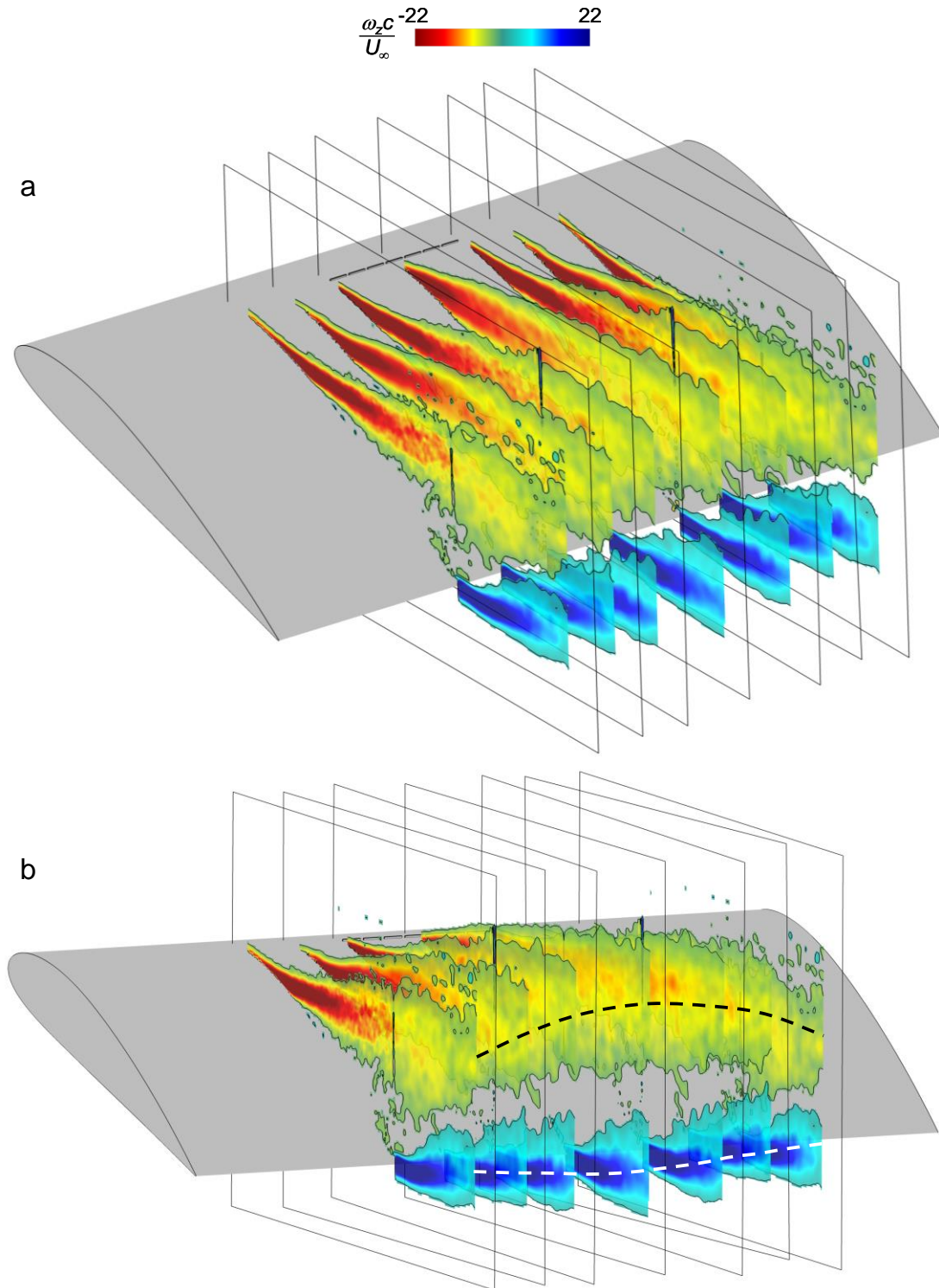


Figure 7.4: Contours of spanwise vorticity obtained in the four spanwise planes in Figure 7.3 ($z/c = 0, 0.16, 0.27$ and 0.39) and mirrored about $z = 0$ showing flow relative to actuators (a) and spanwise variations across the wake (b). The PIV planes (as edges) and actuators (as rectangular blocks) are outlined, and the streamwise fences are not included.

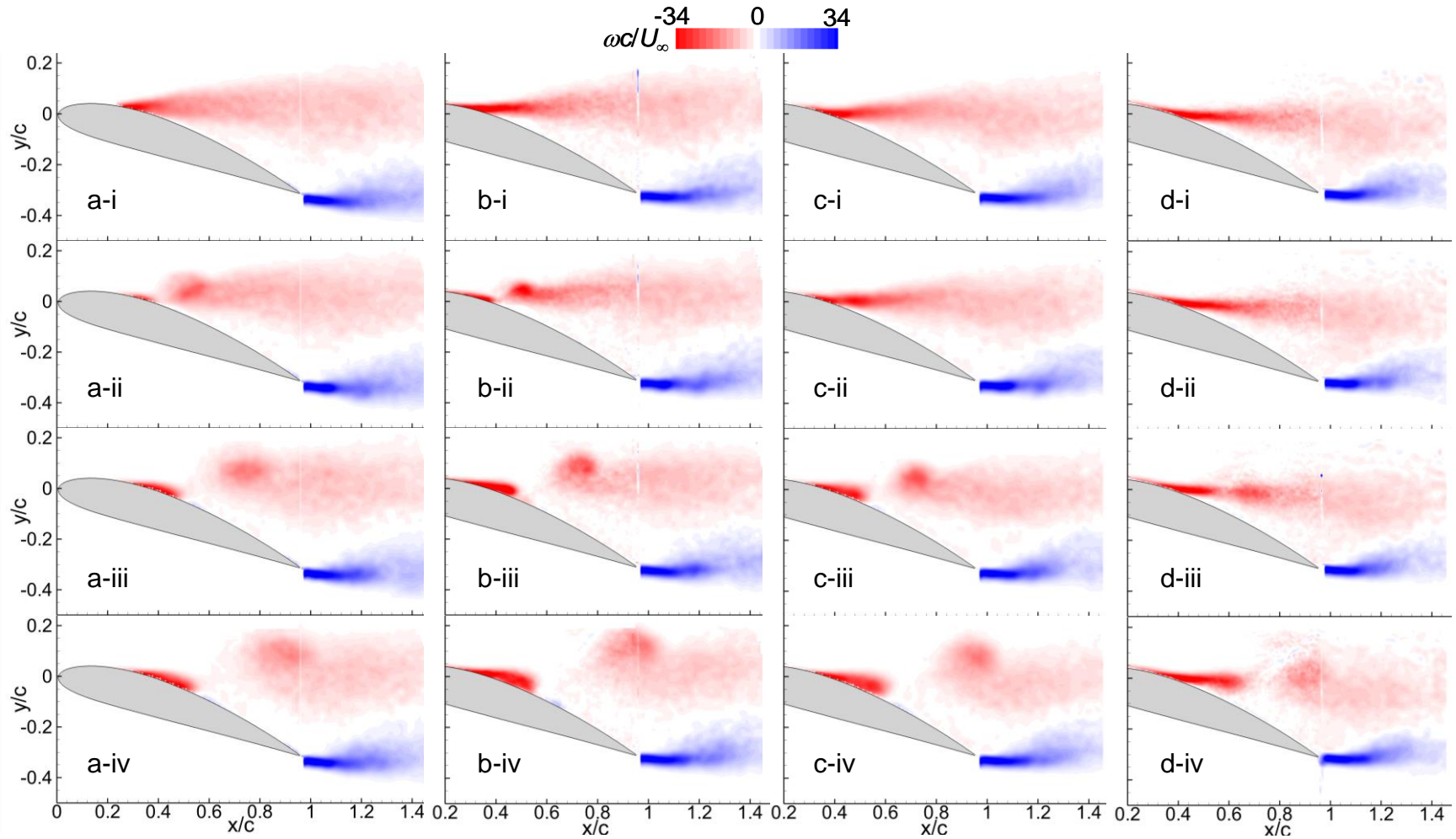


Figure 7.5: Phase-averaged PIV measurements of spanwise vorticity following single pulse actuation for the planes located at $z/c = 0$ (column a), 0.17 (b), 0.27 (c), and 0.39 (d) at $t/T_{\text{conv}} = 0$ (row i), 0.4 (ii), 0.64 (iii), 0.88 (iv), 1.12 (v), 1.52 (vi), 1.76 (vii), and 2.64 (viii).

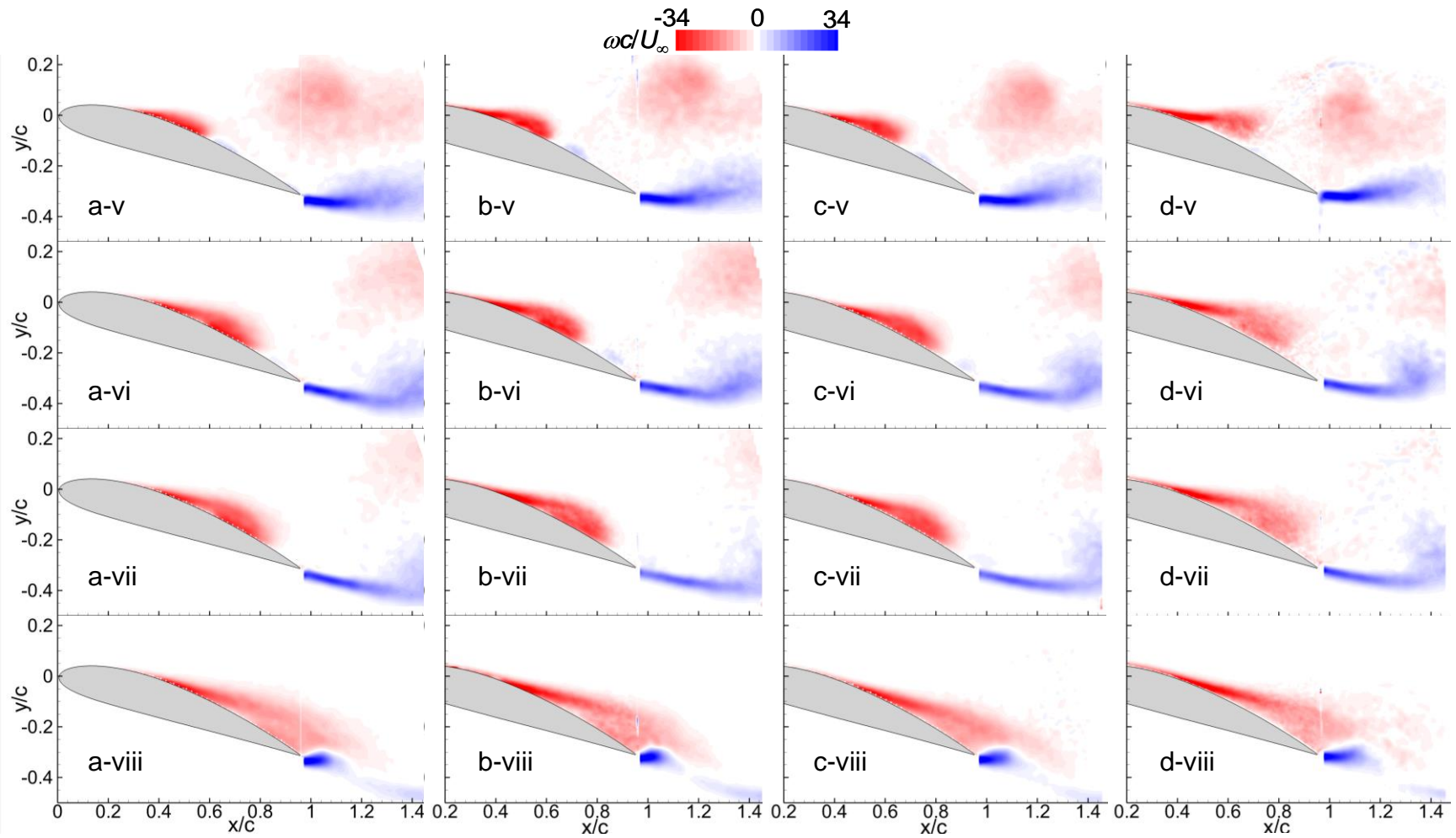


Figure 7.5: (Continued).

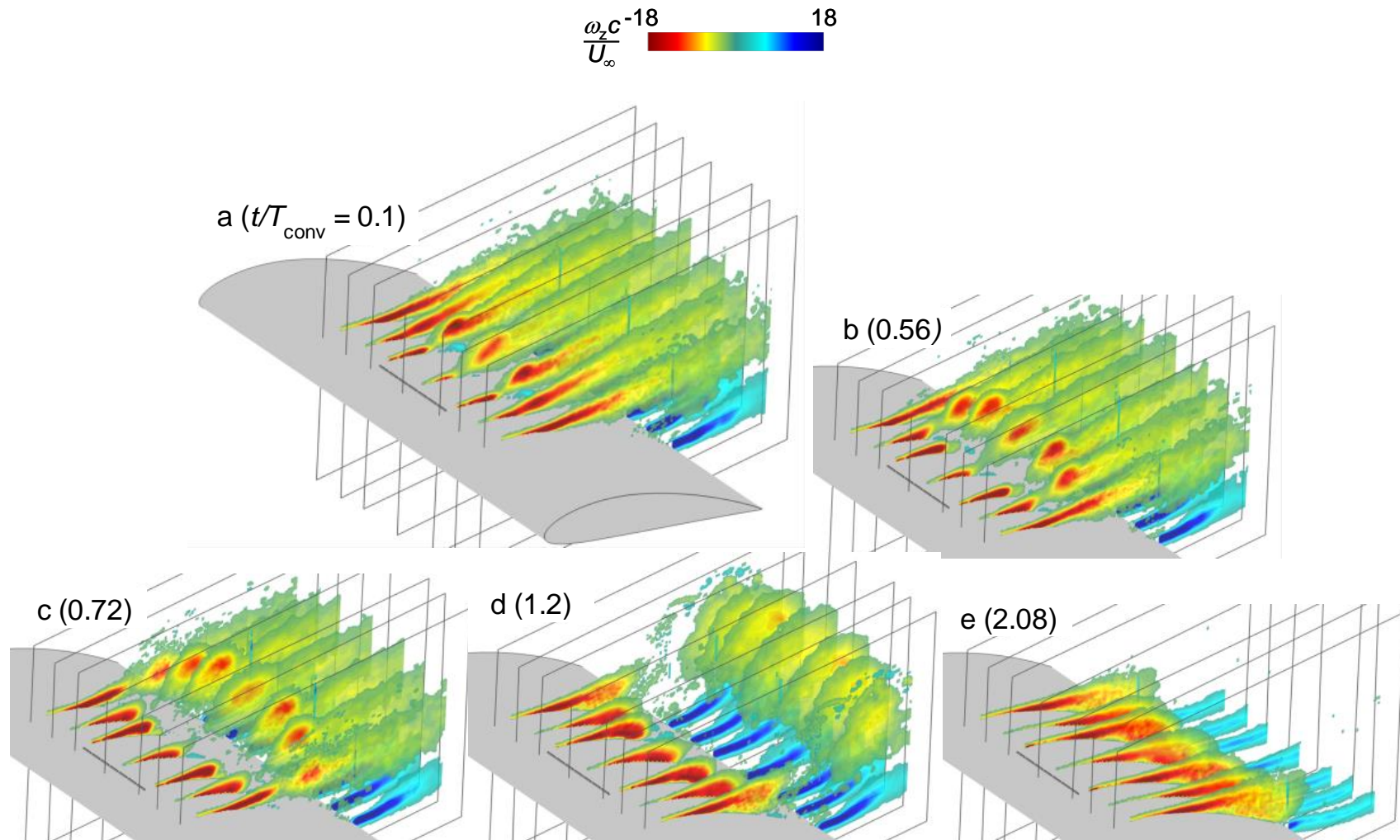


Figure 7.6: Phase-averaged spanwise vorticity following single pulse actuation for the PIV planes located at $z/c = 0, 0.17, 0.27,$ and 0.39 , which are also mirrored about $z = 0$: $t/T_{\text{conv}} = 0.1$ (a), 0.56 (b), 0.72 (c), 1.2 (d) and 2.08 (e). The outline of measurement frames is included.

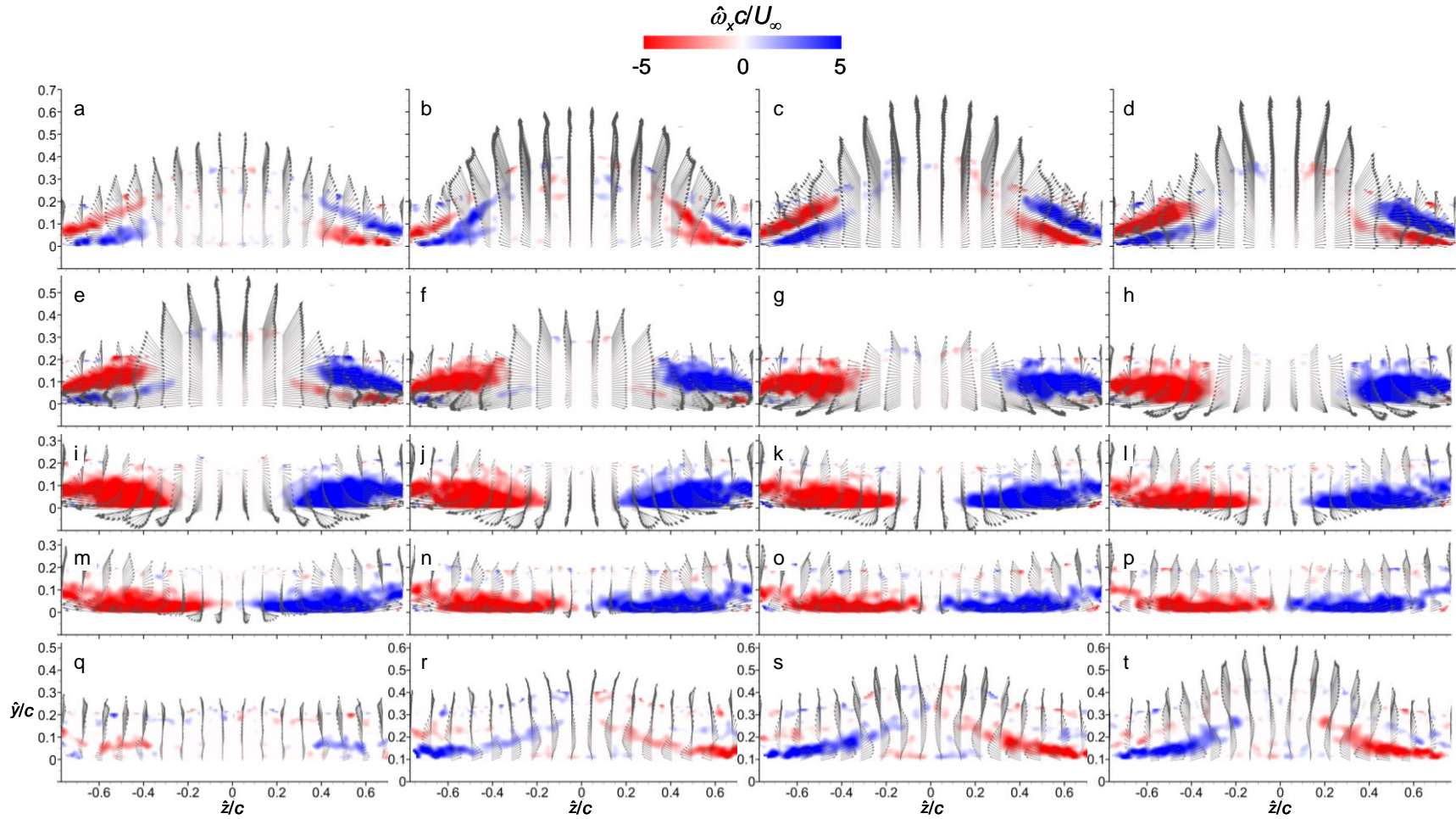


Figure 7.7: Phase-averaged raster plot of $\hat{\omega}_x$ obtained from stereoscopic PIV measurements at $0.2c$ from the trailing edge following single pulsed actuation $t/T_{\text{conv}} = 0$ (a), 0.88 (b), 1.04 (c), 1.12 (d), 1.2 (e), 1.28 (f), 1.36 (g), 1.44 (h), 1.52 (i), 1.6 (j), 1.68 (k), 1.76 (l), 1.84 (m), 1.92 (n), 2.0 (o), 2.08 (p), 2.96 (q), 5.12 (r), 5.92 (s) and 6.56 (t). The data are mirrored about $z = 0$.

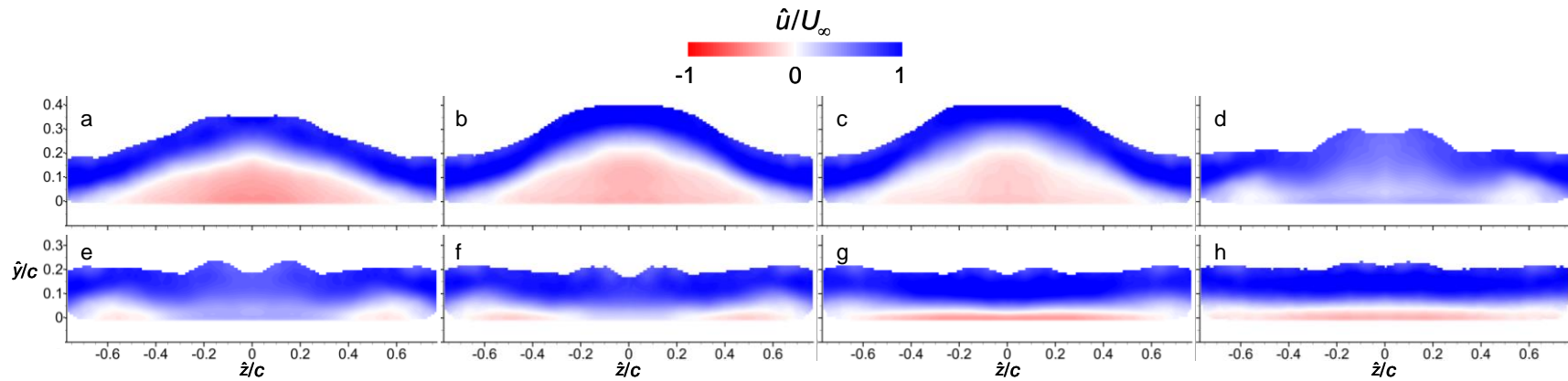


Figure 7.8: Phase-averaged raster plot of streamwise velocity, \hat{u} , obtained from stereoscopic PIV measurements at $x/c = 0.78$ angled 30° to the vertical following single pulsed actuation; $t/T_{\text{conv}} = 0$ (a), 0.8 (b), 0.88 (c), 1.28 (d), 1.44 (e), 1.6 (f), 1.92 (g) and 2.96 (h). The data are mirrored about $z = 0$.

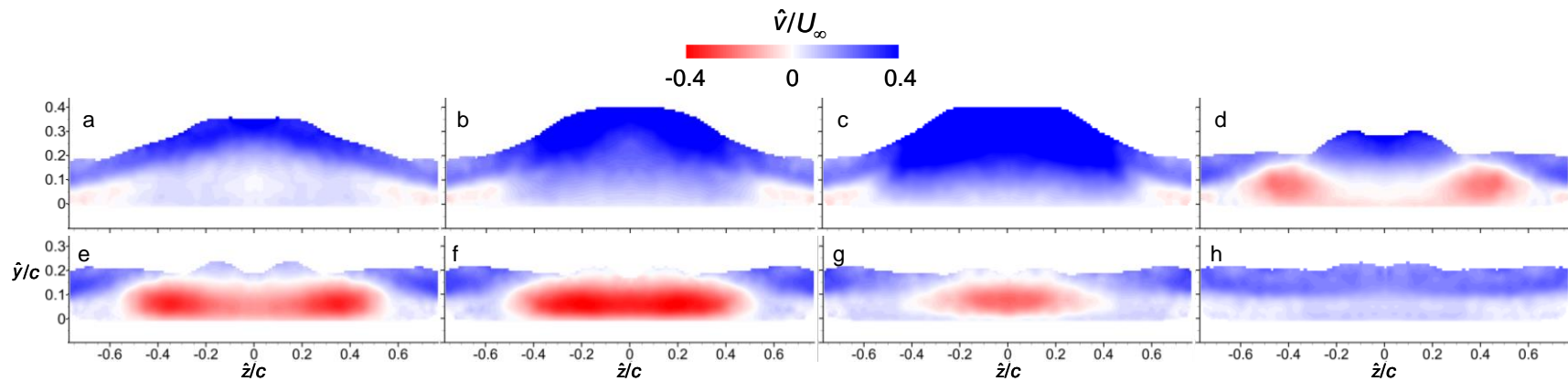


Figure 7.9: Phase-averaged raster plot of cross stream velocity, \hat{v} , obtained from stereoscopic PIV measurements at $x/c = 0.78$ angled 30° to the vertical following single pulsed actuation; $t/T_{\text{conv}} = 0$ (a), 0.8 (b), 0.88 (c), 1.28 (d), 1.44 (e), 1.6 (f), 1.92 (g) and 2.96 (h). The data are mirrored about $z = 0$.

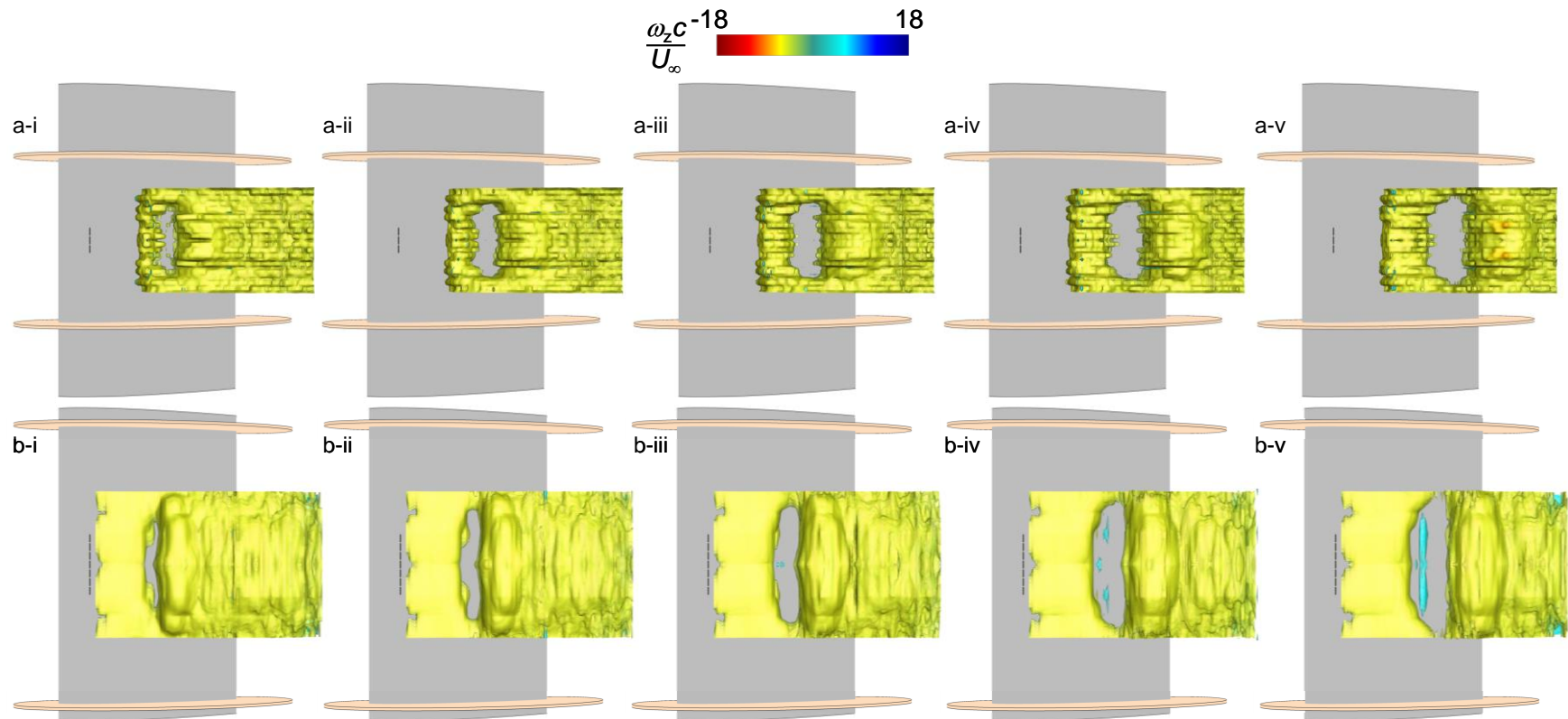


Figure 7.10: Iso-surfaces of the phase-averaged spanwise vorticity viewed from above the airfoil for the unbounded actuation in the 2-D (row “a”), and 3-D (row “b”) base flows following actuation ($t = 0$) at $t/T_{\text{conv}} = 0.56$ (i), 0.64 (ii), 0.72 (iii), 0.8 (iv), 0.88 (v), 0.96 (vi), 1.04 (vii), 1.12 (viii) and 1.2 (ix). The data are mirrored about $z = 0$.

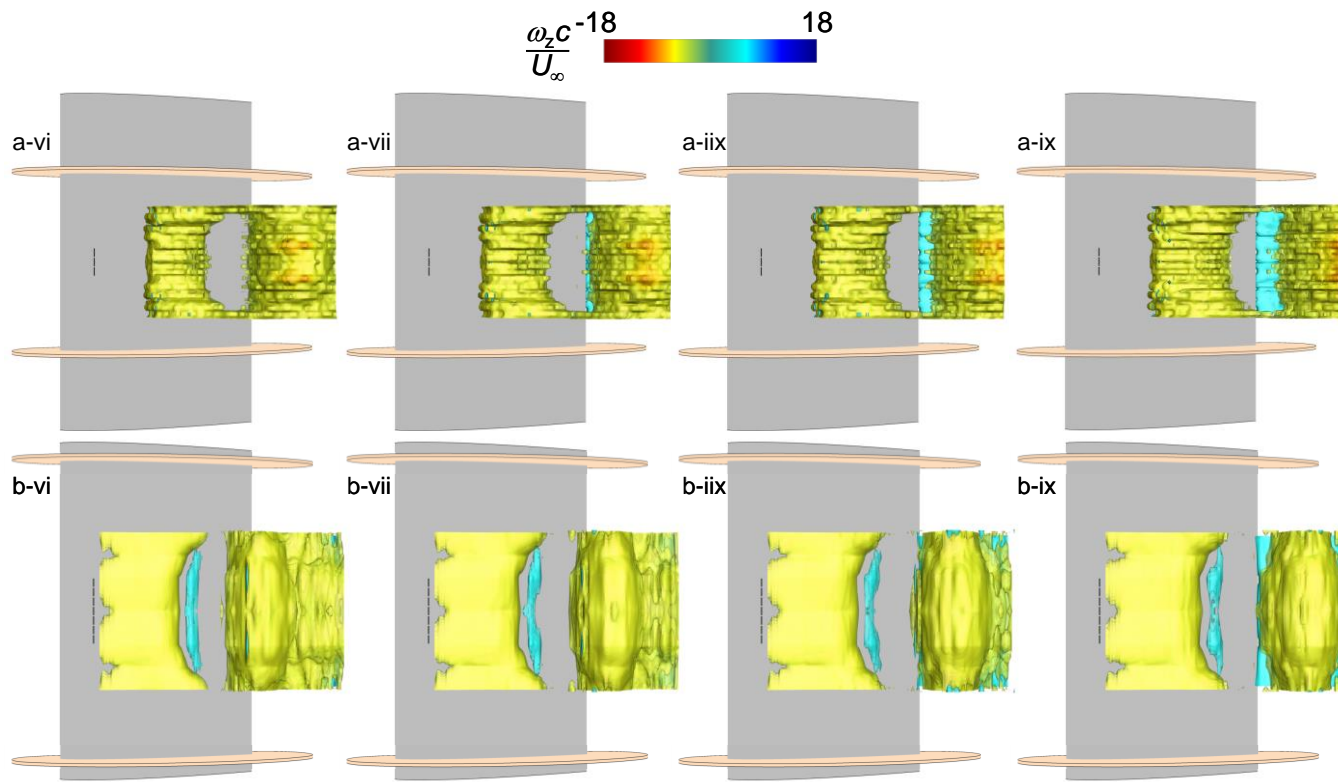


Figure 7.10: (Continued)

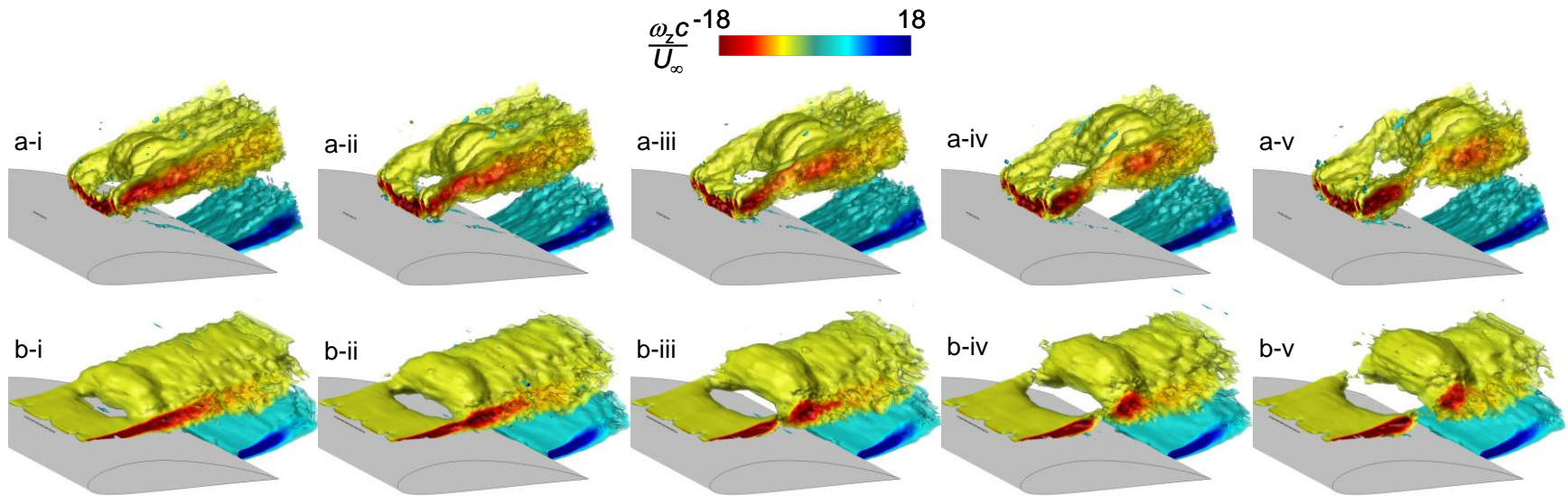


Figure 7.11: Iso-surfaces of the phase-averaged spanwise vorticity for the unbounded actuation in the 2-D (row “a”) and 3-D (row “b”) base flows following actuation ($t = 0$) at $t/T_{\text{conv}} = 0.56$ (i), 0.64 (ii), 0.72 (iii), 0.8 (iv), 0.88 (v), 0.96 (vi), 1.04 (vii), 1.12 (viii), 1.2 (ix) and 2.4 (x). The data are mirrored about $z = 0$.

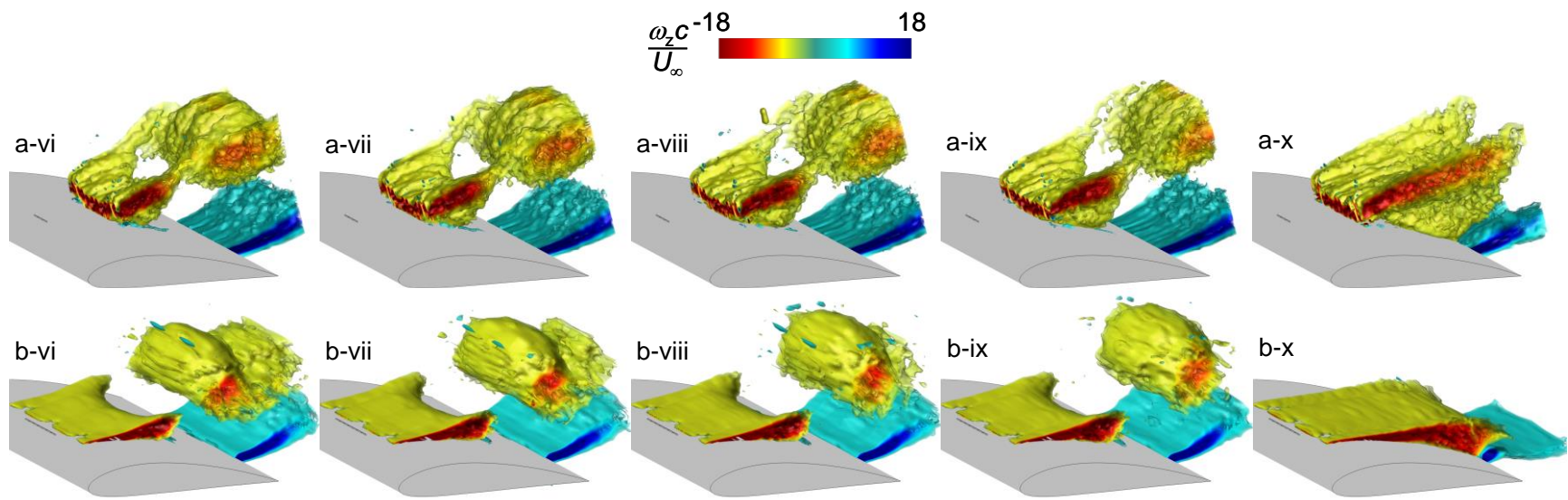


Figure 7.11: (Continued)

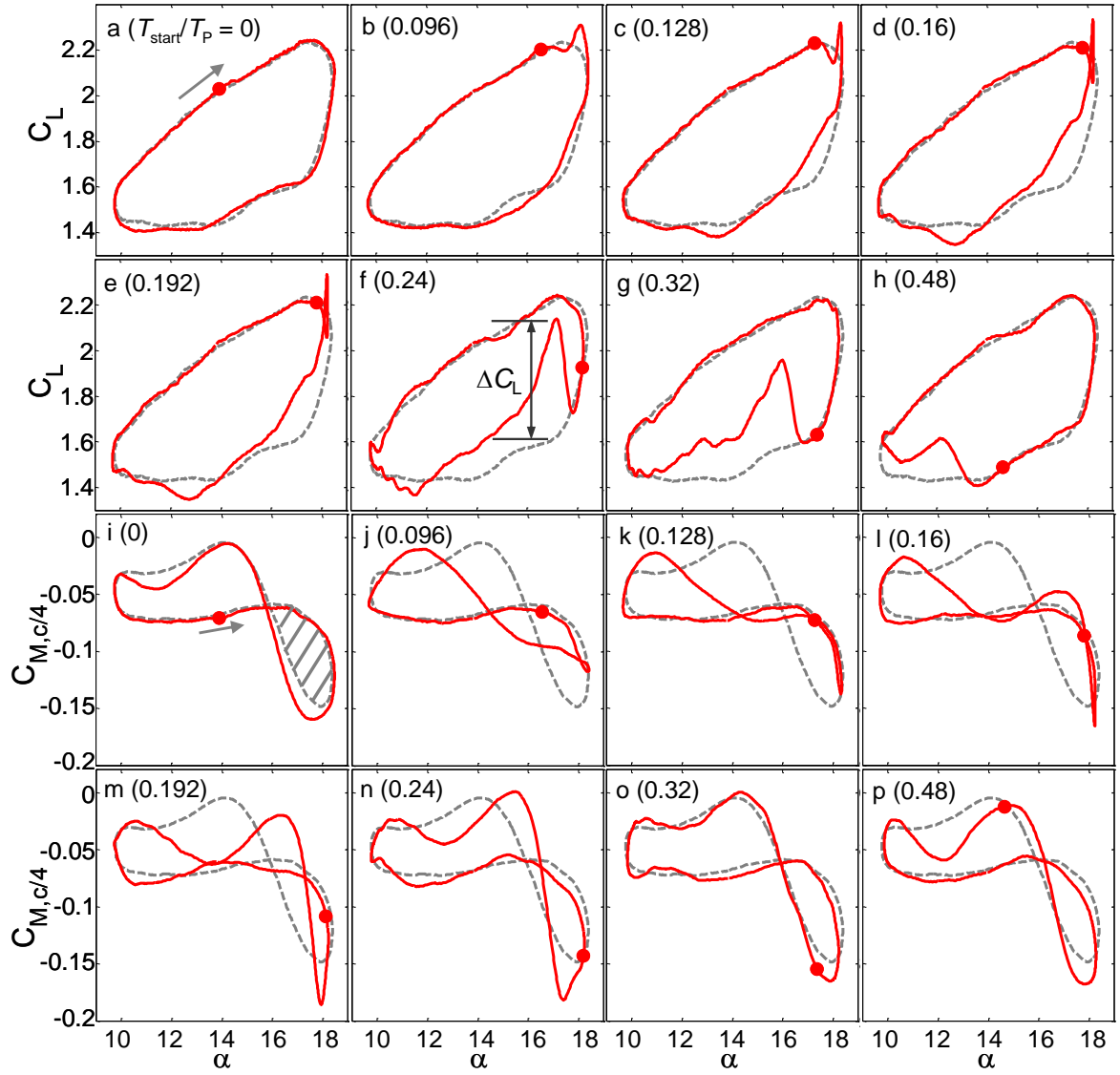


Figure 7.12: Variation of C_L , (a-h) and $C_{M,c/4}$, (i-p) with α during the pitch cycle ($k = 0.115$). Single-pulse actuation marked with \bullet is applied at $T_{start}/T_P = 0$ (a,i), 0.096 (b,j), 0.128 (c,k), 0.16 (d,l), 0.192 (e,m), 0.24 (f,n), 0.32 (g,o) and 0.48 (h,p). The corresponding traces for the base flow are shown in dashed curves and the directions of the phase plots are indicated by an arrow (a, i).

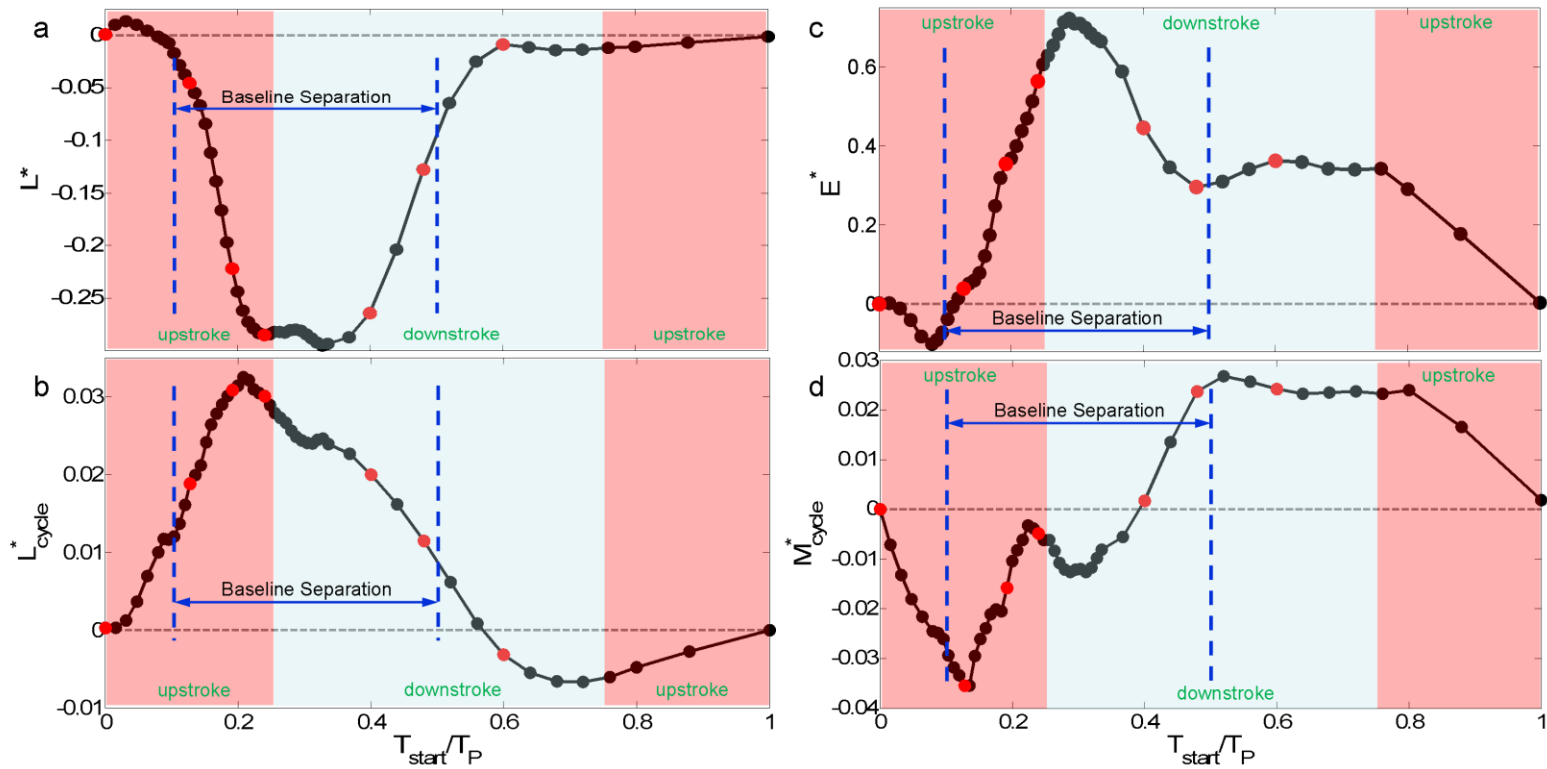


Figure 7.13: Variations in hysteresis of (a, c) and cycle-averaged (b, d) unsteady C_L (a-b) and C_M (c-d) lift (a and b) for single-pulse actuation applied during the pitchy cycle with different T_{start} (●). The background colors represent the up- (red), and downstrokes (light blue). The corresponding actuation cases in Figure 7.12 are included (●).

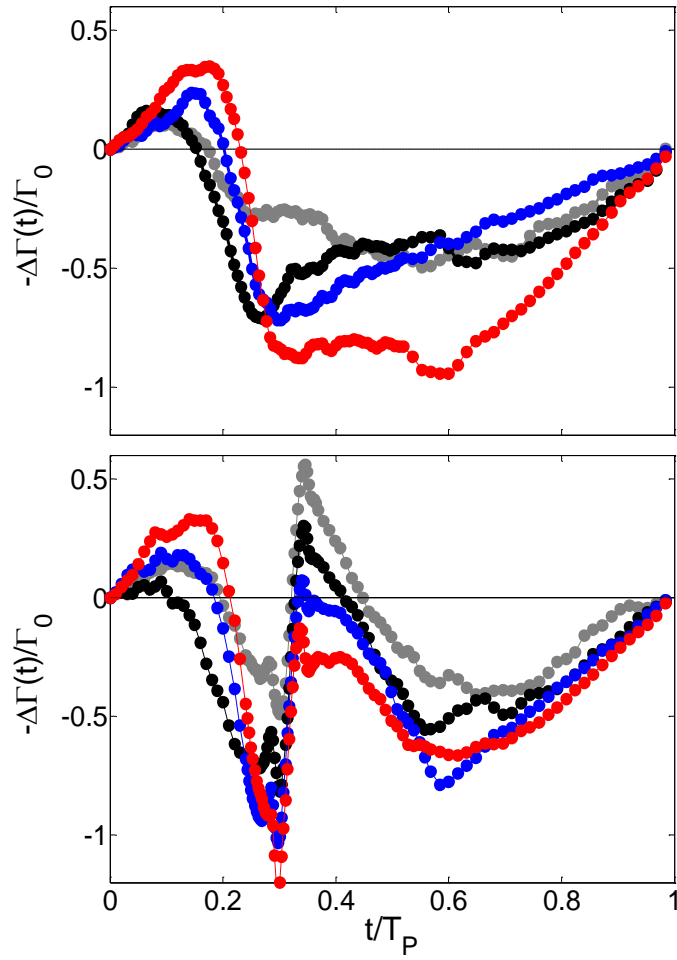


Figure 7.14: Variations with time of the phase-averaged circulation increments for the base flow (a) and following single pulse actuation at $T_{\text{start}} = 150$ ms (b) at $z/S_{\text{act}} = 0$ (\bullet), 0.47 (\bullet), 0.78 (\bullet) and 1.11 (\bullet).

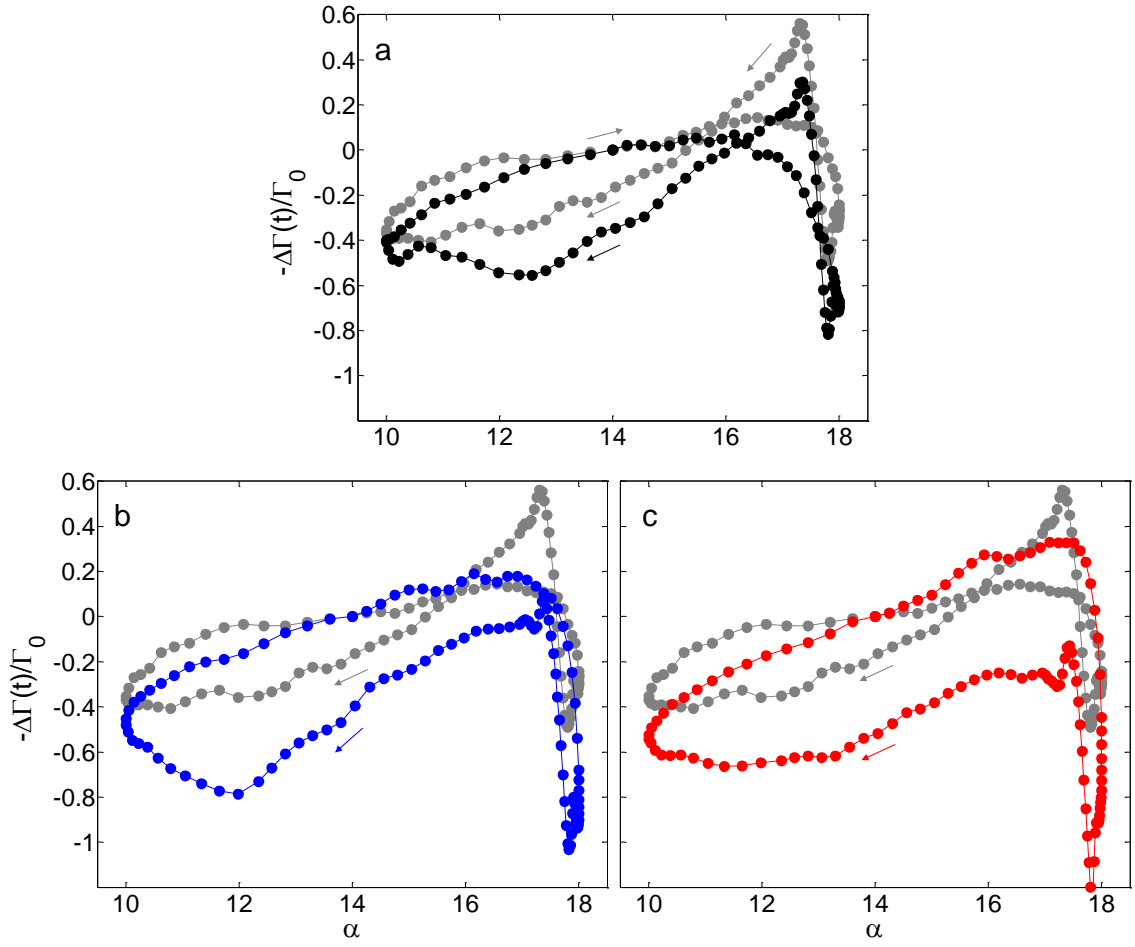


Figure 7.15: Variations of phase-averaged circulation increments with α following single pulse actuation at $T_{start} = 150$ ms at $z/S_{act} = 0$ (\bullet), 0.47 (\bullet), 0.78 (\bullet) and 1.11 (\bullet).

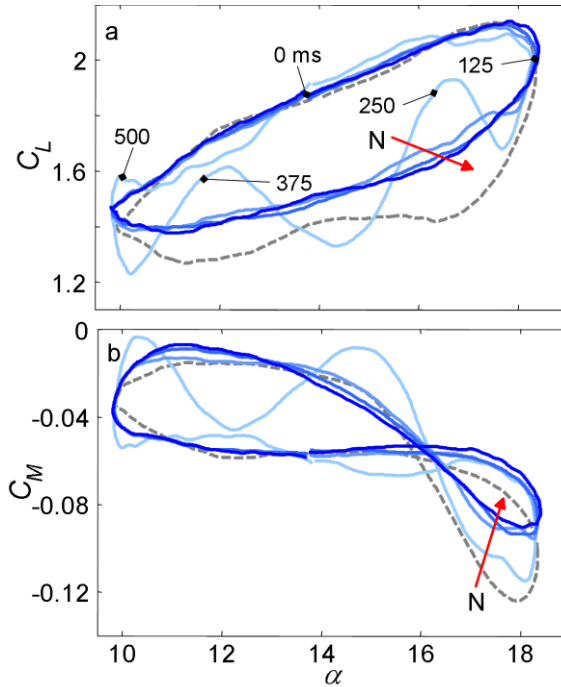


Figure 7.16: Variations in lift C_L (a), and pitching moment $C_{M,c/4}$ (b) of $N = 5, 10, 15$ and 20 actuation pulses evenly-distributed in time during the pitching cycle. The base flow curves are shown in gray.

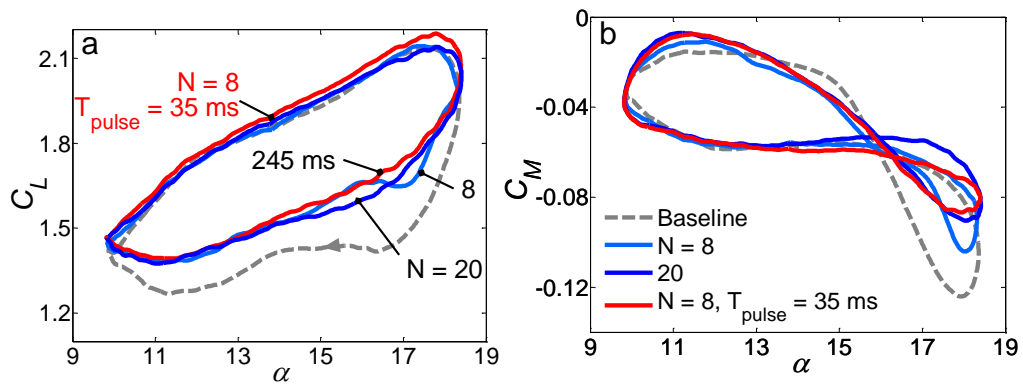


Figure 7.17: Variations in lift C_L (a), and pitching moment $C_{M,c/4}$ (b) of $N = 8$ and 20 actuation pulses evenly-distributed in time during the pitching cycle, and the 8-pulse “rapid” actuation sequence. The baseline curves are shown in gray.

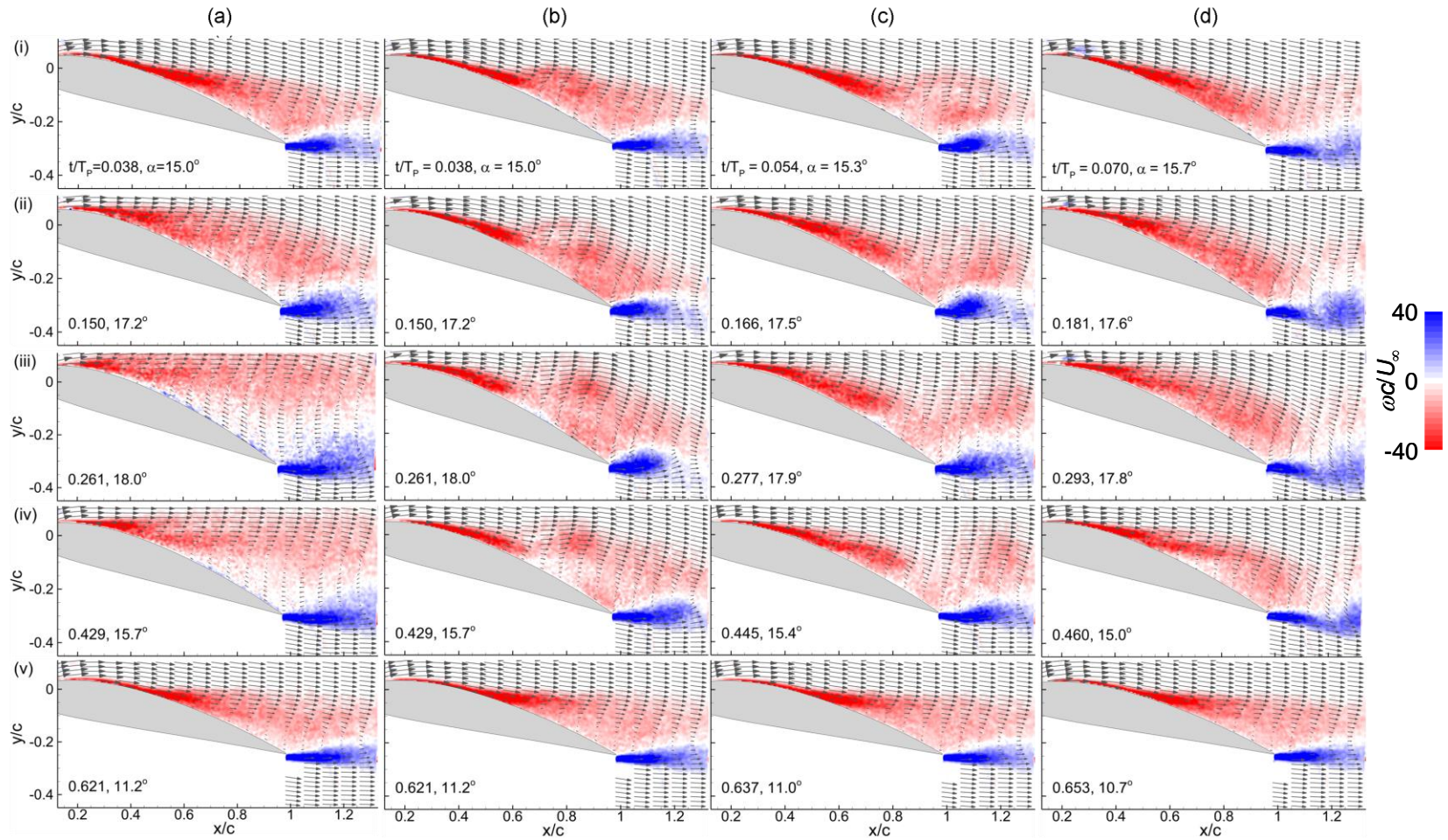


Figure 7.18: Phase-averaged vorticity maps and velocity distributions above the airfoil and in the near wake during the pitching cycle; baseline (column a) and pulsed actuation (columns b-d). In columns (a) and (b): $\alpha = 15.0^\circ$ ($t/T_p = 0.038$), (i), 17.2° ($t/T_p = 0.150$), (ii), 18° , ($t/T_p = 0.261$), (iii), 15.7° ($t/T_p = 0.429$), (iv) and 11.2° ($t/T_p = 0.621$) (v). The images in columns c and d are taken at fixed delays relative to column b of $\Delta t/T_p = 0.016$ and 0.032 , respectively.

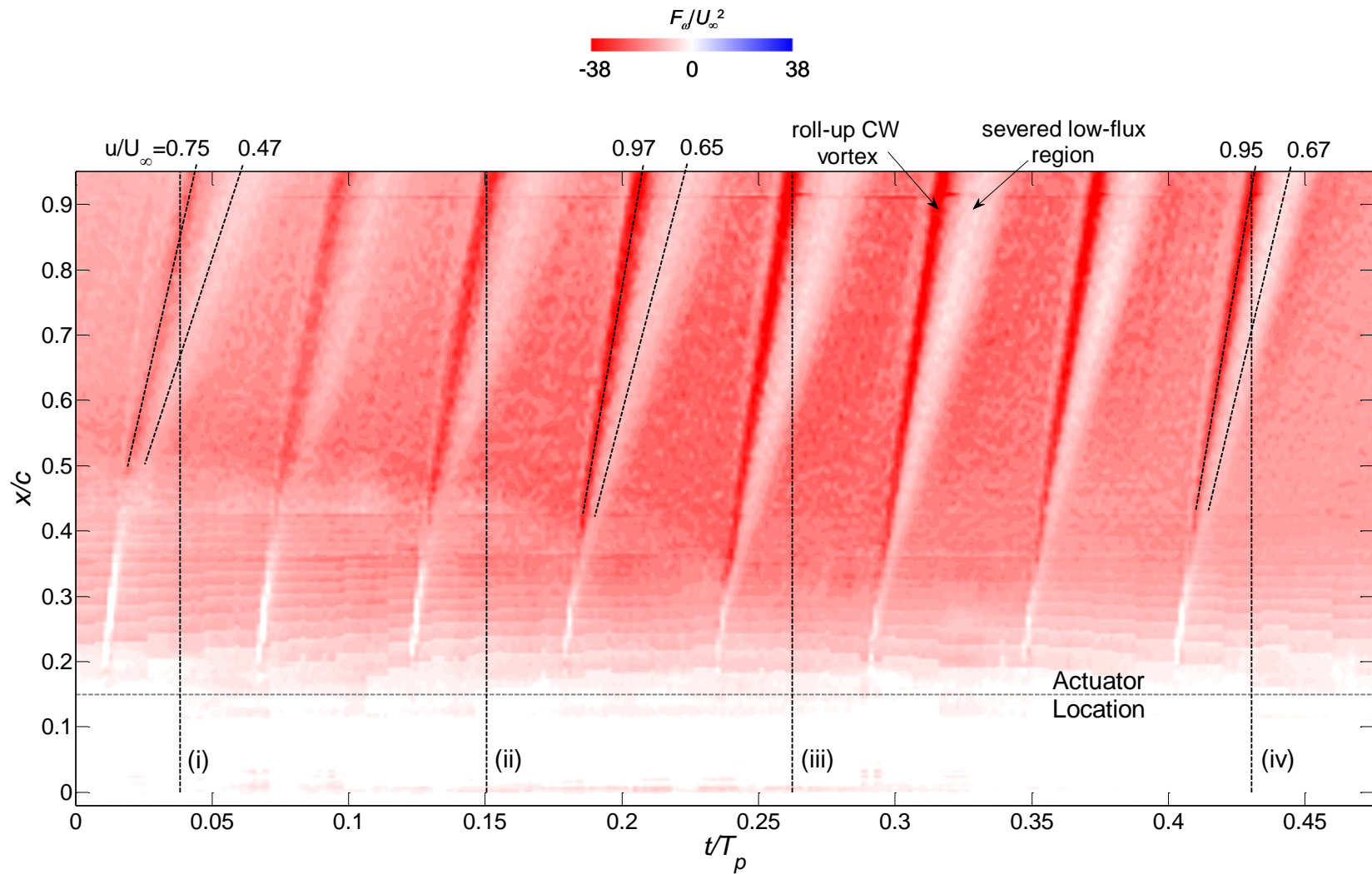


Figure 7.19: x - t raster plot of phase-averaged vorticity flux for 8-pulse actuation showing propagation velocities of the induced CW vorticity concentrations.

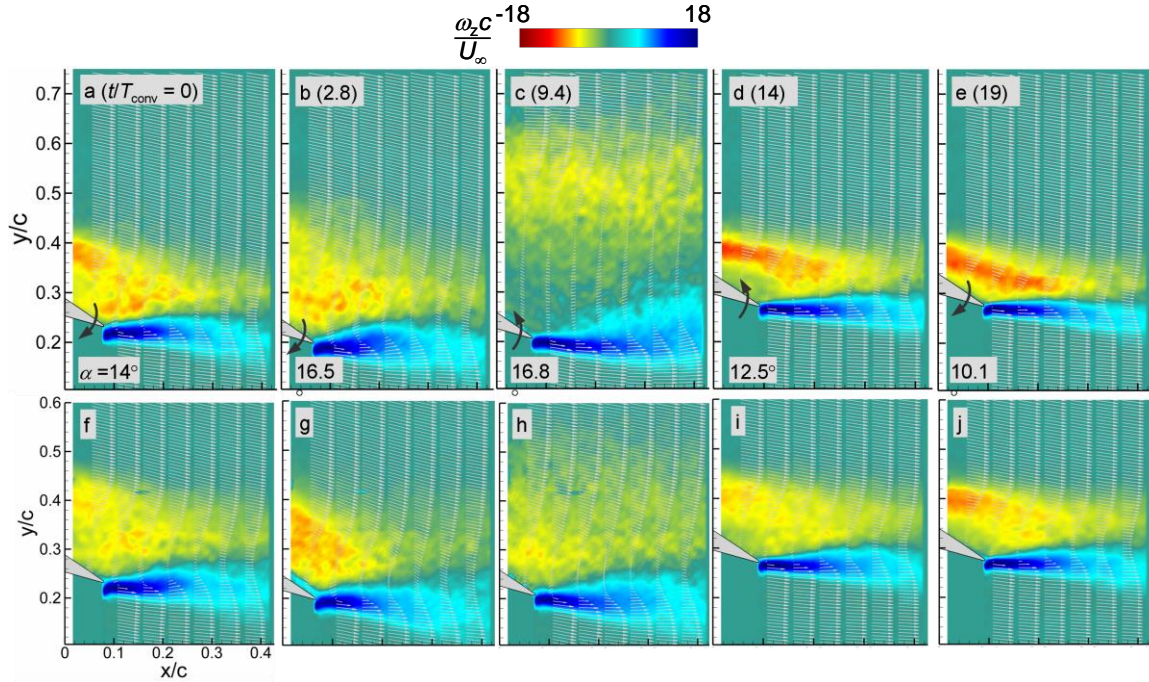


Figure 7.20: Phase-averaged vorticity and velocity maps in the near wake during the pitching cycle of the airfoil in the absence (a-e) and presence (f-j) of actuation. The timing of the images in each row is measured relative to t_0 when the airfoil is pitching up through $\alpha_0 = 14^\circ$. (a,f) $t/T_{conv} = 0$ (14° upstroke), (b,g) 2.8 (16.5° upstroke), (c,h) 9.4 (16.8° downstroke), (d,i) 14 (12.5° downstroke), and (e,j) 19 (10.1° upstroke). Pulsed actuation is applied using $N = 8$ pulses equally spaced in time ($T_{rep} = 35$ msec), triggered at the start of the pitching cycle (i.e. $T_{start} = 0$).

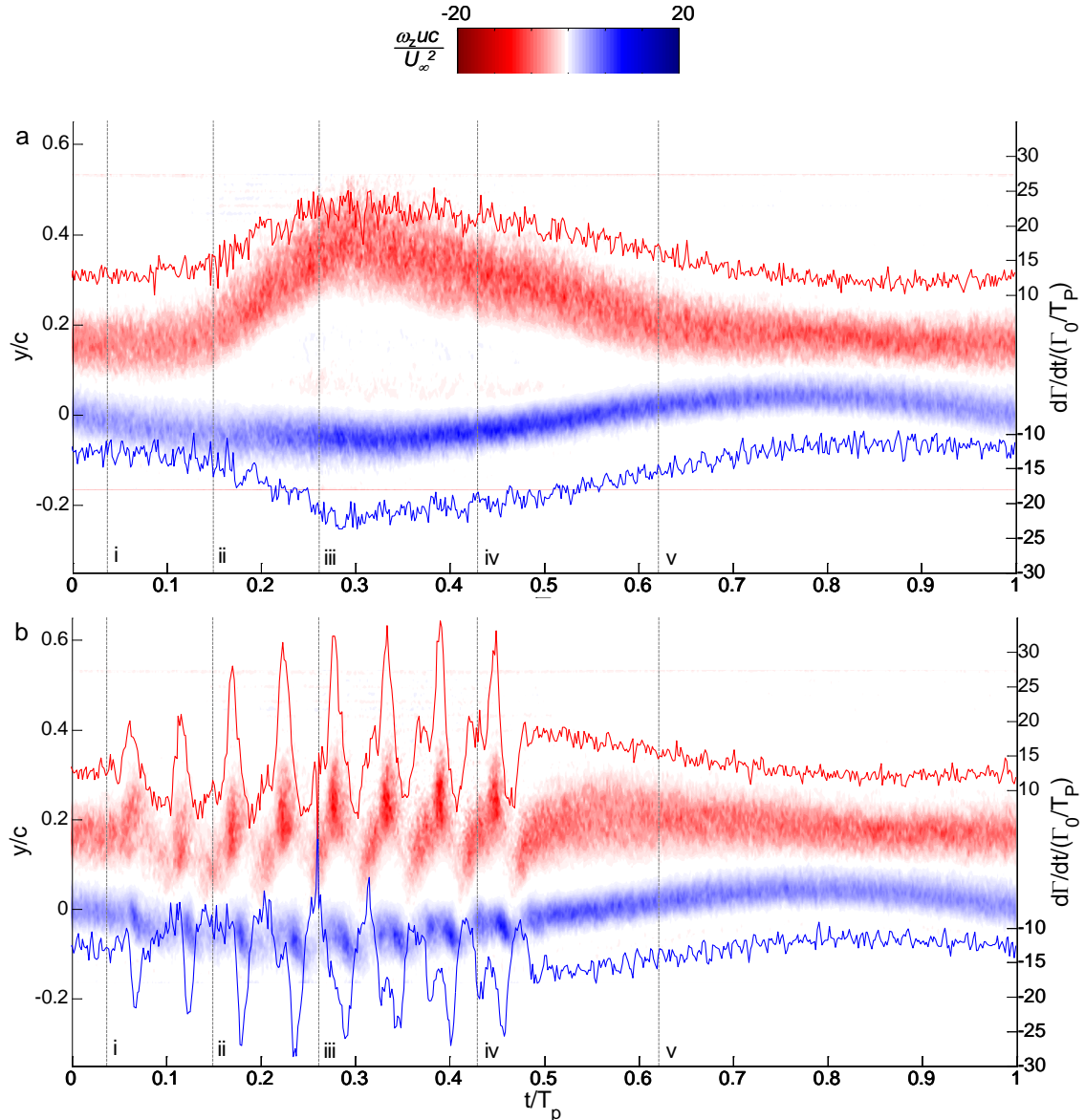


Figure 7.21: Raster plots of the phase-averaged cross stream distribution of vorticity flux (**CW** and **CCW**) during the pitching cycle of the airfoil measured at $0.25c$ downstream of the trailing edge in the absence (a) and presence (b) of actuation. Included are the corresponding line traces of the time-rate change of circulation: $(d\Gamma/dt)_{cw}$ and $(d\Gamma/dt)_{ccw}$. Also included for reference are the five instances during the cycle (i through v) that are marked in Figures 7.18 and 7.19.

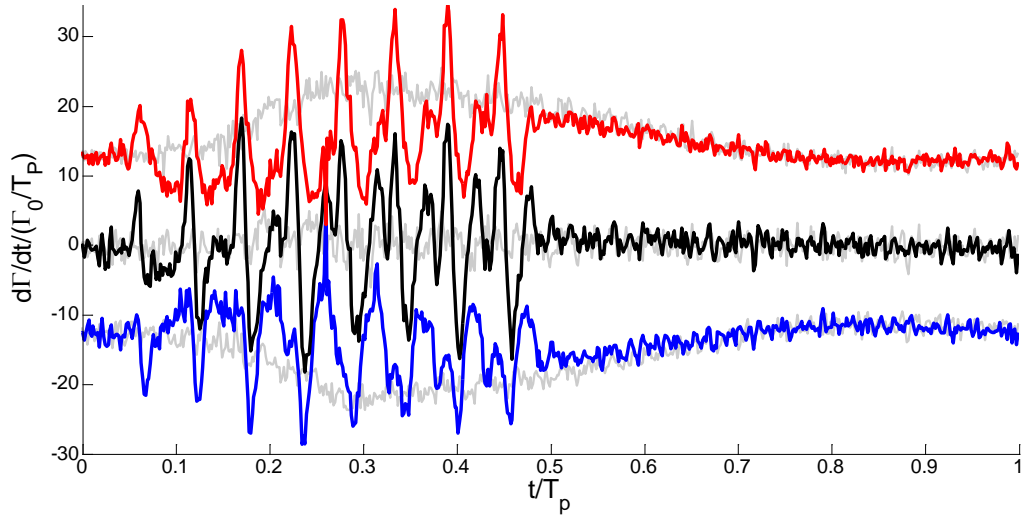


Figure 7.22: Phase-averaged line traces of $(d\Gamma/dt)_{cw}$, $(d\Gamma/dt)_{ccw}$ and their sum $d\Gamma/dt$ in the presence of actuation. The corresponding time traces for the baseline flow are shown for reference (gray).

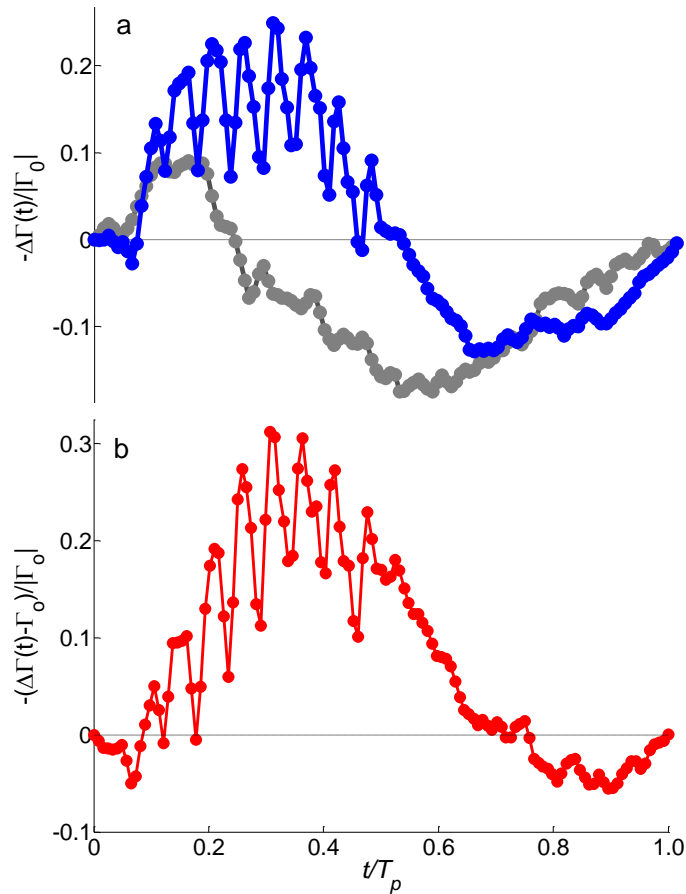


Figure 7.23: (a) Phase-averaged circulation increment for the pitch cycle in the absence (●) and presence (●) of pulsed actuation ($N = 8$, $T_{pulse} = 1.4T_{conv}$, ●), and (b) Phase-averaged net change in global circulation due to the actuation relative to the base flow (●).

CHAPTER VIII

CONCLUSIONS

8.1. Overview

The experimental research program focused on investigations of the fundamental mechanisms of *transitory control of separating flows* on static and dynamically-pitching airfoils. The underlying concept is based on earlier discovery at Georgia Tech that the separated flow is highly receptive to transitory actuation using a brief [$O(0.1T_{\text{conv}})$] impulse at the flow boundary that leads to a collapse of the separated flow domain and to a large, transitory increase in circulation on a much longer time scale [$O(10T_{\text{conv}})$].

Transitory flow attachment effected by pulsed actuation was investigated in wind tunnel experiments on a statically and dynamically stalled 2-D, NACA-4415 airfoil model ($c = 457$ mm, $Re_c = 570,000$). The model was mounted on a traverse mechanism that allowed static and time-periodic variations in angle of attack. Two- and three-dimensional attachment was effected over the center segment (S_{fence}) of the airfoil using a spanwise array ($S_{\text{act}} \leq 0.35c$) of discrete pulsed (combustion-based) jet actuators placed at $x/c = 0.15$ and operating on a time scale that is an order of magnitude shorter than the convective time scale of the base flow. In the two-dimensional configuration, the center segment and the actuator array were bounded by streamwise partitions ($S_{\text{fence}} = S_{\text{act}}$), while in the three-dimensional configuration the partitions were moved outboard ($S_{\text{fence}} > S_{\text{act}}$) to enable interactions between actuated and unactuated spanwise flow segments in nominally 2- and 3-D base flows. The effects of transitory actuation on the aerodynamic characteristics of the airfoil were assessed using force and torque

measurements along with surface pressure measurements, and planar and stereoscopic particle image velocimetry (PIV).

Two-dimensional transitory separation control was investigated on a static airfoil at $\alpha = 19^\circ$ using a single actuation pulse across the entire stalled flow segment between streamwise partitions $S_{\text{fence}} = S_{\text{act}} = 0.35c$ apart. Phase-locked, high-speed PIV measurements in the symmetry (mid) plane over the suction surface and in the near wake were used to characterize the transitory changes in and the characteristic time scales of the vorticity flux, and the increments in the circulation about the airfoil with specific emphasis on the onset and termination of the actuation. High-resolution flow field data in the vicinity of the actuators coupled with pressure measurements were acquired to elucidate the interactions between the pulsed jet and the cross flow. These findings were applied in successive single-pulse actuation to extend the flow attachment and enhance its global aerodynamic performance. Several actuation timing configurations were investigated to engender flow interactions that resulted in enhanced circulation.

Three-dimensional effects of the transitory actuation were investigated on two base stalled flows when the spanwise extent of the stalled flow bounded by the fences was increased beyond the edges of the actuators. In the first configuration of this unbounded actuation ($S_{\text{fence}} \approx c$) the base flow was nominally 2-D. The interactions between the 3-D actuation and the cross flow for two actuation widths ($S_{\text{act}} = 0.17c$ and $0.35c$ i.e., $S_{\text{act}}/S_{\text{fence}} \approx 0.17$ and 0.35) were examined using PIV measurements acquired in multiple cross stream planes phase-locked to the actuation that captured spanwise variations of the induced 3-D flow and in distribution of the sectional circulation. In the second configuration of unbounded actuation, the spanwise extent of the base flow was enlarged

by placing the partitions at the airfoil tips ($S_{\text{fence}} \approx 1.7c$), such that the base flow exhibits 3-D effects. Unbounded attachment was induced using single-pulse actuation ($S_{\text{act}} = 0.35c$) on static and the dynamically-pitching airfoils. In addition to the multi-plane PIV measurements, phase-locked stereoscopic PIV data were obtained across the span to extract the transient actuation effects, and the corresponding flow effects of the transitory actuation on the aerodynamic characteristics of the airfoil were assessed using phase-locked force and torque measurements. The effects of the actuation timing relative to the phase of the pitch cycle of the airfoil on dynamic control of lift and pitching moment on the airfoil were also investigated.

8.2. Bounded, 2-D Actuation

The 2-D dynamic response of the stalled flow ($S_{\text{fence}} = 0.35c$) over a static airfoil to single actuation pulse that is bounded ($S_{\text{act}} = S_{\text{fence}}$) is rather remarkable. Following the actuation, the separated vorticity layer is severed, becomes detached, and rolls into a large-scale $[O(0.5c)]$ CW vortex that is advected into the wake. The subsequent migration of the attached surface vorticity layer upstream of the CW vortex toward the trailing edge is accompanied by a transitory increase in circulation and lift. The attachment continues through $0.6c$ within about $2T_{\text{conv}}$ from the onset of the actuation and is followed by a considerably longer (about $10T_{\text{conv}}$) relaxation process that is characterized by a lift-off of the partially attached flow and an upstream migration of the separation point.

In the near wake, the onset of bounded actuation is first manifested in the shedding of a starting CCW vortex $[O(0.1c)]$ from the pressure surface at $t/T_{\text{conv}} \approx 0.5$ likely owing to the abrupt introduction of the pulsed jets that leads to a brief ($\sim 0.08T_{\text{conv}}$), small (3%

peak) increase in base flow circulation, and the subsequent shedding of the large-scale CW vortex from the suction surface induced by the jet interactions with the shear layer that leads to a decrease in circulation ($1 < t/T_{\text{conv}} < 1.8$, 13% peak). However, following the shedding of the CW vortex, there is a decrease in flux of CW vorticity in the near wake during flow attachment and accumulation of CW vorticity over the airfoil, leading to a rapid increase in circulation ($1.8 < t/T_{\text{conv}} < 2.2$, 22% peak) and in suction pressure on the surface that is followed by a lengthy, monotonic decrease (through $t/T_{\text{conv}} = 12$) to the level of the base flow during relaxation.

The brief ($0.1T_{\text{conv}}$) penetration of the pulsed jet into the nominally 2-D cross flow boundary layer upstream of separation that is accompanied by the formation of counter-rotating vorticity concentrations leads to a transient blockage disruption that deflects the oncoming flow away from the airfoil surface. The cross flow immediately upstream and downstream of the orifice respectively decelerated and accelerated almost symmetrically about the orifice. This abrupt blockage leads to temporal and spatial severing of the CW vorticity layer. The impulse associated with deflection of the flow upstream of the jet is marked by thrusting of the jet-induced CCW vorticity concentration into the outer flow, well above the separating shear layer while the CW vorticity merges with the same sense vorticity within the surrounding boundary layer.

The severing of the vorticity layer results in the roll-up of CW vorticity concentrations at its downstream and upstream edges. At the downstream edge, a large scale CW vortex that is formed by and engulfs the separating shear layer effectively advects the separated flow domain off the surface of the airfoil. Concomitantly, the blockage induced upstream of this large scale CW vortex that is marked by the presence

of a stagnation point upstream of the separated flow domain, leads to the roll-up of a “bull nose” CW vorticity concentration at the downstream edge of the attached upstream boundary layer. The flow at the downstream edge of the attached boundary layer introduces a cross stream pressure gradient ($dp/dy > 0$) that contributes to entrainment of faster cross flow fluid towards the airfoil’s surface thereby enhancing the streamwise spreading of boundary layer attachment beyond the separation point of the base flow upstream of the detached CW vortex even in the presence of the transitory, adverse streamwise pressure gradient and the upwash that are associated with the presence of the detached vortex.

Given that the celerity of the detached CW vortex ($\sim 0.8U_\infty$) is significantly higher than the celerity of the edge of the attaching boundary layer ($\sim 0.36U_\infty$), the domain of lower CW vorticity concentrations between them is extended and results in a temporal reduction in the flux of CW vorticity from the airfoil that along with accumulation of CW in the attaching boundary layer contributes to an overall increase in circulation about the airfoil. The blockage effect induced by the detached CW vortex decreases with increasing streamwise distances from the edge of the attaching boundary layer, and ultimately the attachment slows down. Following the shedding of the detached CW vortex, the attaching boundary layer begins to lift off the surfaces and the separation moves upstream again.

The disparity between the time scales of flow attachment and ultimate re-separation can be exploited to extend the duration and streamwise extent of flow attachment by successive actuation pulses that are repeated at T_{rep} . Repetitive actuation on a time scale that is comparable to the convective time scale, i.e., $T_{\text{rep}} = T_{\text{conv}}$ ($St_{\text{act}} = 1$) leads to a

circulation peak that increases monotonically with the number of actuation pulses until it saturates at about 55% above the level of the stalled base flow within $14T_{\text{conv}}$. The rise time and saturation level of the circulation are not significantly altered when the repetition rate of the pulse train is increased to $T_{\text{rep}} = 0.4T_{\text{conv}}$ (or $St_{\text{act}} = 2.5$). However, the severing and roll-up of the separated CW vorticity layer following each pulse during successive actuation diminishes in strength as the separating shear layer becomes increasingly attached. As the repetition rate increases (T_{rep} decreases, e.g., $St_{\text{act}} = 2.5$ and 3.5), these CW vortices begin to interact and ultimately become diffused and vanish resulting in a reduction in temporal variations of the circulation. Therefore, an increased number of successive actuation pulses are needed to attain the same overall circulation increment at higher repetition rates.

8.3. Unbounded Actuation

When pulsed actuation is effected by an unbounded actuator array the flow becomes attached by similar transitory mechanisms to the bounded 2-D separated flow (namely, severing of the separated CW vorticity layer, the shedding of a large-scale CW vortex, and attachment of the upstream boundary layer). However, the absence of spanwise bounds leads to spanwise spreading of transitory 3-D attachment *well beyond the spanwise edges of the actuators*, and, in general, to improved aerodynamic response (as may be measured by sectional circulation) compared to the 2-D actuation. Details of the evolution of the attached domain depend on whether the base flow is nominally 2- or 3-D which is varied with the spacing between the spanwise partitions S_{fence} that bound the flow domain over the airfoil.

When $S_{\text{fence}} \approx c$, the base flow between the partitions is nominally 2-D. As demonstrated using two actuation widths, $S_{\text{act}} = 0.13c$ and $0.35c$, when the actuation is unbounded the reduction in CW vorticity flux from the suction surface is prolonged compare to bounded actuation and the induced increase in sectional circulation (at mid-span) is larger (up to 60% relative to the base flow). As discussed in §VIII.2, the duration of the decrease in flux of CW vorticity is associated with the celerity dynamics of the detached and boundary layer CW vorticity concentrations. It appears that when the detached CW vortex is “free” (i.e., not confined by the partitions) its motion is affected such that the duration of the vorticity accumulation over the airfoil is prolonged as facilitated by the additional spanwise flow around the blockage induced by the finite-span actuation. Time traces of the circulation show that the unbounded actuation has two prominent effects. First, the increased sectional circulation is also accompanied by the presence of a second peak that is not present when the actuation is spanwise-bounded, and second, the outboard spanwise spreading of the affected flow domain well beyond the edges of the actuator.

The spanwise edges of the actuation effects can be discerned when the actuator span is sufficiently small (e.g., $S_{\text{act}} = 0.13c$). The edge of the affected flow domain is marked by the transition between the “inner” attached and “outer” separated flows. The spanwise edge of the detached CW vortex spreads by roll-up into the adjacent separated flow at about $0.3U_{\infty}$ as it is advected downstream. This spanwise spreading is non-uniform along its span and leads to similar, concomitant spreading of the low-vorticity domain upstream of the vortex and of the attached boundary layer. Owing to the spanwise decrease in the

strength of the detached CW vortex, the intensity of the severed vorticity domain and of the attachment of the boundary layer also diminish with spanwise distance.

The base flow becomes three dimensional as manifested by the formation of stall cells and outboard reduction in the cross stream width of the separated domain when the spanwise spacing of the flow partitions is increased to the airfoil's tips ($S_{\text{fence}} \approx 1.8c$). The flow response to single-pulse actuation ($S_{\text{act}} = 0.35c$) is unchanged for the most part compared to the nominally 2-D base flow, although the spanwise reduction in separation improves the spanwise spreading of the actuation effects. Stereoscopic PIV measurements across the span at $x/c \approx 0.78$ show that the base flow is characterized by the formation of spanwise-symmetric wall jets that form towards the outboard segments of the airfoil as a result of the spanwise spreading of the separated domain, and lead to the formation of counter-rotating streamwise vorticity concentrations on each side of center span. The presence of these streamwise vortices is not apparent in the 2-D base flow. The actuation has a profound effect of the 3-D structure of the flow. The significant reduction of the cross stream width of the separated flow leads to squashing and intensification of these vortices and to their spreading towards mid-span that is followed by complete suppression of the wall jets and disappearance of the streamwise vortices altogether rendering the attached spanwise segment of the flow nearly 2-D with no discernable transition (attached to separated) flow region.

The receptivity of the stalled flow over a 2-D airfoil to 3-D pulsed actuation (or the control authority of the actuation) can be further extended for controlling time-periodic separation on an airfoil that is undergoing time-periodic pitch beyond its stall limit ($10^\circ < \alpha < 18^\circ$, $k = 0.115$) by direct coupling between the timing of the actuation relative

to the pitch motion to take advantage of controlled temporal interactions with the unsteady 3-D separation. Despite the stall on the outboard, unactuated segments of the airfoil, single pulse actuation applied at different delays relative to the pitch cycle leads to an increase in lift during significant fractions of the oscillation cycle. Actuation during the upstroke can result in the higher transitory C_L at high angles of attack as the onset of stall is briefly delayed, while actuation during the downstroke following dynamic stall results in a prolonged, larger increase in C_L above base flow. Proper timing of the actuation can result in increased cycle average lift (up to about 3%, using only 20%-span actuation) accompanied by reduction in the time-dependent lift hysteresis. It is also shown that the synchronization of the actuation to the pitch cycle can significantly mitigate the effects of dynamic stall on pitch stability as measured by the extent of negative damping during the pitch cycle.

It is demonstrated that a burst of as few as eight actuation pulses ($1.41T_{\text{conv}}$ apart) that is triggered on the upstroke at $\alpha(t) = 14^\circ$ for the first 40% of the pitching cycle ($10T_{\text{conv}}$) can mitigate hysteretic effects during the up- and down-strokes of the oscillation cycle where the cyclic lift increases by 20% and the extent of “negative damping” of the pitching moment decreases by 71% relative to the baseline. In the presence of the actuation, the circulation (at the center plane) builds up for almost the entire pitching cycle and is about 44.7% higher than in the base flow. These timed interactions of pulsed actuation with the 3-D unsteady separated flow can regulate the evolution of vorticity on the airfoil and effectively altered the circulatory lift across the airfoil span to enhance the total unsteady lift on the airfoil throughout the entire pitching cycle. The results indicated that even in the presence of strong 3-D effects, tuning the timing of the

actuation pulses during the cycle can lead to an “optimal” pulsed actuation sequence that can effectively control and trap the vorticity concentrations that are associated with dynamic stall while minimizing actuation power.

8.4. Contributions of the Present Work

Contributions of the present investigations include some elements of the canonical behavior of transitory attachment on a static and pitching airfoil in 2- and 3-D base flows:

- Extension of pulsed combustion powered actuation technology (first developed by Crittenden and Glezer (2001) and by Brzozowski and Glezer (2006)) for transitory control of separation on static and pitching airfoil.
- Detailed measurements of the flow field associated with transitory 2- and 3-D, of single- and multiple-pulse actuation including static and dynamic pressure distributions.
- New insights into the attachment mechanisms effected by single and successive pulsed jets, and the role of the time scales of the onset and termination of actuation in circulation build-up.
- Demonstration that both 2- and 3-D stalled base flows are highly susceptible to pulse actuation, and illustrating the role of finite-span actuation over a fraction of the airfoil’s span in spanwise spreading of the attachment.
- Demonstration of the effectiveness of the coupling of actuation timing to the motion of a pitching airfoil for control of dynamic stall, and of the effectiveness of distributed discrete actuation through the pitching for improvement of unsteady lift and pitching moment.

8.5. Recommendations for Future Work

Based on the work presented in the dissertation, it is recommended that future experimental work should include:

- **Advances in COMPACT Technology**

The current understanding of the complex flows inside the combustion chamber and the combustion limits the design of the COMPACT. In order to develop versatile and robust actuator designs, the combustion physics inside the actuators require further research to better understand how to exploit the mixing parameters, and the chamber and orifice geometries to maximize the combustion effectiveness.

- **Pulsed Jet Geometry and Alignment Relative to the Flow**

Investigate effects of orifice geometry, aspect ratio, orientation and alignment of COMPACT and other conventional pulsed jets. Blockage produced by pulsed fluidic actuation should also be compared with mechanical actuation having similar dynamic characteristics (e.g., surface retractable fence).

- **Actuator Streamwise Placement and Spanwise Spacing**

The flow dynamics induced by pulsed jets at multiple streamwise locations upstream and downstream of separation should be examined to determine how vorticity roll-up can occur with and without severing of the shear layer. Different spanwise spacing of individual actuator orifices should also be investigated to understand possible role of edge effects on flow attachment.

- Increased Airfoil Aspect Ratio and Effect of Airfoil's Sweep

The effectiveness of pulsed actuation in the presence of multiple stall cells when the airfoil's aspect ratio is increased and in the presence of sweep should be examined.

- Airfoil Tip Effects

This study of the impulsive jet actuation on the separated shear layer flows over the airfoil is concentrated on the isolated separation between streamwise partitions. These flows should be examined to determine whether the actuation form relevant flow structures without the fences and over a finite airfoil to induce attachment.

- Analysis with Different Flow Conditions

For rotor blade applications, it would be useful to perform wind tunnel experiments with multiple airfoil motions at an elevated Mach number to account for compressibility effects in addition to matching Reynolds numbers for an extensive set of rotor blade sections including radial edge. It would also be useful to relate characteristic flow control times to a full-scale helicopter (e.g., UA-60) and investigate how the characteristic flow control times relate to the pitch and return times of a rotorcraft blade.

- Closed-Loop Flow Control

It would be helpful to extend the present findings to include closed-loop control to dynamic stall, and accommodate real-time variations in the flow field during the pitch cycle.

APPENDIX A

PARTICLE IMAGE VELOCIMETRY DATA

In this section, the experimental conditions for the particle image velocimetry acquired in the current investigation are tabulated. In Table A.1, the conditions for the static airfoil experiments (discussed in §IV - VII) are listed, while Table A.2 contains the conditions for the dynamic pitching airfoil experiments (discussed in §VII).

Table A.1: Static Airfoil PIV Data.

Experimental Conditions ($Re_c = 570,000$, $\alpha = 19^\circ$)	# of views	Image pairs/view	# of phases	# of planes	Image resolution ($\mu\text{m}/\text{pixel}$)	Interrogation spot size (pixels)
<i>Above airfoil, $S_{act} = S_{fence} = 0.35c$</i>						
$N = 1$ (single pulse)	3	200	20	1 ($z = 0$)	240.09	32 x 32
$N = 5$, $St_{act} = 1$, $T_{delay} = 100$ ms (two bursts)	3	200	185	1 ($z = 0$)	240.09	33 x 32
Continuous Actuation, $St_{act} = 1$	3	200	75	1 ($z = 0$)	240.09	34 x 32
<i>Near wake, $S_{act} = S_{fence} = 0.35c$</i>						
$N = 1$ (single pulse with decay)	2	200	75	1 ($z = 0$)	243.77	32 x 32
$N = 5$, $St_{act} = 1$ with decay	2	200	100	1 ($z = 0$)	243.77	32 x 32
$N = 10$, $St_{act} = 1$ with decay	2	200	165	1 ($z = 0$)	243.77	32 x 32
$N = 5$, $St_{act} = 1$, $T_{delay} = 100$ ms (two bursts)	2	200	185	1 ($z = 0$)	243.77	32 x 32
Continuous Actuation $St_{act} = 1$	2	200	75	1 ($z = 0$)	243.77	32 x 32
<i>Near wake, $S_{act} = S_{fence} = 0.35c$</i>						
$N = 25$, $St_{act} = 1$ with decay	3	210	225	1 ($z = 0$)	212.46	32 x 32
$N = 50$, $St_{act} = 2.5$ with decay	3	210	525	1 ($z = 0$)	212.46	32 x 32
<i>Near actuators, $S_{act} = S_{fence} = 0.35c$</i>						
$N = 1$ (single pulse with decay)	1	400	50	1 ($z = 0$)	217.67	16 x 16
$N = 10$ pulses at $St_{act} = 1$	1	400	250	1 ($z = 0$)	217.67	16 x 16
$N = 10$ pulses at $St_{act} = 2.5$	1	400	110	1 ($z = 0$)	217.67	16 x 16
$N = 10$ pulses at $St_{act} = 3.5$	1	400	90	1 ($z = 0$)	217.67	16 x 16
$N = 25$ pulses at $St_{act} = 1$	1	400	625	1 ($z = 0$)	217.67	16 x 16
$N = 50$ pulses at $St_{act} = 2.5$	1	400	510	1 ($z = 0$)	217.67	16 x 16

Table A.1: (Continued).

<i>Near wake, $S_{act} = 0.35c$, $S_{fence} \approx c$</i>						
$N = 1$ (single pulse with decay)	2	400	100	3 ($z/c = 0, 0.22, 0.33$)	219.87	32 x 32
<i>Near wake, $S_{act} = 0.13c$, $S_{fence} \approx c$</i>						
$N = 1$ (single pulse with decay)	2	250	200	24 ($0 \leq z/c \leq 0.295$)	280.23 320.55	32 x 32
<i>Above airfoil, $S_{act} = 0.35c$, $S_{fence} \approx 1.67c$</i>						
$N = 1$ (single pulse with decay)	1	160 - 180	88	4 ($0 \leq z/c \leq 0.39$) 1 (stereo) ($x \approx 0.78c$)	288.35	32 x 32
$N = 1$ (single pulse with decay)	1	200	88	($-0.27 \leq z/c \leq 0.76$)	302.79	32 x 32
<i>Near wake, $S_{act} = 0.35c$, $S_{fence} \approx 1.67c$</i>						
$N = 1$ (single pulse with decay)	1	160 - 180	88	4 ($0 < z/c < 0.39$)	312.33	32 x 32

Table A.2: Dynamic Pitching Airfoil PIV Data.

Experimental Conditions ($Re_c = 570,000$, $T_p = 625$ ms, $k = 0.115$, $\alpha_0 = 14^\circ$, $\alpha_p = 4^\circ$)	# of views	Image pairs/view	# of phases	# of planes	Image resolution ($\mu\text{m}/\text{pixel}$)	Interrogation spot size (pixels)
<i>Above airfoil, $S_{act} = 0.35c$, $S_{fence} \approx 1.67c$</i>						
$N = 1$ ($T_{start} = 150$ ms)	1	160 - 180	110	4 ($0 \leq z/c \leq 0.39$)	288.35	32 x 32
Baseline	1	160 - 180	100	4 ($0 \leq z/c \leq 0.39$) 1 (stereo) ($x \approx 0.78c$)	288.35	32 x 32
$N = 1$ ($T_{start} = 150$ ms)	1	200	110	($-0.27 \leq z/c \leq 0.76$) 1 (stereo) ($x \approx 0.78c$)	302.79	33 x 32
Baseline	1	200	110	($-0.27 \leq z/c \leq 0.76$)	302.79	33 x 32
$N = 8$ ($T_{start} = 0$, $T_{pulse} = 35$ ms)	3	200	625	1 ($z = 0$)	249.18	33 x 32
Baseline	3	200	625	1 ($z = 0$)	249.18	32 x 32
<i>Near wake, $S_{act} = 0.35c$, $S_{fence} \approx 1.67c$</i>						
$N = 1$ ($T_{start} = 150$ ms)	1	160 - 180	110	4 ($0 \leq z/c \leq 0.39$)	312.33	32 x 32
Baseline	1	160 - 180	110	4 ($0 \leq z/c \leq 0.39$)	312.33	32 x 32
$N = 8$ ($T_{start} = 0$, $T_{pulse} = 35$ ms)	2	250	125	1 ($z = 0$)	186.23	33 x 32
Baseline	2	200	125	1 ($z = 0$)	186.23	33 x 32

APPENDIX B

PRESSURE PORT DATA

The pressure port locations on the airfoil surface at midspan are shown in Table B.1 and are used in the integration to compute time-averaged airfoil lift.

Table B.1: Pressure Port Locations on Airfoil at $\alpha = 0^\circ$.

Port #	x/c	y/c	Port #	x/c	y/c	Port #	x/c	y/c
1	0.9324	0.0192	25	0.0950	0.0763	49	0.1097	-0.0401
2	0.8752	0.0349	26	0.0673	0.0654	50	0.1256	-0.0409
3	0.8104	0.0510	27	0.0578	0.0611	51	0.1557	-0.0417
4	0.7164	0.0713	28	0.0480	0.0560	52	0.1717	-0.0418
5	0.6787	0.0784	29	0.0388	0.0507	53	0.1877	-0.0416
6	0.6336	0.0861	30	0.0297	0.0449	54	0.2037	-0.0413
7	0.5864	0.0929	31	0.0228	0.0399	55	0.2197	-0.0408
8	0.5439	0.0989	32	0.0158	0.0340	56	0.2356	-0.0403
9	0.4968	0.1041	33	0.0097	0.0276	57	0.2516	-0.0397
10	0.4549	0.1079	34	0.0045	0.0206	58	0.2769	-0.0382
11	0.4173	0.1104	35	0.0011	0.0137	59	0.2982	-0.0372
12	0.3778	0.1123	36	0.0001	0.0061	60	0.3264	-0.0358
13	0.3508	0.1126	37	0.0007	-0.0029	61	0.3538	-0.0343
14	0.3262	0.1125	38	0.0045	-0.0100	62	0.3783	-0.0331
15	0.2959	0.1116	39	0.0098	-0.0156	63	0.4549	-0.0292
16	0.2743	0.1103	40	0.0169	-0.0206	64	0.4968	-0.0268
17	0.2516	0.1092	41	0.0242	-0.0244	65	0.5439	-0.0241
18	0.2373	0.1077	42	0.0308	-0.0270	66	0.5892	-0.0214
19	0.2232	0.1060	43	0.0381	-0.0294	67	0.6336	-0.0188
20	0.2088	0.1040	44	0.0463	-0.0317	68	0.6787	-0.0162
21	0.1947	0.1018	45	0.0546	-0.0335	69	0.7138	-0.0143
22	0.1465	0.0920	46	0.0622	-0.0350	70	0.8040	-0.0097
23	0.1233	0.0852	47	0.0706	-0.0363	71	0.8529	-0.0073
24	0.1078	0.0806	48	0.0949	-0.0390	72	0.8986	-0.0053

REFERENCES

- Abbott, I. H. and von Doenhoff, A. E., “*Theory of Wing Sections, Including a Summary of Airfoil Data*,” Courier Dover Publications, Mineola, NY, 1959.
- Adrian, R. J., and Westerweel, J., “*Particle Image Velocimetry*,” Cambridge University Press, Cambridge, UK, 2011.
- Ahuja, K. K., and Burrin, R. H., “Control of Flow Separation by Sound,” 9th Aeroacoustics Conference, AIAA Paper 1984-2298, October, 1984.
- Amitay, M., and Glezer, A., “Controlled Transients of Flow Reattachment over Stalled Airfoils,” *International Journal of Heat and Fluid Flow*, **23**(5), 690-699, 2002.
- Amitay, M., and Glezer, A., “Flow Transients Induced on a 2-D Airfoil by Pulse-Modulated Actuation,” *Experiments in Fluids*, **40**(2), 329-331, 2006.
- Ayers, R. F., and Wilde, M. R., “An Experimental Investigation of the Aerodynamic Characteristics of a Low Aspect Ratio Swept Wing with Blowing in a Spanwise Direction from the Tips,” The College of Aeronautics, Note 57, Cranfield, UK, 1956.
- Baker, C. J., “*Vortex Flow Around the Bases of Obstacles*,” Ph.D. Dissertation, St. Catharine’s College, University of Cambridge, 1978.
- Baker, C. J., “The Laminar Horseshoe Vortex,” *Journal of Fluid Mechanics*, **95**(2), 347-367, 1979.

- Bloxham, M. J., and Bons, J. P., "Combined Blowing and Suction to Control Both Midspan and Endwall Losses in a Turbomachinery Passage," ASME Turbo Expo 2010: Power for Land, Sea, and Air, 1609-1618, 2010.
- Bloxham, M. J., and Bons, J. P., "A Global Approach to Turbomachinery Flow Control: Passage Vortex Control," *Journal of Turbomachinery*, **136**(4), 041003, 2014.
- Bradley, R. G., and Wray, W. O., "A Conceptual Study of Leading-Edge-Vortex Enhancement by Blowing," *Journal of Aircraft*, **11**(1), 33-38, 1974.
- Brunn, A., Wassen, E., Sperber, D., Nitsche, W., and Thiele, F., "Active Drag Control for a Generic Car Model," In *Active Flow Control*, King, R., (Ed.), 247-259, Springer-Verlag Berlin Heidelberg, Berlin, Germany, 2007.
- Brzozowski, D. P., "*Dynamic Control of Aerodynamic Forces on a Moving Platform using Active Flow Control*," Ph.D. Dissertation, George W. Woodruff School of Mechanical Engineering, Georgia Institute of Technology, 2011.
- Brzozowski, D., and Glezer, A., "Transient Separation Control using Pulse-Combustion Actuation," 3rd Flow Control Conference, AIAA Paper 2006-3024, June, 2006.
- Cantwell, B., Coles, D., and Dimotakis, P., "Structure and Entrainment in the Plane of Symmetry of a Turbulent Spot," *Journal of Fluid Mechanics*, **87**, 641-672, 1978.
- Carr, L. W., "Progress in Analysis and Prediction of Dynamic Stall," *Journal of Aircraft*, **25**(1), 6-17, 1988.
- Carta, F. O., "An Analysis of the Stall Flutter Instability of Helicopter Rotor Blades," *Journal of the American Helicopter Society*, **12**(4), 1-18, 1967.

- Caruana, D., "Plasmas for Aerodynamic Control," *Plasma Physics and Controlled Fusion*, **52**(12), 124045, 2010.
- Caruana, D., Rogier, F., Dufour, G., and Gleyzes, C., "The Plasma Synthetic Jet Actuator, Physics, Modeling and Flow Control Application on Separation," Aerospace Lab Issue 6, 2013.
- Cattafesta III, L. N., and Sheplak, M., "Actuators for Active Flow Control," *Annual Review of Fluid Mechanics*, **43**, 247-272, 2011.
- Crittenden, T. M., "*Fluid Actuators for High Speed Flow Control*," Ph.D. Dissertation, George W. Woodruff School of Mechanical Engineering, Georgia Institute of Technology, 2003.
- Crittenden, T., Glezer, A., Funk, R., and Parekh, D., "Combustion-Driven Jet Actuators for Flow Control," 31st Fluid Dynamics Conference, AIAA Paper 2001-2768, June, 2001.
- Chang, P. K., "*Separation of Flow*," Pergamon Press, Oxford, UK, 1970.
- Chatellier, L., Laumonier, J., and Gervais, Y., "Active Control of the Aeroacoustics of Cavity Flows from the Downstream Edge," *Comptes Rendus Mécanique*, **334**(4), 259-265, 2006.
- Davidhazy, A., "Introduction to Shadowgraph and Schlieren Imaging," Rochester Institute of Technology, Technical Report, 2006.
- Desalvo, M., Whalen, E., and Glezer, A., "High-Lift Enhancement using Active Flow Control," 6th Flow Control Conference, AIAA Paper 2011-3355, June, 2012.

- Donovan, J. F., Kral, L. D., and Cary, A. W., "Active Flow Control Applied to an Airfoil," 36th Aerospace Sciences Meeting, AIAA Paper 1998-210, January, 1998.
- Duraisamy, K., and Baeder, J. D., "Active Flow Control Concepts for Rotor Airfoils using Synthetic Jets," 1st Flow Control Conference, AIAA Paper 2002-2835, June, 2002.
- Florea, R., and Wake, B. E., "Parametric Analysis of Directed-Synthetic Jets for Improved Dynamic-Stall Performance," 41st Aerospace Sciences Meeting, AIAA Paper 2003-216, January, 2003.
- Funk, R., Parekh, D., Crittenden, T., and Glezer, A., "Transient Separation Control using Pulse Combustion Actuation," 3rd Flow Control Conference, AIAA Paper 2002-3166, June, 2002.
- Gad-el-Hak, M., "*Flow Control: Passive, Active and Reactive Flow Management*," Cambridge University Press, Cambridge, UK, 2007.
- Gad-el-Hak, M., "Introduction to Flow Control," In *Flow Control*, Gad-el-Hak, M., Pollard, A., and Bonnet, J-P. (Ed.), 1-107, Springer-Verlag Berlin Heidelberg, Berlin, Germany, 1998.
- Gardner, A. D., Richter, K., Mai, H., Altmikus, A. R. M., Klein, A., and Rohardt, C. H., "Experimental Investigation of Dynamic Stall Performance for the EDI-M109 and EDI-M112 Airfoils," *Journal of the American Helicopter Society*, **58**(1), 1-13, 2013.

- Gardner, A. D., Richter, K., Mai, H., and Neuhaus, D., "Experimental Investigation of High-Pressure Pulsed Blowing for Dynamic Stall Control," *CEAS Aeronautical Journal*, **5**(2), 185-198, 2014.
- Giguere, P., and Selig, M. S., "Freestream Velocity Corrections for Two-Dimensional Testing with Splitter Plates," *AIAA Journal*, **35**(7), 1195-1200, 1997.
- Gilarranz, J. L., Traub, L. W., and Rediniotis, O. K., "A New Class of Synthetic Jet Actuators - Part II: Application to Flow Separation Control," *Journal of Fluids Engineering*, **127**(2), 377-387, 2005.
- Glezer, A., Kibens, V., Parekh, D., and Amitay, M., "The Dynamics of Flow Reattachment over a Thick Airfoil Controlled by Synthetic Jet Actuators," 37th Aerospace Sciences Meeting, AIAA Paper 1999-1001, January, 1999.
- Godard, G., and Stanislas, M., "Control of a Decelerating Boundary Layer. Part 1: Optimization of Passive Vortex Generators," *Aerospace Science and Technology* **10**(3), 181-191, 2006.
- Godard, G., Foucaut, J-M., and Stanislas, M., "Control of a Decelerating Boundary Layer. Part 2: Optimization of Slotted Jets Vortex Generators," *Aerospace Science and Technology*, **10**(5), 394-400, 2006.
- Godard, G., and Stanislas, M., "Control of a Decelerating Boundary Layer. Part 3: Optimization of Round Jets Vortex Generators," *Aerospace Science and Technology*, **10**(6), 455-464, 2006.

- Gorton, S. A., Owens, L. R., Jenkins, L. N., Allan, B. G., and Schuster, E. P., "Active Flow Control on a Boundary-Layer-Ingesting Inlet," 42nd Aerospace Sciences Meeting, AIAA Paper 2004-1203, January, 2004.
- Graham, D. J., Nitzberg, G. E., and Olson, R. N., "A Systematic Investigation of Pressure Distributions at High Speeds over Five Representative NACA Low-Drag and Conventional Airfoil Sections," Technical Report 832, NACA, 1945.
- Greenblatt, D., Ben-Harav, A., and Mueller-Vahl, H., "Dynamic Stall Control on a Vertical-Axis Wind Turbine using Plasma Actuators," *AIAA Journal*, **52**(2), 456-462, 2014.
- Greenblatt, D., and Wygnanski, I., "Dynamic Stall Control by Periodic Excitation, Part 1: NACA 0015 Parametric Study," *Journal of Aircraft*, **38**(3), 430-438, 2001.
- Haering, S., and Moser, R., "Numerical Study of Impulse Actuated Stall Control," *Bulletin of the American Physical Society*, **58**, 2013.
- Hasselbrink, E. F., and Mungal, M. G., "Transverse Jets and Jet Flames. Part 2. Velocity and OH Field Imaging," *Journal of Fluid Mechanics*, **443**, 27-68, 2001.
- Hazen, D. C., "Boundary-Layer Control," The National Committee for Fluid Mechanics Films, No. 21614, 1968.
- Hefner, J. N., and Bushnell, D. M., "Viscous Drag Reduction via Surface Mass Injection," In *Viscous Drag Reduction in Boundary Layers*, Bushnell, M. D., and Hefner, J. N., (Ed.), 457-476, AIAA, Washington, DC., 1990.
- Heine, B., Mulleners, K., Joubert, G., and Raffel, M., "Dynamic Stall Control by Passive Disturbance Generators," *AIAA Journal*, **51**(9), 2086-2097, 2013.

- Honohan, A. M., “*The Interaction of Synthetic Jets with Cross Flow and the Modification of Aerodynamic Surfaces*,” Ph.D. dissertation, George W. Woodruff School of Mechanical Engineering, Georgia Institute of Technology, 2003.
- Honohan, A. M., Amitay, M., and Glezer, A., “Aerodynamic Control using Synthetic Jets,” Fluids 2000 Conference, AIAA Paper 2000-2401, June, 2000.
- Kamotani, Y., and Greber, I., “Experiments on a Turbulent Jet in a Cross Flow,” *AIAA Journal*, **10**(11), 1425-1429, 1972.
- Kelso, R. M., Lim, T. T., and Perry, A. E., “An Experimental Study of Round Jets in Cross-Flow,” *Journal of Fluid Mechanics*, **306**, 111-144, 1996.
- Kukainis J., “Effects of Three-Dimensional Boundary Layer Control Devices on a Quasi-Two-Dimensional Swept Wing at High Subsonic Speeds,” Technical Report No. AEDC-TR-69-251, Arnold Air Force Base, TN, 1969:
- Kutay, A. T., Culp, J. R., Muse, J. A., Brzozowski, D. P., Glezer, A., and Calise, A. J., “A Closed-Loop Flight Control Experiment using Active Flow Control Actuators,” 45th Aerospace Sciences Meeting, AIAA Paper 2007-114, January, 2007.
- Lee, T., and Gerontakos, P., “Dynamic Stall Flow Control via a Trailing-Edge Flap,” *AIAA Journal*, **44**(3), 469-480, 2006.
- Lin, J. C., “Control of Turbulent Boundary-Layer Separation using Micro-Vortex Generators,” 30th Fluid Dynamics Conference, AIAA Paper 1999-3404, June, 1999.
- Liu, X., and Katz, J., “Instantaneous Pressure and Material Acceleration Measurements using a Four-Exposure PIV System,” *Experiments in Fluids*, **41**(2), 227-240, 2006.

- Lorber, P., McCormick, D., Anderson, T., Wake, B., MacMartin, D., Pollack, M., Corke, T., and Breuer, K., "Rotorcraft Retreating Blade Stall Control," Fluids 2000 Conference, AIAA Paper 2000-2475, June, 2000.
- Lorber, P. F., McCormick, D. C., Wake, B. E., and Florea, R., "Separation Control for Rotorcraft," Technical Report 2002-5.200.0015-5, United Technologies Research Center, East Hartford, CT, 2002.
- Luff, J. D., Drouillard, A. M., Rompage, M., Linne, M. A., and Hertzberg, J. R., "Experimental Uncertainties Associated with Particle Image Velocimetry (PIV) Based Vorticity Algorithms," *Experiments in Fluids*, **26**(1-2), 36-54, 1999.
- Marshall, L. A., "Boundary-Layer Transition Results from the F-16XL-2 Supersonic Laminar Flow Control Experiment," NASA TM-1999-209013, Dryden Flight Research Center, 1999.
- Martin, P. B., Wilson, J. S., Berry, J. D., Wong, T. C., Moulton, M., and McVeigh, M., "Passive Control of Compressible Dynamic Stall," 26th Applied Aerodynamics Conference, AIAA Paper 2008-7506, August, 2008.
- Maslov, A., Sidorenko, A. A., Zanin, B. Y., Postnikov, B. V., Budovsky, A. D., and Malmuth, N. D., "Plasma Control of Flow Separation on Swept Wing at High Angles of Attack," 46th Aerospace Sciences Meeting, AIAA Paper 2008-540, January, 2008.
- Matalanis, C. G., Min, B.-Y., Bowles, P. O., Jee, S., Wake, B. E., Crittenden, T., Woo, G., and Glezer, A., "Combustion-Powered Actuation for Dynamic Stall Suppression

- Simulations and Low-Mach Experiments,” American Helicopter Society 70th Annual Forum, 2014.
- McCroskey, W. J., “Unsteady Airfoils,” *Annual Review of Fluid Mechanics*, **14**(1), 285-311, 1982.
- McLachlan, B. G., “Study of a Circulation Control Airfoil with Leading/Trailing-Edge Blowing,” *Journal of Aircraft*, **26**(9), 817-821, 1989.
- Mueller-Vahl, H., Strangfeld, C., Nayeri, C. N., Paschereit, C. O., and Greenblatt, D., “Thick Airfoil Deep Dynamic Stall,” In *Wind Energy-Impact of Turbulence*, Hölling, M., Peinke, J., and Ivanell, S., (Ed.), 35-40, Springer-Verlag Berlin Heidelberg, Berlin, Germany, 2014.
- Mukherjee, R., and Gopalarathnam, A., “Post-Stall Prediction of Multiple-Lifting-Surface Configurations using a Decambering Approach,” *Journal of Aircraft*, **43**(3), 660-668, 2006.
- Mulleners, K., and Raffel, M., “The Onset of Dynamic Stall Revisited,” *Experiments in Fluids*, **52**(3), 779-793, 2012.
- Muppidi, S., and Mahesh, K., “Study of Trajectories of Jets in Crossflow using Direct Numerical Simulations,” *Journal of Fluid Mechanics*, **530**, 81-100, 2005.
- Neuburger, D., and Wygnanski, I., “The Use of a Vibrating Ribbon to Delay Separation on Two-Dimensional Airfoils: Some Preliminary Observations,” *Workshop II on Unsteady Separated Flow Proceedings*, 333-341, 1988.
- O’Donnell, K., Schober, S., Stolk, M., Marzocca, P., De Breuker, R., Abdalla, M., Nicolini, E., and Gürdal, Z., “Active Aeroelastic Control Aspects of an Aircraft

- Wing by using Synthetic Jet Actuators: Modeling, Simulations, Experiments,” In *SPIE 14th International Symposium on: Smart Structures and Materials and Nondestructive Evaluation and Health Monitoring*, **6523**, 0901-0909, 2007.
- Ozen, C. A., and Rockwell, D., “Flow Structure on a Rotating Plate,” *Experiments in Fluids*, **52**(1), 207-223, 2012.
- Panickar, P., and Raman, G., “Using Linear Stability Analysis as a Tool to Evaluate Jet and Cavity Flow Control Situations,” *International Journal of Flow Control*, **1**(1), 43-72, 2009.
- Pape, A. L., Costes, M., Joubert, G., David, F., and Deluc, J. M., “Dynamic Stall Control using Deployable Leading-Edge Vortex Generators,” *AIAA Journal*, **50**(10), 2135-2145, 2012.
- Perry, A. E., and Chong, M. S., “A Description of Eddying Motions and Flow Patterns using Critical-Point Concepts,” *Annual Review of Fluid Mechanics*, **19**(1), 125-155, 1987.
- Ponizy, B., and Wojcicki, S., “On Modeling of Pulse Combustors,” In *Symposium (International) on Combustion*, **20**, 2019-2024, 1985.
- Post, M. L., and Corke, T. C., “Separation Control on High Angle of Attack Airfoil using Plasma Actuators,” *AIAA Journal*, **42**(11), 2177-2184, 2004.
- Post, M. L., and Corke, T. C., “Separation Control using Plasma Actuators: Dynamic Stall Vortex Control on Oscillating Airfoil,” *AIAA Journal*, **44**(12), 3125-3135, 2006.

- Putnam, A. A., Belles, F. E., and Kentfield, J. A. C., "Pulse Combustion," *Progress in Energy and Combustion Science*, **12**(1), 43-79, 1986.
- Raffel, I. M., Willert, C. E., and Kompenhans, J., "*Particle Image Velocimetry*," Springer-Verlag Berlin Heidelberg, Berlin, Germany, 1998.
- Raghu, S., "Feedback-Free Fluidic Oscillator and Method," U.S. Patent No. 6,253,782, Washington, DC, 2001.
- Rajendar, A., Crittenden, T., and Glezer, A., "Characterization of the Internal Flow Dynamics of Combustion Powered Actuators," 4th Flow Control Conference, AIAA Paper 2008-3760, June, 2008.
- Rajendar, A., Crittenden, T., and Glezer, A., "Effect of Inlet Flow Configuration on Combustion Powered Actuators," 48th Aerospace Sciences Meeting, AIAA Paper 2010-1258, January, 2010.
- Richter, K., Pape, A. L., Knopp, T., Costes, M., Gleize, V., and Gardner, A. D., "Improved Two-Dimensional Dynamic Stall Prediction with Structured and Hybrid Numerical Methods," *Journal of the American Helicopter Society*, **56**(4), 1-12, 2011.
- Rival, D., and Tropea, C., "Characteristics of Pitching and Plunging Airfoils under Dynamic-Stall Conditions," *Journal of Aircraft*, **47**(1), 80-86, 2010.
- Sau, A., Sheu, T. W., Hwang, R. R., and Yang, W. C., "Three-Dimensional Simulation of Square Jets in Cross-Flow," *Physical Review E*, **69**(6), 066302, 2004.
- Schlichting, H., and Klaus G., "*Boundary-Layer Theory*," 8th Ed., Springer-Verlag Berlin Heidelberg, Berlin, Germany, 2000.

- Schrenk, O., "Experiments with Suction-Type Wings," NACA Technical Report, **773**, 1935.
- Seal, C. V., Smith, C. R., Akin, O., and Rockwell, D., "Quantitative Characteristics of a Laminar, Unsteady Necklace Vortex System at a Rectangular Block-Flat Plate Juncture," *Journal of Fluid Mechanics*, **286**, 117-135, 1995.
- Seal, C. V., Smith, C. R., and Rockwell, A. D., "Dynamics of the Vorticity Distribution in Endwall Junctions," *AIAA Journal*, **35**(6), 1041-1047, 1997.
- Seifert, A., Bachar, T., Koss, D., Shepshelovich, M., and Wygnanski, I., "Oscillatory Blowing: A Tool to Delay Boundary-Layer Separation," *AIAA Journal*, **31**(11), 2052-2060, 1993.
- Seifert, A., Darabi, A., and Wygnanski, I., "Delay of Airfoil Stall by Periodic Excitation," *Journal of Aircraft*, **33**(4), 691-698, 1996.
- Settles, G. S., "*Schlieren and Shadowgraph Techniques: Visualizing Phenomena in Transparent Media*," Springer-Verlag Berlin Heidelberg, Berlin, Germany, 2001.
- Singh, C., Peake, D. J., Coton, F., Kokkalis, A., Khodagolian, V., Coton, F., and Galbraith, R. A., "Parametric Study of an Air-Jet Vortex Generator Configuration to Control Rotorcraft Retreating Blade Stall," 43rd Aerospace Sciences Meeting, AIAA Paper 2005-1366, January, 2005.
- Smith, A. E., and Gordeyev, S., "Evaluation of Passive Boundary Layer Flow Control Methods for Aero-Optic Mitigation," 51st Aerospace Sciences Meeting, AIAA Paper 2013-718, January, 2013.

- Smith, B. L., and Glezer, A., "The Formation and Evolution of Synthetic Jets," *Physics of Fluids*, **10**(9), 2281-2297, 1998.
- Sosa, R., Artana, G., Moreau, E., and Touchard, G., "Flow Control with EHD Actuators in Middle Post Stall Regime," *Journal of the Brazilian Society of Mechanical Sciences and Engineering*, **28**(2), 200-207, 2006.
- Srinivasan, S., Girgis, B., and Menon, S., "Large-Eddy Simulation of a Combustion Powered Actuator," 44th Joint Propulsion Conference, AIAA Paper 2008-4680, July, 2008.
- Taylor, H. D., "The Elimination of Diffuser Separation by Vortex Generators," Technical Report 4012-3, United Technologies Research Center, East Hartford, CT, 1947.
- Tuck, A., and Soria, J., "Active Flow Control over a NACA 0015 Airfoil using a ZNMF Jet," In *15th Australasian Fluid Mechanics Conference*, 13-17, Sydney, Australia, 2004.
- Vasile, J. D., and Amitay, M., "Interactions of an Array of Finite Span Synthetic Jets and a Crossflow," *AIAA Journal*, **51**(10), 2503-2512, 2013.
- Visbal, M. R., "Numerical Investigation of Deep Dynamic Stall of a Plunging Airfoil," *AIAA Journal*, **49**(10), 2152-2170, 2011.
- Volino, R. J., "Separation Control on Low-Pressure Turbine Airfoils using Synthetic Vortex Generator Jets," ASME Turbo Expo 2003, 845-859, 2003.
- Wake, B. E., and Lurie, E. A., "Computational Evaluation of Directed Synthetic Jets for Dynamic Stall Control," American Helicopter Society 57th Annual Forum, 2001.

- Warta, B. J., “*Characterization of High Momentum Flux Combustion Powered Fluidic Actuators for High Speed Flow Control*,” M.S. Dissertation, George W. Woodruff School of Mechanical Engineering, Georgia Institute of Technology, 2007.
- Weaver, D., McAlister, K., and Tso, J., “Suppression of Dynamic Stall by Steady and Pulsed Upper-Surface Blowing,” 16th Applied Aerodynamics Conference, AIAA Paper 1998-2413, June, 1998.
- Weaver, D., McAlister, K., and Tso, J., “Control of VR-7 Dynamic Stall by Strong Steady Blowing,” *Journal of Aircraft*, **41**(6), 1404-1413, 2004.
- Williams, D. R., Quach, V., Kerstens, W., Buntain, S., Tadmor, G., Rowley, C., and Colonius, T., “Low-Reynolds Number Wing Response to an Oscillating Freestream with and without Feed Forward Control,” 47th Aerospace Sciences Meeting, AIAA Paper 2009-143, January, 2009.
- Winkelman, A. E., and Barlow, J. B., “Flowfield Model for a Rectangular Planform Wing Beyond Stall,” *AIAA Journal*, **18**(8), 1006-1008, 1980.
- Woo, G. T. K., Crittenden, T., and Glezer, A., “Transitory Control of a Pitching Airfoil using Pulse Combustion Actuation,” 4th Flow Control Conference, AIAA Paper 2008-4324, June, 2008.
- Woo, G. T. K., Crittenden, T. M., and Glezer, A., “Transitory Separation Control on a ROBIN Fuselage using Pulsed Actuation,” 37th European Rotorcraft Forum, Milan, Italy, 2011.
- Wood, N. J., and Roberts, L., “Experimental Results of the Control of a Vortical Flow by Tangential Blowing,” NASA Technical Report 30094, 1986.

- Wood, N. J., and Roberts, L., "Control of Vortical Lift on Delta Wings by Tangential Leading-Edge Blowing," *Journal of Aircraft*, **25**(3), 236-243, 1988.
- Wu, J. Z., Lu, X. Y., Denny, A. G., Fan, M., and Wu, J. M., "Post-Stall Flow Control on an Airfoil by Local Unsteady Forcing," *Journal of Fluid Mechanics*, **371**, 21-58, 1998.
- Wynanski, I., Sokolov, M., and Friedman, D., "On a Turbulent Spot in a Laminary Boundary Layer," *Journal of Fluid Mechanics*, **78**, 785-819, 1976.
- Yen, J., and Ahmed, N. A., "Parametric Study of Dynamic Stall Flow Field with Synthetic Jet Actuation," *Journal of Fluids Engineering*, **134**(7), 071106, 2012.
- Yilmaz, T., Ol, M., and Rockwell, D., "Scaling of Flow Separation on a Pitching Low Aspect Ratio Plate," *Journal of Fluids and Structures*, **26**(6), 1034-1041, 2010.
- Yu, Y. H., Lee, S., McAlister, K. W., Tung, C., and Wang, C. M., "Dynamic Stall Control for Advanced Rotorcraft Application," *AIAA Journal*, **33**(2), 289-295, 1995.
- Zanin, B. Y., Zverkov, I. D., Kozlov, V. V., and Pavlenko, A. M., "Vortex Structure of Separated Flows on Model Wings at Low Freestream Velocities," *Fluid Dynamics*, **43**(1), 938-944, 2008.
- Zanotti, A., Melone, S., Nilifard, R., and D'Andrea, A., "Experimental-Numerical Investigation of a Pitching Airfoil in Deep Dynamic Stall," *Journal of Aerospace Engineering*, **228**(4), 557-566, 2014.

Zhang, S., and Zhong, S., "An Experimental Investigation of Turbulent Flow Separation Control by an Array of Synthetic Jets," 5th Flow Control Conference, AIAA Paper 2010-4582, June, 2010.

Zinn, B. T., "Pulse Combustion: Recent Applications and Research Issues," In *Symposium (International) on Combustion*, **24**(1), 1297-1305, 1992.

VITA

George Woo is the youngest of four children and he grew up in Honiara, Solomon Islands with his parents, Jack and Huirong, and his brothers, Stephen and David, and sister, Mary. In 1997, following the footsteps of his eldest brother, Stephen, he moved with his other siblings to Nelson, New Zealand for high school as a boarding student. At Nelson College, he developed an increased affinity toward the physical sciences and was inspired by the achievements of Lord Ernst Rutherford, a Chemist Nobel laureate and an “old boy” of Nelson College, to pursue a future academic career. He graduated high school in 2000, and was named dux of the school, and chose to attend University of Canterbury (formerly, Canterbury College when Lord Rutherford attended) in Christchurch, New Zealand. There, he became interested in fluid mechanics while studying in the Mechanical Engineering Department, and decided to pursue a post-graduate degree following some work experience. He worked at WhisperTech and graduated with his undergraduate Engineering degree in 2004 before moving to California, USA in 2005 to pursue a Masters degree. He completed his M.S. at Stanford University in 2007 working with Professors John Eaton and Godfrey Mungal, and joined Professor Ari Glezer’s research group at the Georgia Institute of Technology that summer to continue his research in experimental fluid mechanics. Inspired by Rutherford, George had always aspired to becoming a professor. However, he decided to pursue a professional career in industry following the completion of his Ph.D. studies.